

Curcuma mangga-MEDIATED SYNTHESIS OF GOLD
NANOPARTICLES AND THEIR PHOTOTHERMAL
AND PROTEIN INTERACTION STUDIES

FOO YIING YEE

FACULTY OF SCIENCE
UNIVERSITY OF MALAYA
KUALA LUMPUR

2018

***Curcuma mangga*-MEDIATED SYNTHESIS OF GOLD
NANOPARTICLES AND THEIR PHOTOTHERMAL
AND PROTEIN INTERACTION STUDIES**

FOO YIING YEE

**THESIS SUBMITTED IN FULFILMENT OF THE
REQUIREMENTS FOR THE DEGREE OF
DOCTOR OF PHILOSOPHY**

**INSTITUTE OF BIOLOGICAL SCIENCES
FACULTY OF SCIENCE
UNIVERSITY OF MALAYA
KUALA LUMPUR**

2018

UNIVERSITY OF MALAYA
ORIGINAL LITERARY WORK DECLARATION

Name of Candidate: FOO YIING YEE

Matric No: SHC130102

Name of Degree: Doctor of Philosophy (Ph.D.)

Title of Thesis: “*Curcuma mangga*-mediated synthesis of gold nanoparticles and their photothermal and protein interaction studies”

Field of Study: Cancer Biology, Biochemistry, Biophysics

I do solemnly and sincerely declare that:

- (1) I am the sole author/writer of this Work;
- (2) This Work is original;
- (3) Any use of any work in which copyright exists was done by way of fair dealing and for permitted purposes and any excerpt or extract from, or reference to or reproduction of any copyright work has been disclosed expressly and sufficiently and the title of the Work and its authorship have been acknowledged in this Work;
- (4) I do not have any actual knowledge nor do I ought reasonably to know that the making of this work constitutes an infringement of any copyright work;
- (5) I hereby assign all and every rights in the copyright to this Work to the University of Malaya (“UM”), who henceforth shall be owner of the copyright in this Work and that any reproduction or use in any form or by any means whatsoever is prohibited without the written consent of UM having been first had and obtained;
- (6) I am fully aware that if in the course of making this Work I have infringed any copyright whether intentionally or otherwise, I may be subject to legal action or any other action as may be determined by UM.

Candidate’s Signature

Date:

Subscribed and solemnly declared before,

Witness’s Signature

Date:

Name:

Designation:

Witness’s Signature

Date:

Name:

Designation:

GREEN SYNTHESIS OF GOLD NANOPARTICLES AND THEIR PHOTOTHERMAL AND PROTEIN INTERACTION STUDIES

ABSTRACT

Utilization of toxic chemicals in the synthesis of gold nanoparticles (AuNPs), poor stability and low biocompatibility of AuNPs in physiological system are some of the factors that limit the clinical applications of AuNPs. Herein, we describe the use of *Curcuma mangga* (CM) extract as an alternative method for the synthesis of safe, stable and biocompatible CM-AuNPs to circumvent these constraints. Effects of time, CM extract and gold (III) chloride trihydrate ($\text{HAuCl}_4 \cdot 3\text{H}_2\text{O}$) concentration on the synthesis of CM-AuNPs were studied using UV-Vis spectroscopy. Incubation of 4 ml of CM extract (10 mg/ml) and 10 ml of HAuCl_4 (1 mM) for 24 h at room temperature was found to produce spherical AuNPs with higher stability, thus these conditions were used to synthesize CM-AuNPs for subsequent studies. Transmission electron microscopic analyses characterized CM-AuNPs as spherical particles with an average particle diameter of 15.6 nm. The field effect scanning electron microscopic data also supported these results. Fourier transform infrared spectral analysis showed importance of carbonyl groups of terpenoids, present in the CM extract used in the synthesis of CM-AuNPs, which act as a reducing agent. Greater stability of CM-AuNPs compared to citrate-AuNPs in various buffers or media was evident from the absence of significant change in the UV-Vis spectral characteristics. CM-AuNPs also exhibited low cytotoxicity to human colon fibroblast, CCD-18Co and human lung fibroblast, MRC-5 cell lines. Furthermore, CM-AuNPs were also found to be red cell-compatible, showing less than 10% hemolysis without any erythrocytes' aggregation. The interaction of CM-AuNPs with human serum albumin (HSA) was also investigated to understand their transport in human circulation. Fluorescence spectral studies suggested that the interaction of CM-AuNPs with HSA was

initiated by dynamic quenching mechanism. The binding constant obtained at 25°C was found to be $0.97 \times 10^4 \text{ M}^{-1}$, indicating moderate binding affinity between CM-AuNP and HSA. Thermodynamic analysis revealed involvement of hydrophobic forces in CM-AuNP-HSA complexation. Alteration in the tertiary structure of the protein was also observed upon interaction of HSA with CM-AuNPs, as analyzed by circular dichroism analysis. Three-dimensional fluorescence spectral results suggested microenvironmental perturbations around protein's fluorophores upon CM-AuNPs interaction with HSA. CM-AuNPs binding site has been predicted to be Sudlow's site II, located in subdomain IIIA of HSA. Photothermal efficiency of CM-AuNPs was evident from the increase in the media temperature upon photoirradiation. The media temperature increased with increasing laser intensity and CM-AuNP concentrations. The percentage viability of MCF-7 breast cancer cells was markedly reduced upon photothermal treatment with CM-AuNPs. CM-AuNP-dependent photothermal-induced MCF-7 cells' death were found to be mediated by apoptosis. All these results suggested potential use of CM-AuNPs as therapeutic agents in cancer therapy.

Keywords: gold nanoparticles, *Curcuma mangga*, human serum albumin, fluorescence quenching, photothermal effect

SINTESIS HIJAU NANOPARTIKEL AURUM DAN KAJIAN FOTOTERMA DAN INTERAKSI PROTEIN

ABSTRAK

Antara faktor-faktor yang menghadkan penggunaan partikel emas nano (AuNPs) dalam bidang perubatan ialah penggunaan bahan kimia toksik untuk sintesis AuNPs, ketidakstabilan AuNPs dalam sistem fisiologi dan keserasian biologi yang rendah. Dalam kajian ini, sintesis hijau dengan ekstrak *Curcuma mangga* (CM) digunakan sebagai kaedah alternatif untuk menghasilkan CM-AuNPs yang selamat, stabil dan bio serasi dalam menangani kekangan tersebut. Kesan masa, kepekatan ekstrak CM dan aurum (III) klorida trihidrat ($\text{HAuCl}_4 \cdot 3\text{H}_2\text{O}$) terhadap sintesis CM-AuNPs telah dikaji dengan menggunakan spektroskopi UV-Vis. Inkubasi 4 ml ekstrak CM (10 mg/ml) dengan 10 ml HAuCl_4 (1 mM) selama 24 jam dalam suhu bilik didapati menghasilkan AuNPs yang berbentuk sfera dengan kestabilan yang lebih tinggi. Oleh itu, keadaan tersebut telah digunakan untuk menghasilkan CM-AuNPs bagi kajian seterusnya. Mikroskopi elektron transmisi mencirikan CM-AuNPs sebagai zarah berbentuk sfera dengan diameter purata zarah sebagai 15.6 nm. Data daripada mikroskop pengimbas elektron kesan medan juga mengesahkan keputusan tersebut. Analisis dari spektroskopi inframerah transformasi fourier menunjukkan kepentingan kumpulan karbonyl dalam terpenoid yang hadir dalam ekstrak CM yang digunakan dalam sintesis CM-AuNP, bertindak sebagai agen reduksi. Kestabilan CM-AuNPs yang lebih tinggi berbanding dengan sitrat-AuNPs di dalam pelbagai buffer atau media disahkan oleh ketidakhadiran perubahan ketara dalam pencirian spektra UV-Vis. CM-AuNPs juga mempamerkan ketoksikan yang rendah terhadap sel-sel fibroplast kolon manusia CCD-18Co dan fibroplast paru-paru manusia MRC-5. Selanjutnya, CM-AuNPs juga telah didapati serasi dengan sel darah merah, menunjukkan peratusan hemolysis yang kurang daripada 10% tanpa sebarang pengagregatan sel darah merah. Interaksi CM-AuNPs dengan albumin serum manusia

(HSA) juga diselidik untuk memahami pengangkutannya dalam sistem peredaran manusia. Spektroskopi fluoresens mencadangkan interaksi antara CM-AuNPs dengan HSA telah dicetuskan oleh mekanisme pelindapkejutan dinamik. Nilai pemalar pengikatan pada 25°C telah didapati sebagai $0.97 \times 10^4 \text{ M}^{-1}$, menunjukkan kekuatan pengikatan yang sederhana antara CM-AuNP dengan HSA. Analisis termodinamik mengutarakan penglibatan daya-daya hidrofobik dalam pengkompleksan CM-AuNP-HSA. Perubahan di dalam struktur tertiar protein juga telah diperhatikan selepas interaksi HSA dengan CM-AuNP, seperti yang dianalisis oleh dikroisma bulatan. Spektroskopi fluoresens 3D mencadangkan perubahan persekitaran mikro di sekitar fluorophores protein ketika interaksi CM-AuNP dengan HSA. Tapak pengikatan CM-AuNP telah diramalkan sebagai tapak II Sudlow, terletak dalam subdomain IIIA HSA. Kecekapan fototerma CM-AuNPs telah ditunjukkan dengan kenaikan suhu media apabila disinarkan dengan laser. Suhu media meningkat dengan peningkatan keamatan laser dan kepekatan CM-AuNP. Peratusan “viability” sel kanser dada MCF-7 telah menurun secara mendadak selepas dirawat dengan CM-AuNP. Kematian sel-sel MCF-7 didorong oleh proses fototerma dan bergantung kepada CM-AuNP telah dicetuskan oleh apoptosis. Semua keputusan tersebut mencadangkan potensi kegunaan CM-AuNP sebagai agen terapeutik bagi rawatan kanser.

Kata kunci: partikel emas nano, *Curcuma mangga*, albumin serum manusia, pelindapkejutan kependarfluoran, kesan fototerma

ACKNOWLEDGEMENTS

I express my deepest gratitude to my supervisors, Associate Professor Vengadesh Periasamy, Professor Saad Tayyab and Professor Datin Sri Nurestri Abd Malek for their continuous support and motivation throughout my doctoral study. I highly appreciate their guidance, invaluable input and willingness to spend their time in completion of this project. It is a great honour to work under their supervision.

My great appreciations to Associate Professor Kiew Lik Voon and Dr. Gnana Kumar for their kind advice and insightful suggestions on the collaborative works. I am thankful to Prof. Rauzah binti Hashim and Dr. Chong Wu Yi for their kindness in allowing me to use the instruments in the laboratories at the Departments of Chemistry and Physics, respectively.

I offer my special thanks to Professor Zanariah Abdullah, Dean, Faculty of Science and Associate Professor Dr. Nurhayati Zainal Abidin, Head, Institute of Biological Sciences, University of Malaya for providing sufficient facilities for research.

I am also particularly grateful to my labmates and friends, especially, Wai Kuan, Yen Fong, Eric Saw, Jaime, Syarifah Nur, Kabir and Musoddiq for their constant help and valuable suggestions for my experimental work. I would also like to acknowledge the staff of Institute of Biological Sciences, Departments of Physics and Chemistry as well as High Impact Research (HIR), who helped me to carried out this work.

Financial support from the University of Malaya in term of University Malaya Fellowship Scheme, HIR Research Fund and Postgraduate Research Fund is greatly acknowledged.

Lastly, I must express my profound gratitude to my family and friends, especially Eng How for being supportive and encouraging me throughout the years of this study.

TABLE OF CONTENTS

ABSTRACT	iii
ABSTRAK	v
ACKNOWLEDGEMENT	vii
TABLE OF CONTENTS	viii
LIST OF FIGURES	xii
LIST OF TABLES	xv
LIST OF SYMBOLS AND ABBREVIATIONS	xvi
CHAPTER 1: INTRODUCTION	1
1.1 Research background	1
1.2 Problem statement and research objectives	3
1.3 Thesis outline	4
CHAPTER 2: LITERATURE REVIEW	5
2.1 Cancer	5
2.1.1 Tumor physiology and enhanced permeability and retention effect	5
2.1.2 Cancer treatment and limitations	6
2.2 Nanotechnology	9
2.2.1 Cancer nanomedicine	9
2.2.2 Gold nanoparticles	12
2.2.2.1 AuNPs synthesis	13
2.2.2.2 Properties of AuNPs	20
2.2.2.3 Applications of AuNPs	23
2.3 Interaction of nanoparticles with plasma proteins	38
2.3.1 Physicochemical properties of HSA	39
2.3.2 Amino acid composition and structural properties of HSA	41

2.3.3	Functions of HSA	44
2.3.4	Ligand binding properties	45
2.3.5	Interaction of AuNPs with HSA	47
CHAPTER 3: MATERIALS AND METHODS		49
3.1	Materials	49
3.1.1	CM-AuNPs synthesis and characterization	49
3.1.2	Cell culture	49
3.1.3	Protein interaction studies	49
3.1.4	Miscellaneous	50
3.2	Methods	50
3.2.1	Synthesis of CM-AuNPs	50
3.2.1.1	Extraction of <i>Curcuma manga</i> extract	50
3.2.1.2	Preparation of stock solutions	50
3.2.1.3	Method of preparation	51
3.2.1.4	Purification and concentration measurements	52
3.2.2	Characterization of CM-AuNPs	52
3.2.2.1	High resolution-transmission electron microscopy	52
3.2.2.2	Field effect scanning electron microscopy and energy dispersive X-ray spectroscopy	52
3.2.2.3	Fourier transform infra-red spectroscopy	53
3.2.2.4	Zeta potential and hydrodynamic size measurements	53
3.2.2.5	<i>In vitro</i> stability study	53
3.2.3	Biocompatibility of CM-AuNPs	54
3.2.3.1	Cytotoxicity study	54
3.2.3.2	Hemocompatibility study	55
3.2.4	Interaction of CM-AuNPs with HSA	57

3.2.4.1	Preparation of stock solutions	57
3.2.4.2	Fluorescence quenching titration	57
3.2.4.3	Absorption spectral analysis	60
3.2.4.4	Analysis of protein structural changes	60
3.2.4.5	Site-specific marker displacement studies	61
3.2.5	Photothermal anticancer activity of CM-AuNPs	62
3.2.5.1	Preparation of media and reagent	62
3.2.5.2	Photothermal heating curves	62
3.2.5.3	<i>In vitro</i> photothermal treatment	63
3.2.5.4	FITC-Annexin V / PI apoptosis assay	64
CHAPTER 4: RESULTS AND DISCUSSION		66
4.1	Green synthesis of CM-AuNPs	66
4.1.1	Effect of reaction time	66
4.1.2	Effect of CM extract concentration	68
4.1.3	Effect of HAuCl ₄ concentration	73
4.2	Characterization of CM-AuNPs	78
4.2.1	Determination of size, shape and composition	78
4.2.2	Identification of reactive functional group	82
4.2.3	Effect of buffers / media on zeta potential and hydrodynamic size	85
4.2.4	<i>In vitro</i> stability	90
4.3	Biocompatibility of CM-AuNPs	92
4.3.1	Cytotoxicity	93
4.3.2	Hemocompatibility	96
4.4	Interaction of CM-AuNPs with HSA	102
4.4.1	Fluorescence quenching	102

4.4.2	Binding constant and thermodynamic parameters	109
4.4.3	Absorption spectra	114
4.4.4	Circular dichroism spectra	116
4.4.5	Three-dimensional fluorescence spectra	119
4.4.6	Identification of CM-AuNP binding site on HSA	125
4.5	Photothermal effects of CM-AuNPs	130
4.5.1	Photothermal properties	131
4.5.2	Laser safety	135
4.5.3	<i>In vitro</i> photothermal cytotoxicity	135
4.5.4	Apoptosis detection in photothermal-induced cell death	138
CHAPTER 5: CONCLUSIONS		143
5.1	Conclusions	143
5.2	Future perspectives	143
REFERENCES		145
LIST OF PUBLICATIONS AND PAPER PRESENTED		170

LIST OF FIGURES

Figure 2.1:	Diagram showing distribution of nanoparticles in normal and tumor tissues.	7
Figure 2.2:	Scheme showing bottom-up and top-down syntheses of gold nanoparticles.	14
Figure 2.3:	Examples of various organisms used in the green synthesis of gold nanoparticles.	17
Figure 2.4:	(A) Photograph of <i>Curcuma mangga</i> rhizome. (B) Chemical structures of some of the known terpenoids, present in <i>Curcuma mangga</i> .	19
Figure 2.5:	Diagram showing various biomedical applications of AuNPs.	24
Figure 2.6:	Diagrams showing photothermal-induced cell death through two mechanisms (A) and proposed apoptosis mechanism as a result from photothermal treatment (B).	33
Figure 2.7:	Amino acid sequence and disulfide bonding pattern of HSA.	43
Figure 2.8:	Ligand binding sites of HSA.	46
Figure 3.1:	Flow chart of research work	65
Figure 4.1:	UV-Vis absorption spectra of CM-AuNPs, synthesized at different incubation times.	67
Figure 4.2:	Plots showing change in the absorbance of λ_{\max} (A) and absorption maximum (B) of the mixture containing CM extract and HAuCl ₄ with increasing incubation time.	69
Figure 4.3:	UV-Vis absorption spectra of CM-AuNPs, synthesized using different concentrations of CM extract.	70
Figure 4.4:	Kinetic plots showing change in absorbance at 535 nm with time for mixtures containing CM extract and HAuCl ₄ .	72
Figure 4.5:	Zeta potential values of CM-AuNPs, synthesized using different concentrations of CM extract.	74
Figure 4.6:	UV-Vis absorption spectra of CM-AuNPs, synthesized using different concentrations of HAuCl ₄ .	75
Figure 4.7:	Zeta potential values of CM-AuNPs, synthesized using different concentrations of HAuCl ₄ .	77
Figure 4.8:	TEM images of CM-AuNPs at magnification of 100,000 \times (A) and 500,000 \times (B).	79

Figure 4.9:	Histogram showing size distribution of CM-AuNPs.	80
Figure 4.10:	(A) FESEM image (50,000× magnification) of CM-AuNPs. (B) EDX spectrum of CM-AuNPs.	81
Figure 4.11:	FTIR spectrum of oven-dried (60 °C) CM extract.	83
Figure 4.12:	FTIR spectrum of freeze-dried residue fraction of CM extract left upon CM-AuNPs synthesis.	84
Figure 4.13:	Proposed mechanism for the formation of CM-AuNPs, synthesized using CM extract as a reducing and stabilizing agent.	86
Figure 4.14:	UV-Vis absorption spectra of CM-AuNPs (A) and citrate-AuNPs (B) after 24 h incubation in various media.	91
Figure 4.15:	Bar diagram showing percentage viability of CCD-18Co cells after treatment with CM-AuNPs for 24 h (A) and 72 h (B).	94
Figure 4.16:	Bar diagram showing percentage viability of MRC-5 cells after treatment with CM-AuNPs for 24 h (A) and 72 h (B).	95
Figure 4.17:	Bar diagram showing percentage viability of CCD-18Co cells after treatment with CM extract for 24 h (A) and 72 h (B).	97
Figure 4.18:	Bar diagram showing percentage viability of MRC-5 cells after treatment with CM extract for 24 h (A) and 72 h (B).	98
Figure 4.19:	Percentage hemolysis of human red blood cells after incubation with AuNPs or CM extract.	100
Figure 4.20:	Micrographs (100× magnification) of red blood cells after incubation with CM-AuNPs, CM extract and CTAB-AuNPs.	101
Figure 4.21:	Quenching of HSA fluorescence induced by CM-AuNPs addition at 25 °C.	104
Figure 4.22:	Quenching of HSA fluorescence induced by CM-AuNPs addition at 30 °C.	105
Figure 4.23:	Quenching of HSA fluorescence induced by CM-AuNPs addition at 35 °C.	106
Figure 4.24:	Stern-Volmer plots for quenching of HSA fluorescence induced by CM-AuNPs addition.	107
Figure 4.25:	Double logarithmic plots for the fluorescence quenching data of CM-AuNP-HSA interaction.	110
Figure 4.26:	van't Hoff plot for the interaction between CM-AuNP and HSA.	112

Figure 4.27:	UV-Vis absorption spectra of HSA in the absence and presence of CM-AuNPs.	115
Figure 4.28:	Far-UV CD spectra of HSA in the absence and presence of CM-AuNPs.	117
Figure 4.29:	Near-UV CD spectra of HSA in the absence and presence of CM-AuNPs.	118
Figure 4.30:	Three-dimensional fluorescence spectrum and corresponding contour map of HSA.	120
Figure 4.31:	Three-dimensional fluorescence spectrum and corresponding contour map of CM-AuNPs:HSA (3:1) mixture.	121
Figure 4.32:	Three-dimensional fluorescence spectrum and corresponding contour map of CM-AuNPs:HSA (6:1) mixture.	122
Figure 4.33:	Three-dimensional fluorescence spectrum and corresponding contour map of CM-AuNPs.	123
Figure 4.34:	Relative fluorescence intensity at 385 nm of WFN:HSA (1:1) mixture with addition of CM-AuNPs.	126
Figure 4.35:	Effect of increasing CM-AuNP concentrations on the fluorescence spectrum of ANS-HSA complex, upon excitation at 295 nm.	128
Figure 4.36:	Effect of increasing CM-AuNP concentrations on the fluorescence spectrum of ANS-HSA complex, upon excitation at 350 nm.	129
Figure 4.37:	Photothermal heating curves of CM-AuNPs upon irradiation with laser of different intensities.	132
Figure 4.38:	Photothermal heating curves of different concentrations of CM-AuNPs upon laser irradiation.	134
Figure 4.39:	Percentage cell viability of MCF-7 cells in DMEM media, upon laser irradiation for varying time periods.	136
Figure 4.40:	Percentage cell viability of MCF-7 cells, upon various treatments with or without laser irradiation.	137
Figure 4.41:	Dot plots showing flow cytometry results of Annexin V-PI apoptosis assay for MCF-7 cells upon photothermal treatment with CM-AuNPs (A), citrate-AuNPs (B) and untreated MCF-7 cells (C).	140
Figure 4.42:	Bar diagram for analysis of the percentage of cell population in each quadrant of the dot plots, shown in Figure 4.41.	141

LIST OF TABLES

Table 2.1:	FDA-approved nanomedicines and those undergoing clinical trials for cancer treatment.	11
Table 2.2:	<i>In vivo</i> applications of gold nanoparticles for cancer imaging.	26
Table 2.3:	<i>In vivo</i> applications of gold nanoparticles in photothermal treatment of various cancers.	30
Table 2.4:	Theranostic applications of gold nanoparticles.	35
Table 2.5:	Physicochemical properties of HSA.	40
Table 2.6:	Amino acid composition of HSA.	42
Table 4.1:	Zeta potential values of CM-AuNPs after 24 h incubation in different buffers / media.	87
Table 4.2:	Hydrodynamic size of CM-AuNPs after 24 h incubation in different buffers / media.	89
Table 4.3:	Values of the Stern-Volmer constant, binding constant and Hill coefficient for the interaction of CM-AuNP with HSA.	108
Table 4.4:	Thermodynamic parameters for the interaction of CM-AuNP with HSA.	113
Table 4.5:	Three-dimensional fluorescence spectral characteristics of HSA in the absence and presence of CM-AuNPs as well as free CM-AuNPs.	124

LIST OF SYMBOLS AND ABBREVIATIONS

~	:	Approximate
λ_{ex}	:	Emission wavelength
λ_{em}	:	Excitation wavelength
>	:	Greater than
<	:	Less than
\leq	:	Less than or equal to
\times	:	Times
a.u.	:	Absorbance unit
Abs	:	Absorbance
AIDS	:	Acquired immune deficiency syndrome
Ala	:	Alanine
ALL	:	Acute lymphocytic leukemia
AML	:	Acute myeloid leukemia
ANS	:	1-Anilinonaphthalene-8-sulfonate
Apaf-1	:	Apoptotic protease activating factor 1
Arg	:	Arginine
Asp	:	Aspartic acid
Au^0	:	Gold atom
Au^+	:	Aurous ion
Au^{3+}	:	Auric ion
AuNPs	:	Gold nanoparticles
^{199}Au	:	Gold-199
Å	:	Amstrong
°C	:	Degree Celcius

CaCl ₂	:	Calcium chloride
Citrate-AuNPs	:	Citrate-gold nanoparticles
CM	:	<i>Curcuma mangga</i>
cm	:	Centimeter
CM-AuNPs	:	Gold nanoparticles synthesized using <i>Curcuma mangga</i> extract
CO ₂	:	Carbon dioxide
CT	:	Computed tomography
CTAB	:	Cetyltrimethylammonium bromide
CTAB-AuNPs	:	CTAB-gold nanoparticles
CXCR4	:	Chemokine receptor type 4
Cys	:	Cysteine
⁶⁴ Cu	:	Copper-64
Da	:	Dalton
DAMPs	:	Damage-associated molecular patterns
dATP	:	Deoxyadenosine triphosphate
dL	:	deciliter
DLS	:	Dynamic light scattering
DMEM	:	Dulbecco's modified Eagle's medium
DMSO	:	Dimethyl sulphoxide
DNA	:	Deoxyribonucleic acid
DOX	:	Doxorubicin
DPSS	:	Diode-pumped solid-state
3-D	:	Three-dimensional
EDTA	:	Ethylenediaminetetraacetic acid
EDX	:	Energy dispersive X-ray
e.g.	:	For example

EMEM	:	Eagle's minimum essential medium
EPR	:	Enhanced permeability and retention
Eq.	:	Equation
FA	:	Folic acid
FBS	:	Fetal bovine serum
FDA	:	Food and drug administration
Fe ₃ O ₄	:	Iron oxide
FESEM	:	Field effect scanning electron microscopy
FITC	:	Fluorescein isothiocyanate
fs	:	femtoseconds
FTIR	:	Fourier transform infrared
g	:	gram
Gd ³⁺	:	Gadolinium ion
GEM	:	Gemcitabine
Glu	:	Glutamic acid
Gly	:	Glycine
ΔG	:	Gibbs free energy change
h	:	Hour
HAuCl ₄	:	Gold (III) chloride
HAuCl ₄ ·3H ₂ O	:	Gold (III) chloride trihydrate
HER2	:	Human epidermal growth factor receptor 2
His	:	Histidine
HSA	:	Human serum albumin
ΔH	:	Enthalpy change
Ile	:	Isoleucine

ISO/TR	:	International organization for standardization / Technical reports
¹²⁵ I	:	Iodine-125
J	:	Joule
K	:	Kelvin
K _a	:	Binding constant
KCl	:	Potassium chloride
KeV	:	Kiloelectronvolts
kJ	:	Kilojoule
k _q	:	Bimolecular quenching rate constant
K _{SV}	:	Stern-Volmer constant
Leu	:	Leucine
Lys	:	Lysine
μl	:	Microliter
min	:	Minute
MALDI-TOF	:	Matrix-assisted laser desorption / ionization-time of flight
Met	:	Methionine
mg	:	Milligram
MgCl ₂	:	Magnesium chloride
ml	:	Milliliter
μM	:	Micromolar
mM	:	Millimolar
mm	:	Millimeter
MP-AES	:	Microwave plasma-atomic emission spectrometry
MRI	:	Magnetic resonance imaging
MTT	:	3-(4,5-Dimethyl-2-thiazolyl)-2,5-diphenyltetrazolium bromide

mV	:	Millivolts
n	:	Hill coefficient
Na ₂ HPO ₄	:	Disodium hydrogen phosphate
NaBH ₄	:	Sodium borohydride
NaCl	:	Sodium chloride
NaHCO ₃	:	Sodium hydrogen carbonate
NIR	:	Near-infrared
nm	:	Nanometer
NPs	:	Nanoparticles
PAI	:	Photoacoustic imaging
PBS	:	Phosphate-buffered saline
PEG	:	Polyethylene glycol
PET	:	Positron emission tomography
Phe	:	Phenylalanine
PI	:	Propidium iodide
Pro	:	Proline
ps	:	picoseconds
PS	:	Phosphatidylserine
PT	:	Photothermal
PTT	:	Photothermal treatment
RBCs	:	Red blood cells
s	:	Second
SERS	:	Surface-enhanced Raman scattering
SPECT	:	Single-photon emission computed tomography
SPR	:	Surface plasmon resonance
ΔS	:	Entropy change

T	:	Temperature
TAA	:	Tumor-associated antigens
TEM	:	Transmission electron microscopy
TNF	:	Tumor necrosis factor
Trp	:	Tryptophan
Tyr	:	Tyrosine
UV-Vis	:	Ultraviolet-visible
Val	:	Valine
viz.	:	Latin phrase <i>videlicet</i> (namely)
W	:	Watt
WFN	:	Warfarin

University of Malaya

CHAPTER 1: INTRODUCTION

1.1 Research background

Ineffectiveness of current cancer therapeutics such as chemotherapy, radiotherapy and surgical removal has led to severe side effects to cancer patients, thus provide insufficient therapeutic benefits (Steichen et al., 2013; Maeda et al., 2013). Nanoparticles have emerged as potential therapeutic agents to replace the use of conventional chemotherapeutic drugs, due to their ability to be delivered to the target sites through enhanced permeability and retention effect (Maeda, 2001). Ease of synthesis and functionalization have made gold nanoparticles (AuNPs) as the nanoparticles of choice for therapeutic use (Daniel & Astruc, 2004). Ability of AuNPs to dissipate the absorbed light as heat has been successfully exploited in using them as a photothermal agent for cancer treatment. Photothermal therapy is a noninvasive cancer therapy, which uses localized heat produced from the photon energy for killing of cancer cells (Huang & El-Sayed, 2011).

Conventional methods of AuNPs synthesis i.e., chemical methods or physical methods often involve the use of hazardous substances, such as cetyl trimethylammonium bromide (CTAB), hydroxylamine and sodium borohydride (PubChem Compound Database, n.d.; Alkilany et al., 2009; Evelo et al., 1998), which can be toxic to human system. For example, CTAB-coated gold nanorods have shown damage to the cell membrane, increased lysosomal membrane permeation and decreased mitochondrial membrane potential, which subsequently induce cell death (Wan et al., 2015). Besides their toxicity to normal cells, chemically synthesized-AuNPs often require additional stabilizing agents for their clinical applications (Moore et al., 2015), as physiological environment is abundant with proteins and salts which may lead to aggregation of AuNPs (Alkilany & Murphy, 2010; Wang et al., 2014). Both toxicity and low stability of AuNPs have limited their use in clinical applications.

In recent years, green synthesis of AuNPs has emerged as an alternative method due to its simplicity, low cost, energy-efficient and minimal production of hazardous waste (Nath & Banerjee, 2013). Green synthesis utilizes natural biomolecules such as phytochemicals, polysaccharides and microbial enzymes as the reducing and stabilizing agents for AuNP synthesis (Basha et al., 2010; Maity et al., 2012; Menon et al., 2017). In contrast to the physical and chemical methods of AuNP synthesis, green synthesis does not require heat or pressure, which ultimately reduces the energy usage and thus lowers the production cost (Du et al., 2012). Plants showing antioxidant activity, including ginger contain phytochemicals which can be potentially used as a reducing agent for AuNPs synthesis. *Curcuma mangga* (CM) is a type of ginger and is traditionally used in the treatment for fever, stomach aches and cancer (Malek et al., 2011). It has been shown to possess anticancer, antioxidant and antimicrobial properties (Malek et al., 2011; Liu & Nair, 2011; Philip et al., 2009). Numerous phytochemicals with antioxidant activity have been reported to be present in CM extract (Liu & Nair, 2011), which can be used as the reducing agent for the synthesis of AuNPs.

Interaction of AuNPs with proteins can affect their biodistribution, uptake, efficacy and cytotoxicity (Wolfram et al., 2014; Nguyen & Lee, 2017). Among various proteins, serum albumin is the most abundant protein in blood plasma and is the major transporter in human circulation, which plays an important role in shuttling of endogenous and exogenous ligands, including drugs and metabolites. It is a globular protein of 66 kDa, consisting of 585 amino acid residues in a single polypeptide chain with only one tryptophan (Trp-214) residue (Ghuman et al., 2005). Ligands mainly bind to human serum albumin (HSA) at either of the three well known ligand binding sites, i.e. Sudlow's site I, Sudlow's site II or site III, located in subdomains IIA, IIIA and IB, respectively (Sudlow et al., 1975; Brunmark et al., 1997). The binding affinity of drug to HSA determines its

delivery, distribution, efficacy and toxicity under *in vivo* system (Ghuman et al., 2005; Sudlow et al., 1975).

1.2 Problem statement and research objectives

Although several plant extracts with antioxidant activity have been used as a reducing agent for AuNPs synthesis, CM extract has not been tested so far for the green synthesis of AuNPs. Since CM extract has been shown to possess antioxidant activity, several questions remain to be answered regarding its use in the green synthesis of AuNPs:

1. Can CM extract be used as a reducing agent for AuNPs synthesis?
2. What are the characteristics of the AuNPs, synthesized using CM extract?
3. How do these AuNPs (CM-AuNPs) interact with the major transport protein of human circulation?
4. Can CM-AuNPs be used as a photothermal agent for treating cancer cells?

In view of the above, the aims of the present study are to synthesize AuNPs using CM extract and study their interaction with HSA as well as their application as a photothermal agent in cancer treatment. In order to achieve these aims, following objectives were set:

1. To synthesize AuNPs using aqueous ethanol extract of *Curcuma mangga*
2. To characterize these AuNPs (CM-AuNPs) using spectroscopic and electron microscopic techniques
3. To investigate cytotoxicity and blood compatibility of CM-AuNPs
4. To study interaction of CM-AuNPs with human serum albumin
5. To evaluate photothermal effect of CM-AuNPs on cancer cells

1.3 Thesis outline

This thesis is comprised of five chapters:

Chapter 1: Introduction. This chapter describes the limitations of current cancer therapy and suggests the use of AuNPs for photothermal treatment. The advantages of green synthesis of gold nanoparticle and importance of protein interaction studies have also been discussed. Research problems and objectives are clearly stated in this chapter.

Chapter 2: Literature review. This chapter presents the background of cancer, nanotechnology and protein interaction studies. Different AuNPs synthesis methods as well as exploitation of AuNPs properties for different biological applications have also been discussed. The importance of interaction of AuNPs with HSA, its physicochemical and structural properties have been included.

Chapter 3: Materials and methods. The materials used and the methods employed in this study were described in detail in this chapter.

Chapter 4: Results and discussion. This chapter includes the analysis of results obtained, along with discussion on the green synthesis of CM-AuNPs, its protein interaction and photothermal studies. There are four highlights in this chapter, which are synthesis and optimization of CM-AuNPs, characterization of CM-AuNPs, interaction of CM-AuNPs with HSA and photothermal effect of CM-AuNPs.

Chapter 5: Conclusions and future perspectives. The research outcomes are summarized in this chapter and future perspectives have also been proposed.

CHAPTER 2: LITERATURE REVIEW

2.1 Cancer

Cancer is one of the leading causes of death globally, responsible for 8.8 million of death in 2015, according to World Health Organization (Forman & Ferlay, 2014). Cancer arises after a series of gene mutations occurring in the normal cells, which lead to abnormal cell growth and tumor formation. As normal cells become tumorigenic (neoplastic state), they acquire several hallmark capabilities that enable tumor growth and metastatic dissemination. These hallmarks include sustained proliferative signaling, evading growth suppressors, resisting cell death, enable replicative immortality, inducing angiogenesis, activating invasion and metastasis, reprogramming energy metabolism and evading immune destruction (Hanahan & Weinberg, 2011).

2.1.1 Tumor physiology and enhanced permeability and retention effect

Understanding of tumor physiology can be exploited for development of more effective therapeutics. As mentioned above, one of the hallmarks of cancer is the uncontrolled proliferation of cancer cells due to their ability to sustain proliferative signaling (Hanahan & Weinberg, 2011). Since the cells obtain nutrients through diffusion in the initial stages of tumor growth, tumor size cannot be greater than $\sim 2 \text{ mm}^3$. In order to grow beyond the limited size and receive enough nutrients for the rapidly growing cells, tumor cells stimulate the growth of new blood vessels through angiogenesis (Brannon-Peppas & Blanchette, 2004). Due to their rapid growth, the angiogenic blood vessels usually have abnormal architecture, which includes lack of smooth muscle layer, irregular vascular alignment and defective endothelial lining with wide fenestrations (Fang et al., 2011). The fenestrations in angiogenic blood vessels may vary from a few hundred nanometers to a few micrometers, depending on tumor type. These fenestrations are much larger than the pore size (2–6 nm), present in the normal blood vessels (Grossman & McNeil, 2012). Thus, macromolecules and blood components can easily

pass through the wide fenestrations in angiogenic blood vessels to the tumor interstitium. This phenomenon is known as enhanced permeability effect (Maeda, 2001). In addition to it, higher levels of vascular effectors, such as bradykinin, vascular endothelial growth factor and nitric oxide in tumor sites also contribute to the vascular permeability of the tumor (Maeda et al., 2013).

Lymphatic system plays an important role in the maintenance of interstitial fluid volume and protein concentration as well as transportation of solutes and macromolecules from tissues back to the circulatory system (Weid & Zawieja, 2004). On the other hand, such lymphatic drainage is impaired in the tumor tissue (Maeda, 2001). Thus, drainage of fluids and wastes is markedly reduced in the tumor tissue. Due to this hindrance in the transportation of solutes and macromolecules from the tumor back to the circulatory system, macromolecules or NPs with size greater than 4 nm are less likely to diffuse and thus, accumulate in the tumor interstitial spaces for a prolonged period. Therefore, retention of macromolecules in tumor is greatly enhanced (Youichiro et al., 1998). Both enhanced permeability of vasculature and poor lymphatic drainage in tumor sites lead to the phenomenon, known as enhanced permeability and retention (EPR) effect. The EPR effect was first introduced by Maeda for selective delivery of macromolecular drugs (Maeda, 2001). Figure 2.1 illustrates distribution of drug molecules and NPs in normal tissues as well as tumor sites according to the concept of EPR effect.

2.1.2 Cancer treatment and limitations

Current therapeutic techniques for cancer treatment are chemotherapy, radiotherapy or in combination with surgical resection (Steichen et al., 2013). Chemotherapy involves the use of chemotherapeutic agents, usually low molecular weight drug molecules which inhibit replication or induce apoptosis of cancer cells. A few examples of the commonly used chemotherapeutic drugs are doxorubicin (DOX), epirubicin, paclitaxel, docetaxel,

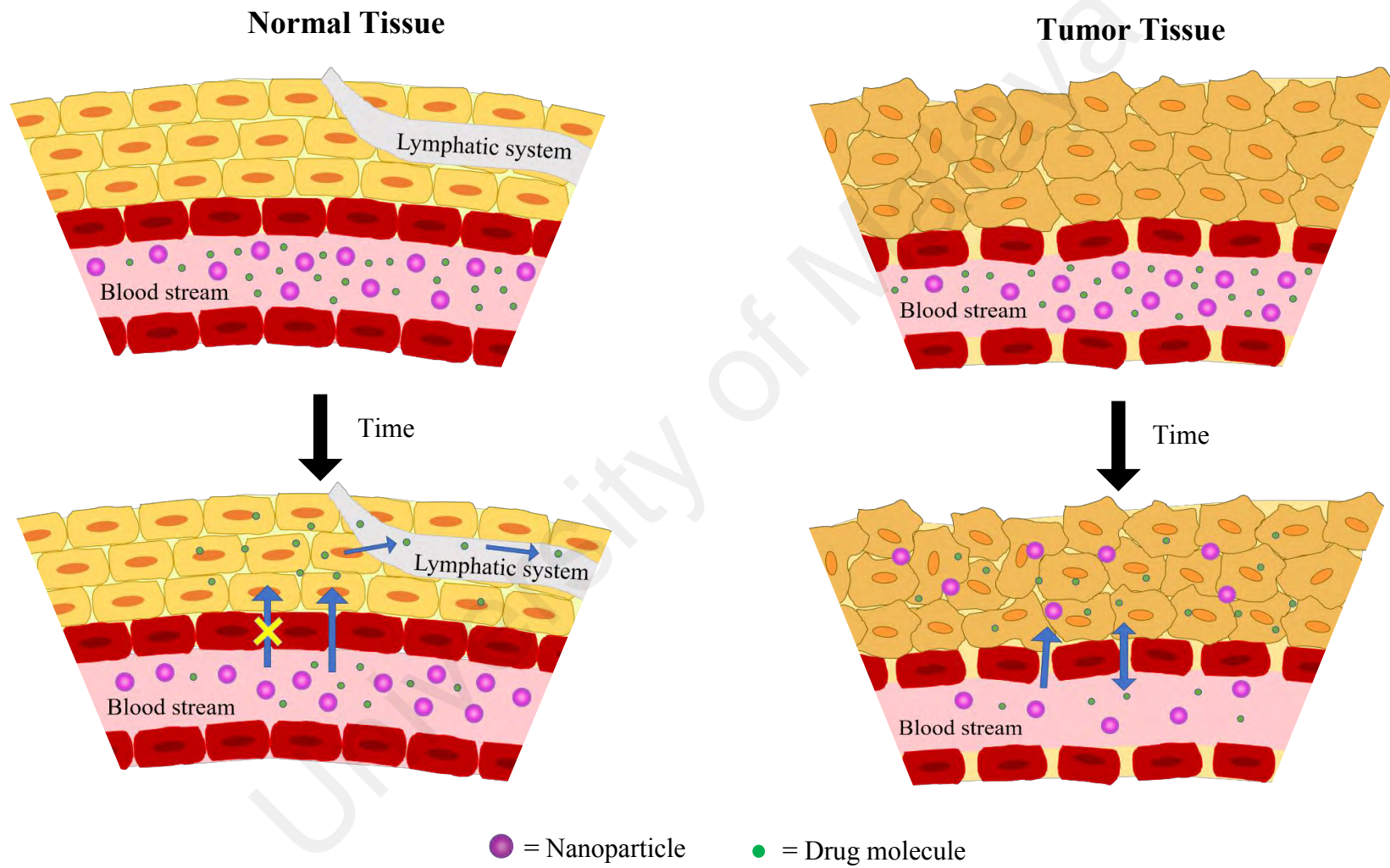


Figure 2.1: Diagram showing distribution of nanoparticles in normal and tumor tissues.

gemcitabine (GEM), cisplatin etc. Doxorubicin and epirubicin, which belong to the ‘anthracyclines’ class of chemotherapeutic drugs, fall in the category of the most effective drugs, used for cancer treatment. Anthracyclines are known to inhibit DNA topoisomerase II, thus initiate DNA damage and induce apoptosis of cells (Minotti et al., 2004). Paclitaxel and docetaxel are taxanes, which inhibit cell proliferation by stabilizing microtubules from depolymerization, thus prevent mitosis at the metaphase/anaphase boundary (Rowinsky, 1997). One of the most widely used pyrimidine analog, gemcitabine functions by inhibiting DNA polymerases and ribonucleotide reductase and blocks DNA synthesis (Minotti et al., 2004; Ciccolini et al., 2016). Similarly, cisplatin, a platinum-compound is also a DNA-damaging agent that triggers apoptosis of cells (Zamble & Lippard, 1995).

Despite significant advancement in cancer diagnosis and treatment over the past few decades, morbidity and mortality of cancers remain high. While successfully inhibiting the replication as well as killing of cancer cells, one of the major limitations of chemotherapeutic drugs is non-specific damage to normal cells (Steichen et al., 2013). Low tumor selectivity of chemotherapeutic drugs leads to non-specific distribution of these drugs in normal tissues and organs as well as tumor sites as shown in Figure 2.1 (Maeda et al., 2013). This non-selective action of chemotherapeutic drugs exerts deleterious effects on both cancer cells and cells with rapid turnover rate such as bone marrow cells and intestinal epithelial cells, thus results in severe side effects in cancer patients (Feng & Chien, 2003). For example, doxorubicin, one of the most widely used chemotherapeutic drugs, produces many side effects, such as fatigue, nausea and cardiotoxicity in cancer patients, which may lead to fatality (Minotti et al., 2004). As a result, these chemotherapeutic drugs provide insufficient therapeutic benefits and cause severe systemic toxicity, namely, dose-limited toxicity (Maeda et al., 2013). Therefore, the current approach for cancer treatment is to find therapeutic formulation with the

ability to selectively target diseased tissue, overcome biological barriers and produce minimal damage to normal tissues and organs.

2.2 Nanotechnology

Nanotechnology has emerged as a potential therapeutic approach to overcome the aforementioned constraints in current cancer treatments, due to physical and biological advantages of nanoparticles (NPs) over conventional drugs. Nanoparticles are structures of any shapes with dimension(s) ranging from 1 to 100 nm according to International Union of Pure and Applied Chemistry recommendations (Vert et al., 2012). This size range is bigger than the size of free drugs. Thus, NPs can accumulate at tumor sites through passive targeting due to EPR effect, which their entry is prevented into normal cells (Maeda, 2001). Such increase in drug accumulation at the diseased sites may allow reduction of the effective dosage, therefore decreasing the toxicity and side effects of therapeutic drugs (Ventola, 2017). Other advantages of NPs are enhanced solubility and increased stability of drugs along with decreased drug resistance (Bhatia, 2016). Furthermore, use of NPs also led to the development of photothermal therapy as an alternative treatment for cancer (Zou et al., 2016).

Generally, NPs can be categorized into organic and inorganic NPs. Organic NPs include carbon-based NPs, protein NPs and polymeric NPs such as liposomes, dendrimers and micelles. Metal NPs and metal oxide NPs, e.g. AuNPs, silver NPs, copper NPs, iron oxide NPs and titanium dioxide NPs are some of the examples of inorganic NPs (Ealia & Saravanakumar, 2017).

2.2.1 Cancer nanomedicine

Nanomedicine is the medical applications of nanotechnology, which includes applications from biological imaging to drug and gene delivery (Pillai & Ceballos-

Coronel, 2013). Some of the nanodrugs (nanoparticle-formulated drugs) have already been approved by FDA for cancer treatment, while many of the nanodrugs are still under clinical trials. A few examples of both FDA-approved nanodrugs and those undergoing clinical trials are given in Table 2.1. Most of the approved nanodrugs utilize organic NPs due to their biocompatible nature. Doxil, Myocet and DaunoXome are liposomal anthracyclines, which were formulated to improve efficacy while reducing toxicity of free anthracyclines (Pillai, 2014). Doxil (PEGylated liposomal doxorubicin) was approved for the treatment of ovarian cancer, breast carcinoma, AIDS-related Kaposi's sarcoma, and multiple myeloma, while Myocet and DaunoXome are being used as nanodrugs for treatment of breast cancer and AIDS-related Kaposi's sarcoma, respectively (Lao et al., 2013; Forssen & Ross, 1994). Sustained-release of cytarabine was made possible by encapsulation of cytarabine in liposome (DepoCyt). This formulation has helped in maintaining therapeutic drug concentration for prolonged periods and reducing the frequency of drug administration for lymphomatous meningitis treatment (Glantz et al., 1999). Marqibo and Vyxeos are two examples of liposomal drugs, used for delivery of vincristine and co-delivery of daunorubicin and cytarabine, respectively. Vincristine is encapsulated in sphingomyelin liposomes to prolong its half-life while decreasing its toxicity for Philadelphia chromosome negative acute lymphocytic leukemia (ALL) treatment (Silverman & Deitcher, 2013; Thomas et al., 2006). Co-delivery of daunorubicin and cytarabine using liposome has improved the efficacy of treatment for acute myeloid leukemia (AML) and AML with myelodysplasia related changes (Lancet et al., 2014).

Other organic NPs formulation, such as Abraxane, an albumin-bound paclitaxel nanosphere has been found advantageous for increasing solubility, bioavailability and accumulation of free drugs at tumor site in treating breast / pancreatic cancers as well as non-small cell lung carcinoma (Miele et al., 2009; Pillai, 2014). Another sustained-release

Table 2.1: FDA-approved nanodrugs and those undergoing clinical trials for cancer treatment. Adapted from (Pillai, 2014; Ventola, 2017; Anselmo & Mitragotri, 2015).

Chemical Nature	Trade Name	Cancer Type
PEGylated doxorubicin HCl nano-liposome	Doxil	<ul style="list-style-type: none"> - Ovarian / Breast cancer - Kaposi's sarcoma - Multiple myeloma
Liposomal doxorubicin	Myocet	<ul style="list-style-type: none"> - Breast cancer
Liposomal daunorubicin	DaunoXome	<ul style="list-style-type: none"> - AIDS-related Kaposi's sarcoma
Liposomal cytarabine	DepoCyt	<ul style="list-style-type: none"> - Lymphomatous meningitis
Liposomal vincristine	Marqibo	<ul style="list-style-type: none"> - Philadelphia chromosome-negative ALL
Liposomal daunorubicin and cytarabine	Vyxeos	<ul style="list-style-type: none"> - Acute myeloid leukemia (AML) - AML with myelodysplasia related changes
Albumin-bound paclitaxel nanospheres	Abraxane	<ul style="list-style-type: none"> - Breast cancer - Non-small cell lung carcinoma - Pancreatic cancer
Leuprolide acetate and polymer	Eligard	<ul style="list-style-type: none"> - Prostate cancer
PEG-conjugated L-asparaginase	Oncaspar	<ul style="list-style-type: none"> - Acute lymphocytic leukemia (ALL)
Denileukin diftitox	Ontak	<ul style="list-style-type: none"> - Cutaneous T-cell lymphoma
TNF- α bound-colloidal gold nanoparticles	Aurimmune (CYT-6091) (In clinical Phase II)	<ul style="list-style-type: none"> - Head and neck cancer
Silica-gold nanoshells coated with PEG	AuroShell (In clinical Phase I)	<ul style="list-style-type: none"> - Head and neck cancer - Primary and/or metastatic lung tumors

formulation was successfully designed for the delivery of leuprolide acetate using biodegradable polymer matrix (Eligard) in treating prostate cancer (Tunn, 2011). On the other hand, conjugation of polyethylene glycol (PEG) to L-asparaginase (Oncaspar) was found to increase the half-life of the enzyme and reduce the allergic response in ALL treatment (Avramis & Tiwari, 2006). Ontak is a fusion protein that combines the targeting protein with diphtheria toxin for specific targeting of T-cells in cutaneous T-cell lymphoma treatment (Ventola, 2017). Apart from the organic NPs-formulated drugs, one of the examples of inorganic NPs-derived nanodrug that is undergoing clinical trials, is Aurimmune, a TNF- α bound colloidal AuNPs, used in treatment of head and neck cancer. Aurimmune has been shown to reduce toxicity of TNF- α and avoid its immediate clearance from the circulatory system (Libutti et al., 2010).

Although nanoformulations offered improved efficacy and reduced toxicity of the drugs, side effects from such treatments (nanoparticle-formulated drugs) still exist. Although nanodrugs have shown higher accumulation in target sites, their delivery to other organs, e.g. liver, spleen, kidney and skin cannot be avoided. This has resulted in toxicity to these organs due to the release of toxic chemotherapeutic drugs in these sites (Park, 2013). Thus, alternative therapies with more localized treatment, such as photothermal and photodynamic therapies using inorganic / organic NPs have been developed. An example of inorganic nanoparticles undergoing clinical trial is AuroShell, a silica-gold nanoshells coated with PEG. Photothermal therapy using AuroShell is a localized tumor treatment, which selectively treats the tumor while reducing the damage to the healthy tissue (Anselmo & Mitragotri, 2015).

2.2.2 Gold nanoparticles

Among the various NPs, gold nanoparticles (AuNPs) have emerged as an attractive candidate for biomedical applications (Daniel & Astruc, 2004). This is due to the inert

gold core, ease of synthesis and functionalization to obtain biocompatible AuNPs suitable for various biomedical applications.

2.2.2.1 AuNPs synthesis

(a) *Conventional methods*

Methods for the synthesis of AuNPs can be categorized into top-down and bottom-up approaches. Top-down approach is normally used to synthesize AuNPs for their applications in the fields of electronics, sensors and catalysis, while AuNPs used for biomedical applications are usually synthesized by bottom-up approach.

Bottom-up approach synthesizes nanoparticles from individual ions / molecules, which involves chemical or biological reactions. Various molecular components self-assemble to build up into more complex assemblies (Nath & Banerjee, 2013). Chemical reaction occurs in two steps: nucleation and successive growth. A few conventional methods that have been used for AuNPs synthesis are *in situ* synthesis, seeded growth synthesis, polymer-mediated synthesis and inert gas condensation (Figure 2.2).

AuNPs synthesis involving nucleation and growth in the same step is known as *in situ* synthesis, which is generally used in preparation of spherical or quasi-spherical AuNPs. A commonly used method of *in situ* synthesis of AuNPs is Turkevich method, which uses trisodium citrate as a reducing and stabilizing agent. This method requires heating of auric salt (normally HAuCl_4) and addition of trisodium citrate with vigorous stirring (Turkevich et al., 1951). In this reaction, the precursor auric ions (Au^{3+}) are reduced to aurous ions (Au^+) and Au^0 , which then coalesce to form AuNPs. AuNPs produced following this procedure can be tailored for a size of 15–150 nm (Frens, 1973). However, AuNPs bigger than 20 nm size are always polydisperse AuNPs. To prepare AuNPs with smaller size (< 10 nm), a stronger reducing agent is needed. Brown and co-workers

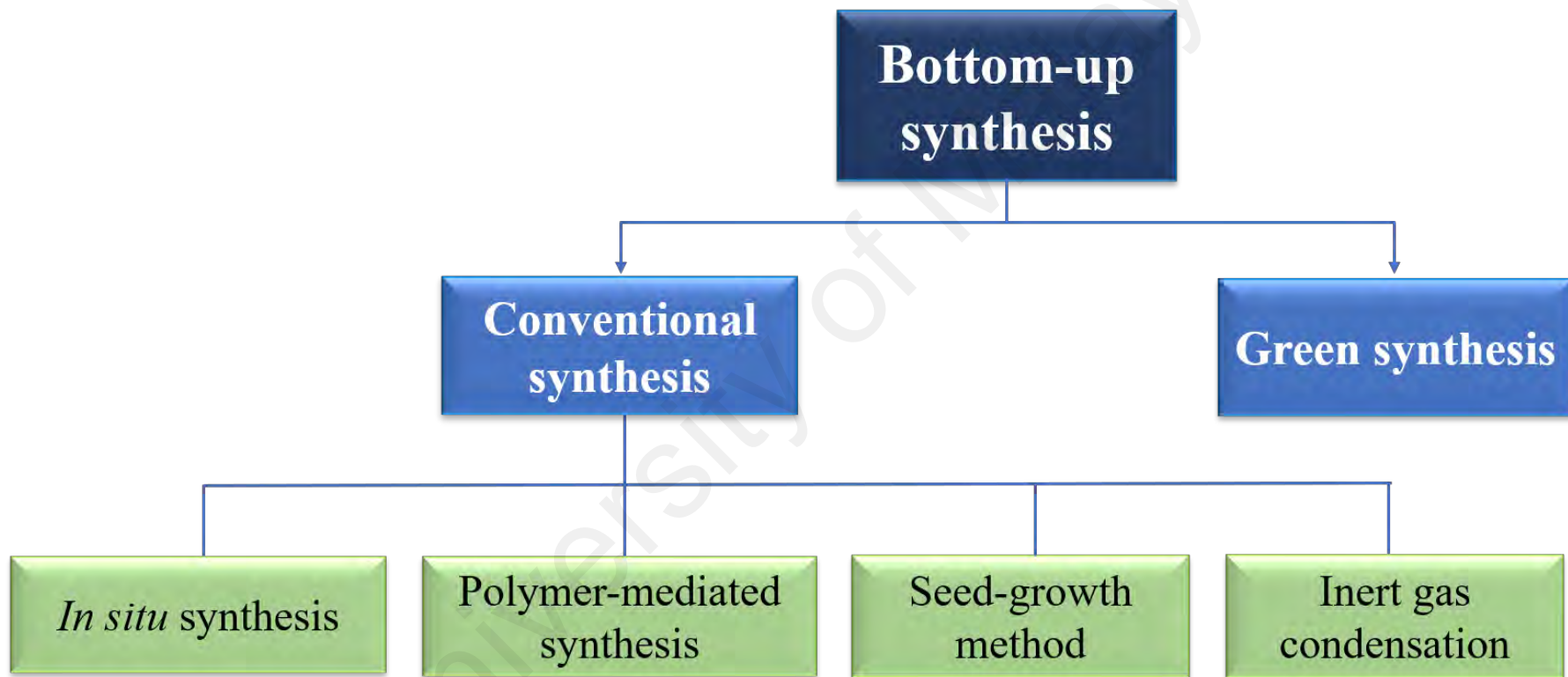


Figure 2.2: Scheme showing bottom-up and top-down syntheses of gold nanoparticles.

introduced the use of sodium borohydride (NaBH_4) as a reducing agent and citrate as a stabilizing agent to prepare AuNPs of 6 nm size (Brown et al., 1996).

Seeded growth synthesis requires two separate steps for nucleation and growth (Zhao et al., 2013). This method has been adopted to produce larger monodispersed AuNPs with spherical, quasi-spherical, rod and anisotropic shapes. Small-sized AuNPs seeds are prepared by using strong reducing agent such as NaBH_4 in the first step of seeded growth method. The seeds are then added to the 'growth' solution, containing auric salt and mild reducing and stabilizing agents. The mild reducing agents such as citrate, hydroxylamine, ascorbic acid can only reduce Au^{3+} ions to Au^0 in the presence of gold seeds, where the newly reduced Au^0 can only assemble on the surface of gold seeds. Nucleation does not occur in the growth solution (Zhao et al., 2013). A commonly used stabilizer is hexadecyltrimethylammonium bromide (CTAB) for the synthesis of gold nanorods with different aspect ratio, which can be produced by adjusting the concentration of CTAB.

Polymer-mediated synthesis can be carried out in one step or two steps, where the HAuCl_4 solution is added to the functionalized polymers, followed by the addition of reducing agent (NaBH_4) to form AuNPs (Zhao et al., 2013). Some commonly used polymers are PEG, polystyrene, polyvinyl pyridine, polyethylenimine, poly(N-isopropylacrylamide) and poly(N,N-dimethylaminoethyl methacrylate) (Mendes et al., 2017; Corbierre et al., 2004; Zhou et al., 2015; Hu et al., 2010; Kusolkamabot et al., 2013; Alinejad et al., 2018). In some cases, co-polymers such as poly(styrene- β -N-isopropylacrylamide) and poly(ethylene oxide)-poly(propylene oxide) were also exploited as both the reducing and stabilizing agents for AuNPs synthesis (Alexandridis & Tsianou, 2011; Liu et al., 2010).

AuNPs synthesized by inert gas condensation method involves evaporation of the metal in ultra-high vacuum chamber filled with inert gas (helium or argon), followed by

condensation into small particles on liquid nitrogen-cooled substrate. The growth of these particles by Brownian coagulation and coalescence leads to the formation of nanocrystals (Nath & Banerjee, 2013). Inert gas condensation technique requires high energy consumption and thus increases the production cost.

Use of the hazardous chemicals as well as high energy consumption in the above-mentioned bottom-up techniques of AuNPs synthesis, limits their *in vivo* applications. Therefore, green synthesis was proposed as an alternative method for the synthesis of AuNPs, which is more economical, simple and non-toxic for *in vivo* use (Prabhu & Poulouse, 2012).

(b) **Green synthesis**

Biological resources, such as bacteria, fungi, algae, actinomycetes and plant extracts have been exploited in the green synthesis of AuNPs, as shown in Figure 2.3 (Baker & Satish, 2015; Castro-Longoria et al., 2011; González-Ballesteros et al., 2017; Ranjitha & Rai, 2017; Ahmad et al., 2018). Both extracellular and intracellular methods have been employed in the green synthesis of AuNPs. Extracellular synthesis of spherical AuNPs of 5–30 nm size has been shown using cell-free supernatant of *Pseudomonas aeruginosa*, *Pseudomonas veronii* and *Klebsiella pneumoniae* (Husseiny et al., 2007; Baker & Satish, 2015; Malarkodi et al., 2013). However, *Klebsiella pneumoniae* has led to significant aggregation of AuNPs, indicating lack of stability of these AuNPs (Malarkodi et al., 2013). Purified sulfite reductase enzyme from *Escherichia coli* has also been used as reducing agent for AuNPs synthesis (Gholami-Shabani et al., 2015). Intracellular synthesis of 5–50 nm-long hexagonal AuNPs has also been reported using *Geobacillus stearothermophilus* (Luo et al., 2015).

Examples for the use of fungi in the intracellular synthesis of AuNPs include *Flammulina velutipes* and *Neurospora crassa*, while *Fusarium oxysporum* and

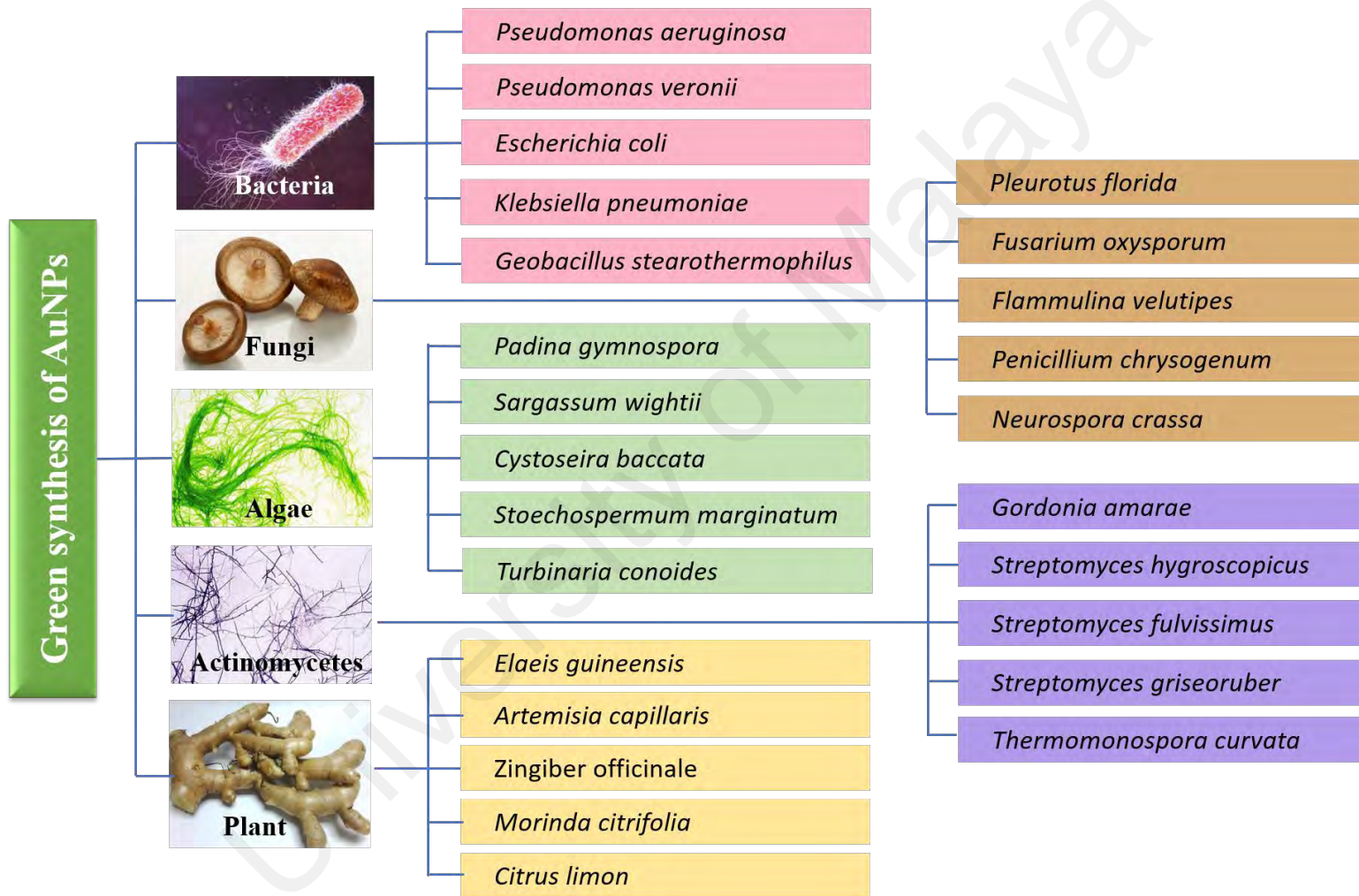


Figure 2.3: Examples of various organisms used in the green synthesis of gold nanoparticles.

Penicillium chrysogenum for extracellular synthesis of AuNPs in the size range of 3–100 nm (Narayanan et al., 2015; Castro-Longoria et al., 2011; Thakker et al., 2013; Magdi & Bhushan, 2015). Water extract of *Pleurotus florida* has also been used for the synthesis of uneven-shaped (10–50 nm) AuNPs (Bhat et al., 2013).

AuNPs of 6–67 nm size have been synthesized using algal extract from *Padina gymnospora*, *Cystoseira baccata*, and *Turbinaria conoides* (Singh et al., 2013; González-Ballesteros et al., 2017; Rajeshkumar et al., 2013). Use of *Sargassum wightii* and *Stoechospermum marginatum* in the AuNPs synthesis has also been reported (Singaravelu et al., 2007; Rajathi et al., 2012). Actinomycetes such as *Gordonia amarae*, *Streptomyces hygrosopicus*, *Streptomyces fulvissimus*, *Streptomyces griseoruber* and *Thermomonospora curvata* have been demonstrated to synthesize 15–60 nm AuNPs (Menon et al., 2017; Sadhasivam et al., 2012; Ranjitha & Rai, 2017).

Extracts from various plants, e.g. *Elaeis guineensis*, *Artemisia capillaris*, *Zingiber officinale*, *Morinda citrifolia* and *Citrus limon* have also been successfully used as reducing and stabilizing agents for synthesis of AuNPs in the size range of 5–80 nm (Ahmad et al., 2018; Lim et al., 2016; Kumar et al., 2011; Suman et al., 2014; Sujitha & Kannan, 2013). Phytochemicals such as phenolic compounds, flavonoids, citric acid and ascorbic acid, present in these extracts were found to be responsible to reduce precursor Au³⁺ ions in the synthesis of AuNPs (Ahmad et al., 2018; Sujitha & Kannan, 2013).

Curcuma mangga (Figure 2.4A) locally known as “temu pauh” or “kunyit mangga”, belongs to the *Zingiberaceae* family and possesses antioxidant activity besides antitumor, antimicrobial and anti-allergic properties (Jitoe et al., 1992; Kirana et al., 2003; Kamazeri et al., 2012; Tewtrakul & Subhadhirasakul, 2007). Major compounds present in CM extract are terpenoids such as labda-8(17),12-diene-15,16-dial, calcatarin, zerumin A, 15,16-bisnor-labda-8(17),11-diene-13-on, longpene A and coronadiene

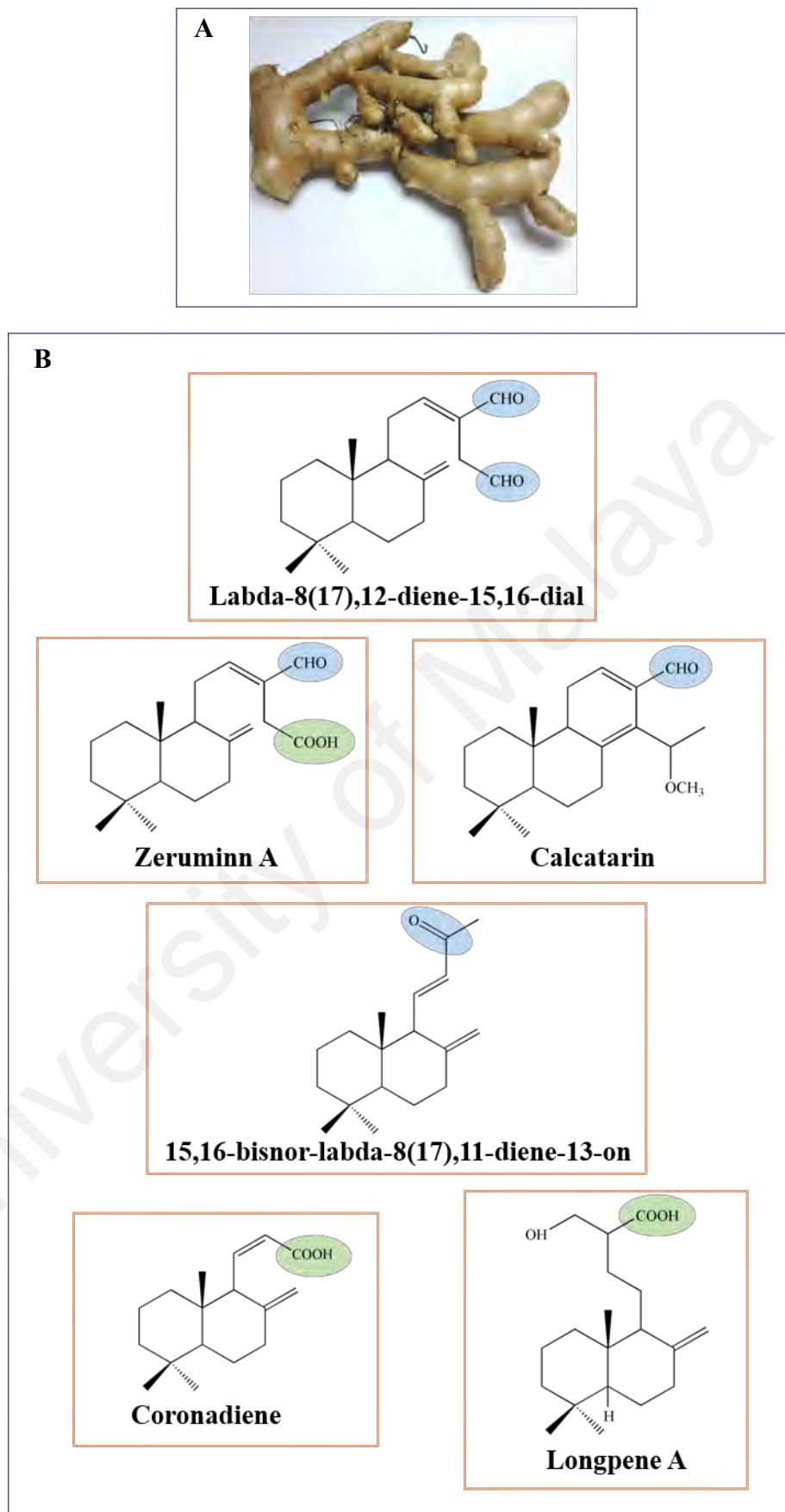


Figure 2.4: (A) Photograph of *Curcuma mangga* rhizome. (B) Chemical structures of some of the known terpenoids, present in *Curcuma mangga*. Adapted from (Malek et al., 2011; Liu & Nair, 2011).

(Liu & Nair, 2011; Malek et al., 2011). As depicted in Figure 2.4B, labda-8(17),12-diene-15,16-dial and calcatarin contain aldehyde group, while zerumin A contain both aldehyde and carboxyl group. A keto-group is noticed in the structure of 15,16-bisnor-labda-8(17),11-diene-13-on, while both longpene A and coronadiene possess a carboxyl group.

2.2.2.2 Properties of AuNPs

AuNPs exhibit unique physicochemical properties such as surface plasmon resonance (SPR), high X-ray absorption coefficient, tunable electronic and optical properties as well as ability to react with amine and thiol groups for surface modification (Daniel & Astruc, 2004; Elahi et al., 2018). AuNPs can be categorized into 4 classes, i.e., 0D, 1D, 2D and 3D nanostructures, based on the number of dimensions which are not confined to the nanoscale range. AuNPs with 0D include nanospheres and nanocubes, while nanorods, nanowires and nanotubes belong to 1D. On the other hand, nanoplates, nanosheets, and nanowalls are known to be 2D AuNPs, while 3D AuNPs include nanocoils and multilayers (Sajanlal et al., 2011; Elahi et al., 2018). Several properties of AuNPs such as size, surface charge and surface coating as well as their administration routes may affect their acute and chronic toxicity (Jia et al., 2017). For example, positively-charged AuNPs (CTAB-AuNPs and polyallylamine hydrochloride-AuNPs) have been shown to cause acute toxicity to *Daphnia magna*, whereas negatively-charged AuNPs (citrate-AuNPs and mercaptopropionic acid-AuNPs) did not affect the mortality of *Daphnia magna* (Bozich et al., 2014). Acute toxicity and subchronic toxicity studies of AuNPs using mice with different administration routes have shown least toxic effect with tail vein injection route compared to oral and intraperitoneal routes (Zhang et al., 2010).

(a) *Optical properties*

The unique optical property of AuNPs is attributed to SPR, which is reflected as intense colour that does not exist in nonmetallic particles. SPR is due to the collective

coherent oscillations of free electrons on the particle surface's induced by oscillating electromagnetic field of light (Daniel & Astruc, 2004; Kerker, 1969). This electron oscillation results in charge separation corresponding to the ionic lattice and form a dipole oscillation along the direction of the electric field of the light. The amplitude of the oscillation reaches maximum at a specific frequency, which is the SPR phenomenon. The SPR is responsible for the strong absorption of incident light that can be detected by UV-Vis spectrometer. Noble metal NPs, such as AuNPs exhibit much stronger SPR than other metallic NPs (Huang & El-Sayed, 2010). Factors affecting electron charge density on NP surface, such as particle size, shape, metal type, composition and the dielectric constant of the surrounding medium can influence the wavelength and intensity of SPR band (Huang & El-Sayed, 2010; Abdelhalim et al., 2012).

In addition to light absorption, AuNPs also possess the ability to scatter light, where the magnitude of scattering efficiency is directly correlated with the particle size (Jain et al., 2006). The magnitude of the visible light scattering by 80 nm gold nanospheres has been found comparable to the scattering from the much larger (300 nm) polystyrene nanospheres, which are generally used in confocal cell imaging. This scattering magnitude has also been found to be five orders of magnitude higher than the light emission from fluorescein molecules, a common fluorescent imaging agent (Jain et al., 2006). The scattering efficiency can be affected by the shape, composition and surrounding medium.

The optical properties of AuNPs are tunable by synthetic control of the particle size, shape, structure and composition. AuNPs with core diameter of < 2 nm, as well as bulk gold do not show SPR band in the UV-Vis spectra. The wavelength of SPR absorption peak is found to increase with increasing size of AuNPs in aqueous medium (Daniel & Astruc, 2004). Upon changing the shape of AuNPs from spheres to rods, the SPR band is

split into two bands, namely, 'transverse band' and 'longitudinal band'. The 'transverse band' is the band that appeared in the visible region at a wavelength similar to that of gold nanospheres, while 'longitudinal band' appears in the near-infrared (NIR) region, corresponding to electron oscillations along the long axis. Increasing the aspect ratio (length/width) of the gold nanorods may lead to a large red shift of the 'longitudinal band' (Huang & El-Sayed, 2010). Structural variation may also contribute to the change in optical property, as this phenomenon can be seen in gold nanoshells and nanocages. Decreasing the thickness of gold nanoshell may lead to a large red shift in SPR band due to the strong coupling between the inner and outer shell plasmons for thinner shell particles (Prodan et al., 2003). The SPR of gold nanocages can be tuned to a specific wavelength by controlling the amount of auric acid used in the synthesis (Chen et al., 2005). This tunable optical property of AuNPs has been successfully exploited to synthesize suitable AuNPs for various applications.

(b) *Non-radiative properties*

Apart from the tunable radiative properties, AuNPs are also capable of converting the absorbed light into heat through a series of nonradiative processes (Huang & El-Sayed, 2010). The energy transformation process is initiated by fast phase loss of the coherently excited electrons via electron-electron collisions, thus forming hot electrons with high temperature. The hot electrons are then thermally equilibrated with the nanoparticle lattice by passing the energy through electron-phonon interactions, leading to a hot lattice with increase in temperature on the order of few tens of degrees (Ahmadi et al., 1996; Link et al., 2000). Two subsequent processes may occur following lattice temperature rise, depending on the energy content. The first process involves the cooling of lattice by heat transfer to the surrounding medium via lattice-environment or phonon-phonon interactions, resulting temperature rise in the surrounding medium. Second possible process is the structural changes of NPs, i.e. NPs melting or fragmentation as a result of

massive heat accumulation within the lattice. The heat accumulation usually occurs when the heating rate is much faster than the cooling rate, as both of these processes are competitive against each other. Melting of gold nanorods into nanospheres of comparable volumes has been reported upon irradiation using a femtosecond (fs) laser of 40 μJ energy, while fragmentation of gold nanorods to smaller nanospheres is observed upon irradiation using nanosecond laser with higher energy (Link et al., 1999). The possible mechanism suggested for the melting of gold nanorods involves heating of electrons at initial absorption on the femtoseconds time scale, followed by electron-phonon relaxation processes in the 1–3 picoseconds (ps) time scale. Since the irradiation time (100 fs) is shorter than the electron-phonon relaxation time (1–3 ps), kinetic energy of the gold atoms is increased, which leads to the melting of gold nanorods (Link et al., 1999). In order to use AuNPs for photothermal therapy, the first process has to be dominated to allow heat dissipation to the surrounding medium for killing of the cancer cells.

2.2.2.3 Applications of AuNPs

The unique properties of AuNPs, i.e. light scattering, conversion of absorbed light into heat and ease of functionalization, have been exploited for various biological applications, such as disease detection, imaging, photothermal therapy and drug delivery (Her et al., 2017), as illustrated in Figure 2.5. The physicochemical characteristics of AuNPs can be tailored for different applications. For example, larger AuNPs are preferred for imaging due to higher scattering efficiency, whereas smaller AuNPs are more preferred for photothermal therapy as the absorbed light energy undergoes a thermal dissipation process to produce localized heat (Jain et al., 2006). Some of these applications are described below.

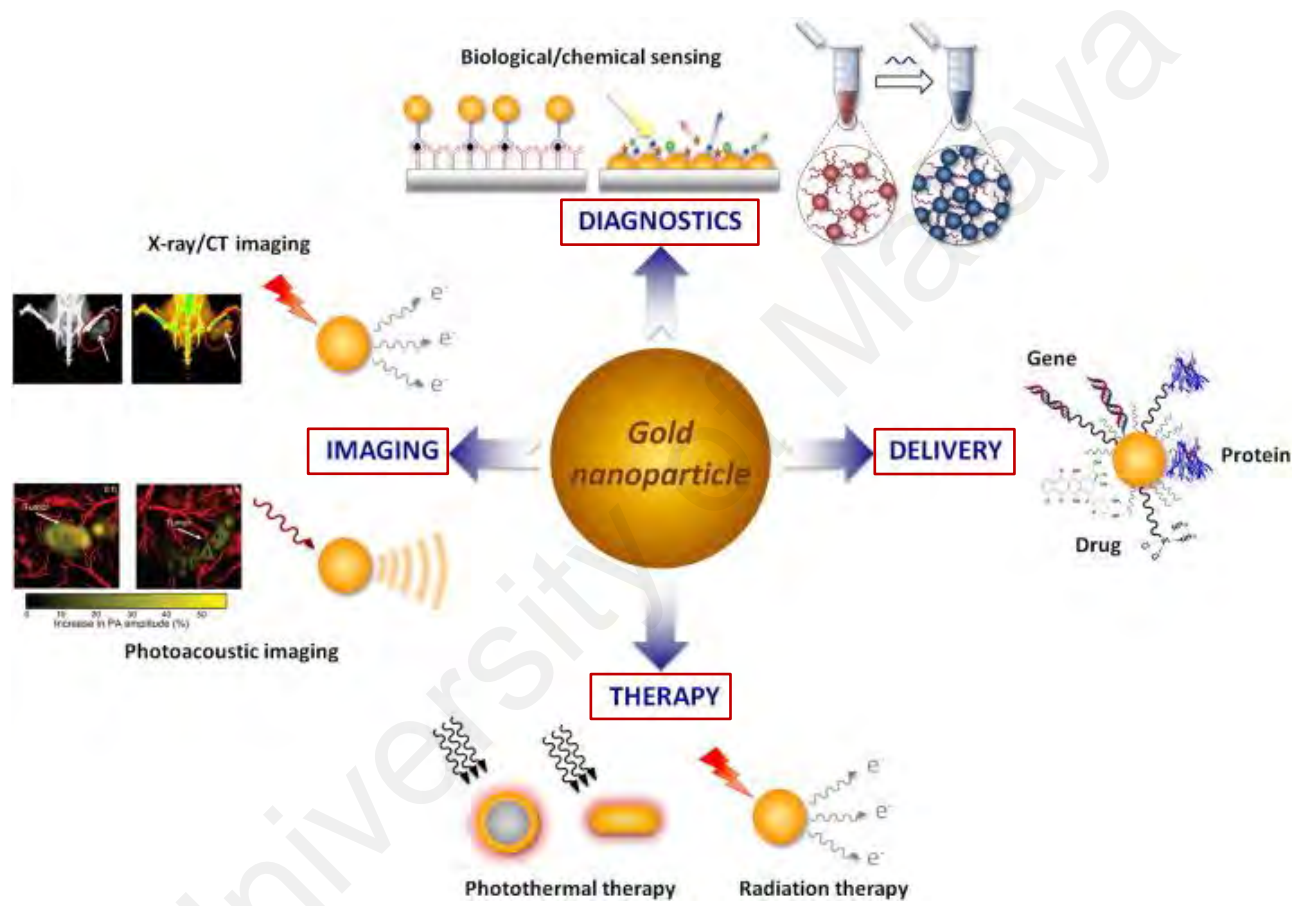


Figure 2.5: Diagram showing various biomedical applications of AuNPs. Adapted with permission from (Her et al., 2017).

(a) ***Cancer imaging***

In vivo imaging plays an important role in early diagnosis and therapy of cancer. Gold nanoparticles have been shown to be an ideal candidate as contrast agent for cellular and biological imaging, owing to their high scattering efficiency and high X-ray attenuation power. In addition, AuNPs can be specifically engineered to carry payloads or prolong circulation time. Earlier reports have demonstrated the use of AuNPs as contrast agent for cellular and tissue imaging using confocal scanning optical microscopy, multiphoton plasmon resonance microscopy and dark field microscopy (Sokolov et al., 2003; Yelin et al., 2003; El-Sayed et al., 2005). Furthermore, use of AuNPs for cellular imaging has overcome the common problems encountered in the use of fluorescent dyes, as AuNPs are brighter, non-susceptible to photobleaching or denaturation and are easily detected at low concentrations (El-Sayed et al., 2005).

Table 2.2 summarizes *in vivo* applications of AuNPs for cancer imaging based on different techniques. Gold nanospheres have been demonstrated for the use as contrast agent for *in vivo* computed tomography (CT) of various types of cancers, due to their high X-ray attenuation power. CT is one of the most extensively used radiography imaging techniques that produces cross-sectional images for 3D image construction (Padmanabhan et al., 2016). Both high spatial and temporal resolution images can be produced with CT at relatively lower cost. However, currently used, iodinated contrast agents in CT have limitations of short circulation half-life, non-specificity and renal toxicity (Cheheltani et al., 2016). On the other hand, use of AuNPs as CT contrast agent has shown to overcome the drawbacks of iodinated contrast agents (Zhou et al., 2016). Gold nanospheres labeled with radioactive isotopes (e.g. ^{125}I and ^{199}Au) have been shown as an effective probe emitting gamma rays for single-photon-emission computed tomography (SPECT) / CT in imaging glioblastoma (Kim et al., 2011; Zhao et al., 2016). Radiolabeled (^{64}Cu) gold nanoshells, nanocages and hollow nanospheres have been

Table 2.2: *In vivo* applications of gold nanoparticles for cancer imaging.

Type of AuNPs	Cancer Type	Imaging Technique	Reference
Gold nanospheres	Glioblastoma (U87MG cells)	SPECT / CT	Kim et al. (2011)
	Lung cancer (SPC- A1 cells)	CT	Peng et al. (2012)
	Epidermal carcinoma (FA receptor-overexpressing KB cells)	CT, MRI	Chen et al. (2013)
	Epidermal carcinoma (KB cells)	CT	Zhou et al. (2016)
	Colon carcinoma (CT26 cells)	CT, Fluorescence imaging	Zhang et al. (2015)
	Melanoma (SKMEL23 cells)	CT	Meir et al. (2015)
	Breast cancer (4T1 cells)	SPECT / CT	Zhao et al. (2016)
Gold nanorods	Ovarian cancer (OV2008, HEY, SKOV3 cells)	PAI, SERS imaging	Jokerst et al. (2012)
	Liver cancer (Huh-7 cells)	PAI, NIR fluorescence imaging	Guan et al. (2017)
Gold nanoshells	Squamous cell carcinoma (SCC-4 cells)	PET / CT	Xie et al. (2010)
	Epithelial carcinoma (A431 cells)	PET	Karmani et al. (2013)
	Colorectal cancer (SW620 cells)	MRI, CT	He et al. (2014)

Table 2.2, continued.

Type of AuNPs	Cancer Type	Imaging Technique	Reference
Gold nanoclusters	Breast cancer (MCF-7 cells)	CT, MRI, NIR fluorescence imaging	Hu et al. (2013)
	Cervix adenocarcinoma (HeLa cells)	NIR fluorescence imaging	Zhang et al. (2014)
	Prostate cancer (PC3 cells)	PET	Zhao et al. (2014)
	Glioblastoma (U87MG cells)	PET, NIR fluorescence imaging	Hu et al. (2014)
	Glioblastoma (U87MG cells)	MRI, SERS imaging	Gao et al. (2017)
Gold nanostars	Ovarian cancer (SKOV3 cells)	SERS imaging	D'Hollander et al. (2016)
	Lung adenocarcinoma (A549 cells)	CT, MRI, NIR fluorescence imaging	Hou et al. (2017)
Gold nanocages	Breast cancer (EMT-6 cells)	PET / CT	Wang et al. (2012)
Hollow gold nanospheres	Hepatocellular carcinoma (VX2 cells)	PET / CT	Tian et al. (2013)
Gold nanoprisms	Colorectal cancer (HT-29 cells)	PAI	Bao et al. (2013)
Gold nanotripods	Glioblastoma (U87MG cells)	PAI	Cheng et al. (2014)

successfully used for positron emission tomography (PET) / CT, which allows tracking of AuNPs *in vivo* distribution (Xie et al., 2010; Wang et al., 2012; Tian et al., 2013).

Although CT is useful for tumor staging, it however offers poor soft tissue contrast and sensitivity. Thus, combination of different imaging techniques has been employed to get a more comprehensive diagnostic information. Chen and co-workers have successfully synthesized gadolinium (Gd^{3+})-chelated gold nanospheres for dual-modal CT and magnetic resonance imaging (MRI), targeting folic acid (FA) receptor-overexpressing KB cells (Chen et al., 2013). The advantage of excellent soft-tissue contrast offered by MRI can complement CT results (Chen et al., 2013). Furthermore, tagging of aggregation-induced emission red dye to PEGylated phospholipid-entrapped AuNPs allows their use as dual-modal fluorescence and CT probes for high spatial resolution and high sensitivity imaging of colon carcinoma (Zhang et al., 2015). Triple modal imaging, involving CT, MRI and fluorescence imaging has also been shown by using gold nanoclusters chelated with Gd^{3+} (Hu et al., 2013; Hou et al., 2017).

Photoacoustic imaging (PAI) produces a tomographic image *in vivo* with very high spatial resolution and deep penetration. Gold nanorods have been synthesized and used for cancer imaging as dual-modal contrast agents for PAI along with surface-enhanced Raman scattering (SERS) imaging or NIR fluorescence imaging (Jokerst et al., 2012; Guan et al., 2017). Gold nanoprisms and gold nanotripods have also been used as contrast agents for PAI in imaging colorectal cancer and glioblastoma (Bao et al., 2013; Cheng et al., 2014). Due to enhancing capacity of Raman signals, gold nanostars have been developed as SERS contrast agent in imaging of ovarian cancer (D'Hollander et al., 2016).

(b) ***Photothermal treatment of cancers***

Photothermal treatment (PTT) utilizes the non-radiative properties of AuNPs to convert absorbed light into heat for photothermal ablation of cancer (Huang & El-Sayed, 2010). Irradiation of AuNPs with light of suitable wavelength increases localized temperature, thus leading to photothermal destruction of cancer cells in the vicinity. PTT can selectively target tumor and cause minimal damage to adjacent normal tissues (Mieszawska et al., 2013).

Photothermal ablation of cancer can be attained using gold nanospheres upon irradiation with pulsed or continuous wave lasers in the visible range. Such treatment is applicable for shallow tumors, e.g., skin and breast cancers. Successful results have been obtained with both *in vitro* and *in vivo* studies. El-Sayed and his group have synthesized anti-epithelial growth factor receptor antibody-conjugated gold nanospheres for selective killing of squamous carcinoma upon laser (514 nm) irradiation (El-Sayed et al., 2006). Gold nanospheres conjugated with anti-Mucin 7 have been shown to kill urothelial cancer cells upon laser (532 nm) irradiation (Chen et al., 2015). Use of gold nanospheres in combination with DOX in PTT has shown improved treatment efficacy for breast cancer (Mendes et al., 2017). Recently, aptamer-conjugated gold nanospheres have been used for selective *in vivo* photothermal destruction of Ehrlich carcinoma, upon irradiation with 532 nm laser (Kolovskaya et al., 2017).

Several earlier reports have also demonstrated *in vivo* PTT of various cancers using AuNPs of different shapes, i.e., nanorods, nanocages, nanoshells, hollow nanospheres and nanoclusters (Table 2.3). These AuNPs possess SPR absorption in NIR region, which allows PTT using NIR laser. NIR light has deeper penetration due to minimal absorption of the hemoglobin and water in tissues in this spectral region, thus making it suitable for PTT of deep-seated tumor within the tissue (Huang & El-Sayed, 2010). Some of the

Table 2.3: *In vivo* applications of gold nanoparticles in photothermal treatment of various cancers.

Type of AuNPs	Cancer Type	Treatment	Reference
Gold nanorods	Melanoma (MDA- MB-435 cells)	Laser: 810 nm, 2 W/cm ² , 5 min	Maltzahn et al. (2009)
	Lung adenocarcinoma (A549 cells)	Laser: 980 nm, 0.84 W/cm ² , 5 min	Shi et al. (2014)
	Lung adenocarcinoma (A549 cells)	Laser: 808 nm, 0.5 W/cm ² , 10 min	Luo et al. (2016)
	Non-small cell lung cancer (PC-9 cells)	Laser: 808 nm, 3.6 W/cm ² , 8 min	Wang et al. (2016)
	Gastric cancer (MGC803 cells)	Laser: 808 nm, 1.5 W/cm ² , 3 min	Liu et al. (2016)
	Colon carcinoma (26 cells)	Laser: 808 nm, 0.24 W/cm ² , 10 min Drug: DOX	Li et al. (2014)
	Breast cancer (4T1 cells)	Laser: 760 nm, 16 W/cm ² , 20 min Drug: DOX	Zhang et al. (2014)
Gold nanocages	Breast cancer (4T1 cells)	Laser: 850 nm, 1 W/cm ² , 10 min	Piao et al. (2014)
	Breast cancer (MDA-MB-231 cells)	Laser: 808 nm, 1 W/cm ² , 5 min Drug: DOX	Wang et al. (2014)

Table 2.3, continued.

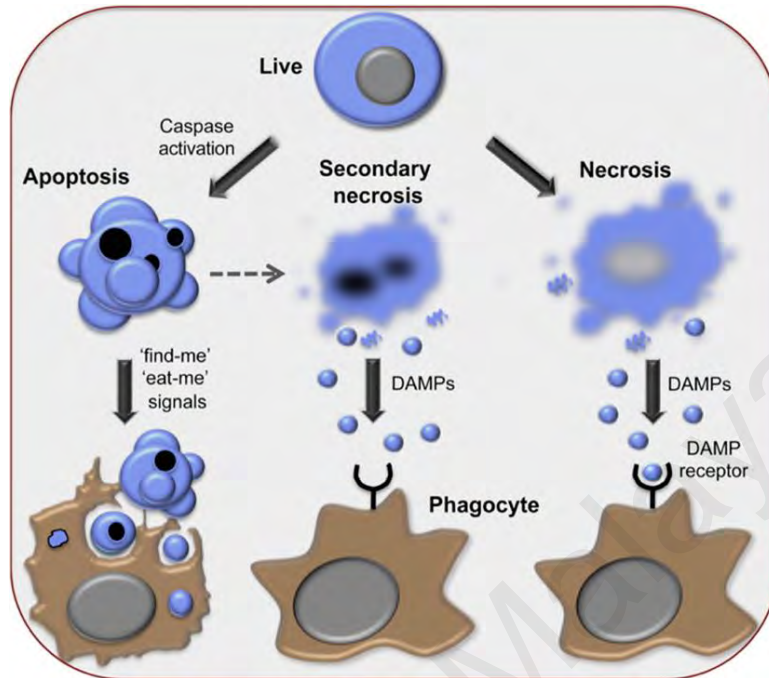
Type of AuNPs	Cancer Type	Treatment	Reference
Gold nanoshells	Breast cancer (MDA-MB-231 cells)	Laser: 810 nm, 2 W/cm ² , 5 min	Ayala-Orozco et al. (2014)
	Breast cancer (4T1 cells)	Laser: 808 nm, 1 W/cm ² , 5 min	Xuan et al. (2016)
	Breast cancer (4T1 cells)	Laser: 808 nm, 1 W/cm ² , 10 min Drug: 10-Hydroxycamptothecin	Li et al. (2014)
	Hepatoma (BEL-7402 cells)	Laser: 808 nm, 1.5 W/cm ² , 2 min Drug: DOX	Wang et al. (2016)
Hollow gold nanospheres	Ovarian carcinoma (SKOV3 cells)	Laser: 808 nm, 1.5 W/cm ² , 3 min	Wang et al. (2015)
	Ovarian carcinoma (SKOV3 cells)	Laser: 808 nm, 0.5 W/cm ² , 2 min (3×) Drug: DOX	Zhou et al. (2015)
Gold nanoclusters	Fibrosarcoma (HT-1080 cells)	Laser: 660 nm, 0.5 W/cm ² , 1 min	Kang et al. (2015)

AuNPs have also been conjugated with targeting moieties, e.g. aptamer, CXCR4 antibody, peptide and hyaluronic acid for active targeting of cancer cells (Shi et al., 2014; Liu et al., 2016; Wang et al., 2015; Wang et al., 2014). Furthermore, these AuNPs can be loaded with chemotherapeutic drugs such as DOX, for simultaneous PTT and chemotherapy (Zhang et al., 2014; Wang et al., 2014).

Photothermal therapy can trigger cell death through two mechanisms, i.e. apoptosis and necrosis, as illustrated in Figure 2.6 A. Cells undergoing apoptosis maintain their membrane integrity and express engulfment signals, leading to their prompt clearance by phagocytes without incurring inflammation (Park & Kim, 2017). Earlier studies have reported that PTT-induced cell death is mediated by apoptosis mechanism (Pérez-Hernández et al., 2015; Ali et al., 2017). Apoptosis can occur through two major pathways, i.e. 'intrinsic' and 'extrinsic' pathways. 'Intrinsic' pathway is more likely to be the major mode of PTT-mediated apoptosis. A proposed intrinsic pathway (mitochondrial apoptosis pathway) for PTT-induced apoptosis is depicted in Figure 2.6 B. Proapoptotic members of Bcl-2 family (Bax/Bak) are activated upon cell stress, which trigger mitochondrial membrane permeabilization and release of cytochrome c. Once cytochrome c is released into cytoplasm, it interacts with Apaf-1, deoxyadenosine triphosphate (dATP) and procaspase 9 to form the apoptosome, which activates executioner caspases-3, -6 and -7 to initiate apoptotic cell death (Melamed et al., 2015; Pérez-Hernández et al., 2015).

Secondary necrosis may occur if the apoptotic cells were not cleared by phagocytes, leading to loss of membrane integrity and release of damage-associated molecular patterns (DAMPs). On the contrary, primary necrotic cells lose their membrane integrity and release DAMPs, resulting in inflammatory response (Melamed et al., 2015). Contrary to earlier reports suggesting involvement of apoptotic mechanism in PTT-induced cell

A



B

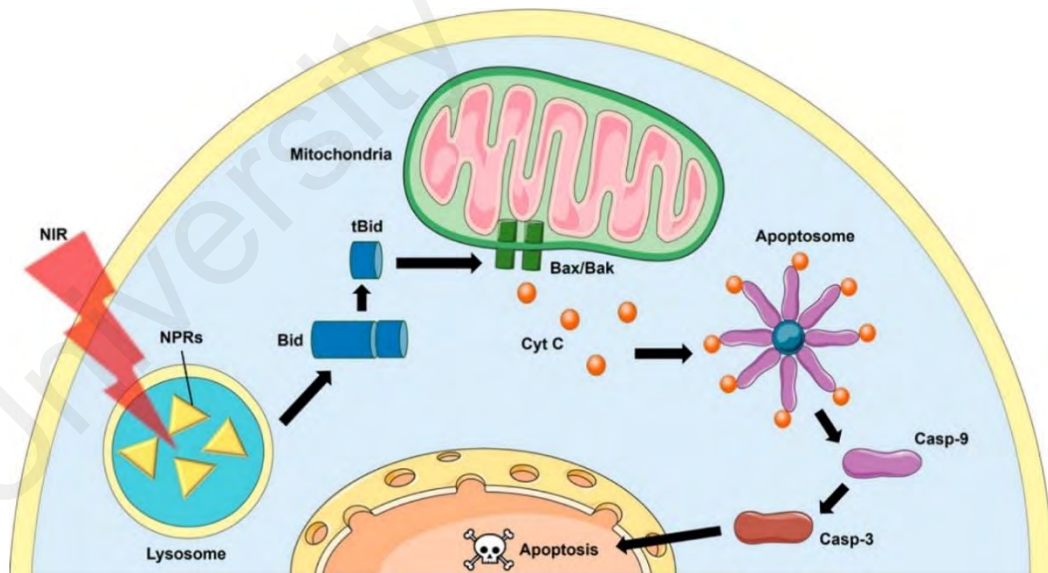


Figure 2.6: Diagrams showing photothermal-induced cell death through two mechanisms, i.e. apoptosis and necrosis (A) and proposed apoptosis mechanism upon gold nanoprism-mediated photothermal treatment (B). Reprinted with permission from (Melamed et al., 2015).

death, there are reports which have suggested necrosis as the primary cell death mechanism in PTT (Kolovskaya et al., 2017; Mocan et al., 2011; Iancu et al., 2011). Apoptosis is considered as a ‘cleaner’ pathway and is preferred over cell death through necrosis. Treatment parameters, such as laser type and laser intensity can be a determination factor for the mechanism of cell death (Huang et al., 2010; Pérez-Hernández et al., 2015). It has been shown that PTT using high intensity (30 W/cm^2) laser is able to induce cell death through necrosis, while reducing the laser intensity to 5 W/cm^2 can induce cell apoptosis (Pérez-Hernández et al., 2015). On the other hand, PTT using nanosecond-pulsed laser triggers cell necrosis, while PTT using continuous wave laser can induce apoptosis or necrosis, depending on the laser intensity (Huang et al., 2010). In view of the beneficial aspect of apoptotic killing of cells, PTT should be designed to trigger apoptosis.

(c) ***Theranostics***

Theranostics is a therapeutic technique that is used for simultaneous diagnosis and treatment of a disease (Ahmed et al., 2012). Apart from the above-mentioned applications, multifunctional AuNPs can be fabricated for theranostic applications, allowing simultaneous targeting and diagnosis as well as cancer therapy (Guo et al., 2017; Gharatape & Salehi, 2017).

Selected examples of theranostic applications of AuNPs are listed in Table 2.4. A dual-modal imaging-guided photothermal tumor ablation has been shown with the help of Prussian blue-coated gold nanospheres for the treatment of colon adenocarcinoma. These nanospheres allow a more precise guidance for PTT using PAI and CT, where location and size of the tumor can be detected as well as presence of photo-absorbing agent can be determined before therapy (Jing et al., 2014). Hybrid gold nanoshells with Fe_3O_4 nanoclusters have also been designed for CT, photoacoustic tomography (PAT) and MRI

Table 2.4: Theranostic applications of gold nanoparticles.

Type of AuNPs	Cancer Type	Imaging Technique	Therapeutic Approach	Reference
Gold nanospheres	Glioblastoma (U87MG cells)	MRI	Drug delivery (DOX)	Cheng et al. (2014)
	Colon adenocarcinoma (HT-29 cells)	PAI, CT	PTT	Jing et al. (2014)
Gold nanorods	Squamous carcinoma (SCC-7 cells)	NIR fluorescence imaging	PTT, PDT	Jang et al. (2011)
	Squamous carcinoma (SCC-7 cells)	PAI	PTT, Drug delivery (DOX)	Chen et al. (2015)
	Epithelial carcinoma (A431 cells)	NIR fluorescence imaging	PTT	Choi et al. (2012)
	Glioblastoma (U87 MG cells)	PET	PTT	Sun et al. (2014)
	Glioblastoma (U87 MG cells)	PAI	PTT	Song et al. (2015)
Hollow gold nanospheres	Glioblastoma (U87 MG cells)	PAI	PTT	Lu et al. (2011)
	Adenocarcinoma (A549 cells)	CT	PTT, Radiotherapy, Drug delivery (DOX)	Park et al. (2015)
Gold nanoshells	Melanoma (B16-F10 cells)	MRI, X-ray imaging, Optical imaging	PTT	Coughlin et al. (2014)

Table 2.4, continued.

Type of AuNPs	Cancer Type	Imaging Technique	Therapeutic Approach	Reference
Hybrid gold nanoparticles	Glioblastoma (C6 cells)	MRI, PAI	PTT	Yang et al. (2013)
	Glioblastoma (U87 MG cells)	X-ray imaging	PTT, Drug delivery (Docetaxel)	Hao et al. (2015)
	Pancreatic adenocarcinoma (AsPC-1 cells)	NIR fluorescence imaging, MRI	PTT	Chen et al. (2014)
	Breast cancer (4T1 cells)	PAI, MRI, SERS imaging	PTT	Huang et al. (2015)
	Lung tumor, Melanoma (A2058)	PET	PTT, Drug delivery (DOX)	Cheng et al. (2016)
	Pancreatic tumor (MiaPaca-2 cells)	Fluorescence imaging	Drug delivery (GEM & DOX)	Croissant et al. (2016)
	Squamous carcinoma (SCC-7 cells)	NIR fluorescence imaging, PAI	PTT	Gao et al. (2016)
	Hepatoma (H22 cells)	CT, PAT, MRI	PTT	Li et al. (2016)

Table 2.4, continued.

Type of AuNPs	Cancer Type	Imaging Technique	Therapeutic Approach	Reference
Gold nanostars	Primary soft-tissue sarcomas	Two-photon luminescence imaging, SERS imaging, CT	PTT	Liu et al. (2015)
	Breast cancer (MDA-MB-231 cells)	MRI, SERS imaging	PTT	Gao et al. (2015)
Gold nanoclusters	Breast cancer (MDA-MB-231 cells), Sarcoma (S180 cells)	NIR fluorescence imaging	Drug delivery (DOX)	Chen et al. (2012)

trimodal imaging-guided tumor PTT and have been used successfully in the treatment of hepatoma (Li et al., 2016). Other imaging techniques (fluorescence and SERS imaging) have also been employed for imaging-guided PTT (Gao et al., 2016; Liu et al., 2015).

A gold nanorod-photosensitizer complex has been exploited to work as a multifunctional platform for NIR fluorescence imaging as well as PTT and PDT to treat squamous carcinoma. This complex can clearly identify tumor site and effectively reduce tumor growth (Jang et al., 2011). Furthermore, targeting ligands such as peptide, biotin and antibody have also been conjugated to multifunctional AuNPs for active targeting of cancer cells. For example, conjugation of Arg-Gly-Asp peptide to ^{64}Cu -integrated gold nanorods has shown high targeting ability towards glioblastoma and has been applied for *in vivo* PET imaging-guided PTT (Sun et al., 2014). Hybrid silica-gold-iron-oxide NPs conjugated with anti-neutrophil gelatinase associated lipocalin antibody can specifically target pancreatic adenocarcinoma cells *in vivo* through dual-modal imaging-guided PTT (Chen et al., 2014). Recent reports have demonstrated combination of chemotherapy with imaging-guided PTT. For example, Chen and colleagues have successfully synthesized biotin-conjugated gold nanorods loaded with DOX for simultaneous cancer-targeted imaging and imaging-guided chemo-photothermal therapy (Chen et al., 2015). Hollow gold nanospheres loaded with DOX have also been developed for CT imaging and triple combination of chemotherapy, PTT and radiotherapy for lung adenocarcinoma treatment (Park et al., 2015).

2.3 Interaction of nanoparticles with plasma proteins

After administration of NPs into blood stream, a dynamic layer of proteins, known as corona is formed around NPs. The interactions between NPs and plasma proteins may influence biocompatibility, distribution and efficacy of nanotherapeutic agents, i.e., NPs (Zanganeh et al., 2016; Nguyen & Lee, 2017). Protein corona has been shown to reduce

cytotoxicity and intracellular oxidative stress of NPs, thus making NPs more biocompatible for various biological applications (Wang et al., 2013; Tedja et al., 2012). Additionally, protein corona can also prolong NPs blood circulation by reducing macrophage recognition and complement activation (Peng et al., 2013). The common carrier proteins present in blood plasma include HSA and α -1-acid glycoprotein. Many studies have been reported on the interaction between ligands and HSA, as it is the most abundant transport protein, which can reversibly bind to a large number of ligands (Korolenko et al., 2007). The following sections describe the physicochemical, structural and ligand binding properties of HSA.

2.3.1 Physicochemical properties of HSA

Table 2.5 summarizes various physicochemical properties of HSA. It has a molecular mass of 66,438 Da, as calculated from its amino acid composition (Peters Jr, 1996), which was in agreement with the molecular mass of 66,437 Da, obtained from matrix-assisted laser desorption/ionization-time of flight (MALDI-TOF) mass spectrometry (Amoresano et al., 1998). The hydrodynamic parameters of HSA, such as diffusion coefficient and sedimentation coefficient were determined to be $6.1 \times 10^{-7} \text{ cm}^2 \text{ s}^{-1}$ and 4.6 s, respectively (Oncley et al., 1947). Polypeptide chain of HSA forms a heart-shaped structure with dimensions of $80 \times 80 \times 30 \text{ \AA}$, based on the results obtained from X-ray crystallography (He & Carter, 1992). The partial specific volume was found to be $0.733 \text{ cm}^3 \text{ g}^{-1}$ (Hunter, 1966). The radius of gyration is 26.7 \AA and was similar to the rotational hydrodynamic radius of 26.4 \AA (Carter & Ho, 1994). An axial ratio of 3.5:1 was obtained from dielectric dispersion results (Ferrer et al., 2001). Values of intrinsic viscosity and frictional ratio of 0.056 dL g^{-1} and 1.28:1, respectively, indicated globular conformation of the protein (Hunter & McDuffie, 1959; Oncley et al., 1947). The isoionic point of HSA was determined as 5.16 (Hughes, 1954). Native HSA possesses an isoelectric point of 4.7, which is increased to 5.8 for defatted HSA (Peters Jr, 1996). Higher value of the molar

Table 2.5: Physicochemical properties of HSA.

Property	Value	Reference
Molecular mass		
- Amino acid composition	66,438 Da	Peters Jr (1996)
- MALDI-TOF	66,437 Da	Amoresano et al. (1998)
Diffusion coefficient, $D_{20,w}$	$6.1 \times 10^{-7} \text{ cm}^2 \text{ s}^{-1}$	Oncley et al. (1947)
Sedimentation coefficient, $S_{20,w}$	4.6 s	Oncley et al. (1947)
Overall dimension	$80 \times 80 \times 30 \text{ \AA}$	He & Carter (1992)
Partial specific volume, \bar{v}_2	$0.733 \text{ cm}^3 \text{ g}^{-1}$	Hunter (1966)
Radius of gyration	26.7 \AA	Carter & Ho (1994)
Axial ratio	3.5:1	Ferrer et al. (2001)
Intrinsic viscosity, $[\eta]$	0.056 dL g^{-1}	Hunter & McDuffie (1959)
Frictional ratio, f/f_0	1.28:1	Oncley et al. (1947)
Isoionic point	5.16	Hughes (1954)
Isoelectric point		
- Native	4.7	Peters Jr (1996)
- Defatted	5.8	Peters Jr (1996)
Extinction coefficient, ϵ at 280 nm	$36,500 \text{ M}^{-1} \text{ cm}^{-1}$	Painter et al. (1998)
Secondary structures		
- α -Helix	67 %	Carter & Ho (1994)
- β -Sheet	10 %	Carter & Ho (1994)
Net charge per molecule		
- Hydrogen ion titration (pH 7.4)	- 19	Tanford (1950)
- Amino acid sequence	- 15	Peters Jr (1996)

extinction coefficient at 280 nm ($36,500 \text{ M}^{-1} \text{ cm}^{-1}$) can be ascribed to the presence of Trp and Tyr residues in HSA (Painter et al., 1998). The secondary structure of the protein is predominantly α -helical (67%), with remaining residues distributed as β -sheets (10%) and flexible regions (23%) (Carter & Ho, 1994). At physiological pH (pH7.4), the net charge of HSA was found to be -19 (Tanford, 1950), which was slightly higher than the calculated value of -15 from its amino acid sequence (Peters Jr, 1996).

2.3.2 Amino acid composition and structural properties of HSA

Human serum albumin is a small globular protein and is comprised of 585 amino acid residues in a single polypeptide chain. The amino acid composition of HSA is shown in Table 2.6. HSA has a single Trp residue, while Met (6) and Ile (8) are also present in small amounts. The protein is rich in the distribution of several hydrophobic amino acids such as Ala (62), Leu (61), Val (41), Phe (31) and Pro (24). Number of charged amino acids is also found to be higher, being 62, 59, 36 and 24 for Glu, Lys, Asp and Arg, respectively. There are 35 Cys residues present in HSA.

As depicted in Figure 2.7, the amino acid residues form nine flexible loops, which are organized into distinct pattern with eight sequential Cys-Cys pairs. The primary structure of HSA is comprised of three domains with long-short-long loops. These domains are encompassed of amino acid residues, 1–195 (domain I), 196–383 (domain II) and 384–585 (domain III). Among the nine loops, the first two loops of each domain, viz. loops 1–2, 4–5 and 7–8 are grouped to form subdomains IA, IIA and IIIA, respectively, while loop 3, 6 and 9 form subdomains IB, IIB and IIIB, respectively. There are 17 intramolecular disulfide bonds, formed by all Cys residues except Cys-34, which stabilize the HSA structure. The three domains of HSA show structural and sequence similarities, with 18–25% sequence homology, which is found highest among the long loops 3, 6 and 9 (Peters Jr, 1996).

Table 2.6: Amino acid composition of HSA. Adapted from (Peters Jr, 1996).

Amino Acid	No. of Residues
Alanine	62
Arginine	24
Asparagine	17
Aspartic acid	36
Cysteine	35
Glutamic acid	62
Glutamine	20
Glycine	12
Histidine	16
Isoleucine	8
Leucine	61
Lysine	59
Methionine	6
Phenylalanine	31
Proline	24
Serine	24
Threonine	28
Tryptophan	1
Tyrosine	18
Valine	41
Total	585

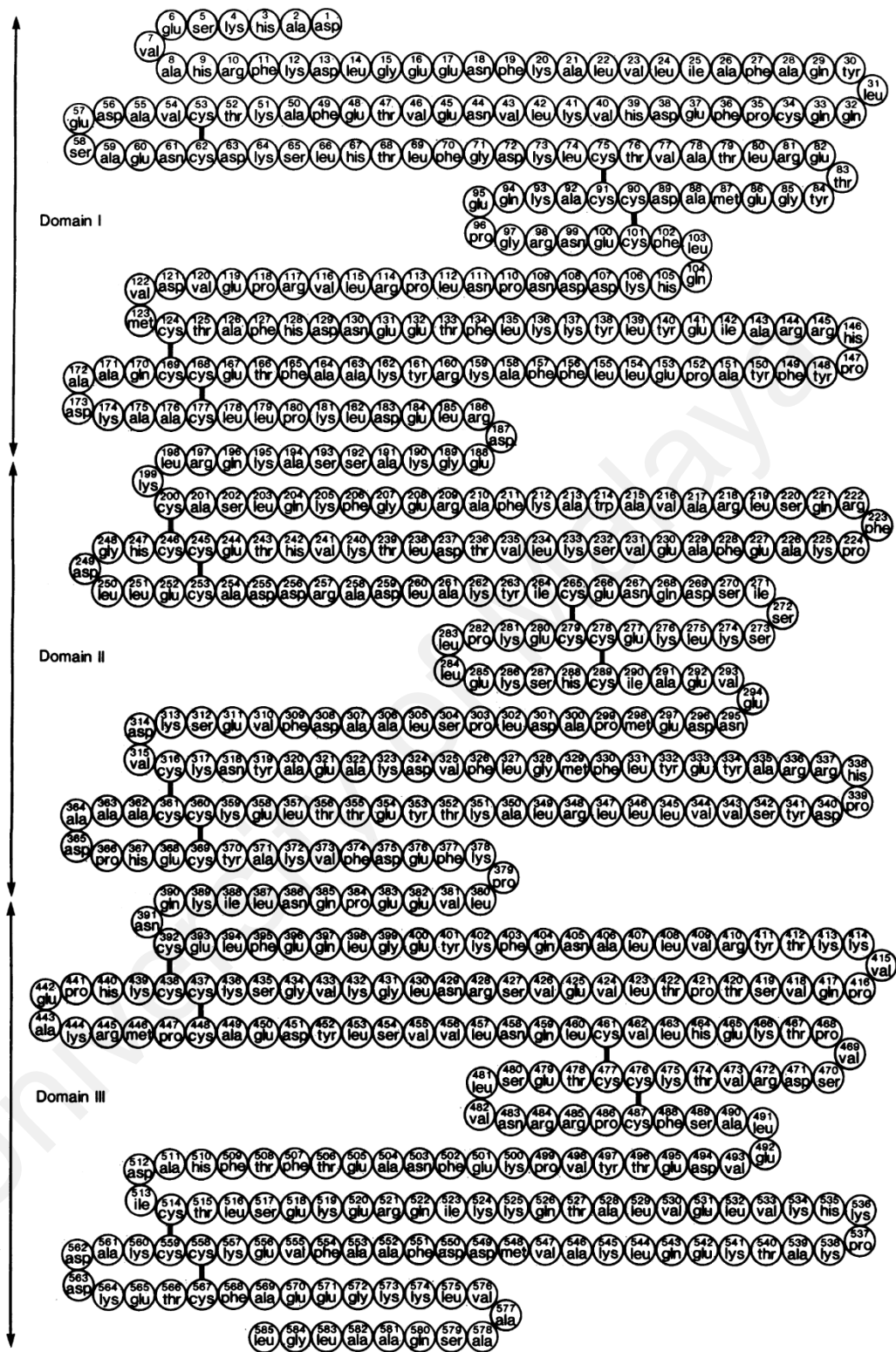


Figure 2.7: Amino acid sequence and disulfide bonding pattern of HSA. The three domains are indicated by arrows, with each domain contains two long and one short loops. Reproduced from (Dugaiczky et al., 1982).

The crystal structure of HSA reveals a heart-shaped structure, which is formed by three homologous domains I, II, and III (Peters Jr, 1996). Each homologous domain is further divided into a pair of subdomains, namely, 'A' and 'B', which are comprised of 6 and 4 α -helices, respectively. The order of helices h1–h4 in subdomains 'A' and 'B' is identical, while two additional short helices (h5 and h6) in subdomain 'A' are arranged in antiparallel fashion. These helices are connected with each other through 17 Cys-Cys disulfide bridges, while the two subdomains are assembled via hydrophobic helix packing interactions. Domains I–II and II–III are connected through extensions of helices, viz., Ib-h4–IIa-h1 and IIb-h4–IIIa-h1, respectively, thus creating two longest helices (Carter & Ho, 1994). Therefore, the actual number of helices in HSA structure is 28 instead of 30.

Although the three domains are structurally similar, their global assembly is highly asymmetric. Domain I is aligned perpendicular to domain II, forming a T-shaped assembly of HSA. Conversely, formation of a Y-shaped assembly is observed due to an angle shift of 45° between domains II and III. Interactions between domains, i.e., domains II to domains I and III involve hydrogen bonds and hydrophobic forces (Sugio et al., 1999). Deep hydrophobic pockets with positively charged residues at the entrances are found in subdomains IIA, IIIA and IB, which form ligand binding sites I, II and III, respectively (Sudlow et al., 1975; Kragh-Hansen et al., 2002).

2.3.3 Functions of HSA

Serum albumin is the most important protein responsible for numerous physiological functions due to its high concentration in the blood plasma. It plays important roles in maintenance of the blood pH, regulation of the colloid osmotic pressure and transportation of variety of small molecules (Figge et al., 1991; Singh-Zocchi et al., 1999; Peters Jr, 1996). Besides, HSA also acts as an antioxidant to protect bound substances

from oxidative damage (Roche et al., 2008). It also possesses enzymatic (esterase) activity (Goncharov et al., 2017).

The major function of HSA is transportation of a vast variety of endogenous and exogenous compounds, such as hormones, prostaglandins, fatty acids, bile acids and therapeutic drugs. It also facilitates the transportation of metal ions such as calcium, iron, copper, zinc and chloride through blood circulation (Peters Jr, 1996). In addition, HSA also acts as a toxic waste carrier to bind bilirubin and delivering it to the liver for hepatic excretion (Inoue et al., 1985).

2.3.4 Ligand binding properties

Serum albumin interacts with different ligands at several high and low affinity binding sites. Sudlow and his group have characterized two specific ligand binding sites, i.e., Sudlow's site I (warfarin binding site) and site II (benzodiazepine binding site) (Sudlow et al., 1975). Furthermore, a third site, namely, site III of HSA has also been identified, which is the preferred binding site for ligands such as digitoxin and hemin (Kragh-Hansen, 1985; Zunszain et al., 2003). Sudlow's site I and site II are located in subdomains IIA and IIIA, respectively, while site III is present in subdomain IB of HSA (Figure 2.8).

Sudlow's site I is characterized as hydrophobic ligand binding pocket, which is comprised of six helices of the subdomain IIA as well as a loop-helix feature of subdomain IB (Kragh-Hansen et al., 2002; Ghuman et al., 2005). It is composed of two clusters with polar residues, an inner cluster at the bottom of the pocket, consisted of Tyr-150, His-242 and Arg-257 residues and an outer cluster at the entrance of the pocket, formed by Lys-195, Lys-199, Arg-218, and Arg-222 residues (Ghuman et al., 2005). Presence of positively-charged residues at the entrance favors the binding of negatively-charged bulky heterocyclic molecules to this site. As illustrated in Figure 2.8, ligands

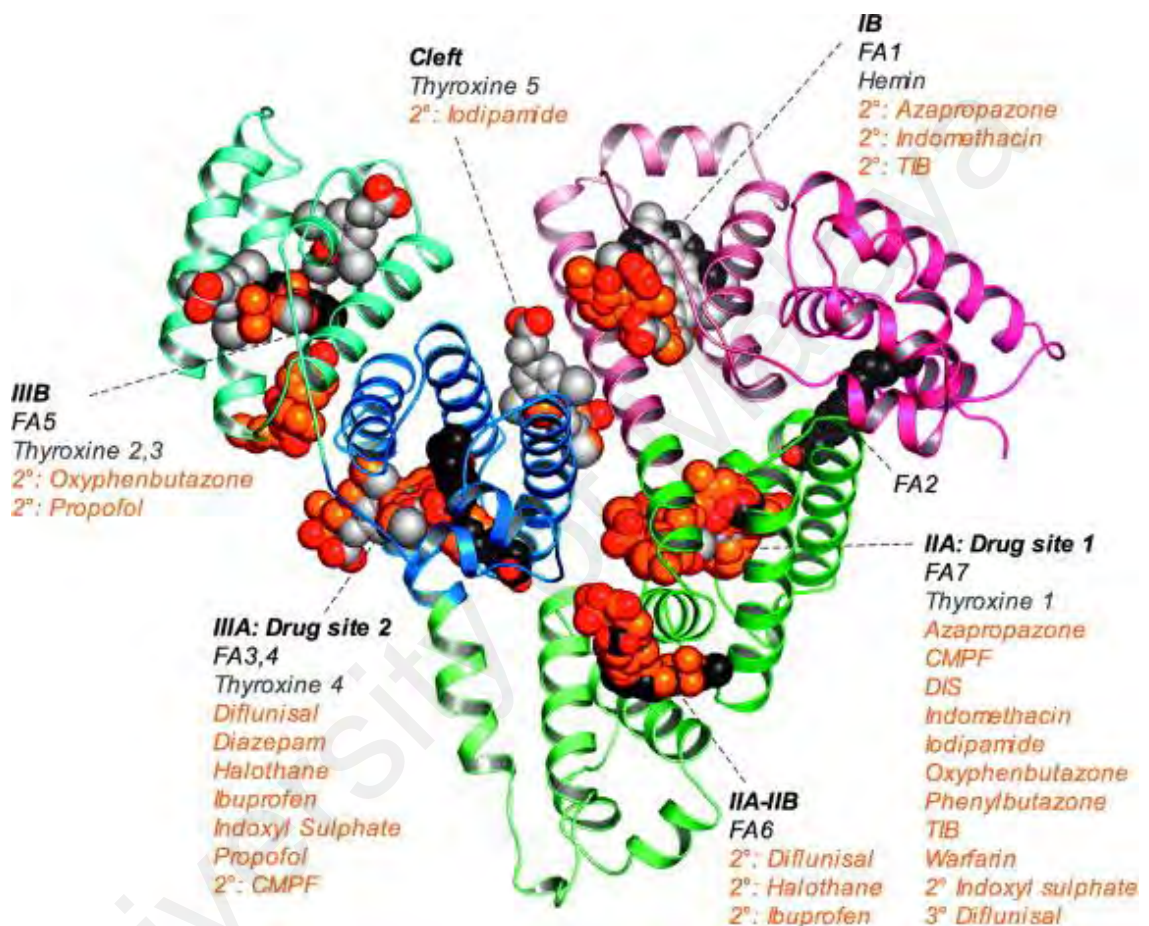


Figure 2.8: Ligand binding sites of HSA. The three domains are displayed in different colors and ligands are shown as space-filling models. Different ligands are represented by different colors: oxygen atoms (red); fatty acids (black); other endogenous ligands (hemin and thyroxine) (light grey) and drugs (orange). Reprinted with permission from (Ghuman et al., 2005).

such as warfarin, azapropazone, indomethacin and phenylbutazone preferably bind to Sudlow's site I (Ghuman et al., 2005).

Sudlow's site II is similar to site I, as it is also comprised of six helices of subdomain IIIA. The interior of the binding pocket is hydrophobic with a single dominant polar patch centered around Arg-410 and Tyr-411 residues near to the entrance (Curry, 2009). This site is more suited for the binding of aromatic carboxylic acids with a negatively-charged group at one end of the molecule away from a hydrophobic center (Kragh-Hansen et al., 2002). Ligands such as diazepam, ibuprofen, diflunisal and ketoprofen are found to have preference for the binding site II.

Apart from these two sites, site III is identified as D-shaped hydrophobic binding cavity, located in subdomain IB (Zunszain et al., 2003). It is the primary binding site for ligands such as hemin, digitoxin and lidocaine (Zunszain et al., 2003; Kragh-Hansen, 1985) and as secondary binding site for site I drugs, viz., warfarin azapropazone and indomethacin (Zsila, 2013). The hydrophobic cavity of site III consists of three basic residues at its entrance and the binding pocket is partly blocked by Tyr-138 and Tyr-161 residues in the absence of ligand (Zunszain et al., 2003).

2.3.5 Interaction of AuNPs with HSA

In view of the ligand binding properties of HSA, several earlier reports have shown the interaction of AuNPs with HSA (Sharma & Ilanchelian, 2015; Cañaveras et al., 2012). The interaction between AuNPs and HSA might influence physicochemical characteristics of the NPs as well as induce structural and conformational changes in the protein. Such structural changes in the protein may affect its normal functions and may lead to physiological complications (Wolfram et al., 2014).

Serum albumin has been shown to interact with AuNPs forming a layer of corona, which stabilizes the AuNPs (Cañaveras et al., 2012). Furthermore, the binding constant, degree of cooperativity, protein conformational changes have been demonstrated to depend on the particle size and nature of NP's surface (Lacerda et al., 2010; Cañaveras et al., 2012). Although these reports have characterized the interaction of chemically-synthesized AuNPs with HSA, interaction of green-synthesized AuNPs with HSA has not been explored. Therefore, the interaction of green-synthesized AuNPs with HSA was studied in detail in terms of binding affinity, forces involved, effect on protein's structure and fluorophores microenvironment as well as location of binding site. These results can help in understanding the biological implications of these AuNPs.

University of Malaysia

CHAPTER 3: MATERIALS AND METHODS

3.1 Materials

3.1.1 CM-AuNPs synthesis and characterization

Gold (III) chloride trihydrate ($\text{HAuCl}_4 \cdot 3\text{H}_2\text{O}$) (lot MKBQ2208V) was procured from Sigma-Aldrich Co., USA. *Curcuma mangga* rhizomes powder was obtained from Yogyakarta, Indonesia. Absolute ethanol (AR grade) was purchased from Merck, Germany. Carbon film-coated 300 mesh copper grids (lot 140604) were supplied by Proscitech, Australia. Disposable folded capillary cells (DTS1070) were the products of Malvern Instruments Ltd., UK.

3.1.2 Cell culture

Eagle's minimum essential medium (EMEM), sodium pyruvate, penicillin/streptomycin, amphotericin B, dimethyl sulfoxide (DMSO) and 3-(4,5-Dimethyl-2-thiazolyl)-2,5-diphenyltetrazolium bromide (MTT) were purchased from Sigma-Aldrich Co., USA. Human normal colon fibroblast cell line (CCD-18Co), human lung fibroblast cell line (MRC-5) and human breast cancer cell line (MCF-7) were procured from American type culture collection (ATCC), USA. Dulbecco's modified Eagle's medium (DMEM) with and without phenol red, fetal bovine serum (FBS), accutase and phosphate-buffered saline (PBS) (10 \times , pH 7.4) were supplied by Nacalai, Japan. Minisart syringe filters (0.2 μm pore size) were obtained from Sartorius, Germany.

3.1.3 Protein interaction studies

Human serum albumin (lyophilized powder, essential fatty acid free, lot 068K7538V) and 1-anilinonaphthalene-8-sulfonate (ANS) and warfarin (WFN) were obtained from Sigma-Aldrich Co., USA. Sodium dihydrogen phosphate (anhydrous) and disodium hydrogen phosphate (anhydrous) were purchased from System, Malaysia.

3.1.4 Miscellaneous

Gold nanoparticles (20 nm, stabilized in citrate buffer, lot MKBS8077V), gold standard for ICP (lot BCBM7955V), calcium chloride (anhydrous) and trisodium citrate dihydrate were procured from Sigma-Aldrich Co., USA. FITC-Annexin V apoptosis detection kit was supplied by BD Biosciences, USA. Potassium chloride, sodium hydrogen carbonate, fuming hydrochloric acid (37%) and nitric acid (65%) were procured from Merck, Germany. Triton-X, sodium chloride, magnesium chloride and dextrose were supplied by Acros Organics, Belgium, Fisher Scientific, UK, R&M Chemicals, UK and HmbG Chemicals, Germany, respectively.

Ultrapure (Type 1) water, obtained from Mili-Q water purification system (Merck, Germany) was used throughout these studies.

3.2 Methods

3.2.1 Synthesis of CM-AuNPs

3.2.1.1 Extraction of *Curcuma mangga* extract

Curcuma mangga rhizomes powder (100 g) was soaked in 300 ml of aqueous ethanol (50% v/v) at room temperature for 3 days. The extract-rich solvent was filtered and dried under reduced pressure using a rotary evaporator. The extract was further dried in the oven (60 °C) until a constant weight was reached. This was used as CM extract.

3.2.1.2 Preparation of stock solutions

Stock HAuCl_4 solution (1% w/v) was prepared by dissolving 1g HAuCl_4 crystals in 100 ml of water. The working HAuCl_4 solution (1 mM) was made by diluting 3.94 ml of the stock solution to 100 ml with water. Stock solution of CM extract (10 mg/ml) was prepared by dissolving 100 mg of the dried CM extract in 10 ml of aqueous ethanol (50% v/v).

3.2.1.3 Method of preparation

Since various factors such as concentrations of reducing agent and HAuCl_4 as well as incubation time are known to affect the synthesis of AuNPs, effects of these factors were studied in the preparation of CM-AuNPs.

Effect of incubation time on the preparation of CM-AuNPs was studied by mixing 4 ml of CM extract (10 mg/ml) and 10 ml of HAuCl_4 (1 mM) followed by incubation at room temperature for varying time periods. UV-Vis absorption spectra were recorded after 15, 30, 45, 60, 90 and 1440 min on BioTek Synergy H1 hybrid reader, in the wavelength range of 300–800 nm.

Influence of CM extract concentration on the preparation of CM-AuNPs was studied by adding 4 ml of CM extract at different concentrations (2–10 mg/ml with 2 mg/ml intervals) to each tube containing 10 ml of HAuCl_4 (1 mM) and incubating the mixture for 1 h at room temperature. The spectral measurements were made in the same way as described above.

Kinetic runs of these samples were also made by recording absorbance of these samples at 535 nm for different time periods (0–300 min). These samples were further incubated for 24 h at room temperature and zeta potential values was measured at 25 °C, using a folded capillary cell (DTS1070) on Malvern Zetasizer Nano ZS.

In order to investigate the effect of HAuCl_4 concentration on the preparation of CM-AuNPs, 4 ml of CM extract (10 mg/ml) was added to each tube containing 10 ml of HAuCl_4 at different concentrations (0.5, 1, 2, 3 and 4 mM). The mixtures were incubated at room temperature for 24 h prior to UV-Vis spectral and zeta potential measurements as described above.

3.2.1.4 Purification and concentration measurements

CM-AuNPs synthesized by incubating 4 ml of CM extract (10 mg/ml) and 10 ml of HAuCl₄ (1 mM) for 24 h were selected for subsequent studies. These CM-AuNPs were purified by repeated (3 times) centrifugation at 14,000 rpm for 30 min. The CM-AuNPs pellet, thus obtained was resuspended in water and stored at 4 °C.

The concentration of CM-AuNPs was determined based on Au mass concentration on Agilent microwave plasma-atomic emission spectrometer (MP-AES) 4100. Gold standard (10 µg/ml) was used to prepare the calibration curve prior to the analysis of the samples. For sample preparation, CM-AuNPs were digested with aqua regia (HCl:HNO₃ = 3:1) by incubating 100 µl of CM-AuNPs with 300 µl of aqua regia for 12 h at room temperature. Digested sample was filtered and diluted 100 times with water before subjecting it to MP-AES analysis.

3.2.2 Characterization of CM-AuNPs

3.2.2.1 High resolution-transmission electron microscopy

Size and shape of CM-AuNPs were studied using JEOL JEM-7600F high resolution-transmission electron microscope (HRTEM) with an accelerating voltage of 120 kV. CM-AuNPs were placed on 300-mesh carbon-coated copper grid, dried in an oven overnight and viewed under HRTEM at magnification of 100,000×, 250,000× and 500,000×. The size distribution of CM-AuNPs was obtained by analyzing the diameter of ~400 particles from HRTEM using Image J software.

3.2.2.2 Field effect scanning electron microscopy and energy dispersive X-ray spectroscopy

JEOL JSM-7600 field effect scanning electron microscope (FESEM) was also employed to evaluate size and shape of CM-AuNPs, using an accelerating voltage of 10 kV at magnification of 50,000×. Gold analysis of CM-AuNPs was performed on

energy dispersive X-ray spectrometer (EDX) attached to FESEM by evaluating the EDS spectrum of a selected spot viewed under FESEM. The sample was prepared in the same way as described above (Section 3.2.2.1).

3.2.2.3 Fourier transform infra-red spectroscopy

Fourier transform infra-red (FTIR) spectroscopy was carried out on a PerkinElmer Spectrum 400 spectrometer to determine the functional group (s) involved in the reduction of Au³⁺. Both untreated CM extract and residual fraction of the CM extract left upon CM-AuNPs synthesis, were subjected to FTIR analysis. Residual fraction of CM extract was prepared by removing CM-AuNPs from the reaction mixture through centrifugation at 14,000 rpm for 30 min. The supernatant was collected and freeze-dried. FTIR spectra of these samples were recorded in the wavelength range of 450-4000 cm⁻¹, using a data pitch of 1 cm⁻¹.

3.2.2.4 Zeta potential and hydrodynamic size measurements

The effect of buffers / media on the zeta potential and hydrodynamic size of CM-AuNPs was studied. CM-AuNPs (2 ml) were added to separate tubes containing 2 ml of HSA (0.5% w/v) / PBS (pH 5.0) / PBS (pH 7.4) / PBS (pH 9.0) / DMEM media / DMEM with FBS (10% v/v), followed by incubation at room temperature for 24 h. Suspension containing CM-AuNPs (2ml) and water (2 ml) was used as negative control. Zeta potential and hydrodynamic size of the CM-AuNPs were measured on Malvern Zetasizer Nano ZS at 25 °C, using a folded capillary cell and 1 cm plastic cuvette, respectively.

3.2.2.5 *In vitro* stability study

In vitro stability of CM-AuNPs was studied according to the published procedure (Basha et al., 2010) with slight modification. The samples were prepared in the same way as above (Section 3.2.2.4). All these samples were subjected to UV-Vis absorption spectral measurements in the in the wavelength range of 300–800 nm.

3.2.3 Biocompatibility of CM-AuNPs

3.2.3.1 Cytotoxicity study

(a) Preparation of media and reagents

EMEM medium was supplemented with FBS (10% v/v), sodium pyruvate (1% v/v), amphotericin B (1% v/v) and penicillin/streptomycin (1% v/v), followed by filtration using sterile syringe filter (0.2 μm pore size diameter). The supplemented medium was stored at 4 °C and used within one month.

MTT solution (5 mg/ml) was prepared by dissolving 25 mg of MTT crystals in 5 ml of PBS (pH 7.4). The solution was stored at 4 °C and used within one month.

(b) Cell culture

CCD-18Co and MRC-5 cells were maintained in supplemented EMEM medium at 37 °C in CO₂ (5%) humidified incubator. For cell viability assay, both cell lines were seeded into 96-well plate at 8000 cells/well and incubated overnight for cell adherence. The supplemented medium in each well was removed and replaced with medium containing CM-AuNPs or CM extract at increasing concentrations (3.13, 6.25, 12.50, 25.00, and 50.00 $\mu\text{g/ml}$). Sample containing untreated cells in EMEM medium was used as negative control. The cells were then incubated in CO₂ incubator at 37 °C for 24 h and 72 h before cell viability was determined using MTT assay.

(c) MTT assay

MTT assay was carried out following the procedure recommended by Mosmann (1983) with slight modification. Medium in each well was removed and replaced with 100 μl of fresh EMEM medium together with 20 μl of MTT solution and incubated at 37 °C for 4 h. The supernatants were then removed and 100 μl of DMSO was added to solubilize the newly formed purple formazan crystals. The absorbance values of each well

were measured using the BioTek Synergy H1 hybrid reader at wavelength of 540 nm.

The cell viability (%) was calculated using the following formula:

$$\text{Cell viability (\%)} = \frac{Abs_{spl}}{Abs_{neg}} \times 100 \quad (1)$$

where Abs_{spl} is the absorbance of treated cells and Abs_{neg} is the absorbance of untreated cells.

3.2.3.2 Hemocompatibility study

(a) Preparation of reagents

Ringer's solution was prepared by dissolving NaCl (0.79 g), KCl (0.0375 g), MgCl₂ (0.02 g), Na₂HPO₄ (0.018 g), NaHCO₃ (0.125 g), CaCl₂ (0.03 g), dextrose (0.2 g) and sodium citrate (0.38 g) in ~ 80 ml water. The solution was then topped-up to 100 ml with water in a volumetric flask. Modified Ringer's solution was prepared in the same way as Ringer's solution but without the addition of sodium citrate.

Fresh human blood (5 ml) was collected from the volunteer donor in EDTA tube. The blood was centrifuged at 1000 × g (4 °C) for 10 min to separate the red blood cells (RBCs) from the blood plasma. The RBCs were then washed 3 times with cold PBS (pH 7.4) and centrifuged at 1000 × g (4 °C) for 10 min. For hemolysis assay, 200 µl of RBC pellet was suspended in 9.8 ml of PBS (pH 7.4) to get 2% RBC suspension. For aggregation assay, 2% RBC suspension was prepared in Ringer's solution / modified Ringer's solution.

(b) Hemolysis assay

Hemolysis assay was performed following the method reported by (Evans et al., 2013) with modification. Mixtures containing 100 µl of 2% RBC suspension and 100 µl of CM-AuNPs / CTAB-AuNPs / CM extract at different final concentrations (3.13, 6.25, 12.50, 25.00, and 50.00 µg/ml) in PBS (pH 7.4) were placed in a 96-well plate (round

bottom). Mixtures containing 100 μ l RBC suspension (2%) + 100 μ l Triton X-100 (1% v/v) and 100 μ l RBC suspension (2%) + 100 μ l PBS (pH 7.4) were included as positive and negative controls, respectively. The samples in the 96-well plate were incubated at 37 °C for 5 h followed by centrifugation at 1000 \times g (4 °C) for 10 min. The supernatant (100 μ l) from each well was transferred to a 96-well plate (flat-bottom) and the absorbance was recorded at 550 nm on a BioTek Synergy H1 hybrid reader. The percentage hemolysis was calculated using the following equation:

$$Hemolysis (\%) = \frac{(Abs_{spl} - Abs_{neg})}{(Abs_{pos} - Abs_{neg})} \times 100 \quad (2)$$

where Abs_{spl} is the absorbance value of the sample, Abs_{neg} is the absorbance value of the negative control and Abs_{pos} is the absorbance value of the positive control.

(c) Aggregation assay

Aggregation assay was carried out according to the published procedure (Singhal & Ray, 2002) with slight modification. Mixtures containing 100 μ l of 2% RBC suspension in Ringer's solution and 100 μ l of CM-AuNPs / CTAB-AuNPs / CM extract at different final concentrations (3.13, 6.25, 12.50, 25.00, and 50.00 μ g/ml) in PBS (pH 7.4) were placed in a 96-well plate (round bottom). Positive and negative controls were prepared by mixing 100 μ l of PBS (pH 7.4) with 100 μ l of 2% RBC suspension, prepared in modified Ringer's solution and Ringer's solution, respectively. The samples in the 96-well plate were incubated at 37 °C for 2 h. At the end of incubation, 10 μ l of RBCs from each well were placed on glass slides and viewed under light microscope. Photomicrographs of these slides were taken at 100 \times magnification.

3.2.4 Interaction of CM-AuNPs with HSA

3.2.4.1 Preparation of stock solutions

HSA stock solution was prepared by dissolving 80 mg of protein crystals in 20 ml of 60 mM sodium phosphate buffer, pH 7.4 and its concentration was determined spectrophotometrically, using a molar extinction coefficient of $36500 \text{ M}^{-1} \text{ cm}^{-1}$ at 280 nm (Painter et al., 1998). The stock solution was stored at $4 \text{ }^{\circ}\text{C}$ and used within one week.

To prepare the ANS stock solution, 5 mg of ANS crystals were dissolved in 5 ml of 60 mM sodium phosphate buffer, pH 7.4. A molar extinction coefficient of $5000 \text{ M}^{-1} \text{ cm}^{-1}$ at 350 nm was used to determine ANS concentration (Johnson et al., 1979). The solution was prepared fresh for each experiment.

The stock solution of WFN was prepared by dissolving 3 mg of WFN crystals in 1 ml of methanol and diluting it to 10 ml with 60 mM sodium phosphate buffer, pH 7.4. A molar extinction coefficient of $13610 \text{ M}^{-1} \text{ cm}^{-1}$ at 310 nm was used to determine WFN concentration (Twine et al., 2003).

CM-AuNPs ($200 \text{ }\mu\text{M}$) were prepared in 60 mM sodium phosphate buffer, pH 7.4.

3.2.4.2 Fluorescence quenching titration

(a) *Titration experiments*

The titration experiments of HSA ($5 \text{ }\mu\text{M}$) with increasing concentrations of CM-AuNPs ($5\text{--}30 \text{ }\mu\text{M}$ with $5 \text{ }\mu\text{M}$ intervals) were carried out at three different temperatures i.e. 25 , 30 and $35 \text{ }^{\circ}\text{C}$ following the published procedure (Kabir et al., 2016). Increasing volumes ($75\text{--}450 \text{ }\mu\text{l}$) of the stock CM-AuNPs suspension were added to a fixed volume ($300 \text{ }\mu\text{l}$) of the stock HSA ($50 \text{ }\mu\text{M}$) solution in different tubes and the total volume in each tube was made to 3 ml with 60 mM sodium phosphate buffer, pH 7.4. The fluorescence spectra of HSA and CM-AuNP-HSA mixtures were recorded after 1 h

incubation at the desired temperature, in the wavelength range, 300–400 nm, using λ_{ex} of 295 nm. An additional incubation time of 10 min at a particular temperature was used after placing the sample in the cuvette for equilibrium attainment.

Fluorescence spectral measurements were performed on Jasco FP-6500 spectrofluorometer, using 1 cm quartz cuvette, placed in a thermostatically-controlled water-jacketed cell holder. For the inner filter effect correction of the fluorescence quenching titration data, absorption spectra of HSA (5 μ M) in the absence and presence of CM-AuNPs (5–30 μ M with 5 μ M intervals) were recorded on Shimadzu UV-2450 spectrophotometer, using a pair of 1 cm quartz cuvettes, in the wavelength range, 295–400 nm, at 25 °C.

(b) Data analysis

i Inner filter effect correction

The fluorescence data were corrected for the inner filter effect as described by Lakowicz (2006) according to the following equation:

$$F_{cor} = F_{obs} 10^{(A_{ex} + A_{em})/2} \quad (3)$$

where F_{cor} and F_{obs} are the corrected and the measured fluorescence intensity respectively, while A_{ex} and A_{em} are the changes in the absorbance at the excitation (295 nm) and the emission wavelength (300–400 nm), respectively, upon the addition of CM-AuNP to HSA.

ii Quenching data analysis

Quenching mechanism involved in CM-AuNP-HSA interaction was probed by analyzing the fluorescence quenching data according to the Stern-Volmer equation (Lakowicz, 2006):

$$F_0/F = 1 + K_{SV} [Q] = 1 + k_q \tau_0 [Q] \quad (4)$$

where F_0 and F are the fluorescence intensity values in the absence and presence of CM-AuNPs and $[Q]$ is the concentration of CM-AuNPs. K_{SV} is the Stern-Volmer constant; k_q is the bimolecular quenching rate constant and τ_0 denotes the fluorescence lifetime of the protein, taken as 6.38×10^{-9} s for HSA (Abou-Zied & Al-Shihi, 2008).

Further analysis of the fluorescence quenching titration data was made following double logarithmic equation (Eq. 5) to determine the values of the binding constant (K_a) and Hill coefficient (n) for the interaction between CM-AuNP and HSA (Bi et al., 2004).

$$\log (F_0 - F) / F = n \log K_a - n \log [1 / ([L_T] - (F_0 - F) [P_T] / F_0)] \quad (5)$$

where $[L_T]$ and $[P_T]$ represent the concentrations of CM-AuNPs and HSA, respectively, while F_0 and F have the same significance as described above.

iii Thermodynamic data analysis

Thermodynamic parameters for CM-AuNP-HSA interaction were determined using van't Hoff equation:

$$\ln K_a = -\Delta H / RT + \Delta S / R \quad (6)$$

where K_a refers to the binding constant, ΔH and ΔS are enthalpy change and entropy change, respectively, R denotes the gas constant ($8.314 \text{ J mol}^{-1} \text{ K}^{-1}$) and T is the absolute temperature ($273 \pm ^\circ\text{C}$).

Gibbs free energy change (ΔG) of the binding reaction was calculated by fitting ΔH and ΔS values into the following equation:

$$\Delta G = \Delta H - T\Delta S \quad (7)$$

3.2.4.3 Absorption spectral analysis

The absorption spectra of HSA ($20 \mu\text{M}$) both in the absence and presence of CM-AuNPs (60 and $120 \mu\text{M}$) were recorded in the wavelength range, $240\text{--}360 \text{ nm}$. Absorption spectra of free CM-AuNPs (60 and $120 \mu\text{M}$) were also recorded in the same wavelength range. Mixtures (3 ml) containing HSA and CM-AuNPs were incubated at room temperature for 1 h before absorption spectral measurements.

3.2.4.4 Analysis of protein structural changes

(a) Circular dichroism

Circular dichroism (CD) spectra were recorded on Jasco J-815 spectropolarimeter, equipped with thermostatically-controlled cell holder, using 1 mm and 10 mm quartz cuvettes in the far-UV ($200\text{--}250 \text{ nm}$) and near-UV ($250\text{--}300 \text{ nm}$) regions, respectively, under constant nitrogen flow. The samples contained either free HSA or CM-AuNP-HSA ($6:1$) mixtures, using a protein concentration of $5 \mu\text{M}$ (far-UV CD spectra) and $10 \mu\text{M}$ (near-UV CD spectra). Transformation of CD values to mean residue ellipticity (MRE) in $\text{deg}\cdot\text{cm}^2\cdot\text{dmol}^{-1}$ was carried out according to the following equation:

$$\text{MRE} = \frac{[\theta_{obs} \times \text{MRW}]}{10 \times l \times C_p} \quad (8)$$

where θ_{obs} is the ellipticity in millidegree; MRW is the mean residue weight (molecular weight of the protein, 66500 divided by total number of amino acid residues, 585); C_p is the protein concentration in mg/ml and l is the path length of cuvette in cm (Chen et al., 1972).

(b) Three-dimensional fluorescence spectral analysis

Three-dimensional (3D) fluorescence spectra of HSA (5 μ M), CM-AuNPs (30 μ M) and CM-AuNP-HSA mixtures (molar ratios of 3:1 and 6:1) were recorded using emission wavelength range of 220–500 nm with a data pitch of 1 nm and excitation wavelength range of 220–350 nm with a data pitch of 5 nm.

3.2.4.5 Site-specific marker displacement studies

To characterize the binding site of HSA involved in CM-AuNP-HSA complex formation, site marker displacement experiments were carried out using WFN and ANS as markers for Sudlow's site I and site II, respectively.

WFN displacement experiment was performed by titrating the WFN-HSA (1:1) mixture (5 μ M each) with increasing concentrations of CM-AuNPs (5, 10, 15, 20, 25, 30 and 100 μ M). The WFN-HSA mixture was pre-incubated for 30 min 25 °C before titrating it with CM-AuNPs. The mixture was further incubated for an additional period of 1 h at 25 °C prior to fluorescence spectral measurements. The fluorescence spectra were obtained in the wavelength range, 360–480 nm upon excitation at 335 nm.

For ANS displacement experiment, the ANS-HSA (1:1) mixture (5 μ M each) was titrated with increasing concentrations of CM-AuNPs (20, 40, 60, 70, 80, 90 and 100 μ M). The ANS-HSA mixture was preincubated for 30 min at 25 °C before titrating it with CM-AuNPs. The mixture was further incubated for an additional period of 1 h at 25 °C prior to fluorescence spectral measurements. The fluorescence spectra were obtained in

the wavelength range, 300–570 nm and 400–600 nm upon excitation at 295 nm and 350 nm, respectively.

3.2.5 Photothermal anticancer activity of CM-AuNPs

3.2.5.1 Preparation of media and reagent

Preparation of MTT solution and supplementation of DMEM medium were made in the same way as described in Section 3.2.3.1 (a) for EMEM medium. On the other hand, DMEM medium (without phenol red) was supplemented with FBS (10% v/v) only. CM-AuNPs and citrate-AuNPs were suspended in supplemented DMEM medium (without phenol red) for photothermal studies.

3.2.5.2 Photothermal heating curves

Photothermal heat generation of CM-AuNPs was studied using a Millenia Prime continuous wave diode-pumped solid-state (DPSS) laser, using wavelength of 532 nm. The temperature change was measured by Omega type T thermocouple.

For temperature measurements, the thermocouple microprobe was submerged in 100 μl of CM-AuNPs (20 $\mu\text{g}/\text{ml}$), followed by laser irradiation at different intensities (1, 2 and 3 W/cm^2), in a 96-well plate. The temperature increase in the medium was recorded every 30 s for 300 s.

A comparison of photothermal heat generation between citrate-AuNPs (20 $\mu\text{g}/\text{ml}$) and CM-AuNPs at different concentrations (5, 10 and 20 $\mu\text{g}/\text{ml}$) upon laser (3 W/cm^2) irradiation was also made, in a 96-well plate. DMEM medium without AuNPs was used as negative control. The temperature increase in the medium was recorded in the same way as described above.

3.2.5.3 *In vitro* photothermal treatment

MCF-7 breast cancer cells were maintained in supplemented DMEM medium at 37 °C in CO₂ incubator. To find a suitable laser intensity and irradiation time for PTT, MCF-7 cells were seeded into 96-well plate at 8000 cells/well and incubated overnight for cell adherence. The medium in each well was then removed and replaced with DMEM medium (without phenol red) and irradiated using laser at different intensities (2 and 3 W/cm²) for different time periods (60, 120, 180, 240 and 300 s). The cell viability was determined by MTT assay after incubating the cells in CO₂ incubator at 37 °C for 24 h.

Cytotoxicity of CM-AuNPs without laser irradiation on MCF-7 cells was investigated using MTT assay. MCF-7 cells were seeded under similar conditions as described above and treated with AuNPs or CM extract at different concentrations (5, 10, 15, 20 and 25 µg/ml). The treated cells were incubated in a CO₂ incubator at 37 °C for 24 h before assessed by MTT assay.

For PTT, MCF-7 cells were seeded and treated with citrate-AuNPs and CM-AuNPs in the same way as described above. The treated cells were incubated in CO₂ incubator at 37 °C for 3 h, followed by irradiation with DPPS laser (3 W/cm²) for 120 s. After laser treatment, the cells were incubated in a CO₂ incubator at 37 °C for another 24 h prior to MTT assay.

For annexin V / PI apoptosis assay, MCF-7 cells were seeded into 24-well plate at 50,000 cells/well and incubated overnight for cell adherence. The medium in each well was replaced with DMEM medium (without phenol red) containing citrate-AuNPs (20 µg/ml) / CM-AuNPs (20 µg/ml). The treated cells were incubated and irradiated in the same way as described above before assessed by annexin V / PI apoptosis assay. Untreated cells and cells treated with doxorubicin (1.5 µg/ml) were also included as negative and positive controls, respectively.

3.2.5.4 FITC-Annexin V / PI apoptosis assay

Annexin V / PI staining was performed following the protocol provided by the manufacturer (BD Biosciences). Briefly, the cells were harvested and washed twice with cold PBS (pH 7.4) before re-suspending them in $1\times$ binding buffer at a concentration of 1×10^6 cells/ml. Cell suspension ($100\ \mu\text{l}$, 1×10^5 cells) was transferred to 1.5 ml centrifuge tube, followed by addition of FITC-Annexin V and PI ($5\ \mu\text{l}$ each). After gentle vortexing, the cell suspension was incubated in the dark at room temperature for 15 min. Then, $400\ \mu\text{l}$ of $1\times$ binding buffer was added to the cell suspension and the samples were analyzed by flow cytometry (BD FACS Canto II cytometer) within 1 h. Unstained positive control, positive control stained with only one dye, ie. FITC-Annexin V or PI only were used to set up compensation and quadrants prior to analyzing the samples. Quadrant statistical analysis yielded the percentage of cell population in each quadrant.

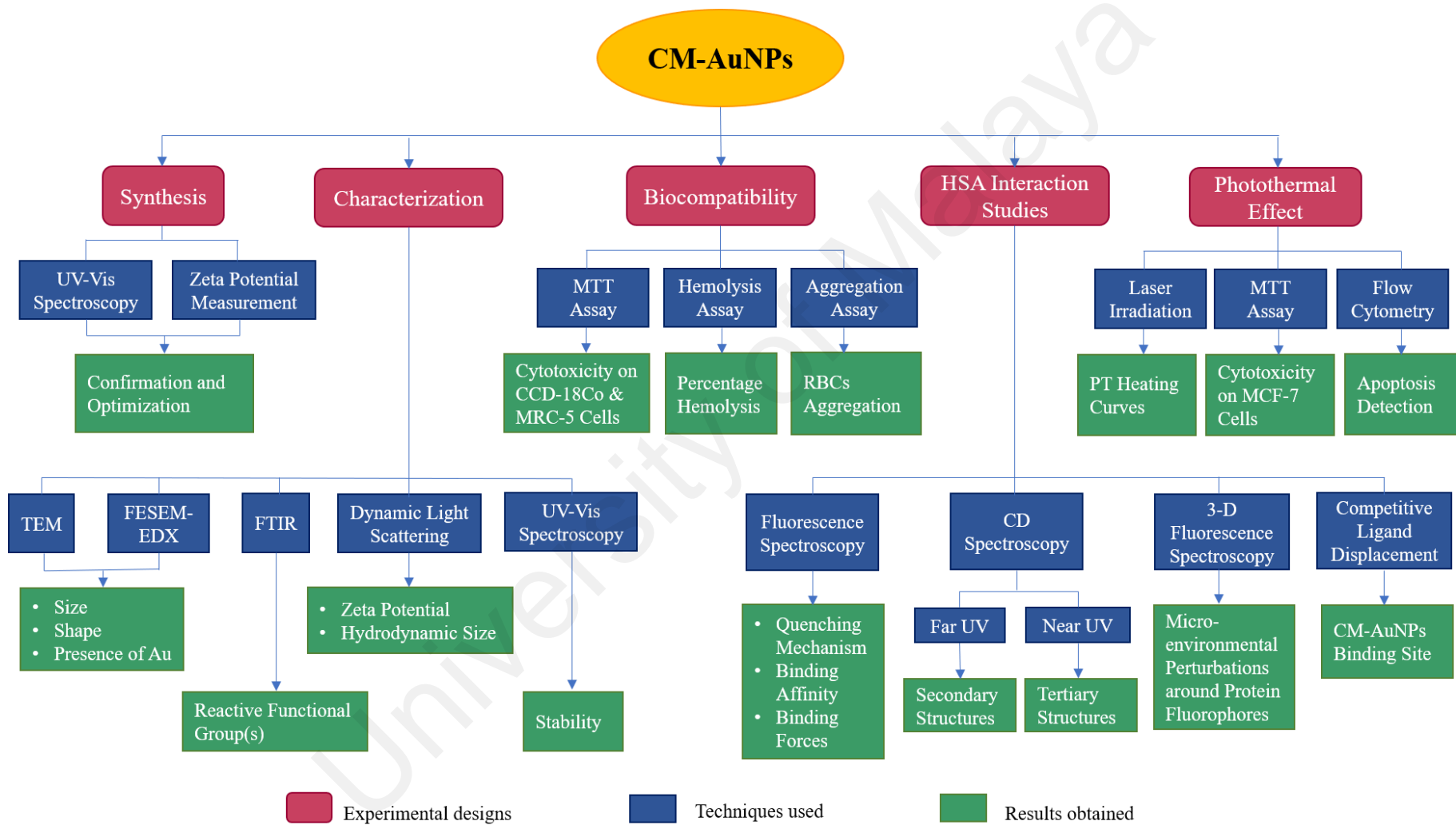


Figure 3.1: Flow chart of research work.

CHAPTER 4: RESULTS AND DISCUSSION

4.1 Green synthesis of CM-AuNPs

In this study, CM-AuNPs were synthesized through bottom-up approach using auric ions (Au^{3+}) from HAuCl_4 as the precursor for CM-AuNPs synthesis. On the other hand, CM extract was used as reducing and stabilizing agent replacing the use of conventional chemicals, such as sodium borohydride and sodium citrate. Green synthesis method is simple and energy-efficient, as it involves the mixing of CM extract and HAuCl_4 at room temperature without heating. The formation of CM-AuNPs can be observed by the colour change in the reaction mixture from light yellow to red-violet. The intense red-violet colour of CM-AuNPs mixture is associated with the SPR of AuNPs, due to the oscillation of free conducting electrons induced by the electromagnetic field (Petryayeva & Krull, 2011). As synthesis of CM-AuNPs depends on the concentrations of HAuCl_4 and reducing agent (CM extract) as well as reaction time, effect of these factors on CM-AuNPs synthesis were studied separately.

4.1.1 Effect of reaction time

UV-Vis spectroscopy was carried out to ascertain the formation of CM-AuNPs. It is well-known that SPR of spherical AuNPs produces an absorption band in the range of 520–580 nm (Haiss et al., 2007). Several factors such as shape, size and surface coating of NPs as well as dielectric constant of the medium may affect the peak position, intensity and band shape of SPR (Kelly et al., 2003). Figure 4.1 shows the UV-Vis absorption spectra of CM-AuNPs synthesized from 10 ml of HAuCl_4 (1 mM) and 4 ml of CM extract (10 mg/ml) at different incubation times (15–1440 min). Appearance of an absorption band at around 546 nm (corresponding to the SPR band of AuNPs) was noticed after 15 min of incubation, which indicated formation of CM-AuNPs. Although significant increase in the intensity of the absorption band was noticed up to 45 min of incubation time, the intensity increased sharply upon increasing the time from 15 to 30 min.

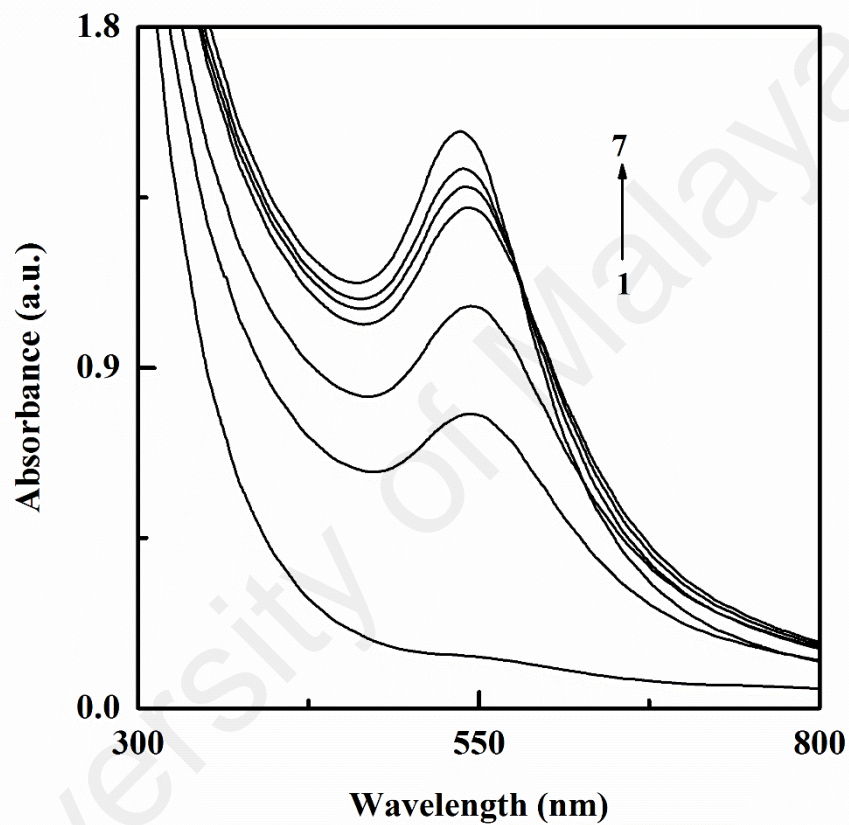


Figure 4.1: UV-Vis absorption spectra of CM-AuNPs, synthesized at different incubation times. Spectra 1-7 were obtained at 0, 15, 30, 45, 60, 90 and 1440 min after addition of 4 ml of CM extract (10 mg/ml) to 10 ml of HAuCl₄ (1 mM) at room temperature.

Sharp increase in the intensity of the absorption band was suggestive of speedy formation of CM-AuNPs. Increasing the incubation time beyond 45 min led to smaller increase in the intensity of the absorption band, indicating slower formation of CM-AuNPs. Even at the highest incubation period used, i.e., 1440 min, increase in the absorbance value was only 0.1 a.u. compared to that observed at 90 min incubation, suggesting attainment of saturation within 90 min. In addition to the increase in the intensity, absorption band also showed a blue shift from 546 nm to 535 nm, while narrowing down its bandwidth upon 90 min incubation (Figure 4.2). As evident from Figure 4.2, the blue shift was more pronounced up to 45 min incubation and became gradually smaller beyond this period. Both these characteristics of the absorption band were indicative of the formation of spherical and monodisperse CM-AuNPs at increasing time periods (Jana et al., 2001). These results were in line with previous studies showing blue shift and increase in intensity of AuNPs SPR band upon longer incubation period (Ahmad et al., 2018; Rajan et al., 2014).

4.1.2 Effect of CM extract concentration

Several earlier reports have shown reducing agent concentration as one of the controlling factors in the synthesis of AuNPs (Chen et al., 2017; Shi et al., 2017). Therefore, effect of CM extract concentration (reducing agent) on the synthesis of CM-AuNPs was also investigated. Figure 4.3 shows the UV-Vis absorption spectra of CM-AuNPs synthesized by incubating fixed concentration (1 mM) of HAuCl₄ and increasing concentrations (0–10 mg/ml) of CM extract for 60 min at room temperature. As can be seen from the inset of Figure 4.3, there was a pronounced increase in the intensity of the absorption band upon increasing the CM extract concentration up to 6 mg/ml, followed by a smaller increase in the intensity. Such increase in the intensity of the absorption band reflected increasing formation of CM-AuNPs with increasing CM extract concentrations. In addition to the increase in the intensity, resolution (narrowness in the bandwidth) as

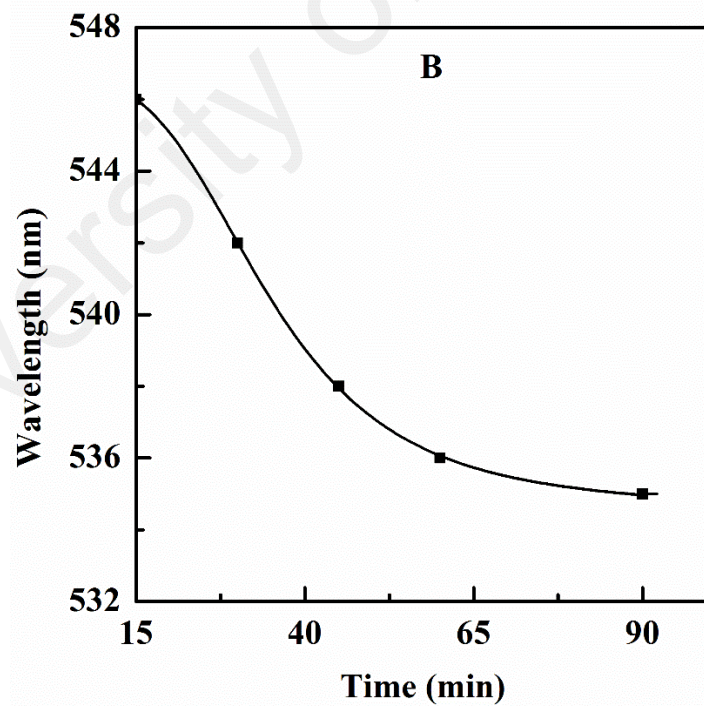
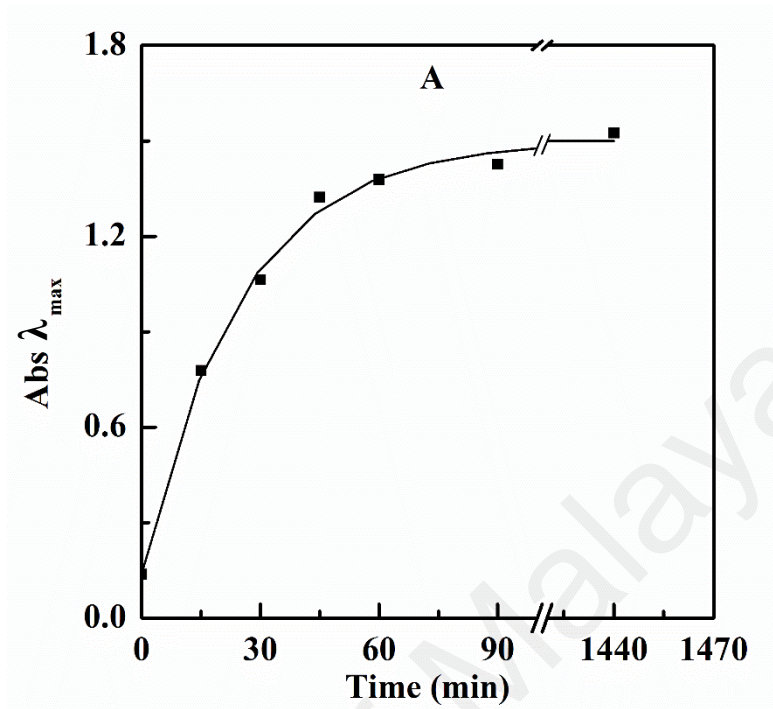


Figure 4.2: Plots showing change in the absorbance of λ_{\max} (A) and absorption maximum (B) of the mixture containing 4 ml of CM extract (10 mg/ml) and 10 ml of HAuCl₄ (1 mM) with increasing incubation time.

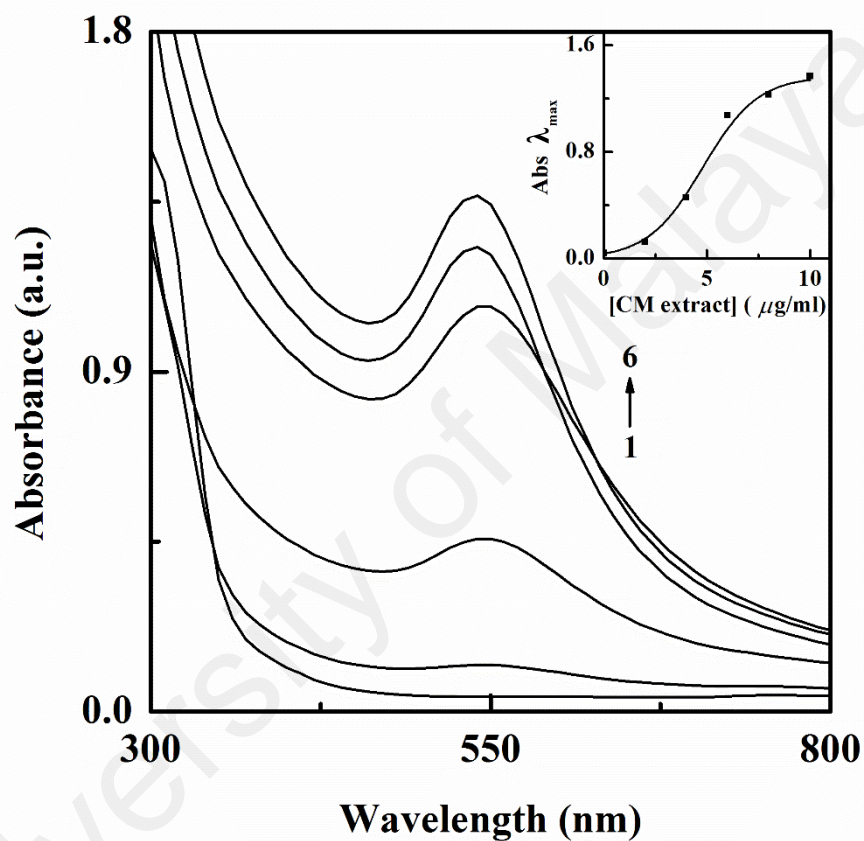


Figure 4.3: UV-Vis absorption spectra of CM-AuNPs, synthesized using different concentrations of CM extract. Spectra 1–6 were obtained for the CM-AuNP mixtures containing 4 ml of CM extract (0 – 10 mg/ml with 2 mg/ml intervals) and 10 ml of HAuCl₄ (1 mM), after 60 min of incubation at room temperature. Inset shows the change in absorbance of λ_{max} with increasing CM extract concentration.

well as blue shift of the absorption band was also noticed upon increasing CM extract concentrations (Figure 4.3). Broader bandwidth and longer wavelength characterized the formation of larger and polydisperse CM-AuNPs, whereas narrow bandwidth and shorter wavelength indicated formation of smaller, spherical and monodisperse CM-AuNPs (Huang & El-Sayed, 2010; Uppal et al., 2010). Formation of large and polydisperse CM-AuNPs at lower concentrations of CM extract maybe due to insufficient concentration of biomolecules that were responsible for capping and stabilizing the AuNPs (Sujitha & Kannan, 2013). Thus, higher concentration of CM extract was needed to produce small, spherical and monodisperse CM-AuNPs. Similar results have been shown in previous reports where lower concentrations of fruit extracts favor the formation of large anisotropic AuNPs (Sujitha & Kannan, 2013; Amin et al., 2012).

Effect of CM extract concentration on the kinetics of CM-AuNPs synthesis was also studied by monitoring the change in absorbance at 535 nm at increasing time periods up to 300 min, and the results are shown in Figure 4.4. As evident from the figure, increase in the incubation time led to an initial linear increase in absorbance at 535 nm, which sloped off and reached saturation at higher incubation time. Such increase in absorbance at 535 nm was indicative of CM-AuNPs formation. Although kinetic plots obtained with different CM extract concentrations were qualitatively similar, quantitative differences were noticed. Increasing CM extract concentrations reduced the linearity zone on the time scale, while making the regression line steeper. In other words, rate of formation of CM-AuNPs, as obtained from the slope values of the regression lines showed positive correlation with CM extract concentration. The initial rate constant increased by ~5 fold upon increasing the concentration of CM extract by 2 mg/ml in the lower concentration range (2–6 mg/ml). Subsequent increase in the CM extract concentration (6–10 mg/ml) with 2 mg/ml intervals led to a smaller increase (2 fold) in rate constant. Such increase in

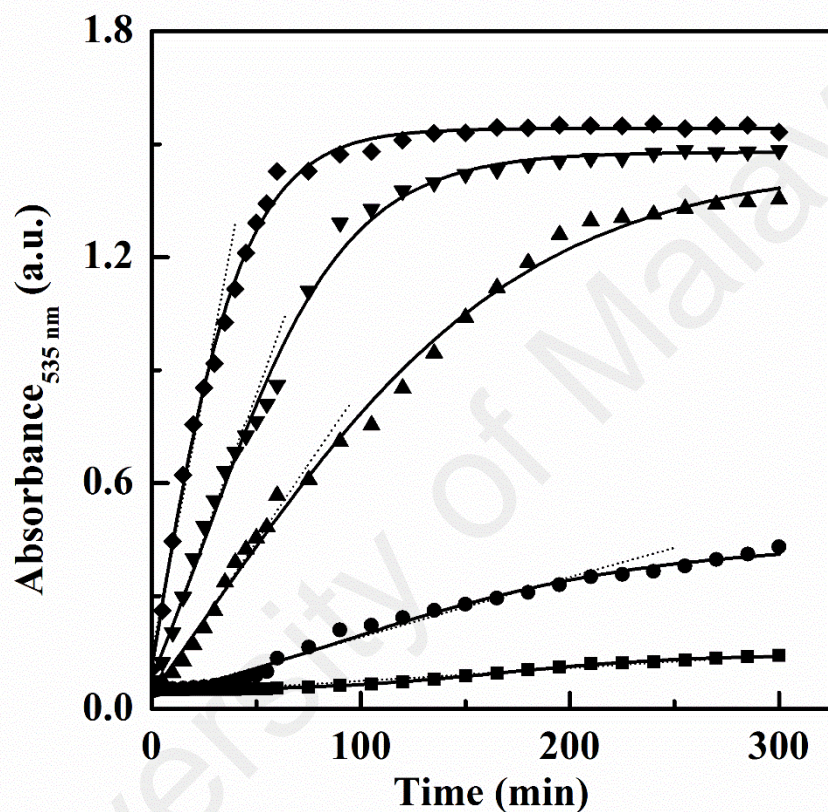


Figure 4.4: Kinetic plots showing change in absorbance at 535 nm with time for mixtures containing 10 ml of HAuCl_4 (1 mM) and 4 ml of CM extract. The concentrations of the CM extract used are shown with different symbols: 2 mg/ml (■); 4 mg/ml (●); 6 mg/ml (▲); 8 mg/ml (▼) and 10 mg/ml (◆). The initial rate constants were obtained from the slope values of the dotted lines.

the rate of CM-AuNPs formation with increasing CM extract concentration can be ascribed to the higher reducing agent concentration (Kumari et al., 2016).

Zeta potential measures the surface charge of NPs in a suspension, thus providing information on the repulsive forces between particles as well as stability of NPs suspension (Xu, 2008). Greater magnitude of zeta potential implies higher repulsive forces between the particles, which offer higher stability to the NPs suspension (Jin et al., 2005). In view of it, CM-AuNPs synthesized with different CM extract concentrations were subjected to zeta potential measurements. Figure 4.5 illustrates the zeta potential values of CM-AuNPs synthesized using different concentrations of CM extract. All CM-AuNPs synthesized were found to possess negative zeta potential and the magnitude of zeta potential of CM-AuNPs increased from -12.0 to -32.2 mV with increasing concentrations of CM extract, used in their syntheses. This indicated that use of increasing concentrations of CM extract can improve the colloidal stability of CM-AuNPs. Hence, it was suggested that CM extract also played a role in stabilizing CM-AuNPs besides acting as reducing agent in their syntheses. Similar results were also reported in earlier studies, where higher amount of plant extract was found to stabilize the AuNPs (Sujitha & Kannan, 2013; Lim et al., 2016).

4.1.3 Effect of HAuCl₄ concentration

Since HAuCl₄ is the precursor of Au³⁺ ions, its concentration is presumed to affect AuNPs synthesis. In order to test this hypothesis, CM-AuNPs synthesis was monitored at increasing HAuCl₄ concentrations using UV-Vis absorption spectral and zeta potential measurements. Figure 4.6 shows the absorption spectra of CM-AuNPs, synthesized with fixed concentration of CM extract (10 mg/ml) and increasing concentrations (0.5, 1, 2, 3 and 4 mM) of HAuCl₄ upon incubation at room temperature for 24 h. The mixture containing 0.5 mM HAuCl₄ did not produce any absorption peak after 24 h of incubation.

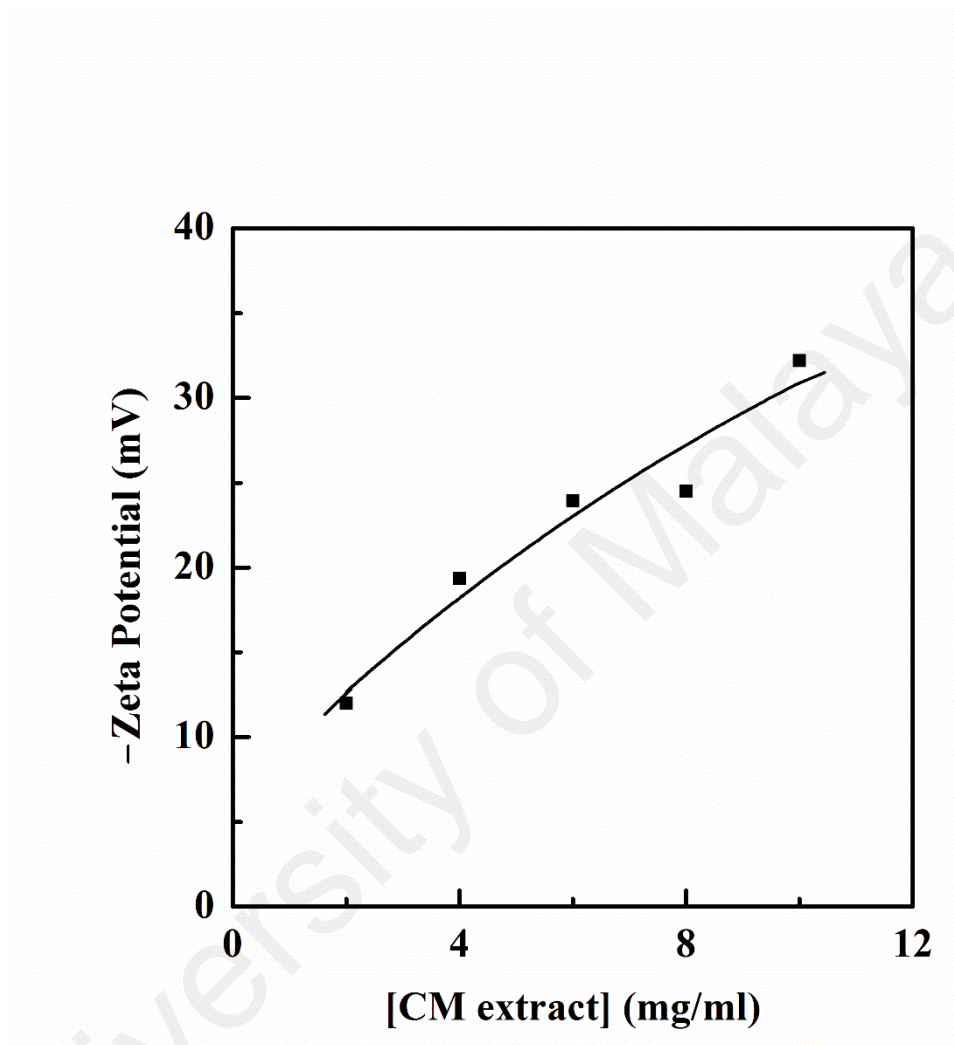


Figure 4.5: Zeta potential values of CM-AuNPs, synthesized using 4 ml of CM extract at different concentrations and 10 ml of H_{AuCl}₄ (1 mM).

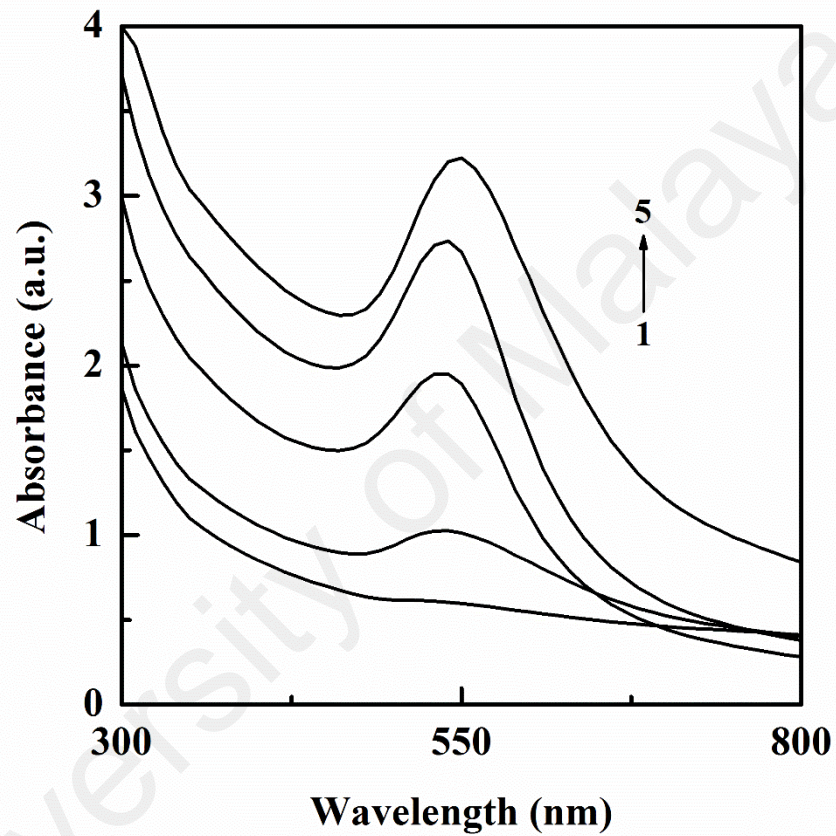


Figure 4.6: UV-Vis absorption spectra of CM-AuNPs, synthesized using different concentrations of HAuCl_4 . Spectra 1–5 were obtained for the CM-AuNP mixtures containing 4 ml of CM extract (10 mg/ml) and 10 ml of HAuCl_4 (0.5, 1, 2, 3 and 4 mM), after 24h of incubation at room temperature.

On the other hand, the intensity of the absorption band increased with the increase in HAuCl_4 concentration. CM-AuNPs synthesized with higher HAuCl_4 concentrations (2–4 mM) produced high intensity absorption band at longer wavelength. Such characteristics of the absorption spectra reflected formation of larger CM-AuNPs (Huang & El-Sayed, 2010). However, CM-AuNPs formed with 1 mM HAuCl_4 showed absorption peak at relatively shorter wavelength, which indicated formation of smaller, spherical and monodispersed CM-AuNPs (Aromal & Philip, 2012). Since a constant amount of CM extract (reducing and stabilizing agent) was used in all the mixtures, higher ratio of $[\text{HAuCl}_4] / [\text{CM extract}]$ resulted in lower capping and stabilizing activity of CM extract. Such conditions might be responsible for exposure of facets on AuNP surface for fusion of nuclei, thus forming larger CM-AuNPs (Chen et al., 2017; Kumari et al., 2016).

Effect of HAuCl_4 concentration on the zeta potential of synthesized CM-AuNPs was also studied. Figure 4.7 shows the zeta potential of CM-AuNPs synthesized with different concentrations (1–4 mM) of HAuCl_4 . Mixture containing 0.5 mM HAuCl_4 was not subjected to zeta potential measurement, since absorption peak at around 535 nm was not visible. As can be seen from the figure, the magnitude of zeta potential decreased with the increase in HAuCl_4 concentration, used in the synthesis. Such decrease in zeta potential can be due to insufficient stabilizing agent at high HAuCl_4 concentrations for CM-AuNPs synthesis, as higher ratio of $[\text{HAuCl}_4] / [\text{CM extract}]$ might reduce the stabilizing activity of CM extract. This further supported the earlier suggestion that CM extract also act as stabilizing agent in CM-AuNPs synthesis.

In view of the above, incubation of 4 ml of CM extract (10 mg/ml) and 10 ml of HAuCl_4 (1 mM) for 24 h was found to produce smaller, spherical and monodispersed AuNPs with higher stability at faster reaction rate. The yield of CM-AuNPs was found to

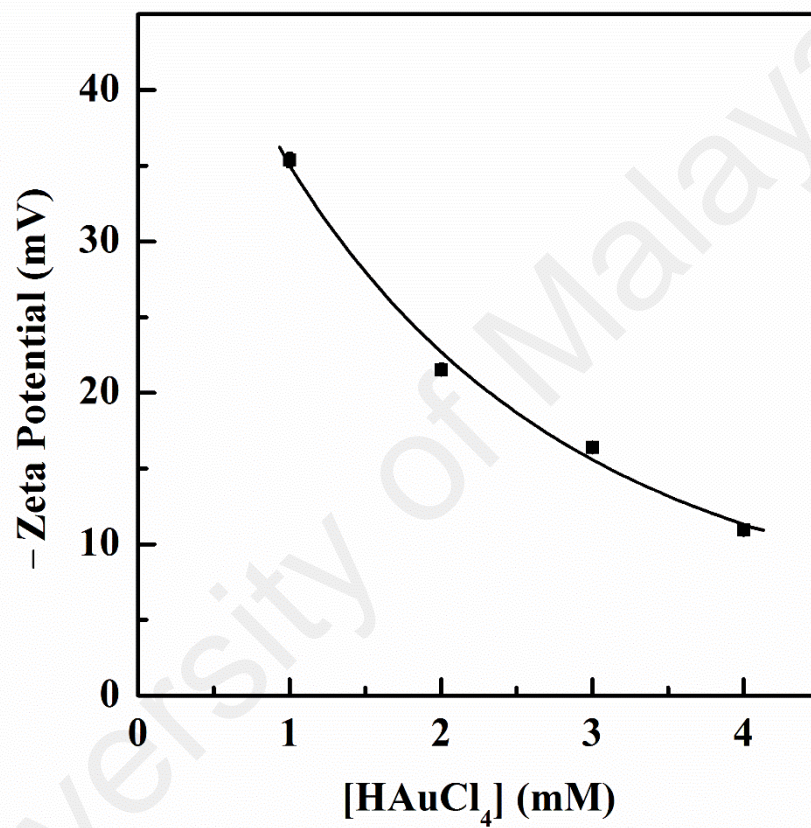


Figure 4.7: Zeta potential values of CM-AuNPs, synthesized using 4 ml of CM extract (10 mg/ml) and 10 ml of HAuCl₄ at different concentrations.

be 52.5%, as determined by MP-AES analysis. Therefore, these conditions were employed to synthesize CM-AuNPs for further studies.

4.2 Characterization of CM-AuNPs

The physicochemical properties of NPs including size, shape, surface charge and composition as well as stability can influence their distribution, uptake and toxicity (Gatoo et al., 2014). Therefore, CM-AuNPs were characterized in terms of size, shape, composition, identification of functional group(s) involved in AuNPs synthesis and *in vitro* stability of CM-AuNPs in various media.

4.2.1 Determination of size, shape and composition

The size and shape of CM-AuNPs were determined by HRTEM and FESEM. HRTEM images of CM-AuNPs at different magnifications are depicted in Figure 4.8. As evident from the figure, CM-AuNPs were largely spherical in shape. The average core size of CM-AuNPs was found to be 15.6 nm. HRTEM histogram (Figure 4.9) revealed CM-AuNPs size distribution ranging from 2 nm to 35 nm. Size distribution of CM-AuNPs was found to be close to normal distribution, as size of 76.8% of CM-AuNPs had fallen in the range of 5–25 nm. In order to confirm the size of CM-AuNPs, FESEM was also employed. Figure 4.10A illustrates the FESEM image of CM-AuNPs at magnification of 50,000 \times , where CM-AuNPs were observed as spherical particles of \sim 15.0 nm diameter. This observation further supported the results obtained from HRTEM image analysis. Earlier studies have shown that NPs with size lesser than 5 nm easily undergo renal clearance (Choi et al., 2007), while NPs with a size greater than 200 nm are retained in the spleen (Blanco et al., 2015). In view of these results, AuNPs with size in the range of 10–100 nm are desirable for systemic administration (Blanco et al., 2015). Thus, CM-AuNPs synthesized in this study fulfilled the criteria for safer usage in systemic administration.

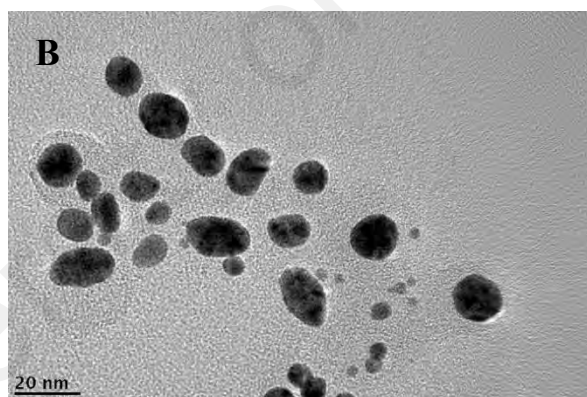
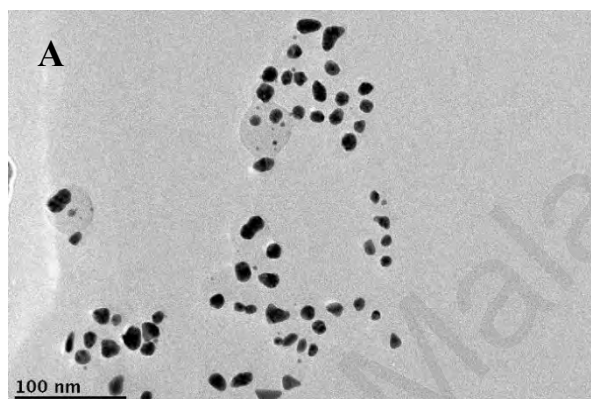


Figure 4.8: TEM images of CM-AuNPs, obtained on a 300 mesh carbon-coated copper grid at magnification of 100,000 \times (A) and 500,000 \times (B). CM-AuNPs were synthesized using 4 ml of CM extract (10 mg/ml) and 10 ml of HAuCl₄ (1 mM) after 24 h incubation at room temperature.

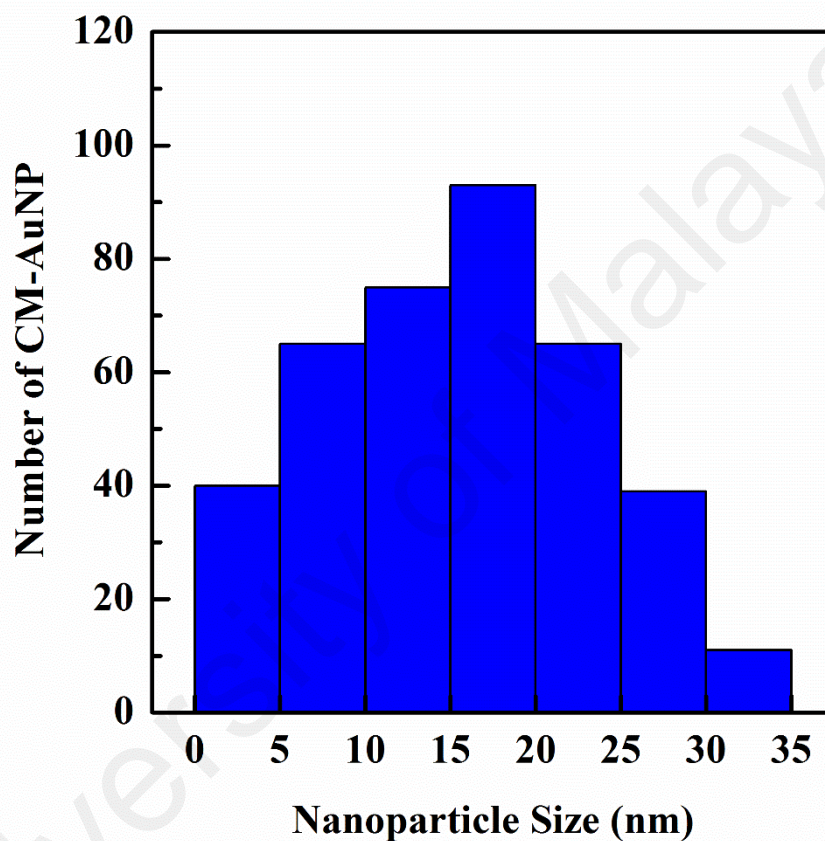


Figure 4.9: Histogram showing size distribution of CM-AuNPs. Results were obtained after analyzing ~400 particles from TEM image using Image J software. CM-AuNPs were synthesized in the same way as described in the legend to Figure 4.8.

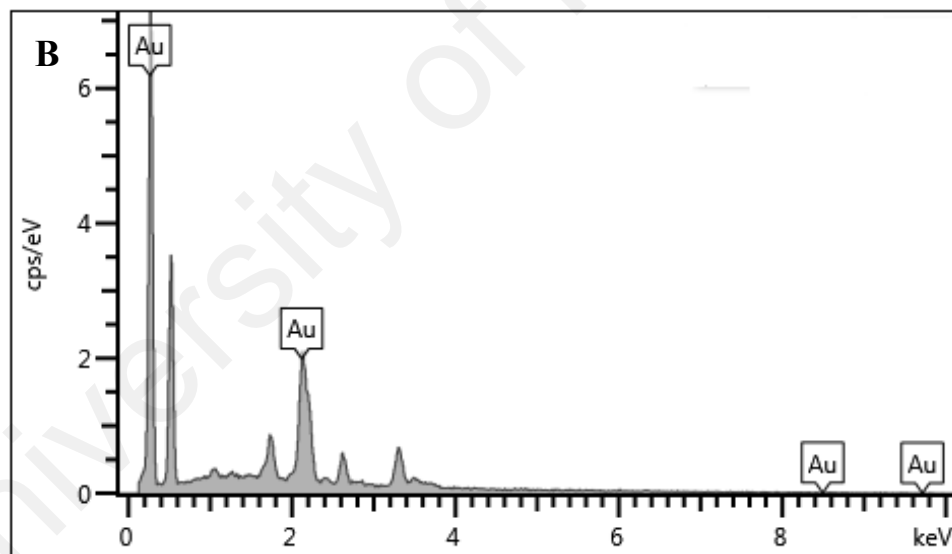
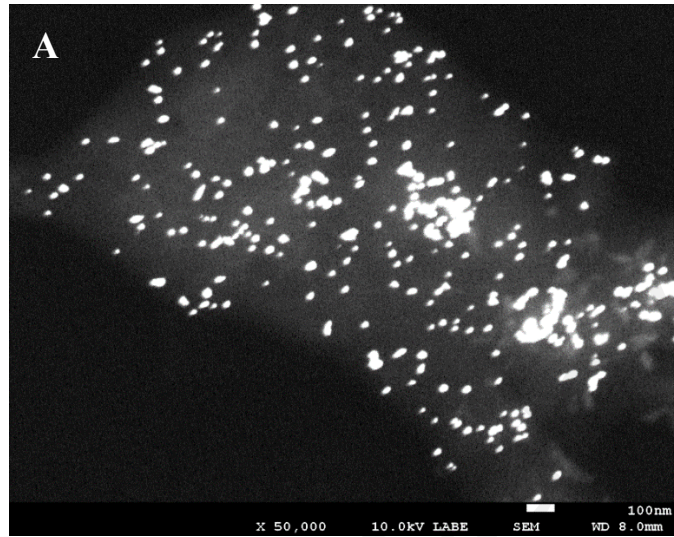


Figure 4.10: (A) FESEM image (50,000 \times magnification) of CM-AuNPs, obtained on a 300 mesh carbon-coated copper grid. CM-AuNPs were synthesized in the same way as described in the legend to Figure 4.10. (B) EDX spectrum of CM-AuNPs.

To confirm the gold composition in the newly formed CM-AuNPs, EDX spectrum of CM-AuNPs was analysed, which is shown in Figure 10B. In line with earlier reports (Ahmad et al., 2018; Irfan et al., 2017), appearance of a strong gold signal at 2.15 keV confirmed the presence of elemental Au in the newly formed NPs. This clearly suggested reduction of Au^{3+} ions to elemental Au during CM-AuNPs synthesis.

4.2.2 Identification of reactive functional group

FTIR spectroscopy was performed to investigate the involvement of functional group(s) in the synthesis of CM-AuNPs. Figures 4.11 and 4.12 illustrate the FTIR spectra of the untreated and the residual fraction of the CM extracts left upon CM-AuNPs synthesis, respectively. Two intense bands appearing at 1036/1038 and 3273/3292 cm^{-1} in both the FTIR spectra, characterized the presence of C–OH and O–H bonds, respectively (Smith, 1999). These results were in accordance to the chemical composition of CM extract, showing presence of polyphenolics, curcuminoids, and terpenoids, molecules rich in C–OH and O–H bonds (Malek et al., 2011). Other bands that were visible in both spectra occurring at 2929/2931 and 1394/1408 signified the presence of CH_2 and CH_3 groups. Bands observed in the wavenumber range, $\sim 500\text{--}868 \text{ cm}^{-1}$ suggested the presence of C–H groups (Smith, 1999) that were abundant in the CM extract. Occurrence of the intense band at 1588 cm^{-1} in the FTIR spectrum of the untreated CM extract (Figure 4.11) reflected the presence of unsaturated carbonyl groups (Bennet et al., 2015), which are commonly found in terpenoids. Interestingly, the intensity of this band was significantly reduced and showed a shift to 1610 cm^{-1} in the FTIR spectrum of the residual fraction (Figure 4.12), obtained after the reduction of Au^{3+} . These results clearly suggested that the carbonyl groups of terpenoids present in the CM extract reduced Au^{3+} in the synthesis of CM-AuNPs.

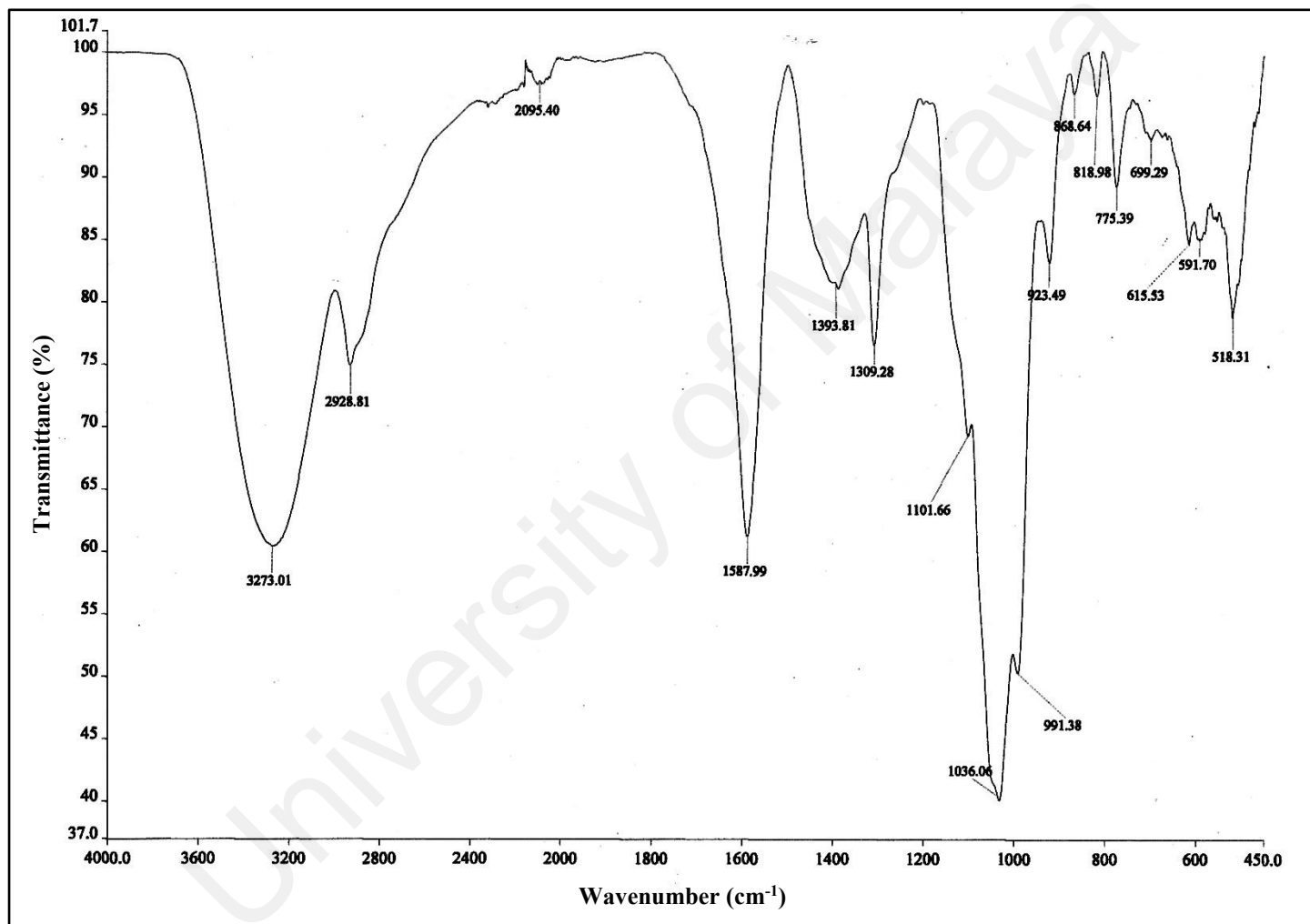


Figure 4.11: FTIR spectrum of oven-dried (60 °C) CM extract in the wavenumber range of 450 to 4000 cm⁻¹.

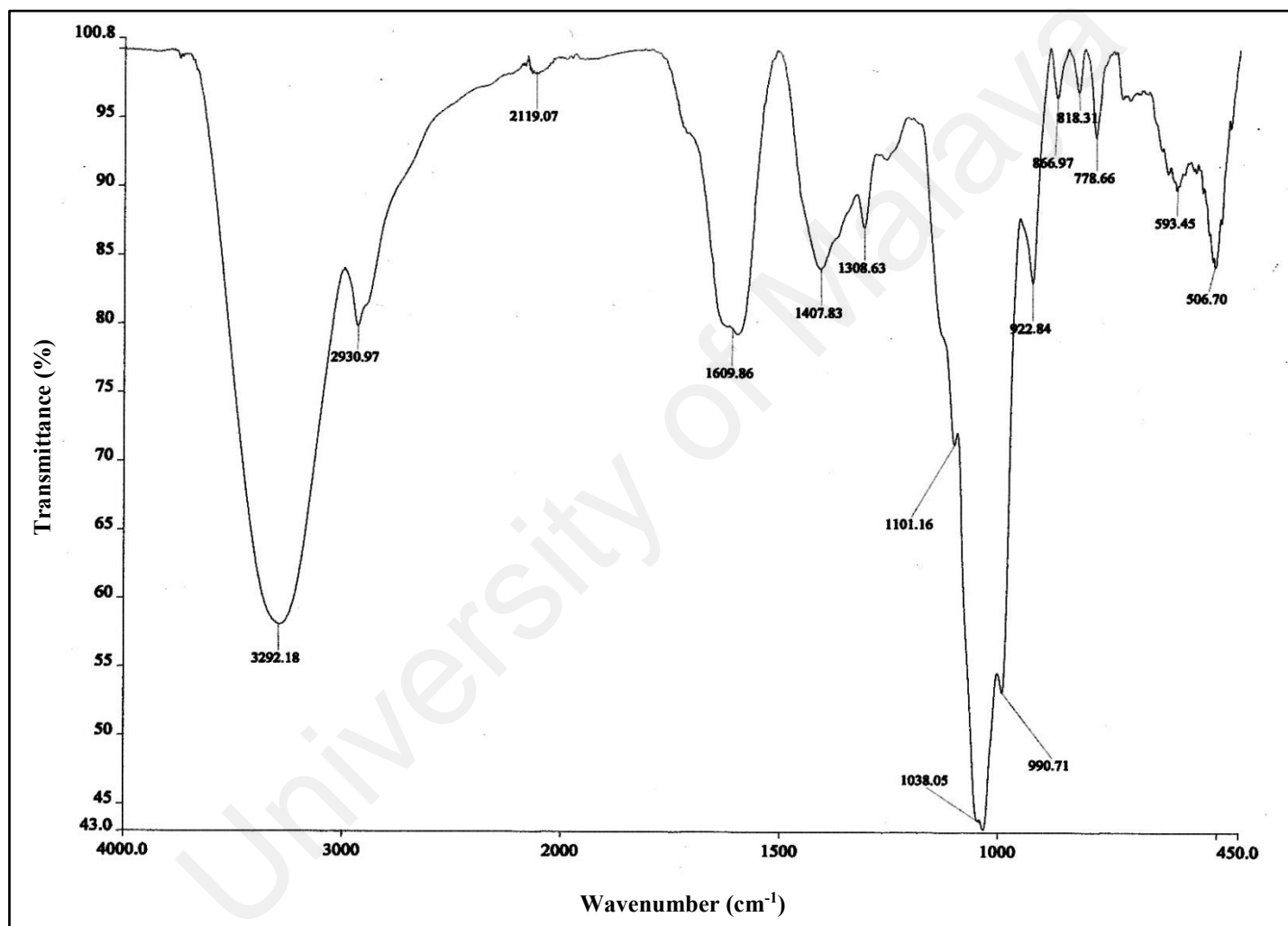


Figure 4.12: FTIR spectrum of freeze-dried residue fraction of CM extract left upon CM-AuNPs synthesis, in the wavenumber range of 450 to 4000 cm⁻¹.

CM extract is composed of terpenoids, such as labda-8(17),12-diene-15,16-dial; 15,16-bisnor-labda-8(17),11-diene-13-on; calcatarin and zerumin A (Liu & Nair, 2011; Malek et al., 2011). Except 15,16-bisnor-labda-8(17),11-diene-13-on, which contains a keto group, rest of the above terpenoids possess aldehyde groups. These carbonyl compounds are capable of reducing Au^{3+} to Au. The FTIR spectral results, obtained in this study were in agreement to a previous study, showing predominant involvement of carbonyl group(s) in the reduction of Au^{3+} ions (Rajan et al., 2014).

Based on the FTIR results as well as published reports, the mechanism of CM-AuNPs formation can be proposed, as shown in Figure 4.13. In the first step of CM-AuNPs synthesis, the precursor Au^{3+} ions were reduced to Au by the carbonyl groups of terpenoids. Nucleation process then occurred, where the gold atoms aggregated and led to the nuclei formation. The newly formed nuclei coalesced and contributed to the growth of CM-AuNPs (Aziz et al., 2014; Polte et al., 2010). Terpenoids with carboxyl groups, such as longpene A, coronadiene and zerumin A can bind to AuNP surfaces and act as a stabilizing agent (Aziz et al., 2014), which stopped further growth of CM-AuNPs.

4.2.3 Effect of buffers / media on zeta potential and hydrodynamic size

Physicochemical changes in CM-AuNPs, occurred, if any, upon 24 h incubation at room temperature in various buffers / media were studied by zeta potential and hydrodynamic size measurements. Zeta potential values of CM-AuNPs, suspended in different buffers or media are shown in Table 4.1. CM-AuNPs, suspended in water showed a zeta potential value of -38.2 ± 0.6 mV. A smaller decrease in the zeta potential was noticed upon their suspension in HSA (0.5% w/v) or PBS (pH 9.0). Lowering the pH value of PBS from pH 9.0 to pH 5.0 or addition of DMEM media led to gradual decrease in the magnitude of zeta potential of CM-AuNPs. Such decrease in the zeta potential can be attributed to either protonation of ionizable groups or increase in ionic strength, which

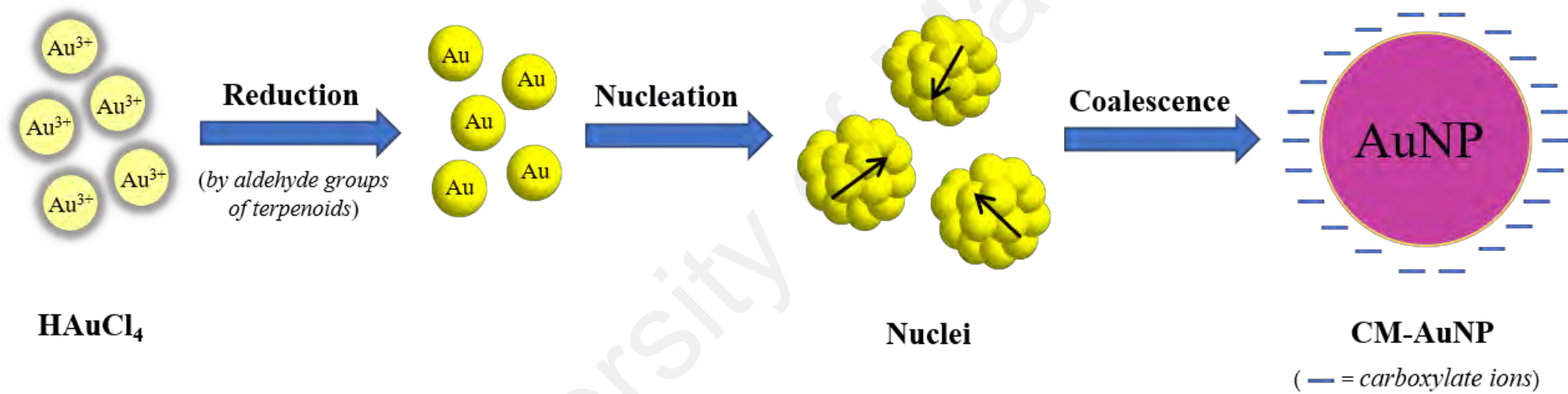


Figure 4.13: Proposed mechanism for the formation of CM-AuNPs, synthesized using CM extract as a reducing and stabilizing agent.

Table 4.1: Zeta potential values of CM-AuNPs after 24 h incubation in different buffers / media. *Significantly different from the negative control value ($p < 0.05$), as analyzed by one-way ANOVA.

Physiological Media	Zeta Potential (mV)
PBS (pH 5.0)	$-26.4 \pm 1.0^*$
PBS (pH 7.4)	$-29.2 \pm 0.8^*$
PBS (pH 9.0)	$-33.3 \pm 0.6^*$
HSA (0.5 % w/v)	$-34.4 \pm 1.0^*$
DMEM	$-20.9 \pm 0.4^*$
DMEM + FBS (10% v/v)	$-13.5 \pm 0.1^*$
Ultrapure water (Negative control)	-38.2 ± 0.6

might have disrupted the surface charges of CM-AuNPs (Yallapu et al., 2015; Pfeiffer et al., 2014). CM-AuNPs, suspended in DMEM media + FBS (10% v/v) showed a marked decrease in the zeta potential, which might be explained due to formation of protein corona on the surface of CM-AuNPs, responsible for screening the negative surface charges (Goy-López et al., 2012). However, no visible aggregation of CM-AuNPs was observed in DMEM media + FBS (10% v/v) despite the low zeta potential value.

The hydrodynamic size of CM-AuNPs in suspension was measured using DLS technique. Table 4.2 shows the hydrodynamic size of CM-AuNPs, obtained after 24 h incubation at room temperature in different buffers / media. The hydrodynamic size of CM-AuNPs in water was determined to be 78.7 ± 0.5 nm, which was much larger than the value of the particle size, obtained from TEM analysis. This was due to different measurement analysis, used in these techniques. Whereas, DLS measures hydrodynamic size, which includes NPs' coating, TEM measures only the core size of NPs (Mefford et al., 2008). Therefore, the hydrodynamic size of NPs is usually bigger than the core size, determined by TEM (Regmi et al., 2011). No significant change in the hydrodynamic size of CM-AuNPs was noticed upon their suspension in PBS (pH 5.0), HSA (0.5% w/v) or DMEM media. On the other hand, the hydrodynamic size of the CM-AuNPs was significantly reduced upon their suspension in PBS of higher pH values, i.e., pH 7.4 and pH 9.0. Surprisingly, CM-AuNPs incubated in DMEM + FBS (10% v/v) showed ~46% increase in the hydrodynamic size. Such increase seems to be a common phenomenon, where proteins present in FBS form protein corona after being adsorbed on NPs surface, thus contributing to their bigger size (Yallapu et al., 2015). This was in agreement to a previous report, where serum was found to promote ~3 fold increase in NPs size (Caracciolo et al., 2010).

Table 4.2: Hydrodynamic size of CM-AuNPs after 24 h incubation in different buffers / media. *Significantly different from the negative control value ($p < 0.05$), as analyzed by one-way ANOVA.

Physiological Media	Hydrodynamic Size (nm)
PBS (pH 5.0)	82.9 ± 1.0
PBS (pH 7.4)	$55.4 \pm 1.5^*$
PBS (pH 9.0)	$68.8 \pm 2.0^*$
HSA (0.5% w/v)	77.3 ± 1.3
DMEM	75.8 ± 1.8
DMEM + FBS (10% v/v)	$114.7 \pm 1.4^*$
Ultrapure water (Negative control)	78.7 ± 0.5

4.2.4 *In vitro* stability

The stability of NPs in buffer and biological media is considered to be an essential criterion before their use in cell-based studies or systemic use. This is important since the bloodstream or culture media contain serum proteins, electrolytes, nutrients and metabolites that contribute to a high ionic strength, which may lead to aggregation of these NPs (Sperling & Parak, 2010). Aggregation of chemically-synthesized AuNPs in the blood stream has been reported in an earlier study, which can limit their use for *in vivo* human applications (Eghtedari et al., 2009).

In order to check if CM extract had stabilized the AuNPs against such aggregation, stability of CM-AuNPs was investigated by suspending them in PBS (pH 5.0), PBS (pH 7.4), PBS (pH 9.0), HSA (0.5% w/v), DMEM, DMEM + FBS (10% v/v) and water (negative control). As shown in Figure 4.14A, UV-Vis absorption spectra of CM-AuNPs in water was characterized by the presence of an SPR band at 535 nm. Although a decrease in the absorbance value of the SPR band was noticed in different buffers / media compared to the value obtained with water after 24 h incubation at room temperature, peak shape of the absorption band was retained in all cases (Figure 4.14A). Whereas, ~9–12 % decrease in the absorbance value was observed in the presence of PBS (pH 5.0) / HSA (0.5% w/v) / DMEM, other media [PBS (pH 7.4) / PBS (pH 9.0) / DMEM + FBS (10 % v/v)] produced ~20 % decrease in the absorbance. Since the absorption band of CM-AuNPs was not markedly affected upon suspending them in all the above buffers / media, it is presumed that CM-AuNPs remained stable under these conditions. This was verified by testing the stability of citrate-AuNPs in the above buffers / media and the results are shown in Figure 4.14B. As can be seen from the Figure 4.14B, the SPR band of citrate-AuNPs which occurred at 520 nm, disappeared completely or markedly reduced in intensity. This was accompanied by the appearance of a new absorption peak at longer wavelength upon their suspension in PBS of different pH and DMEM media. These

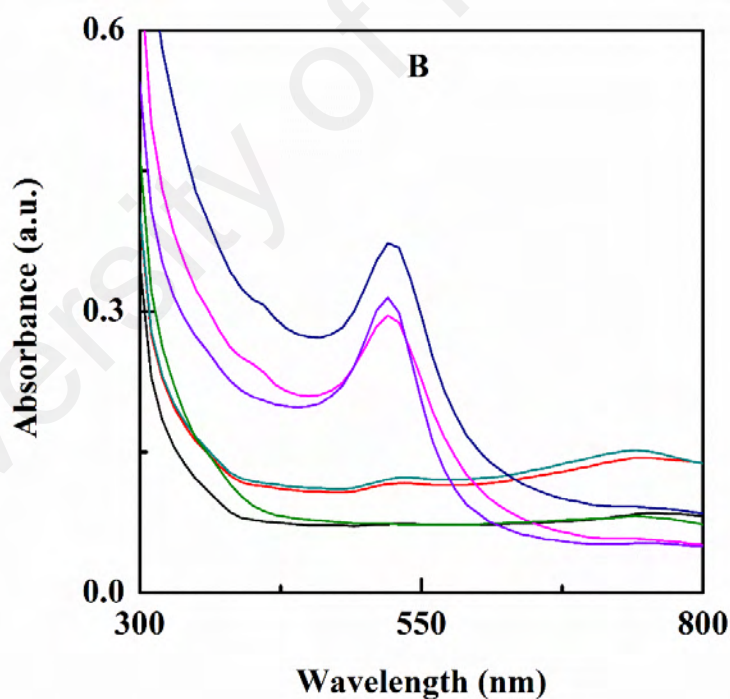
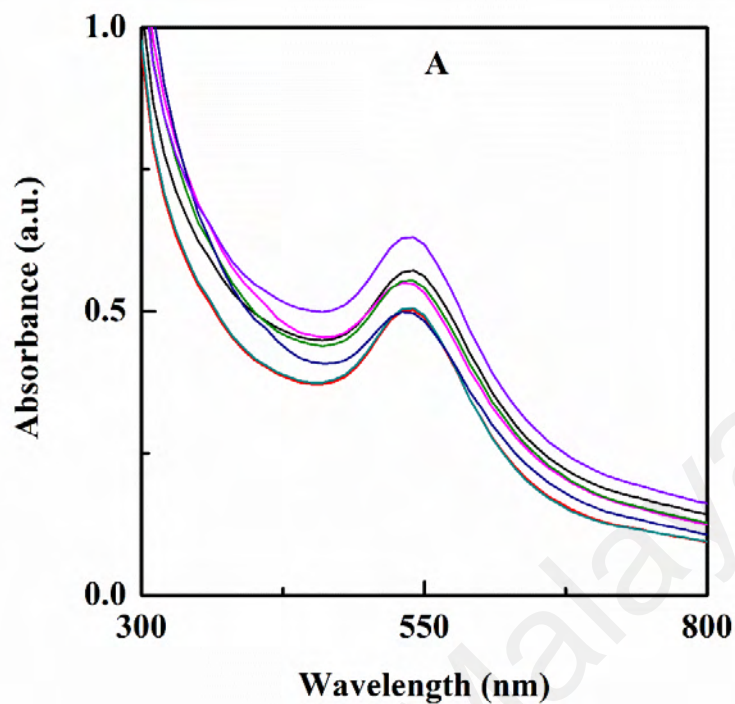


Figure 4.14: UV-Vis absorption spectra of CM-AuNPs (A) and citrate-AuNPs (B) after 24 h incubation in various media. CM-AuNPs were synthesized in the same way as described in the legend to Figure 4.10. Different media used are shown with different colours: PBS-pH 5.0 (black); PBS-pH 7.4 (red); PBS-pH 9.0 (light blue); HSA (0.5% w/v) (pink); DMEM (green); DMEM + 10% FBS (dark blue) and DI water (purple).

results indicated aggregation of citrate-AuNPs. Similar results have been reported earlier on chemically-synthesized AuNPs, such as citrate-AuNPs and CTAB-AuNPs, which were found unstable and had undergone aggregation in PBS (Du et al., 2012; Wang et al., 2014). The SPR band of citrate-AuNPs suspended in HSA (0.5% w/v) or DMEM + FBS (10% v/v) retained characteristic features (peak shape and absorbance value) as shown by the negative control. This can be ascribed to the adsorption of proteins, present in FBS or HSA on the surface of AuNPs, which prevented their aggregation (Cañaveras et al., 2012; Goy-López et al., 2012). In view of the above, CM-AuNPs were found to be more stable than citrate-AuNPs, as evident from the retention of the SPR band as well as absence of longer wavelength peak in different buffers / media. Terpenoids, present in the CM extract might have added more to steric repulsion in addition to electrostatic repulsion in order to stabilize CM-AuNPs in high ionic strength buffers / media. On the other hand, citrate-AuNPs, which are stabilized predominantly by electrostatic repulsion, required addition of proteins or polymers to prevent their aggregation in buffers / media (Shi et al., 2012; Liu et al., 2007). Thus, CM-AuNPs offer additional advantage over the use of chemically-synthesized AuNPs for biological applications.

4.3 Biocompatibility of CM-AuNPs

Biocompatibility of NPs is an important criterion for therapeutic applications of NPs, so as to produce minimal effect on normal cells. Earlier reports have shown abnormal sedimentation, hemagglutination and hemolysis of RBCs upon treatment with various NPs (Lin & Haynes, 2010; Khullar et al., 2012; Li et al., 2008). Therefore, it is essential to evaluate the cytotoxicity and hemocompatibility of CM-AuNPs, synthesized in this study.

4.3.1 Cytotoxicity

In order to investigate the *in vitro* toxicity profile of CM-AuNPs, cells were treated with CM-AuNPs for a desired time period and cell viability was checked using MTT assay. MTT is a water-soluble yellow tetrazolium dye, which can only be reduced by live cells to produce a water-insoluble purple formazan product. MTT assay is more convenient compared to other cytotoxic assays as no washing steps are required after removal of aqueous medium prior to solubilization of MTT-formazan product.

Two normal human fibroblast cell lines, i.e., human colon fibroblast cells (CCD-18Co) and human lung fibroblast cells (MRC-5) were employed to check cytotoxicity of CM-AuNPs. The percentage viability of CCD-18Co cells after treatments with increasing concentrations of CM-AuNPs for 24 h and 72 h is shown in Figures 4.15A and B, respectively. As evident from Figure 4.15A, treatment of cells with increasing concentration of CM-AuNPs up to 50 $\mu\text{g/ml}$ for 24 h did not produce any toxic effect, as $> 90\%$ cell viability was observed under these conditions. On the other hand, increasing the incubation time to 72 h produced significant ($\sim 39\%$) inhibition of cell viability upon treatment with 50 $\mu\text{g/ml}$ CM-AuNPs (Figure 4.15B). Greater than 80% cell viability was noticed upon treatment with CM-AuNPs' concentrations up to 25 $\mu\text{g/ml}$ for 72 h (Figure 4.15B).

Figures 4.16A and B illustrate the percentage viability of MRC-5 cells after CM-AuNPs treatment with increasing concentrations for 24 h and 72 h, respectively. MRC-5 cells did not experience any toxicity of CM-AuNPs up to 25 $\mu\text{g/ml}$ concentration for both 24 h and 72 h treatments, as $> 80\%$ cell viability was observed under these conditions. However, treatment with higher concentration of CM-AuNPs (50 $\mu\text{g/ml}$) showed a pronounced toxic effect to MRC-5 cells, as $\sim 71\%$ and $\sim 16\%$ cells remained viable upon 24 h and 72 h treatments, respectively.

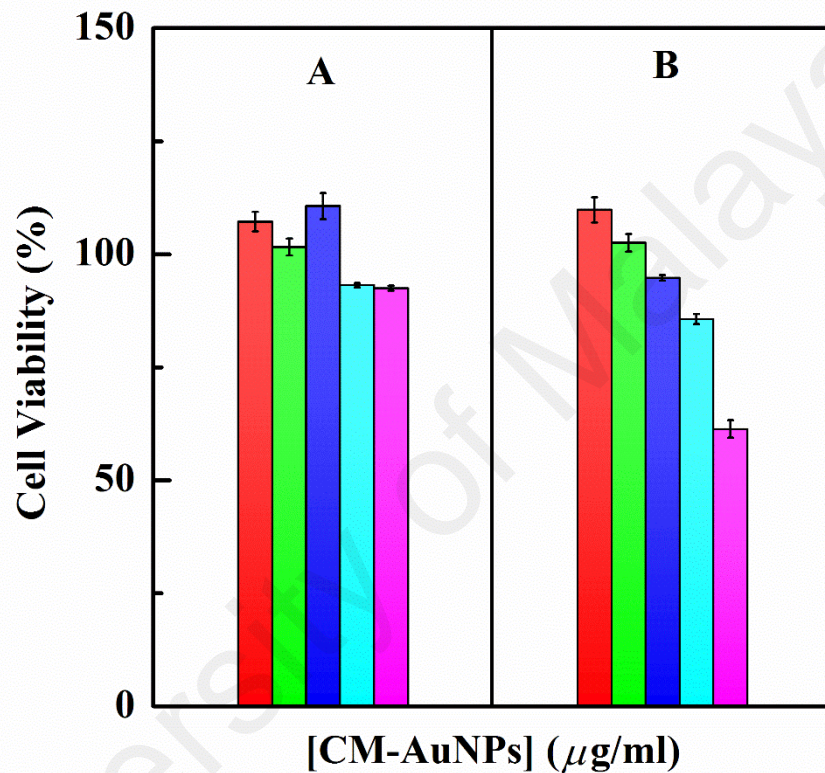


Figure 4.15: Bar diagram showing percentage viability of CCD-18Co cells after treatment with increasing concentrations of CM-AuNPs for 24 h (A) and 72 h (B), as analyzed by MTT assay. The concentrations of CM-AuNPs used are shown with different colours: 3.13 μg/ml (red); 6.25 μg/ml (green); 12.50 μg/ml (blue); 25.00 μg/ml (cyan) and 50.00 μg/ml (magenta).

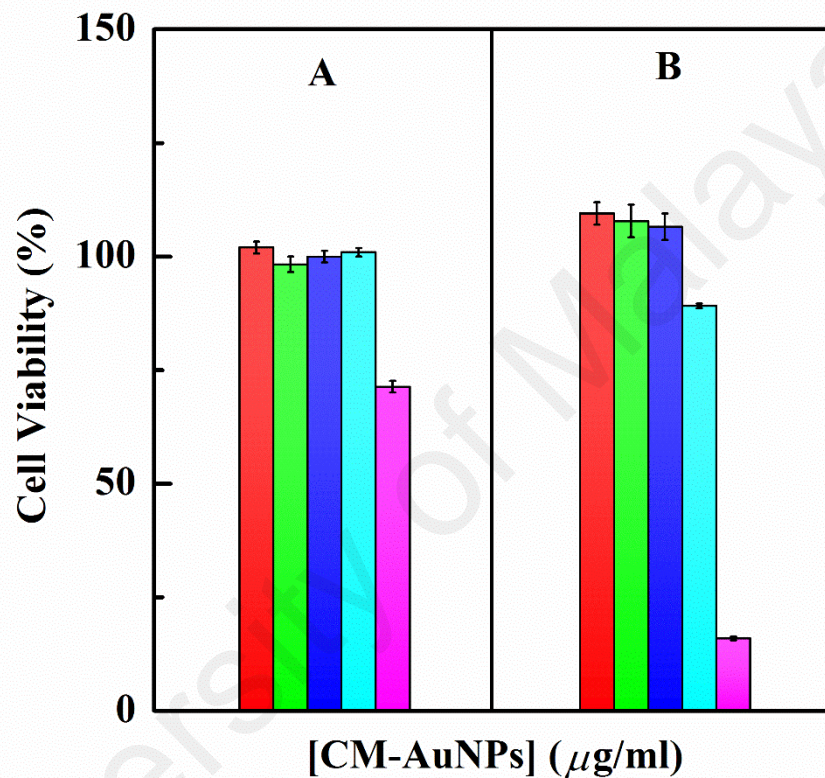


Figure 4.16: Bar diagram showing percentage viability of MRC-5 cells after treatment with increasing concentrations of CM-AuNPs for 24 h (A) and 72 h (B), as analyzed by MTT assay. The concentrations of CM-AuNPs used are shown with different colours: 3.13 $\mu\text{g/ml}$ (red); 6.25 $\mu\text{g/ml}$ (green); 12.50 $\mu\text{g/ml}$ (blue); 25.00 $\mu\text{g/ml}$ (cyan) and 50.00 $\mu\text{g/ml}$ (magenta).

To check if CM extract had contributed towards toxicity of CM-AuNPs, cytotoxicity of CM extract on both of these cell lines was also investigated. The percentage viability of CCD-18Co and MRC-5 cells after treatment with increasing concentrations of CM extract for 24 h and 72 h was checked by MTT assay and the results are depicted in Figures 4.17 and 4.18, respectively. As evident from these figures, treatment of cells with CM extract at increasing concentrations up to 50 $\mu\text{g/ml}$ for 24 h as well as 72 h did not produce any toxic effect, as the percentage viability was found to be $> 95\%$ in both CCD-18Co and MRC-5 cells.

The cytotoxicity results, as described above suggested that CM-AuNPs with concentrations up to 25 $\mu\text{g/ml}$ did not produce any toxic effect on the two normal human fibroblast cell lines. Such non-toxicity of CM-AuNPs can be attributed to the biocompatibility of CM extract, which was used as a stabilizing agent in the preparation of CM-AuNPs. On the contrary, residual contamination from synthesis or desorption of the stabilizing agent from AuNPs often contribute to the toxicity of chemically-synthesized AuNPs. For example, the common capping agent, CTAB, used in the preparation of gold nanorods, has been found to be highly toxic to cells, which may contribute to the cytotoxicity of CTAB-capped gold nanorods at nanomolar concentrations. Therefore, overcoating the CTAB-capped gold nanorods with polymers is required to reduce the toxicity of CTAB-capped gold nanorods (Alkilany et al., 2009). Herein, we demonstrated the use of phytochemicals as biocompatible capping agents, which might be a better option for the biological applications of AuNPs.

4.3.2 Hemocompatibility

Hemocompatibility test is an important parameter to evaluate the toxicity profile of nanoparticles for intravenous use. Both hemolysis and aggregation of RBCs were examined to measure the loss of RBCs, if it occurs, upon exposure to CM-AuNPs.

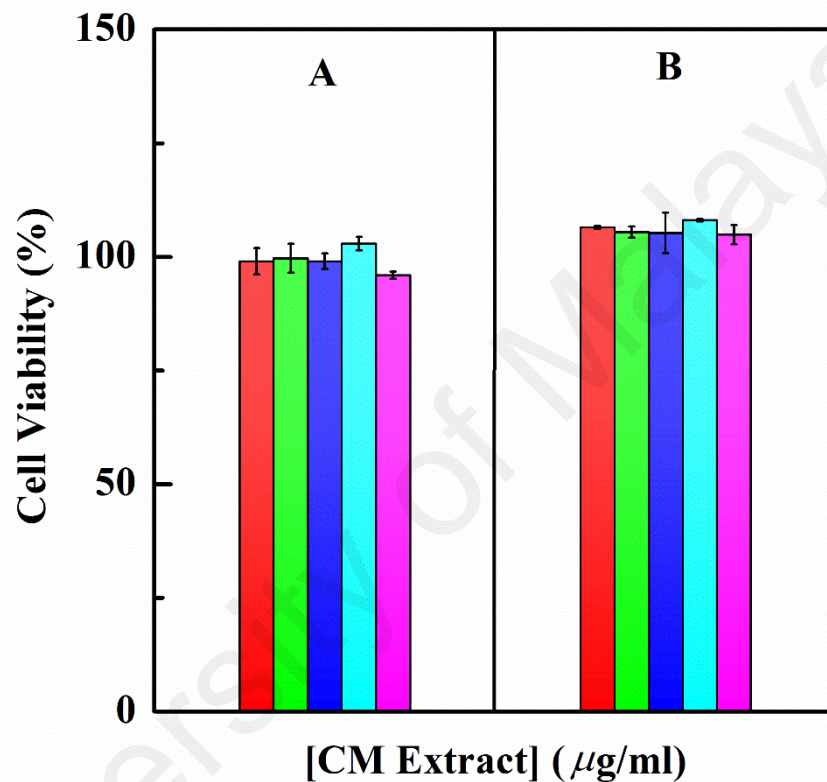


Figure 4.17: Bar diagram showing percentage viability of CCD-18Co cells after treatment with increasing concentrations of CM extract for 24 h (A) and 72 h (B), as analyzed by MTT assay. The concentrations of CM extract used are shown with different colours: 3.13 $\mu\text{g/ml}$ (red); 6.25 $\mu\text{g/ml}$ (green); 12.50 $\mu\text{g/ml}$ (blue); 25.00 $\mu\text{g/ml}$ (cyan) and 50.00 $\mu\text{g/ml}$ (magenta).

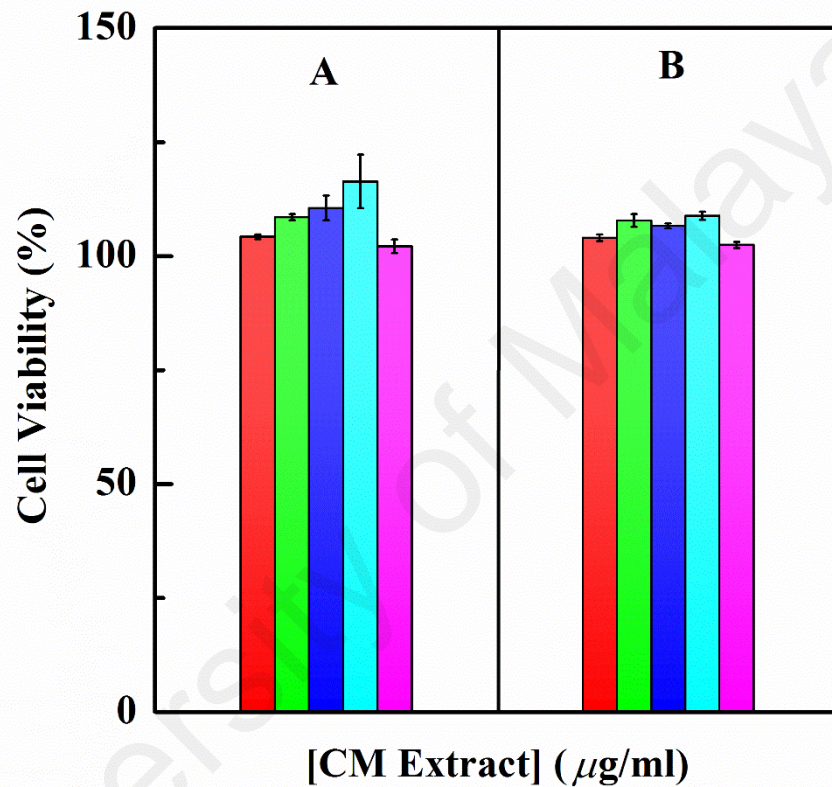


Figure 4.18: Bar diagram showing percentage viability of MRC-5 cells after treatment with increasing concentrations of CM extract for 24 h (A) and 72 h (B), as analyzed by MTT assay. The concentrations of CM extract used are shown with different colours: 3.13 $\mu\text{g/ml}$ (red); 6.25 $\mu\text{g/ml}$ (green); 12.50 $\mu\text{g/ml}$ (blue); 25.00 $\mu\text{g/ml}$ (cyan) and 50.00 $\mu\text{g/ml}$ (magenta).

The hemolysis assay is a colorimetric assay, used to estimate the amount of released red-colored hemoglobin, which indicate the extent of damage of RBCs (Evani & Ramasubramanian, 2011). Hemolytic results of RBCs, incubated with increasing concentrations of different AuNPs as well as CM extract alone are shown in Figure 4.19. As evident from Figure 4.19, percentage hemolysis of RBCs was found to be $\leq 10\%$, upon exposure to either CM-AuNPs or CM extract, being $\sim 10\%$ and 0% , respectively. A value of percentage hemolysis $< 10\%$ has been considered as the safe hemolytic ratio for biomaterials according to ISO/TR7406 (Jain et al., 2016). On the other hand, exposure of RBCs to CTAB-AuNPs of concentrations 25 and 50 $\mu\text{g/ml}$ resulted in 45 % and 96 % hemolysis, respectively.

Microscopic images, shown in Figure 4.20 depict results of RBCs' aggregation assay upon treatment with increasing concentrations of CM-AuNPs / CM extract / CTAB-AuNPs. RBCs treated with either CM-AuNPs or CM extract maintained healthy smooth biconcave shape and possessed similar morphology, as noticed with the negative control. No clear aggregation was observed in the RBCs treated with CM-AuNPs or CM extract at all the concentrations tested. On the other hand, RBCs treated with lower concentrations (3–12.5 $\mu\text{g/ml}$) of CTAB-AuNPs showed cell deformation, while treatment with higher concentrations (25 $\mu\text{g/ml}$) resulted in hemolysis of RBCs. For treatment with 50 $\mu\text{g/ml}$ of CTAB-AuNPs, only cell debris was visible due to complete hemolysis of RBCs.

In view of the above results, CM-AuNPs were found to possess good hemocompatibility due to low percentage hemolysis and lack of RBC aggregation up to 50 $\mu\text{g/ml}$ treatment. The hemocompatible characteristic of CM-AuNPs can be attributed to its negative surface charge, contributed by the carboxylate group of terpenoids present in CM extract, as negative surface charged-NPs have been found to be more

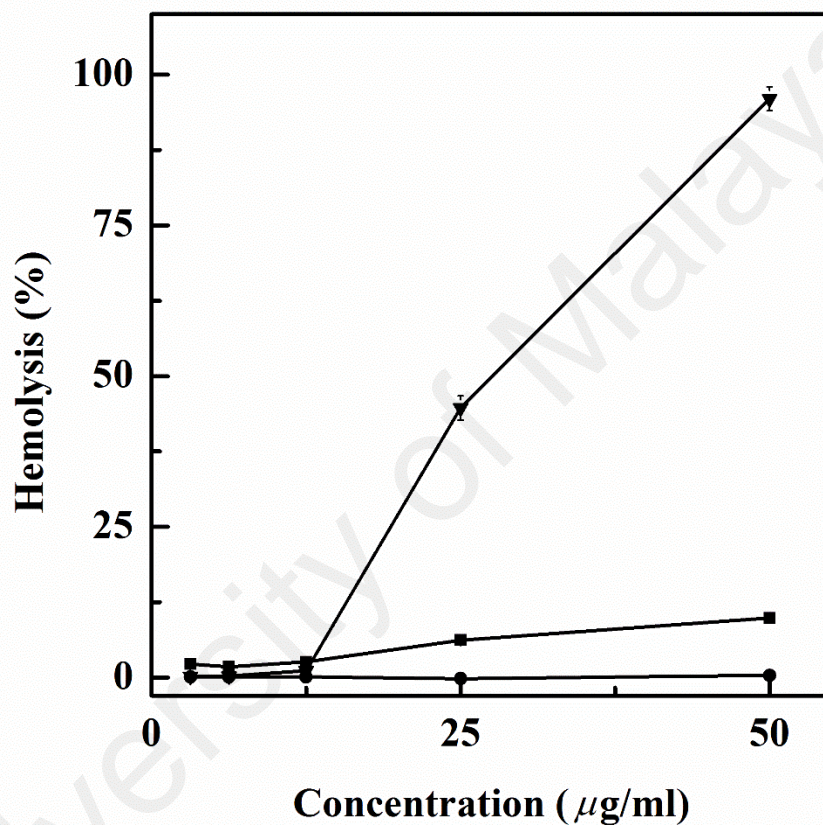


Figure 4.19: Percentage hemolysis of human red blood cells after incubation with increasing concentrations of AuNPs or CM extract for 5 h at 37°C. Different AuNPs or CM extract are shown with different symbols: CTAB-AuNPs (▼), CM-AuNPs (■), Citrate-AuNPs (▲) and CM extract (●).

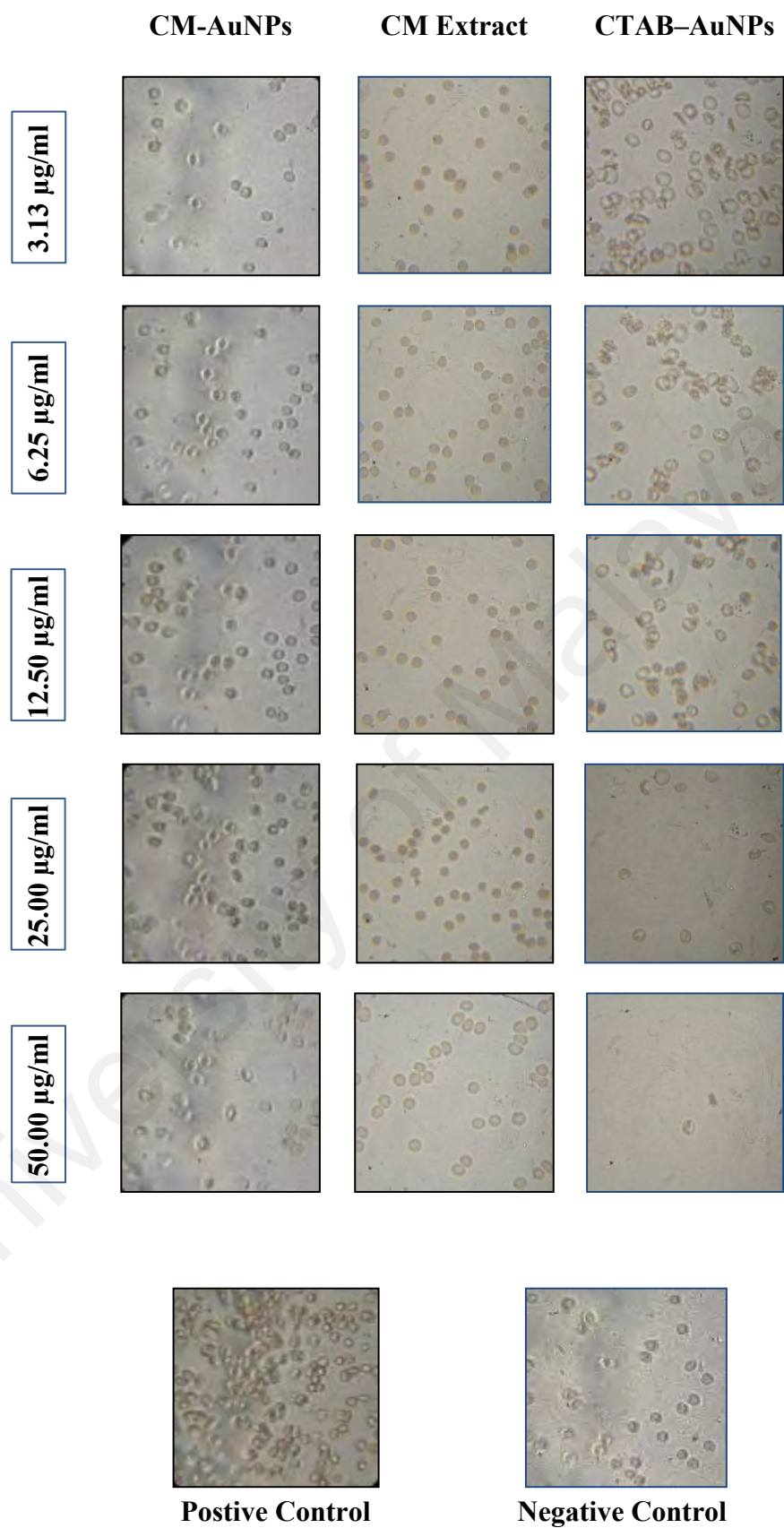


Figure 4.20: Micrographs (100 \times magnification) of red blood cells after incubation with increasing concentrations of CM-AuNPs, CM extract and CTAB-AuNPs for 2 h at 37 $^{\circ}\text{C}$.

biocompatible (Alkilany et al., 2009). On the other hand, desorption of CTAB from CTAB-AuNPs seems to be responsible for significant hemolysis of RBCs. This was in agreement with a previous report, suggesting RBCs lysis at lower concentrations of free CTAB molecules (Lin & Haynes, 2010). Besides, the positive surface charge of CTAB-AuNPs might be responsible for attachment of CTAB-AuNPs to RBCs, thus leading to their lysis.

4.4 Interaction of CM-AuNPs with HSA

Upon NPs administration into circulatory system, proteins can form a dynamic layer around NPs, known as the protein corona (Wolfram et al., 2014). Interaction of NPs with proteins can affect their biodistribution, uptake, efficacy and cytotoxicity (Wolfram et al., 2014; Nguyen & Lee, 2017). The major transport protein found in human plasma, namely, HSA is known to bind different ligands including NPs (Yamasaki et al., 2013; Cañaveras et al., 2012). Earlier reports have shown that adsorption of albumin on NPs surface can reduce their cytotoxicity (Peng et al., 2013; Tedja et al., 2012). In addition, protein corona enriched with albumin or apolipoproteins on NPs was found to reduce macrophage recognition and complement activation, thus prolonged NPs blood circulation time (Nguyen & Lee, 2017; Peng et al., 2013). In view of the above, it would be important to study the binding characteristics of CM-AuNP to HSA.

4.4.1 Fluorescence quenching

The interaction of nanoparticles with proteins often leads to changes in the fluorescence properties of the biomolecule. Thus, intrinsic fluorescence quenching was employed to study the interaction of CM-AuNP with HSA (Boulos et al., 2013; Sharma & Ilanchelian, 2015). Figure 4.21 illustrates the fluorescence spectra of HSA in the absence and presence of increasing CM-AuNP concentrations at 25 °C, upon excitation at 295 nm. These spectra were obtained after treating the measured fluorescence spectra

for inner filter effect correction according to Eq. (3) in order to avoid the interference of light absorption by CM-AuNPs. As can be seen from Figure 4.21, free HSA showed an emission maximum at 343 nm. The excitation wavelength of 295 nm was selected to avoid the contribution from tyrosine (Tyr) residues. Hence, the fluorescence spectrum observed was solely contributed by the lone Trp residue, located at position 214 in the primary sequence of HSA (Peters Jr, 1996). Addition of increasing CM-AuNP concentrations quenched HSA fluorescence gradually without noticeable change in the emission maximum (Figure 4.21). Reduction in the fluorescence intensity can be ascribed to the changes in the polarity of the microenvironment around Trp residue due to either movement of charged groups in its vicinity or its exposure to polar environment (Khanna et al., 1986). Either one or both of these mechanisms seem to be responsible for the decrease in the fluorescence intensity upon complexation of CM-AuNP with HSA.

The fluorescence quenching of HSA can be characterized as either dynamic quenching or static quenching. These two quenching mechanisms can be distinguished by their temperature dependence or by lifetime measurements (Lakowicz, 2006). Increase in temperature results in larger diffusion coefficient, thus, increases dynamic quenching and the Stern-Volmer constant (K_{SV}), while dissociation of weakly-bound complex can occur at higher temperature, thus decreases static quenching and K_{SV} (Lakowicz, 2006). In order to characterize the mechanism of CM-AuNP-induced quenching of HSA fluorescence, titration experiments were performed at three different temperatures. The results of the fluorescence quenching titrations obtained at 30 °C and 35 °C are shown in Figures 4.22 and 4.23, respectively. The fluorescence quenching data were treated according to Eq. (4) and the resulting Stern-Volmer plots for CM-AuNP-HSA system, obtained at 25, 30 and 35 °C are depicted in Figure 4.24. Values of the K_{SV} were obtained from the slope of the Stern-Volmer plots and are given in Table 4.3.

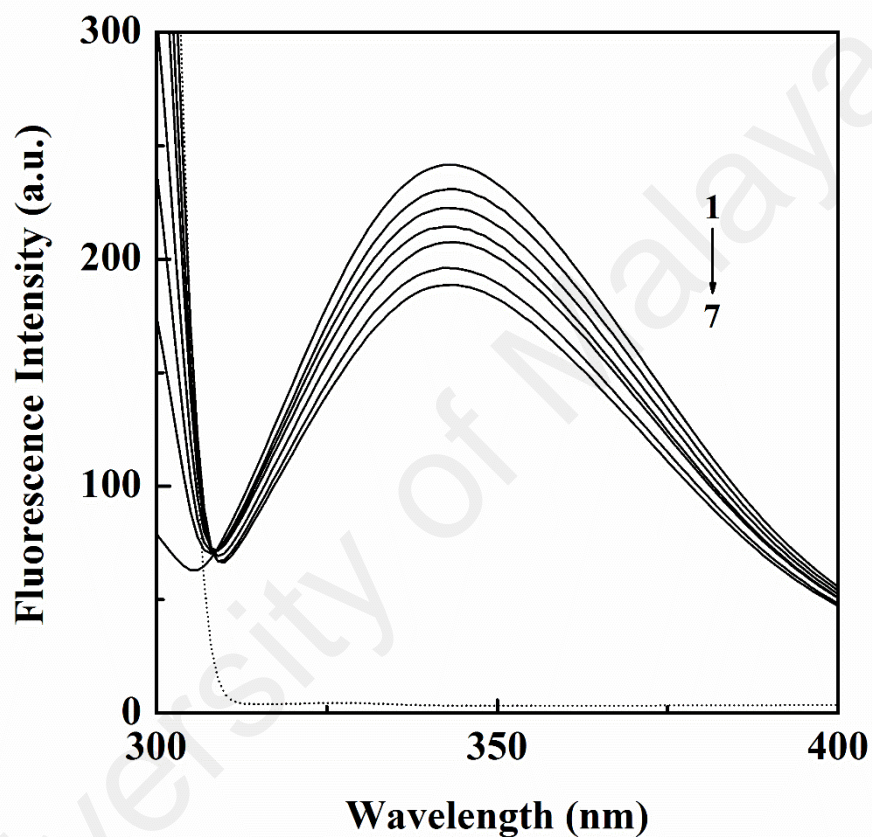


Figure 4.21: Quenching of HSA fluorescence induced by CM-AuNPs addition. Spectrum 1 refers to the fluorescence spectrum of HSA (5 μM), while spectra 2–7 were obtained in the presence of increasing CM-AuNP concentrations (5–30 μM with 5 μM intervals). The spectra were recorded in 60 mM sodium phosphate buffer, pH 7.4 at 25 $^{\circ}\text{C}$, upon excitation at 295 nm. The fluorescence spectrum of free CM-AuNPs (30 μM) is shown by dotted line.

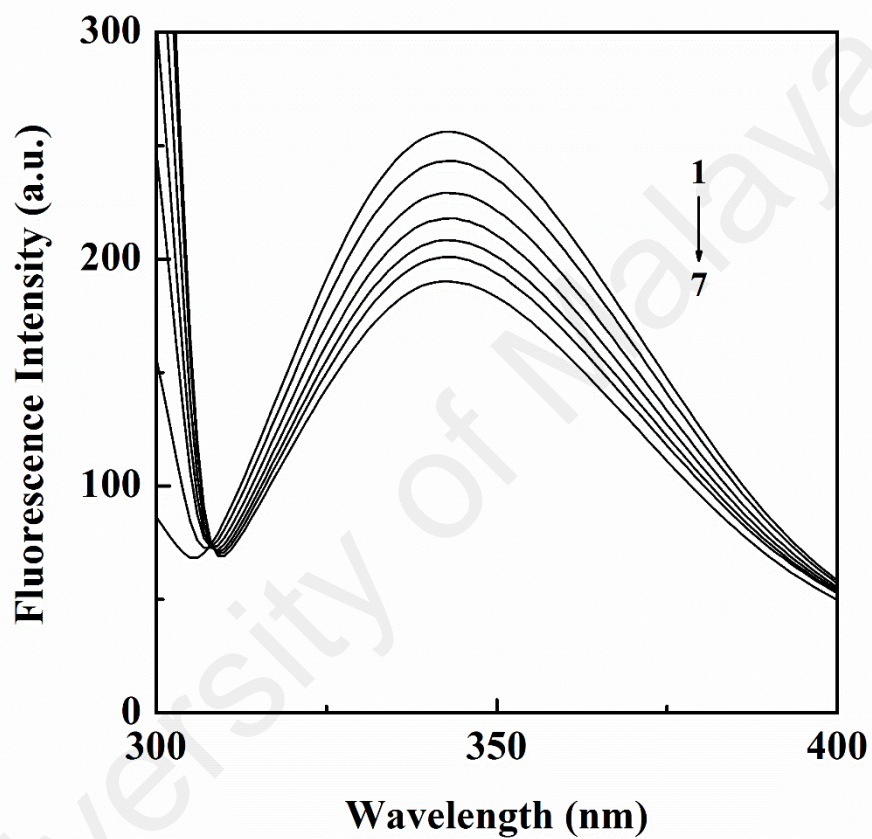


Figure 4.22: Quenching of HSA fluorescence induced by CM-AuNPs addition. Spectrum 1 refers to the fluorescence spectrum of HSA (5 μM), while spectra 2–7 were obtained in the presence of increasing CM-AuNP concentrations (5–30 μM with 5 μM intervals). The spectra were recorded in 60 mM sodium phosphate buffer, pH 7.4 at 30 $^{\circ}\text{C}$, upon excitation at 295 nm.

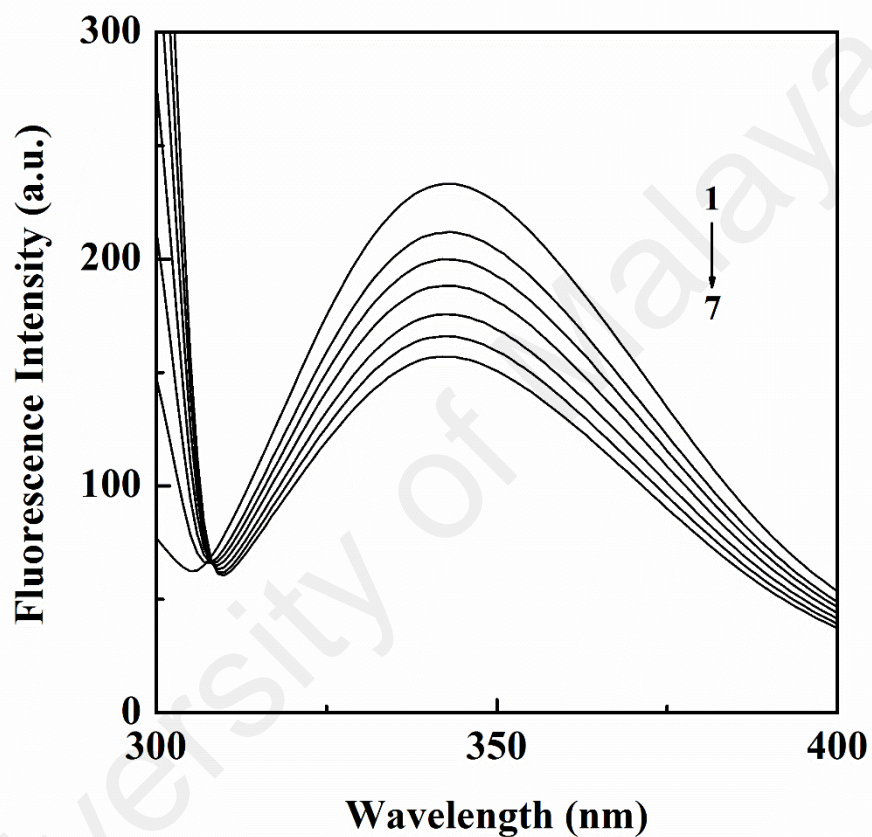


Figure 4.23: Quenching of HSA fluorescence induced by CM-AuNPs addition. Spectrum 1 refers to the fluorescence spectrum of HSA (5 μM), while spectra 2–7 were obtained in the presence of increasing CM-AuNP concentrations (5–30 μM with 5 μM intervals). The spectra were recorded in 60 mM sodium phosphate buffer, pH 7.4 at 35 $^{\circ}\text{C}$, upon excitation at 295 nm.

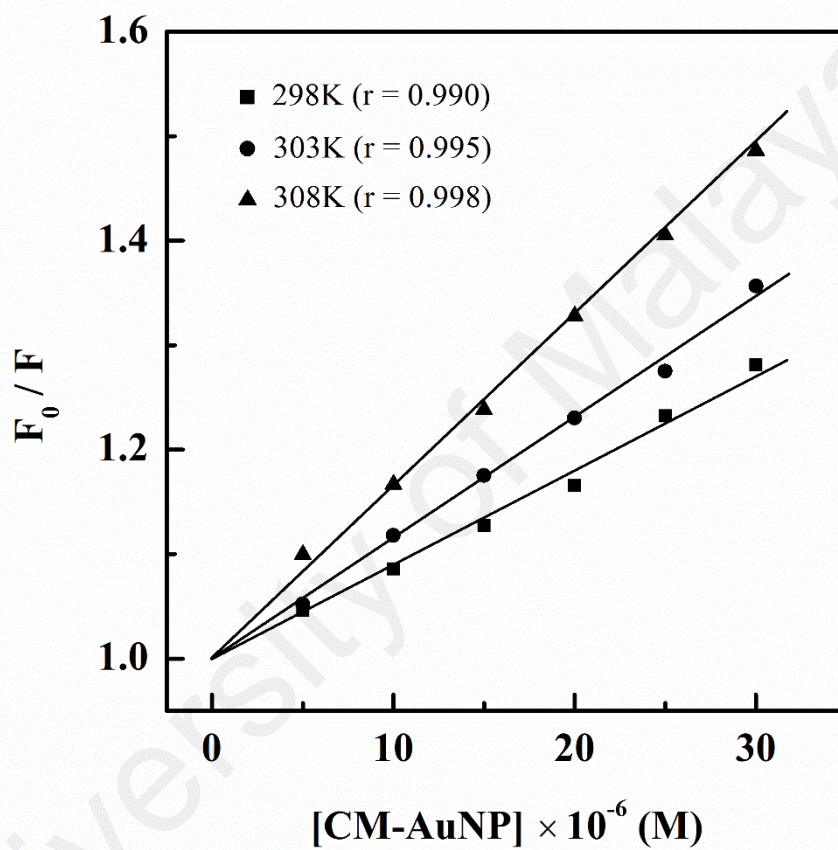


Figure 4.24: Stern-Volmer plots for quenching of HSA fluorescence induced by CM-AuNPs addition, acquired at three different temperatures. The plots were obtained by treating the fluorescence quenching data (Figures 4.21–4.23) according to Eq. (4).

Table 4.3: Values of the Stern-Volmer constant, binding constant and Hill coefficient for the interaction of CM-AuNP with HSA, obtained from the fluorescence quenching titration experiments at three different temperatures.

T (°C)	$K_{SV} \times 10^4$ (M ⁻¹)	$k_q \times 10^{12}$ (M ⁻¹)	$K_a \times 10^4$ (M ⁻¹)	<i>n</i>
25	0.94 ± 0.01	1.44 ± 0.02	0.97 ± 0.06	1.03 ± 0.05
30	1.14 ± 0.03	1.72 ± 0.08	1.33 ± 0.06	1.04 ± 0.03
35	1.52 ± 0.05	2.34 ± 0.11	1.54 ± 0.07	1.01 ± 0.08

As can be seen from Table 4.3, value of K_{SV} increased with increasing temperature, thus characterizing the CM-AuNP-induced quenching of HSA fluorescence as dynamic quenching. These results were in line with the findings reported earlier, where the quenching of HSA fluorescence by gold nanoclusters was characterized as collisional quenching (Yin et al., 2017). The values of the bimolecular quenching rate constant (k_q) were obtained by substituting the value of K_{SV} into Eq. (4) and are also listed in Table 4.3. Value of k_q , which is an indicator for the efficiency of quenching or fluorophore accessibility to the quencher has been suggested to lie in the range of $10^{10} \text{ M}^{-1}\text{s}^{-1}$ for diffusion-controlled quenching (Lakowicz, 2006). However, several earlier reports have characterized the ligand-induced quenching of protein fluorescence as dynamic quenching based on the positive correlation of K_{SV} with temperature, even though the k_q values obtained in these studies had fallen in the range of 10^{12} or higher (Li et al., 2013; Lakshmi et al., 2017; Yin et al., 2017). Involvement of dynamic quenching was further supported by time-resolved fluorescence data in these studies (Li et al., 2013; Lakshmi et al., 2017). In view of the above, it seems plausible to assume dynamic quenching as the mechanism involved in the CM-AuNP-induced quenching of HSA fluorescence, based on the positive correlation of K_{SV} with temperature.

4.4.2 Binding constant and thermodynamic parameters

Assuming independent binding of CM-AuNP to its binding site on HSA, values of the binding constant, K_a of CM-AuNP-HSA interaction at different temperatures were obtained after treating the fluorescence quenching data according to the double logarithmic equation (Eq. (5)). Figure 4.25 shows the double logarithmic plots, obtained at three different temperatures. The K_a values, as obtained from the intercept of these plots are listed in Table 4.3. The K_a values were found to lie in the range of $0.97\text{--}1.54 \times 10^4 \text{ M}^{-1}$, indicating moderate binding affinity between CM-AuNP and HSA.

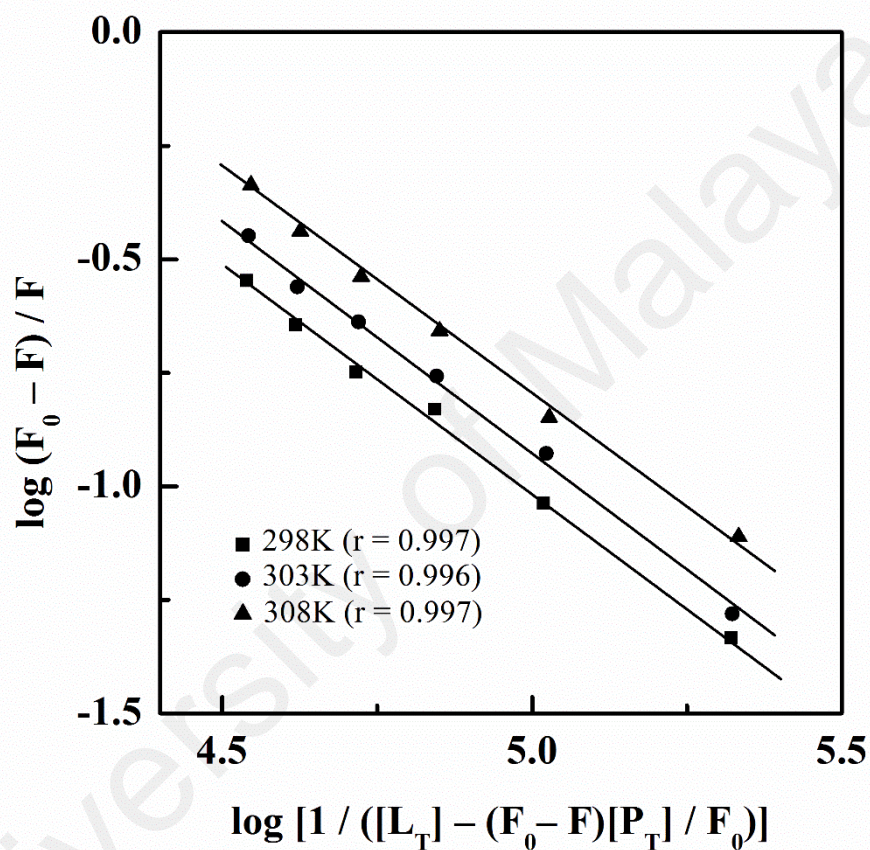


Figure 4.25: Double logarithmic plots of $\log (F_0 - F) / F$ versus $\log [1 / ([L_T] - (F_0 - F) [P_T] / F_0)]$ for the fluorescence quenching data of CM-AuNP-HSA interaction, acquired at three different temperatures. The plots were obtained by treating the fluorescence quenching data (Figures 4.21–4.23) according to Eq. (5).

Increasing trend of the K_a value with temperature also suggested CM-AuNP-induced quenching mechanism as dynamic quenching. The slope value from the double logarithmic plot yielded Hill coefficient, ' n '. As shown in Table 4.3, value of ' n ' was found to be close to 1.0, which suggested non-cooperative binding of the protein molecules on the nanoparticles' surface (Weiss, 1997; Sharma & Ilanchelian, 2015).

In order to characterize the forces involved in CM-AuNP-HSA interaction, temperature dependence of the binding constant was analyzed by using Eq. (6). No structural change in the protein is expected to occur within the selected temperature range, as the protein is known to remain stable within this range (Sun et al., 2009). Figure 4.26 shows the van't Hoff plot for CM-AuNP-HSA interaction. Values of the enthalpy change (ΔH) and the entropy change (ΔS) of the binding reaction were obtained from the slope and intercept, respectively, of the van't Hoff plot.

Substitution of ΔH and ΔS values into Eq. (7) yielded values of the Gibbs free energy change (ΔG) at different temperatures. The values of ΔH , ΔS and ΔG are tabulated in Table 4.4. The negative values of ΔG indicated spontaneous binding reaction between HSA and CM-AuNPs. The binding reaction was found to be entropically driven ($\Delta S = +195.6 \text{ J mol}^{-1} \text{ K}^{-1}$), as the larger $T\Delta S$ value offsets the positive value of ΔH , thus making the ΔG value negative. Positive value of ΔS can be ascribed to the disruption of the ordered water molecules upon CM-AuNP-HSA complex formation, that were previously arranged in an organized fashion around CM-AuNPs as well as protein molecules in their free forms. The hydrophobic amino acid residues in HSA, which were previously exposed to water molecules seem to have been buried upon binding of CM-AuNP, thus resulted in removal of these water molecules from the binding site (Ross & Subramanian, 1981; Amroabadi et al., 2018). Although a positive value of ΔS also suggest the involvement of electrostatic interactions, the value of ΔH has been found to be either extremely small or

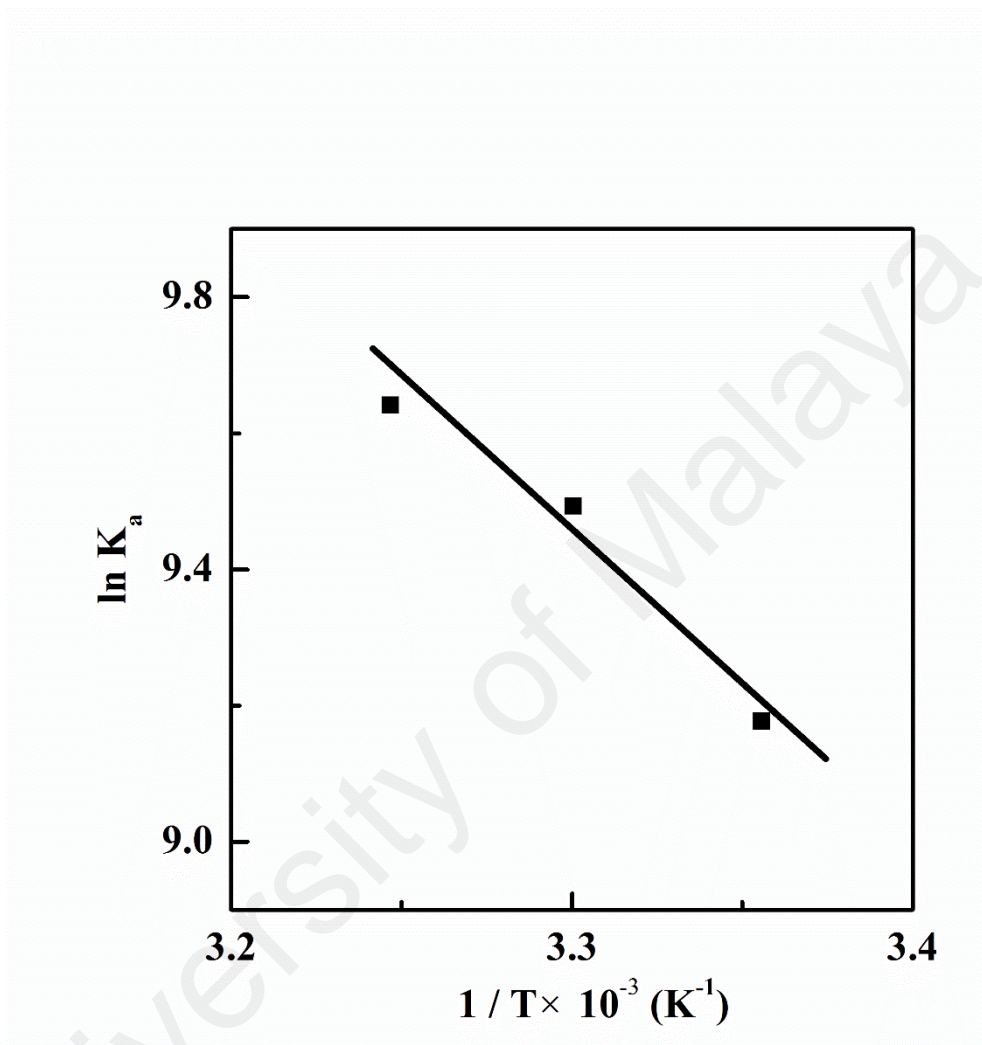


Figure 4.26: van't Hoff plot for the interaction between CM-AuNP and HSA.

Table 4.4: Thermodynamic parameters for the interaction of CM-AuNP with HSA, obtained from the fluorescence quenching titration experiments at three different temperatures.

T (°C)	ΔS (J mol ⁻¹ K ⁻¹)	ΔH (kJ mol ⁻¹)	ΔG (kJ mol ⁻¹)
25			-22.8
30	+195.6	+35.5	-23.8
35			-24.8

close to zero for these interactions (Ross & Subramanian, 1981). Since the value of ΔH , as obtained in this study for CM-AuNP-HSA interaction was found to be $+35.5 \text{ kJ mol}^{-1}$, involvement of electrostatic interactions can be ruled out. In view of this, interaction of CM-AuNP with HSA is supposed to be facilitated by hydrophobic forces. Involvement of hydrophobic interactions in the CM-AuNP binding to HSA was further supported by the positive signs of ΔH and ΔS , as suggested by Ross and Subramanian (1981). It seems plausible to consider the involvement of hydrophobic forces in CM-AuNP-HSA interaction due to the presence of cyclic hydrocarbon structures in terpenoids, the major components of the CM extract (Foo et al., 2017). In previous reports, interaction between serum albumin and metallic NPs has also been shown to be stabilized by hydrophobic interactions (Bhogale et al., 2014; Yin et al., 2017).

4.4.3 Absorption spectra

CM-AuNP-induced quenching mechanism of HSA fluorescence was further verified by UV-vis absorption spectral analysis. According to Lakowicz (2006), dynamic quenching only affects the excited state of the fluorophore (Trp) without changing its absorption spectra. UV-vis absorption spectra of HSA in the absence and presence of CM-AuNPs (60 and 120 μM) are illustrated in Figure 4.27. These absorption spectra were obtained after subtracting the absorption spectrum of free CM-AuNPs from the absorption spectra of CM-AuNP-HSA mixtures. Presence of an absorption maximum at 278 nm in the absorption spectrum of HSA was due to the aromatic amino acid residues in HSA (Sharma & Ilanchelian, 2015). No significant difference in the peak position and the peak amplitude was observed in the absorption spectrum of HSA upon addition of CM-AuNPs (Figure 4.27). This observation further supported the involvement of dynamic quenching in the CM-AuNP-HSA system and was in agreement with a previous report on the binding of gold nanoclusters to HSA, where dynamic quenching was also

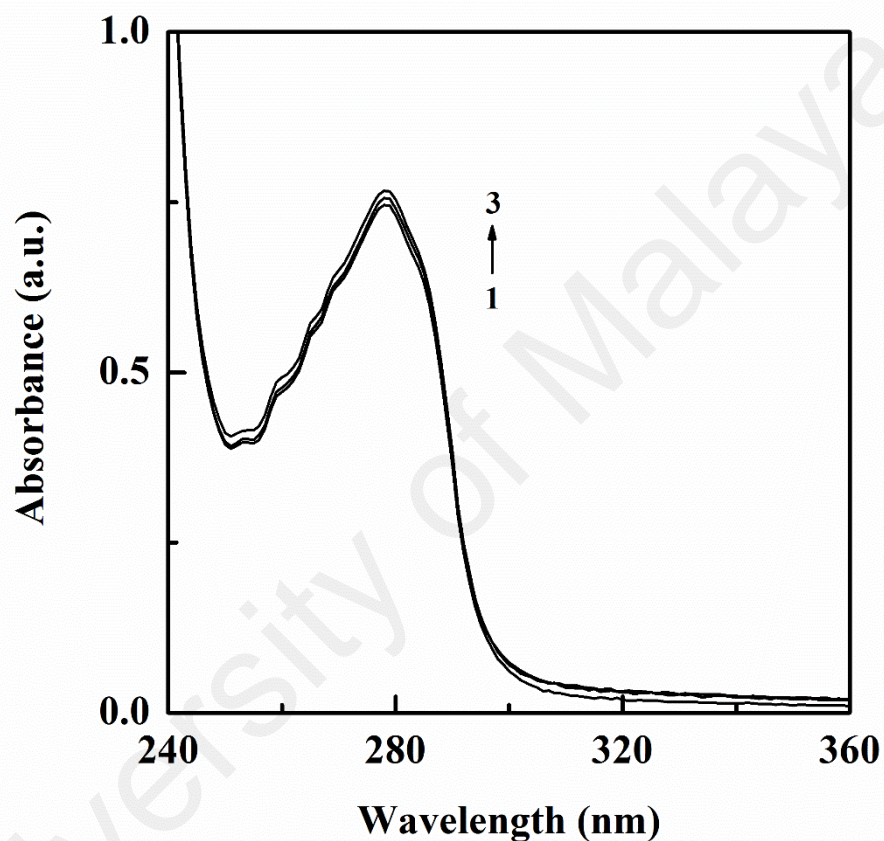


Figure 4.27: UV-Vis absorption spectra of HSA in the absence and presence of CM-AuNPs. Spectrum 1 refers to the absorption spectrum of HSA (20 μM), while spectra 2 and 3 were obtained in the presence of CM-AuNPs at concentrations of 60 and 120 μM , respectively. The spectra were recorded in 60 mM sodium phosphate buffer, pH 7.4 at 25 $^{\circ}\text{C}$. The spectra (2 and 3) were acquired after subtracting the absorption spectra of CM-AuNPs from the respective absorption spectra of CM-AuNP-HSA mixtures.

proved by the absence of absorption spectral changes upon addition of the nanoclusters (Yin et al., 2017).

4.4.4 Circular dichroism spectra

The influence of CM-AuNP interaction with HSA on the secondary and tertiary structures of the protein was evaluated by far-UV and near-UV CD spectral analyses. Figures 4.28 and 4.29 represent the far-UV and the near-UV CD spectra of HSA, respectively, in the absence and presence of CM-AuNP ([CM-AuNP]:[HSA] = 6:1). The distribution of different secondary structures in native HSA has been reported as ~70% α -helix, ~4% β -sheet, ~10% β -turn and ~12% random coil (Ali et al., 2016). Dominance of the α -helical structure in the protein was evidenced by the appearance of two minima at 208 and 222 nm (Kelly et al., 2005) in the far-UV CD spectrum of HSA (Figure 4.28). Overlapping of the far-UV CD spectra displayed by CM-AuNP-HSA mixture and HSA apparently suggested absence of secondary structural change in the protein upon binding to CM-AuNP. A similar observation has been reported by Yallapu et al. (2015), where the interaction of magnetic NPs with human serum protein did not produce significant change in the secondary structure of the protein. Since the far-UV CD spectrum represents the average secondary structures of a protein, it seems probable that there had been secondary structural changes among different secondary structures of the protein upon CM-AuNP binding but were not detectable by the far-UV CD spectra.

The near-UV CD spectrum of HSA was characterized by the appearance of two minima around 261 and 268 nm and shoulders around 282 and 291 nm, which can be attributed to the aromatic chromophores and disulfide bonds present in the protein (Sun et al., 2005). Addition of CM-AuNPs to HSA produced significant change in the near-UV CD spectrum of HSA, suggesting alteration in the tertiary structure of HSA upon interaction of CM-AuNP with HSA. These results were in agreement with earlier

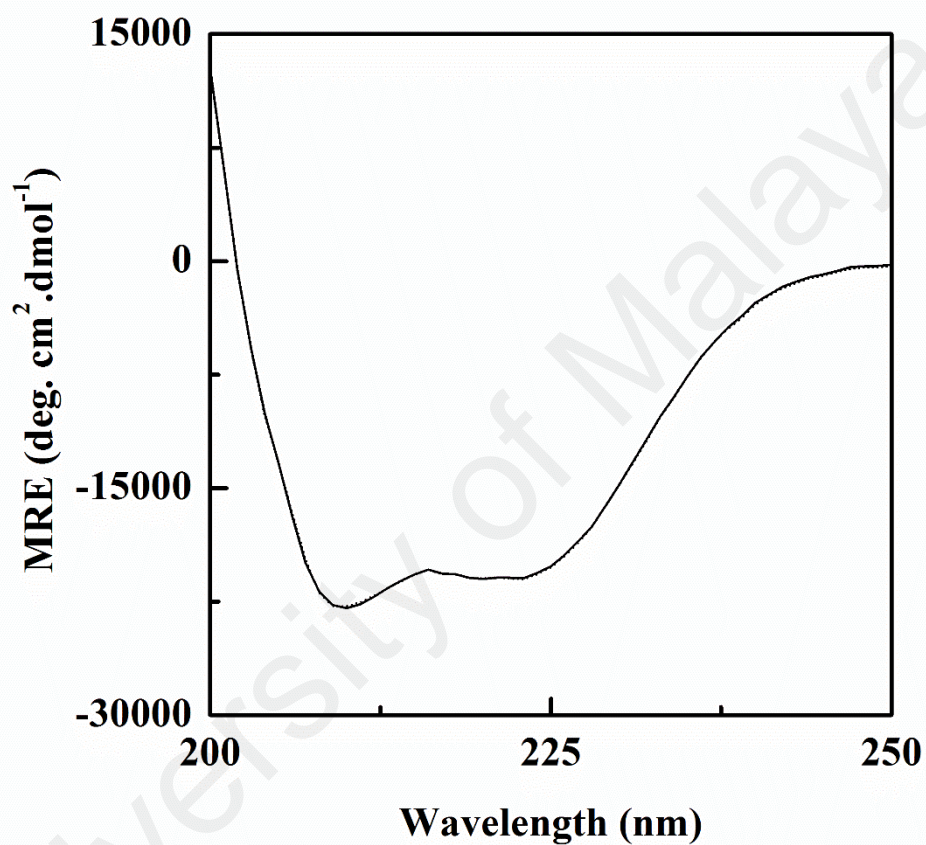


Figure 4.28: Far-UV CD spectra of HSA (5 μM) in the absence (solid line) and presence (dotted line) of CM-AuNPs (30 μM), obtained in 60 mM sodium phosphate buffer, pH 7.4 at 25 $^{\circ}\text{C}$.

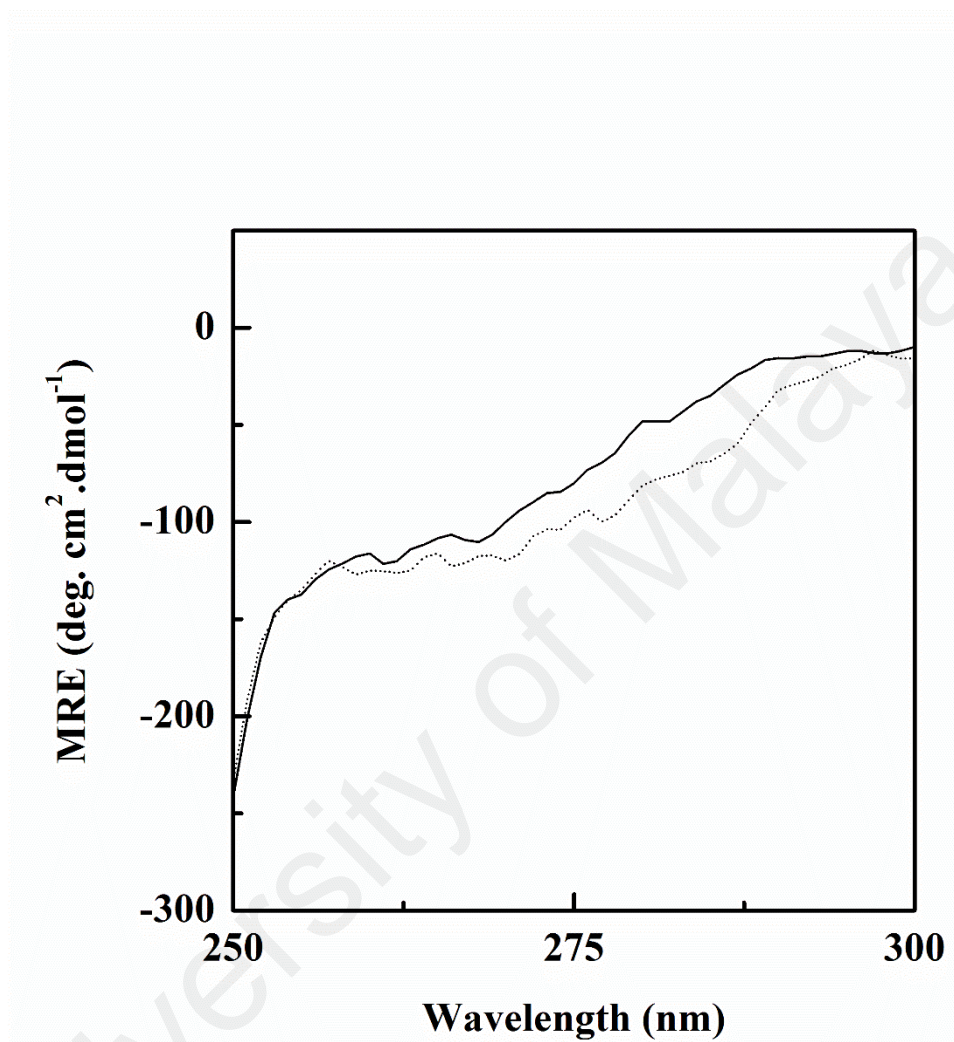


Figure 4.29: Near-UV CD spectra of HSA (10 μM) in the absence (solid line) and presence (dotted line) of CM-AuNPs (60 μM), obtained in 60 mM sodium phosphate buffer, pH 7.4 at 25 °C.

reports, suggesting tertiary structural changes in protein in the presence of nanoparticles (Aghili et al., 2016; Cukalevski et al., 2011).

4.4.5 Three-dimensional fluorescence spectra

Three-dimensional (3D) fluorescence spectra were used to monitor the changes in the microenvironment around Tyr and Trp residues of the protein upon its complexation with CM-AuNP. Figures 4.30–4.32 illustrate the 3D fluorescence spectra and corresponding contour maps of HSA, CM-AuNP-HSA (3:1) and CM-AuNP-HSA (6:1), respectively. In order to check the fluorescence contribution of CM-AuNPs, 3D fluorescence spectrum of CM-AuNPs was also studied and the results are shown in Figure 4.33. The 3D fluorescence spectral characteristics of the above samples are summarized in Table 4.5. As evident from Figures 4.30–4.32 and Table 4.5, four peaks were observed in the 3D fluorescence spectra of HSA as well as CM-AuNP-HSA mixtures. Two of the peaks, namely, ‘a’ and ‘b’ were characterized as scattering peaks, representing the first-order Rayleigh scattering peak ($\lambda_{\text{ex}} = \lambda_{\text{em}}$) and the second-order Rayleigh scattering peak ($2\lambda_{\text{ex}} = \lambda_{\text{em}}$), respectively. These peaks were visible in all 3D fluorescence spectra including the one obtained with CM-AuNPs (Figure 4.33). On the other hand, origin of peak 1 ($\lambda_{\text{ex}} = 280 \text{ nm}$; $\lambda_{\text{em}} = 338/339 \text{ nm}$) and peak 2 ($\lambda_{\text{ex}} = 230 \text{ nm}$; $\lambda_{\text{em}} = 335\text{--}338 \text{ nm}$) can be ascribed to the fluorescence spectral characteristics of aromatic fluorophores (Trp and Tyr) of the protein (Bortolotti et al., 2016). Addition of CM-AuNPs to the protein solution produced significant decrease in the fluorescence intensity of both peaks, being 23% and 22% in peak 1 and peak 2, respectively, at CM-AuNP:HSA molar ratio of 3:1 (Table 4.5). The percentage decrease in the fluorescence intensity became more pronounced (~40% and 36% decrease in peaks 1 and 2, respectively) at higher (6:1) CM-AuNP:HSA molar ratio (Table 4.5). A marginal red shift (1–3 nm) in the emission maxima of these peaks was also observed. Decrease in the fluorescence intensity along with red shift in the emission maximum usually occurs upon transferring the fluorophores (Tyr/Trp) from non-polar

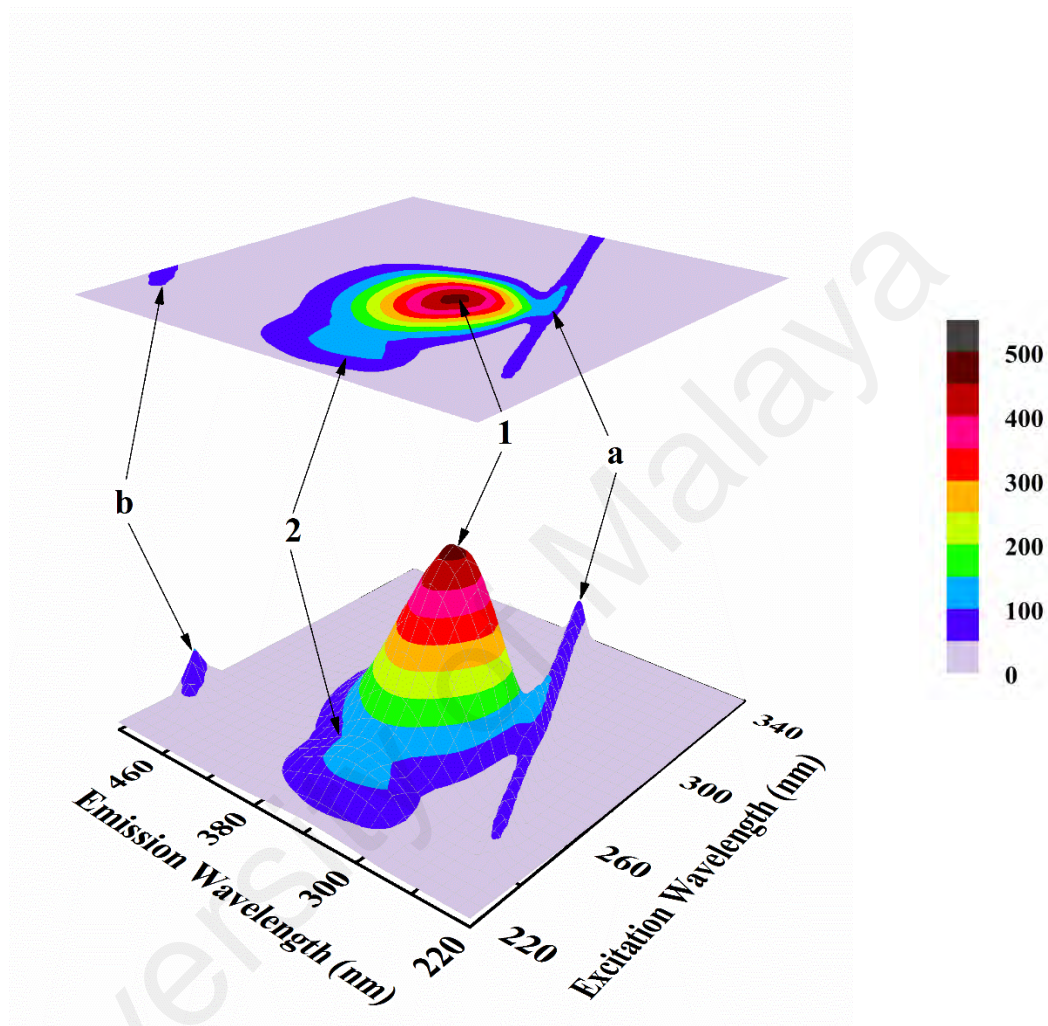


Figure 4.30: Three-dimensional fluorescence spectrum and corresponding contour map of HSA (5 μM), obtained in 60 mM sodium phosphate buffer, pH 7.4 at 25 °C.

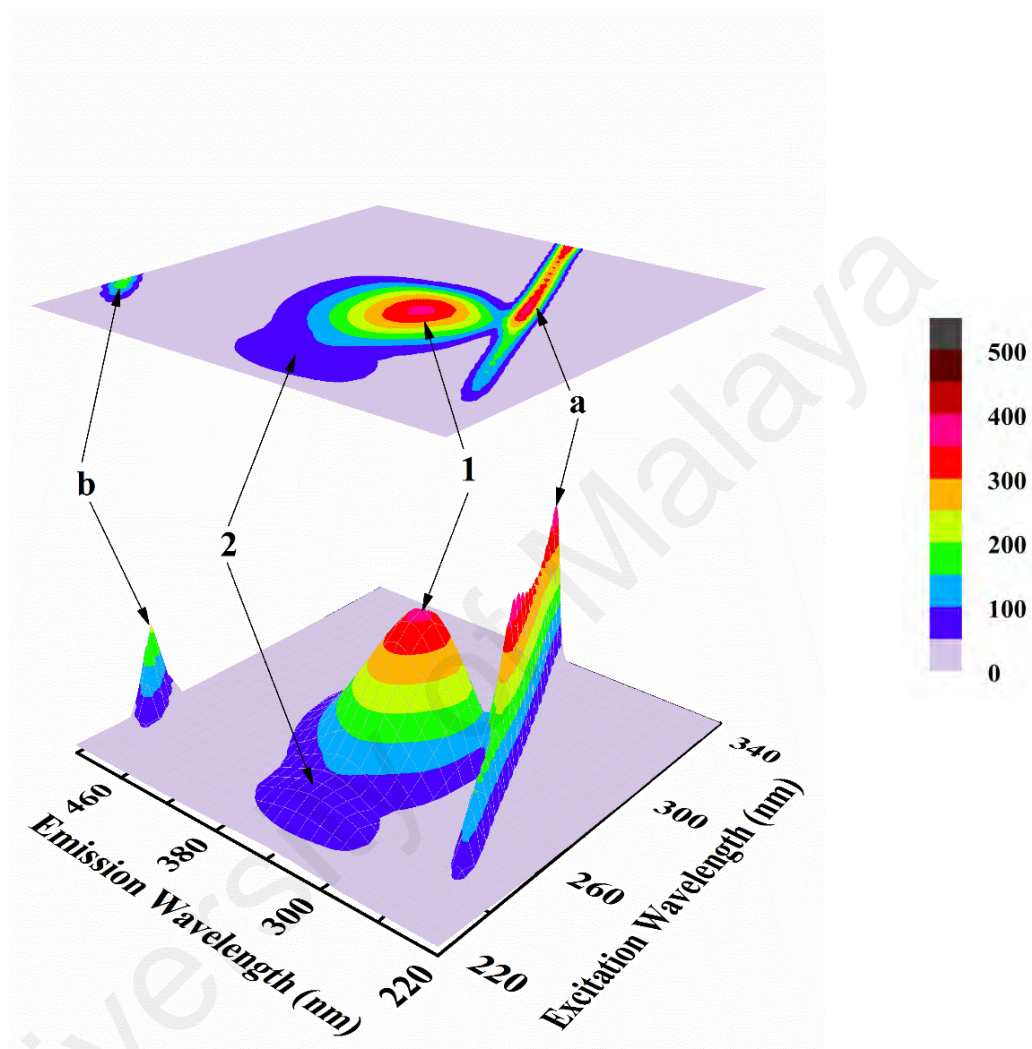


Figure 4.31: Three-dimensional fluorescence spectrum and corresponding contour map of HSA (5 μM) in the presence of CM-AuNPs (15 μM), obtained in 60 mM sodium phosphate buffer, pH 7.4 at 25 $^{\circ}\text{C}$.

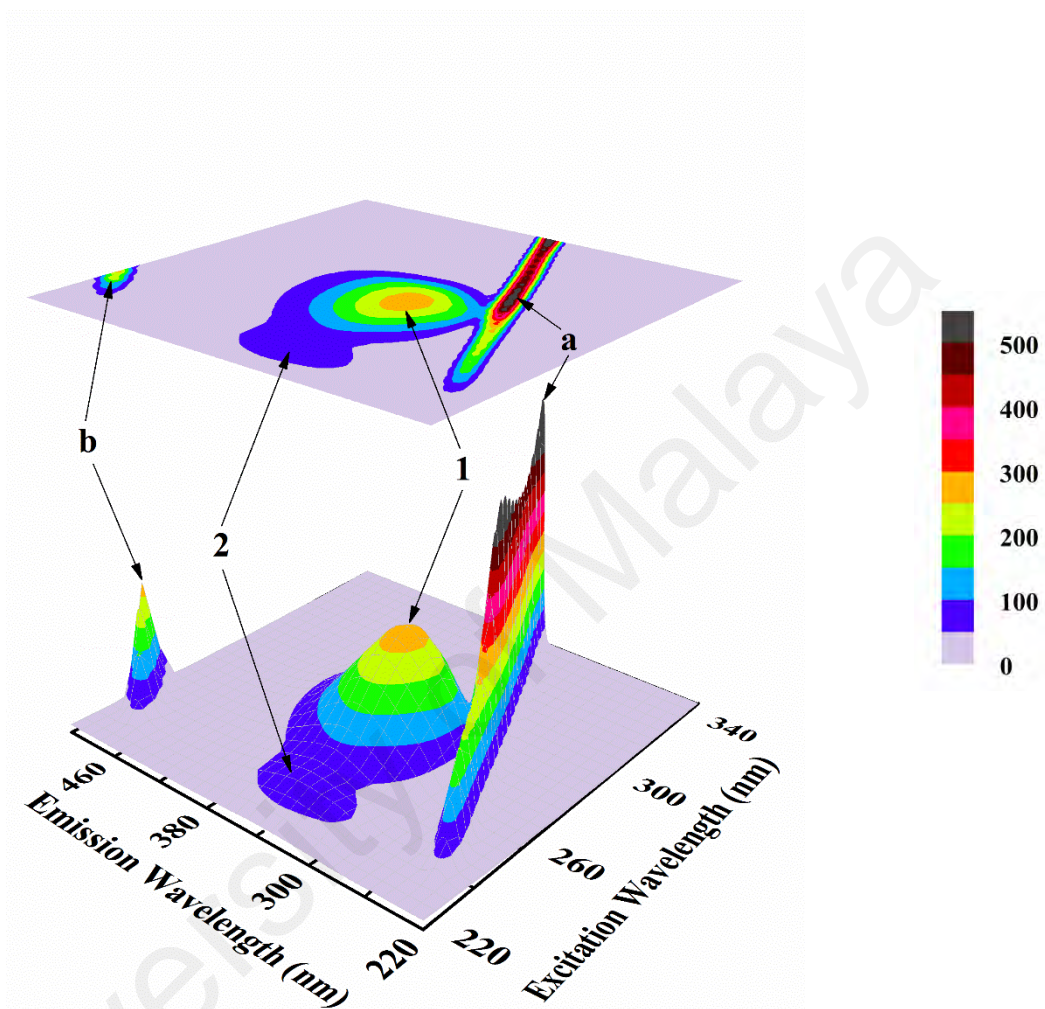


Figure 4.32: Three-dimensional fluorescence spectrum and corresponding contour map of HSA (5 μM) in the presence of CM-AuNPs (30 μM), obtained in 60 mM sodium phosphate buffer, pH 7.4 at 25 $^{\circ}\text{C}$.

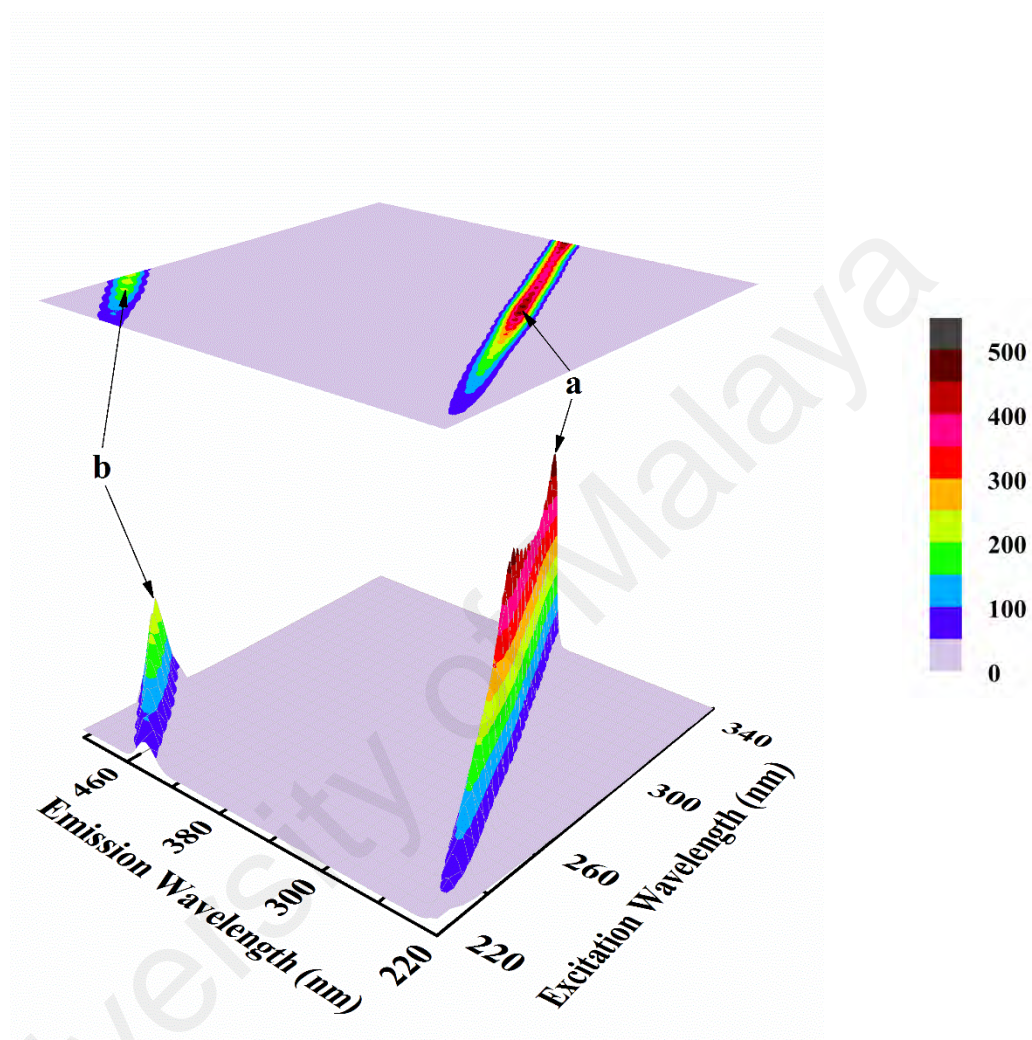


Figure 4.33: Three-dimensional fluorescence spectrum and corresponding contour map of CM-AuNPs (30 μ M), obtained in 60 mM sodium phosphate buffer, pH 7.4 at 25 $^{\circ}$ C.

Table 4.5: Three-dimensional fluorescence spectral characteristics of HSA in the absence and presence of CM-AuNPs as well as free CM-AuNPs, obtained at 25 °C.

System	Peak	Peak Position [$\lambda_{ex}/\lambda_{em}$ (nm/nm)]	Intensity
HSA (5 μ M)	a	230/230 \rightarrow 350 / 350	18.0 \rightarrow 95.5
	b	250/500	105.0
	1	280/338	470.6
	2	230/335	94.2
[CM-AuNP]:[HSA] (3:1)	a	230/230 \rightarrow 350 / 350	19.2 \rightarrow 395.8
	b	250/500	219.3
	1	280/339	363.7
	2	230/336	73.7
[CM-AuNP]:[HSA] (6:1)	a	230/230 \rightarrow 350 / 350	20.1 \rightarrow 631.4
	b	250/500	281.3
	1	280/339	282.3
	2	230/338	60.5
CM-AuNP (30 μ M)	a	230/230 \rightarrow 350 / 350	76.9 \rightarrow 636.4
	b	250/500	311.6

to polar medium (Ghisaidoobe & Chung, 2014). In view of this, presence of CM-AuNP in the mixture had led to the change in the microenvironment around Tyr and Trp residues of HSA from non-polar to polar, thus suggesting complexation between CM-AuNP and HSA.

4.4.6 Identification of CM-AuNP binding site on HSA

Site marker displacement experiments using site-specific markers, i.e., WFN and ANS were performed to characterize the binding site of HSA involved in the interaction with CM-AuNPs.

WFN binds specifically to Sudlow's site I, located in subdomain IIA of HSA (Yamasaki et al., 1996). The WFN-HSA complex produced an emission peak at 385 nm upon excitation at 335 nm (Figure 4.34A). No significant change in the fluorescence intensity at 385 nm was observed upon addition of CM-AuNPs. This can be clearly seen from Figure 4.34B, where relative fluorescence intensity at 385 nm is plotted against CM-AuNP concentration. As evident from the Figure 4.34, treatment of WFN-HSA (1:1) complex with increasing concentrations of CM-AuNPs (5–100 μ M) did not significantly affect the fluorescence signal of the WFN-HSA complex. This clearly suggested that CM-AuNP did not bind to the WFN binding site on HSA (Sudlow's site I).

Although ANS is known to bind to HSA at two independent classes of binding sites, the binding site located in subdomain IIIA has been shown to be the primary high affinity ANS binding site (Bagatolli et al., 1996), while subdomain IIA houses the binding region of two additional ANS molecules with lower affinity. The high affinity ANS binding site is also characterized as Sudlow's site II, which is a hydrophobic cavity formed by non-polar residues (Sudlow et al., 1975). Therefore, ANS in the bound form to this site produces a fluorescence signal at 470 nm, which can be markedly reduced in the presence of a competitive ligand due to ANS displacement from this site. Hence, this property was

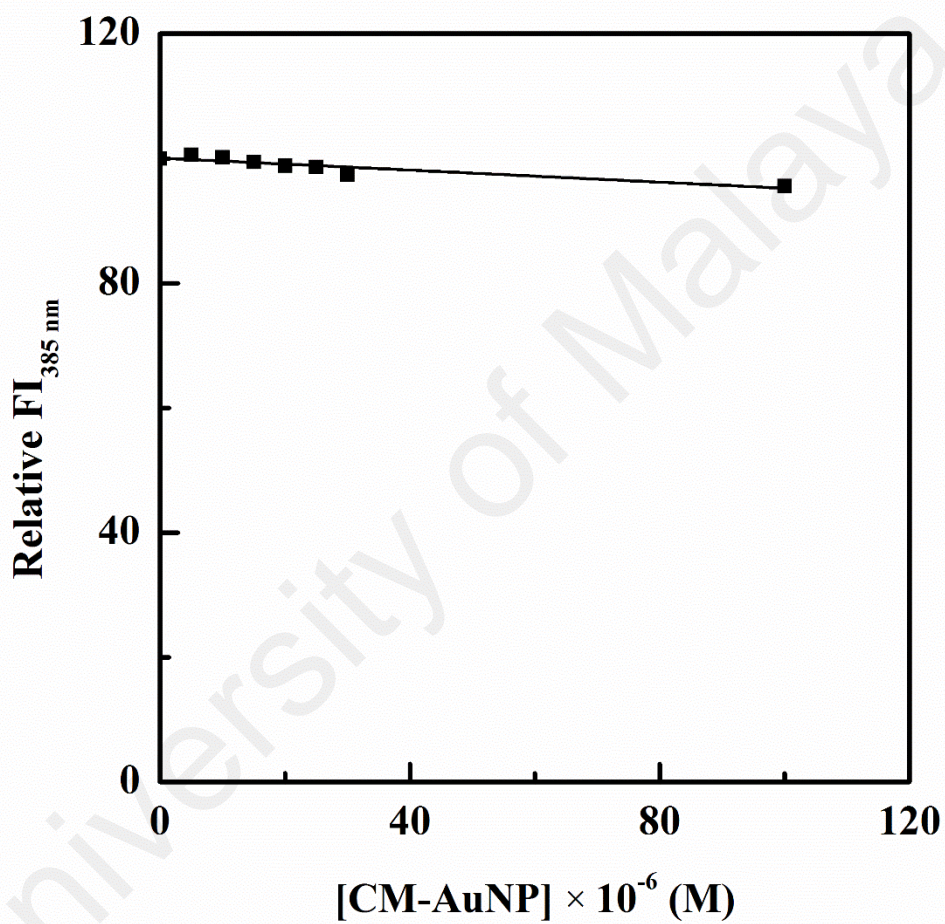


Figure 4.34: Relative fluorescence intensity at 385 nm (RFI_{385 nm}) of WFN-HSA (1:1) complex with increasing concentrations of CM-AuNPs (5–100 μM), upon excitation at 335 nm.

exploited to identify the CM-AuNP binding site on HSA. In order to probe the CM-AuNP binding site on HSA, ANS-HSA (1:1) mixture was titrated with increasing concentrations of CM-AuNPs, as described in Section 3.2.4.5. Use of 1:1 ANS:HSA molar ratio was made to saturate the high affinity ANS binding site as well as to confirm the involvement of this site in CM-AuNP complexation.

As shown in Figure 4.35, ANS-HSA complex (1:1) exhibited two emission peaks at 341 nm and 466 nm, when excited at 295 nm. Since free HSA produced an emission maximum at 341 nm (spectrum 'a'), appearance of the peak at 341 nm can be attributed to the presence of Trp residue in the protein. On the other hand, emergence of the peak at 466 nm can be characterized as ANS fluorescence peak, exhibited by protein-bound ANS molecules. This was in accordance to a previous report, showing occurrence of the ANS fluorescence signal at 460–470 nm (Holm et al., 2012; Cañaveras et al., 2012). ANS in free form shows weak emission in aqueous solution, but produces strong fluorescence signal, when bound to the hydrophobic sites in the protein (Cattoni et al., 2009). This can also be seen from the fluorescence spectrum of free ANS (spectrum 'b' of Figure 4.35). Since ANS shows absorption peaks at 270 and 350–370 nm (Hawe et al., 2010; Kuznetsova et al., 2012), ANS-HSA mixture was also excited at 350 nm. Figure 4.36 shows the fluorescence spectra of ANS-HSA complex upon excitation at 350 nm. The fluorescence spectrum shows the emission maximum at 466 nm, which was similar with the emission maximum of the second peak shown in Figure 4.35, thus confirming the appearance of peak 2 in Figure 4.35 was due to the ANS fluorescence.

As can be seen from Figures 4.35 and 4.36, ANS-HSA complex produced relatively higher fluorescence intensity at 466 nm, when excited at 295 nm compared to the fluorescence spectra obtained upon excitation at 350 nm. The observed change in the fluorescence intensity can be ascribed to the Förster resonance energy transfer, where

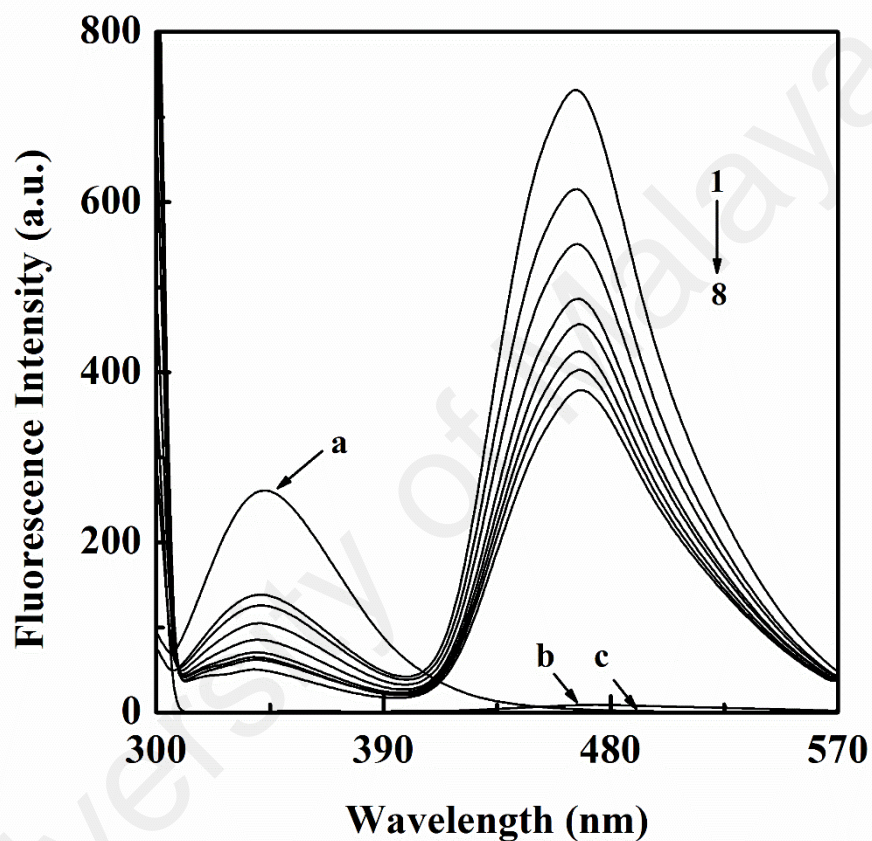


Figure 4.35: Effect of increasing CM-AuNP concentrations on the fluorescence spectrum of ANS-HSA complex. Spectrum 1 refers to the fluorescence spectrum of ANS-HSA (5 μM each) mixture, while spectra 2–8 were obtained in the presence of increasing CM-AuNP concentrations (20, 40, 60, 70, 80, 90 and 100 μM). The spectra were recorded in 60 mM sodium phosphate buffer, pH 7.4 at 25 $^{\circ}\text{C}$, upon excitation at 295 nm. Fluorescence spectra of HSA (5 μM), ANS (5 μM) and CM-AuNPs (100 μM) were also recorded under similar conditions and are represented by 'a', 'b' and 'c' respectively.

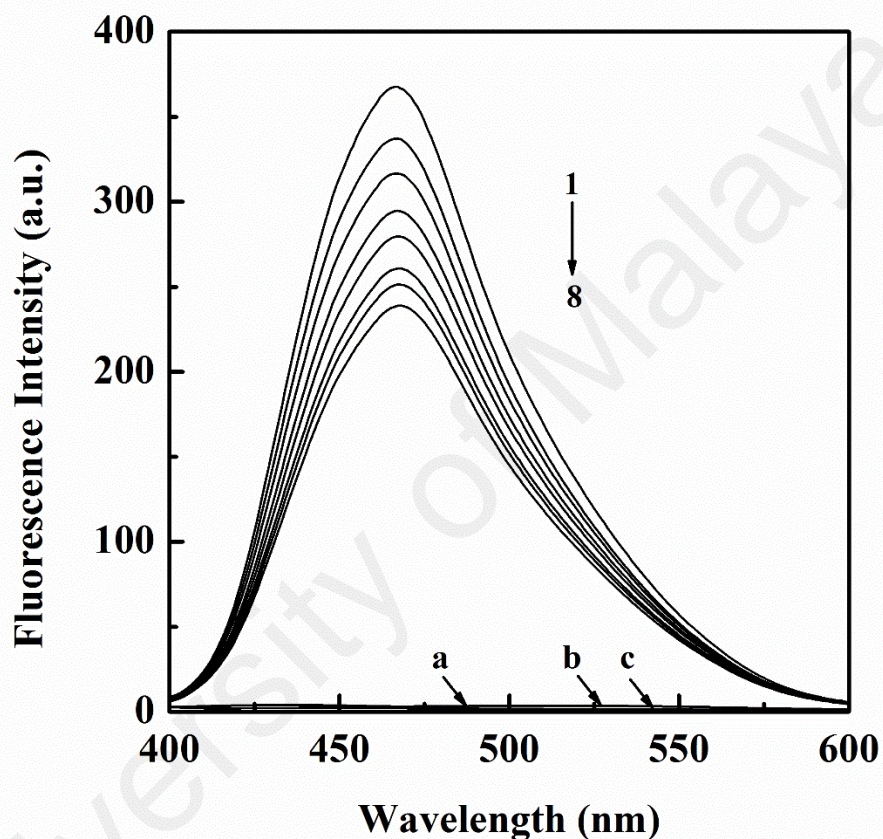


Figure 4.36: Effect of increasing CM-AuNP concentrations on the fluorescence spectrum of ANS-HSA complex. Spectrum 1 refers to the fluorescence spectrum of ANS-HSA (5 μM each) mixture, while spectra 2–8 were obtained in the presence of increasing CM-AuNP concentrations (20, 40, 60, 70, 80, 90 and 100 μM). The spectra were recorded in 60 mM sodium phosphate buffer, pH 7.4 at 25 $^{\circ}\text{C}$, upon excitation at 350 nm. Fluorescence spectra of HSA (5 μM), ANS (5 μM) and CM-AuNPs (100 μM) were also recorded under similar conditions and are represented by ‘a’, ‘b’ and ‘c’ respectively.

Trp-214 in HSA acts as a donor while the bound ANS acts as acceptor (Togashi & Ryder, 2008; Qin et al., 2014). There was more than 50% decrease in Trp emission at 341 nm (Figure 4.35), which suggested the energy transfer to bound ANS molecules, thus resulting in a higher fluorescence intensity at 466 nm. Since Trp was not excited at 350 nm, energy transfer from Trp to ANS did not occur. Hence, observed peak at 466 nm in Figure 4.36 was solely contributed by bound ANS molecules, showing relatively lesser fluorescence intensity.

Addition of increasing concentrations of CM-AuNP to ANS-HSA (1:1) mixture led to a progressive decrease in the fluorescence intensity at 466 nm, irrespective of the excitation wavelengths used (Figures 4.35 and 4.36). On the other hand, free CM-AuNP (spectrum 'c' in Figures 4.35 and 4.36) did not produce any fluorescence signal in the recorded wavelength range. Since ANS is known to bind to site II of HSA with high affinity, decrease in the ANS fluorescence intensity at 466 nm can be attributed to the displacement of ANS from site II. This clearly indicated that both CM-AuNP and ANS compete for the same binding site on HSA. Thus, binding of CM-AuNP to HSA seems to occur preferentially through Sudlow's site II. Involvement of ANS binding hydrophobic sites has also been shown in the binding of polyvinylthiol functionalized-silver NPs to HSA (Ali et al., 2015). This suggested that binding of CM-AuNP to HSA involved hydrophobic interactions, which was in good accordance to the thermodynamic data.

4.5 Photothermal effects of CM-AuNPs

Photothermal (PT) therapy is a noninvasive cancer therapy, which employs heat generated from the conversion of photon energy for destruction of cancer cells. Heating sources such as near infrared or visible light, ultrasound waves, microwaves and radiofrequency waves are commonly used to increase temperature at the targeted site

(hyperthermia) for the killing of cancer cells (Huang & El-Sayed, 2011). Cancer cells are usually found to be more sensitive to heat than normal cells due to the more hypoxic, acidic and nutrient-deficient microenvironment of tumor (Luk et al., 1980; Abadeer & Murphy, 2016). This allows selective thermal ablation of cancer cells while producing minimal effect on the normal cells in vicinity of the tumor. The ability of AuNPs to efficiently dissipate heat from the absorbed light, allows their application as a PT agent. Thus, PT heating efficiency and photocytotoxicity of CM-AuNPs to estrogen-dependent human breast cancer (MCF-7) cells were examined. In these studies, CM-AuNPs were suspended in phenol red free DMEM medium to avoid optical interference from phenol red due to the overlap of their absorption bands.

4.5.1 Photothermal properties

In order to study the PT efficiency of CM-AuNPs, DPSS laser with wavelength of 532 nm was used, as CM-AuNPs displayed a strong absorption signal at 535 nm (Figure 4.1). Photothermal heating of CM-AuNPs (20 $\mu\text{g/ml}$) irradiated with different laser intensities for different irradiation time was monitored to optimize the laser power and irradiation time suitable for PTT. Results on the temperature increase of the media upon irradiation with different laser intensities (1, 2 and 3 W/cm^2) are depicted in Figure 4.37. As can be seen from the heating curves shown in the figure, increasing the irradiation time led to a progressive increase in the temperature, which sloped off at longer irradiation time. The temperature increase was large at the first 120 s of irradiation and became smaller beyond this time. Furthermore, this effect was positively correlated with the laser intensity, showing higher temperature increase with higher laser intensity. These results were in agreement with previously published reports (Hou et al., 2015; Song et al., 2016). Laser intensity of 1 W/cm^2 increased the medium temperature by 12.7 $^\circ\text{C}$, reaching to a final value of 39.5 $^\circ\text{C}$ after 300 s of irradiation. Increase in medium temperature became more pronounced when laser of higher intensities i.e., 2 and 3 W/cm^2 were employed,

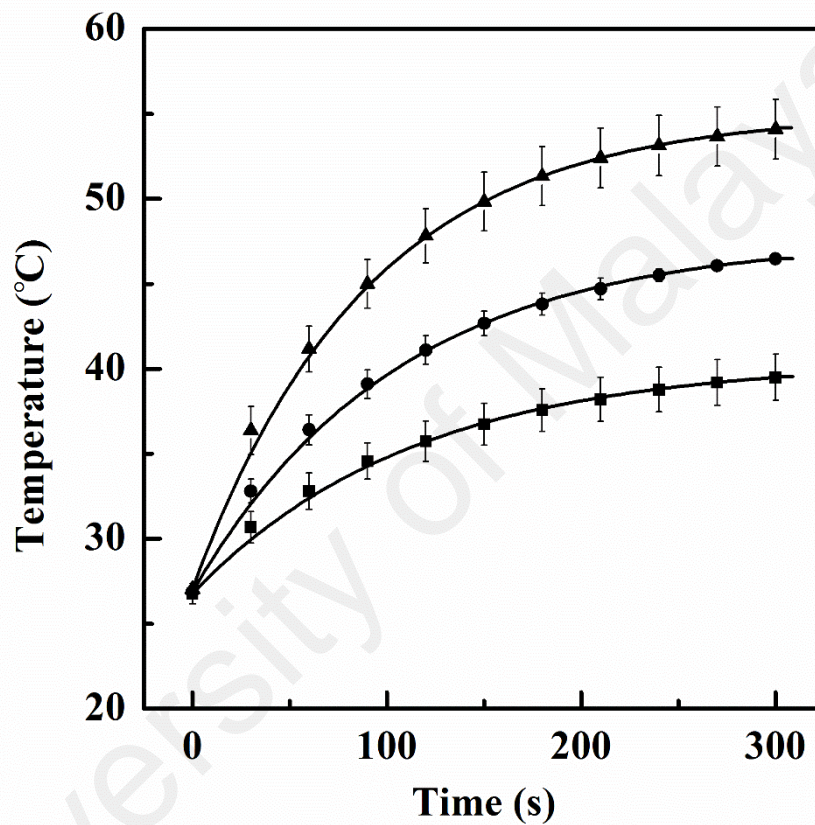


Figure 4.37: Photothermal heating curves of CM-AuNPs, suspended in DMEM media, upon laser irradiation. Different laser intensities are shown with different symbols: 1 W/cm² (■); 2 W/cm² (●) and 3 W/cm² (▲).

being 19.6 and 27.1 °C, respectively. The final medium temperature was reached to 46.5 and 54.1 °C after 300 s of irradiation upon treatment with 2 and 3 W/cm² laser intensity, respectively. It was observed that even with 120 s of irradiation time using 3 W/cm² laser intensity, the medium temperature was increased to 46.6 °C. Therefore, a laser intensity of 3 W/cm² for 120 s was selected in subsequent studies, as irradiation with a shorter time was sufficient to heat up the medium to the desired temperature. The selected laser intensity (3 W/cm²) and irradiation time (120 s) seems to be a promising choice for PTT as the temperature range, 41–48 °C is known to effectively destruct cancer cells (Bharathiraja et al., 2018). Higher temperature was not desired, as increasing thermal dose from 52 °C to 60 °C can result in cell necrosis (Song et al., 2014).

Figure 4.38 shows the heating curves of CM-AuNPs at different concentrations (5, 10 and 20 µg/ml) as well as of citrate-AuNPs (20 µg/ml) upon irradiation with 3 W/cm² laser intensity for different time periods. Results of irradiation of DMEM medium alone without AuNPs are also included as a control in Figure 4.38. As can be seen from the figure, similar trend of temperature increase with irradiation time, as shown in Figure 4.37 was observed at all concentrations of CM-AuNPs used. Furthermore, temperature increase was found to be directly correlated with CM-AuNP concentrations, being higher with higher CM-AuNP concentrations. The final medium temperature reached to a value of 41.5, 46.9 and 53.8 °C after 300 s irradiation with 5, 10 and 20 µg/ml CM-AuNP concentrations, respectively. Irradiation of the medium without AuNPs also produced a slight increase in the temperature to 38.1 °C under similar conditions. On the other hand, citrate-AuNPs of 20 µg/ml concentration was found to increase the medium temperature up to 48 °C against 53.8 °C, observed with CM-AuNPs under similar conditions. These results clearly showed that CM-AuNPs can convert the photon energy into localized heat more efficiently than citrate-AuNPs, thus would be a better PT agent compared to citrate-AuNPs. Therefore, CM-AuNPs at a concentration of 20 µg/ml were chosen for PTT

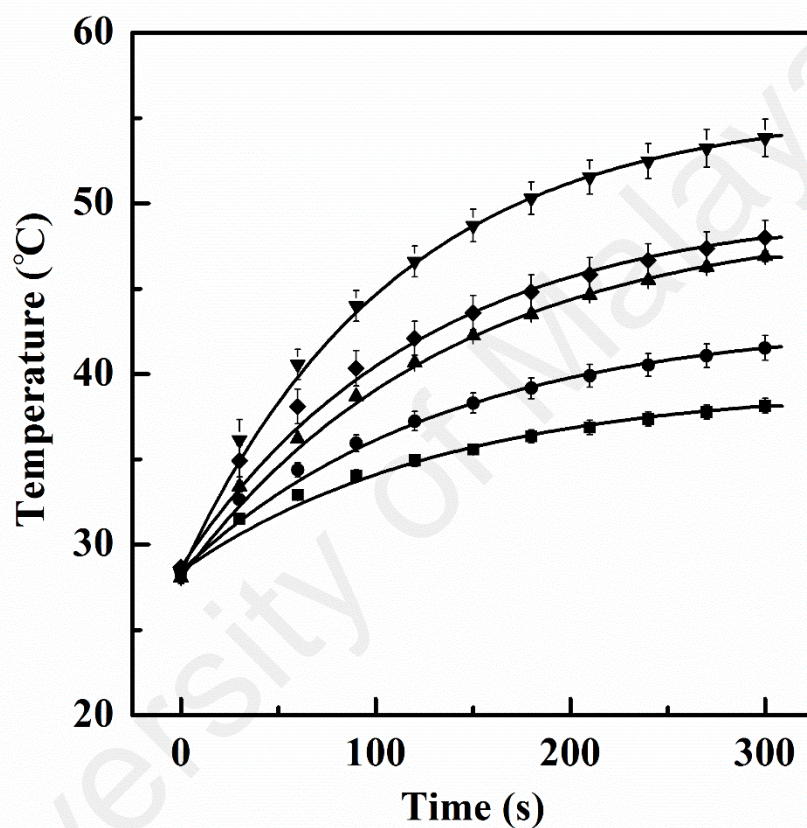


Figure 4.38: Photothermal heating curves of different concentrations of CM-AuNPs, suspended in DMEM media, upon laser irradiation at intensity of $3\text{W}/\text{cm}^2$. The concentrations of CM-AuNPs are shown with different symbols: $5\ \mu\text{g}/\text{ml}$ (●); $10\ \mu\text{g}/\text{ml}$ (▲) and $20\ \mu\text{g}/\text{ml}$ (▼). Heating curves obtained with DMEM media (■) and citrate-AuNPs (◆) are also included for comparison.

of MCF-7 cancer cells in subsequent study. This concentration of CM-AuNPs was also found to be non-toxic to normal cells (Figure 4.15 and 4.16).

4.5.2 Laser safety

Selection of laser intensity and irradiation time is important to ensure its safety as to produce minimal effects on the normal cells in the absence of AuNPs. Since laser intensity of higher than 1 W/cm^2 was required for effective heat conversion of CM-AuNPs (Figure 4.37), effect of laser at different intensities (2 and 3 W/cm^2) and irradiation time in the absence of AuNPs on cell viability was investigated. Since cancer cells have been shown to be more prone to high temperature compared to normal cells, MCF-7 cells were chosen for this investigation. Figure 4.39 shows the percentage cell viability of MCF-7 cells upon irradiation with laser intensity of 2 and 3 W/cm^2 for different time periods. Cell viability of MCF-7 remained at 100 % upon irradiation up to 180 s for both 2 and 3 W/cm^2 laser intensities. Increasing the irradiation time beyond 180 s led to a slight decrease in the viability of MCF-7 cells with both laser intensities. Since irradiation with 3 W/cm^2 laser intensity for 120 s can effectively heat up the medium with CM-AuNPs ($20 \text{ }\mu\text{g/ml}$) to $\sim 47 \text{ }^\circ\text{C}$, this irradiation condition was chosen to determine the PT cytotoxicity of CM-AuNPs on MCF-7 cells.

4.5.3 *In vitro* photothermal cytotoxicity

Photothermal therapeutic property of CM-AuNPs on MCF-7 cells was evaluated for its potential use as PT agent. Figure 4.40 shows cell viability of MCF-7 cells, as assessed by MTT assay after treatment with increasing concentrations of CM-AuNPs or citrate-AuNPs followed by photoirradiation (3 W/cm^2 for 120 s). Results of CM-AuNPs-treated cells without photoirradiation are also included in Figure 4.40 for comparison. In the absence of photoirradiation, CM-AuNPs showed $\sim 33\%$ decrease in the percentage viability of MCF-7 cells at $25 \text{ }\mu\text{g/ml}$ concentration. On the other hand, treatment of

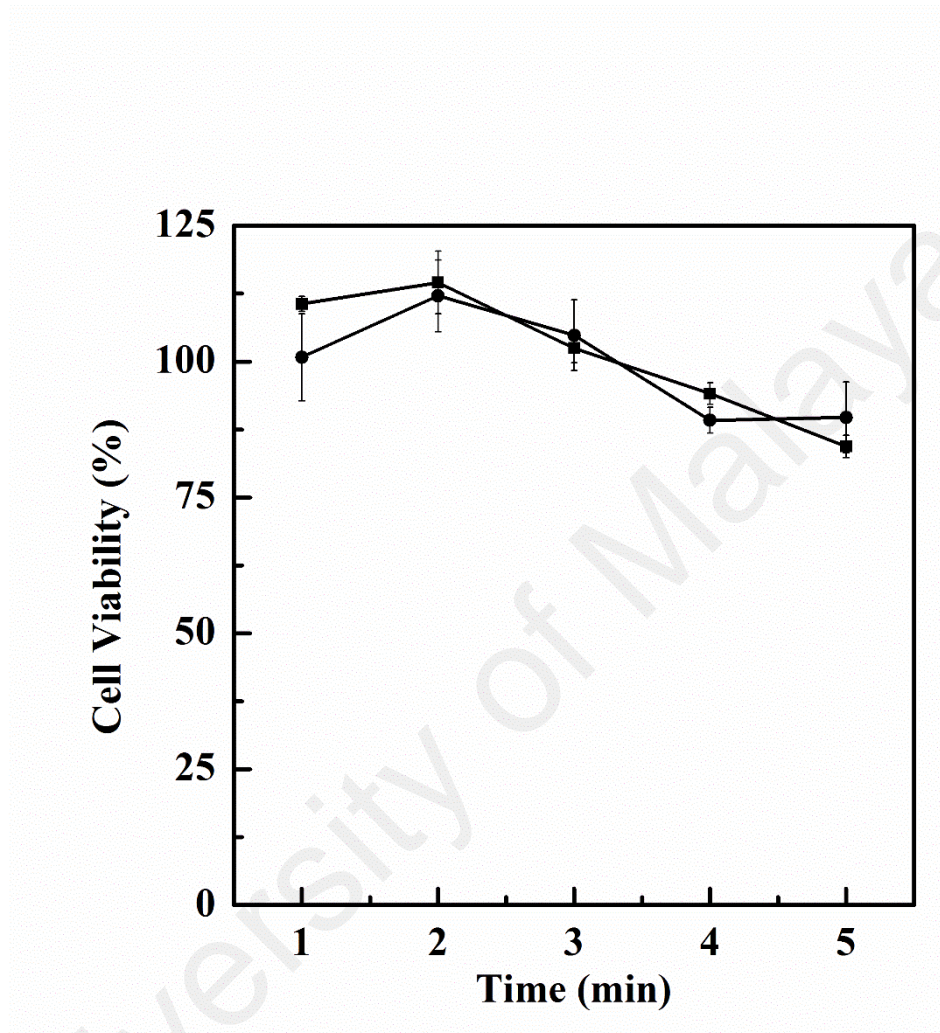


Figure 4.39: Percentage cell viability of MCF-7 cells in DMEM media, upon laser irradiation for varying time periods, as analyzed by MTT assay. Different laser intensities are shown with different symbols: $2\text{W}/\text{cm}^2$ (■) and $3\text{W}/\text{cm}^2$ (●).

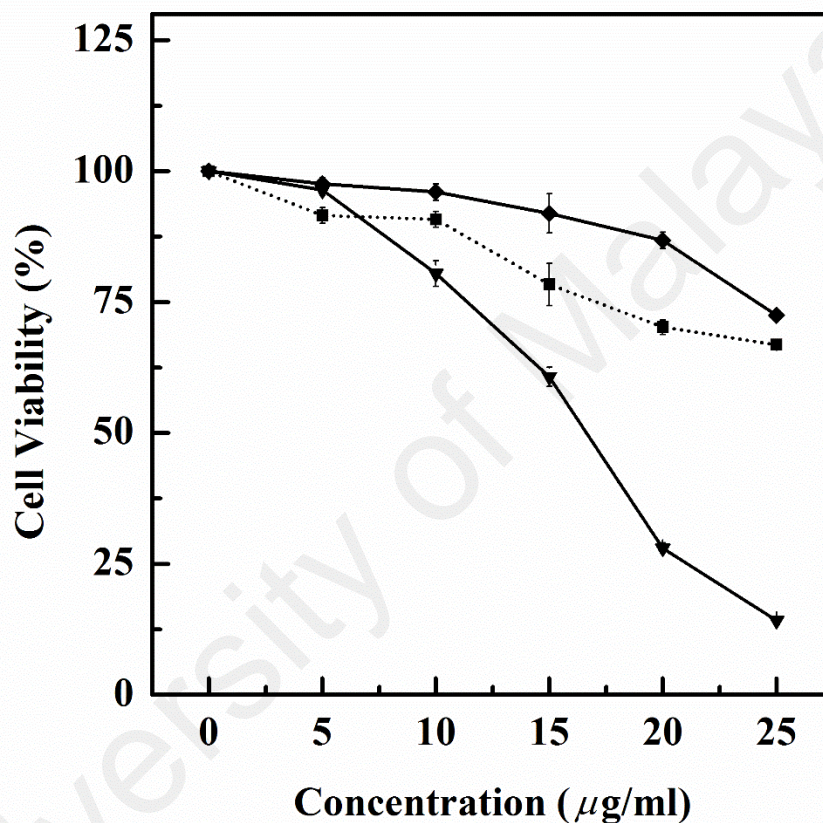


Figure 4.40: Percentage cell viability of MCF-7 cells, as analyzed by MTT assay, upon treatment with or without laser irradiation. The percentage cell viability upon laser irradiation (3 W/cm^2 for 120 s) and after treatment with increasing concentrations of nanoparticles are shown with different symbols: citrate-AuNPs (\blacklozenge) and CM-AuNPs (\blacktriangledown). The percentage cell viability after treated with increasing concentrations of CM-AuNPs for 24 h without laser irradiation ($\bullet\blacksquare$) is also included.

MCF-7 cells with increasing CM-AuNP concentrations and photoirradiation markedly reduced (~86%) the percentage cell viability to 14.2%, with an IC_{50} value of 16.5 $\mu\text{g/ml}$. These results suggested greater enhancement in cytotoxicity of CM-AuNPs upon laser irradiation. Treatment of CM-AuNPs coupled with laser irradiation can induce localized hyperthermia to kill MCF-7 cells. Such increase in the temperature may result in thermal denaturation of proteins, which may be the main factor of cell injury and cell death (Feng et al., 2015; He et al., 2004). Contrary to it, treatment of MCF-7 cells with increasing citrate-AuNPs and photoirradiation led to smaller decrease in cell viability, being 26% at 25 $\mu\text{g/ml}$ concentrations. This decrease was markedly lesser than the one observed with CM-AuNPs with photoirradiation. In view of it, CM-AuNPs were found to be a more efficient PT agent compared to citrate-AuNPs.

4.5.4 Apoptosis detection in photothermal-induced cell death

In general, cell death induced by PTT can occur via two mechanisms, i.e. apoptosis and necrosis (Pattani et al., 2015). However, necrosis is more commonly observed for *in vitro* cellular responses to PTT (Melamed et al., 2015). Apoptosis is defined as programmed cell death that attenuates inflammatory responses and is considered as a 'cleaner' pathway of cell death (Majno & Joris, 1995). Conversely, necrosis is characterized by cell swelling, followed by loss of membrane integrity, resulting in leakage of cytoplasmic components into extracellular space. Pro-inflammatory factors from the cytoplasm are released during the final step of necrosis, inducing inflammation, which can also harm surrounding tissues (Trump et al., 1997; Pattani et al., 2015). Thus, induction of apoptosis is preferred over necrosis to minimize the inflammatory responses that may promote the destruction of surrounding healthy tissues (Ali et al., 2017).

In order to detect whether the CM-AuNP-dependent PT-induced cell death of MCF-7 cells occurred through apoptosis or necrosis, FITC-annexin V / PI apoptosis assay was

performed using flow cytometry. Annexin V binds with high affinity to phosphatidylserine (PS), which is normally present in the inner leaflet of the plasma membrane. During early apoptosis, apoptotic cell loses its membrane asymmetry, exposing PS to the outer leaflet of the plasma membrane, while the membrane remains intact. On the contrary, necrotic cells lose membrane integrity, thus are permeable to vital dye such as PI. Therefore, measurement of FITC-annexin V coupled with dye exclusion test (PI staining) can be used to distinguish early apoptotic cells from necrotic cells (Vermees et al., 1995).

Figures 4.41 A and B show representative dot plots of MCF-7 cells after 24 h PTT in the presence of CM-AuNPs (20 $\mu\text{g/ml}$) and citrate-AuNPs (20 $\mu\text{g/ml}$), respectively. The dot plot of untreated MCF-7 cells (negative control) is shown in Figure 4.41 C. Cell population in the lower left quadrant (Annexin V⁻ / PI⁻) represents viable cells, since viable cells have intact membrane and absence of PS in the outer leaflet. Presence of early apoptotic cells is shown in the lower right quadrant (Annexin V⁺ / PI⁻), while late apoptotic cells or secondary necrotic cells can be seen in the upper right quadrant (Annexin V⁺ / PI⁺). Cells in the upper left quadrant (Annexin V⁻ / PI⁺) are necrotic or dead cells. Analysis of the percentage of cells in each quadrant is summarized in Figure 4.42. As can be seen from the figure, the percentage of viable MCF-7 cells decreased from 77% (negative control) to 5% and 14% upon PTT with CM-AuNP and citrate-AuNP, respectively. After 24 h of PTT with CM-AuNPs, most of the MCF-7 cells (69%) were found to be Annexin V⁺ / PI⁻, indicating early phase of apoptosis, while 25% of MCF-7 cells were in the phase of late apoptosis or secondary necrosis. Relatively lower percentage of MCF-7 cells was noticed in both early and late phases of apoptosis for the cells treated with citrate-AuNPs compared to CM-AuNPs. PTT with citrate-AuNPs also produced higher percentage (9%) of necrotic cells compared to CM-AuNPs. Presence of secondary necrotic cells in MCF-7 cells treated with either CM-AuNPs or citrate-AuNPs

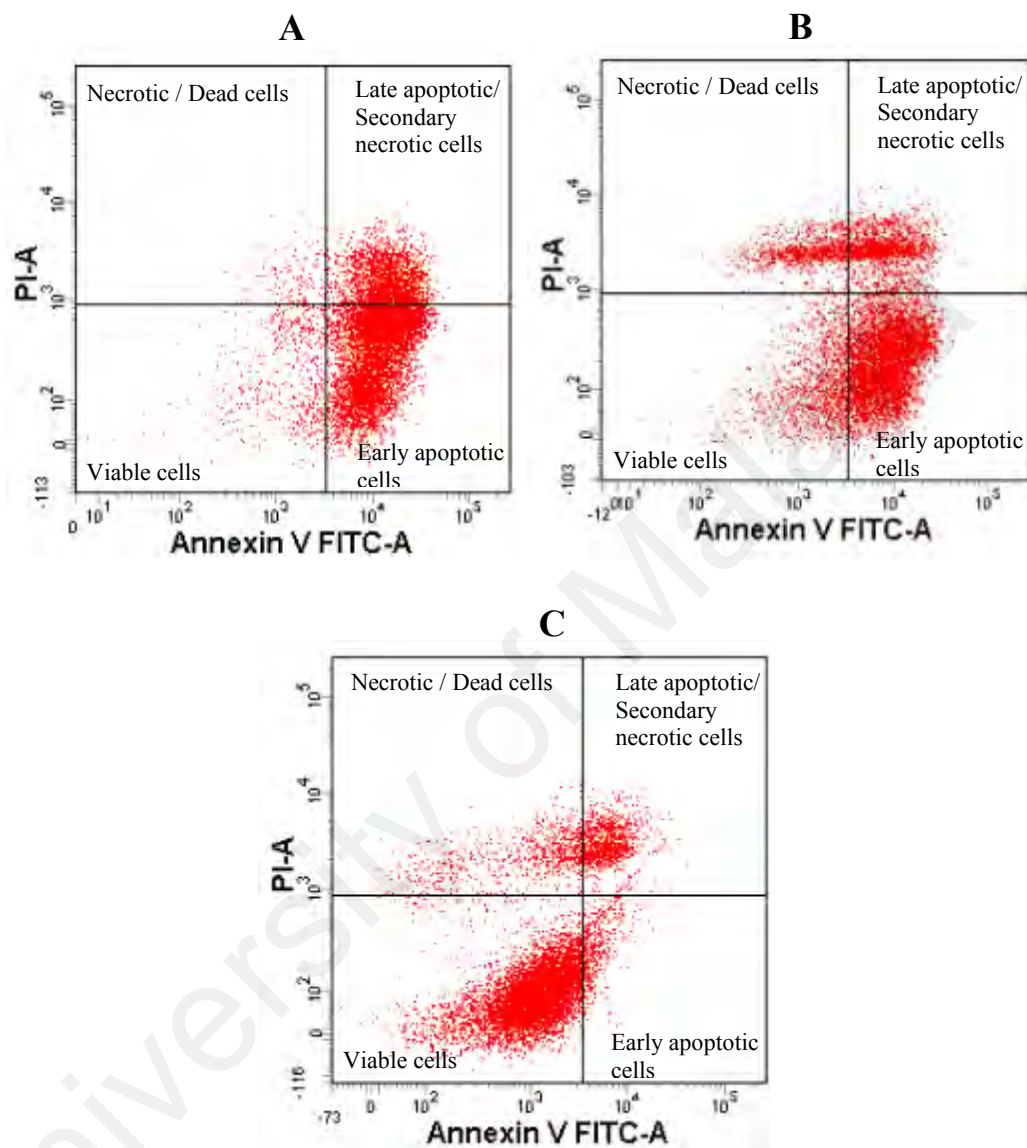


Figure 4.41: Dot plots showing flow cytometry results of Annexin V-PI apoptosis assay for MCF-7 upon photothermal treatment. The results were obtained after 24 h photothermal treatment (laser irradiation at 3 W/cm² for 120 s) with 20 μg/ml of CM-AuNPs (A) and citrate-AuNPs (B). (C) Dot plot of untreated MCF-7 cells. The cell populations are categorized based on the four quadrants on the dot plot as viable (lower left), early apoptotic (lower right), late apoptotic (upper right) and dead cells/ debris (upper left).

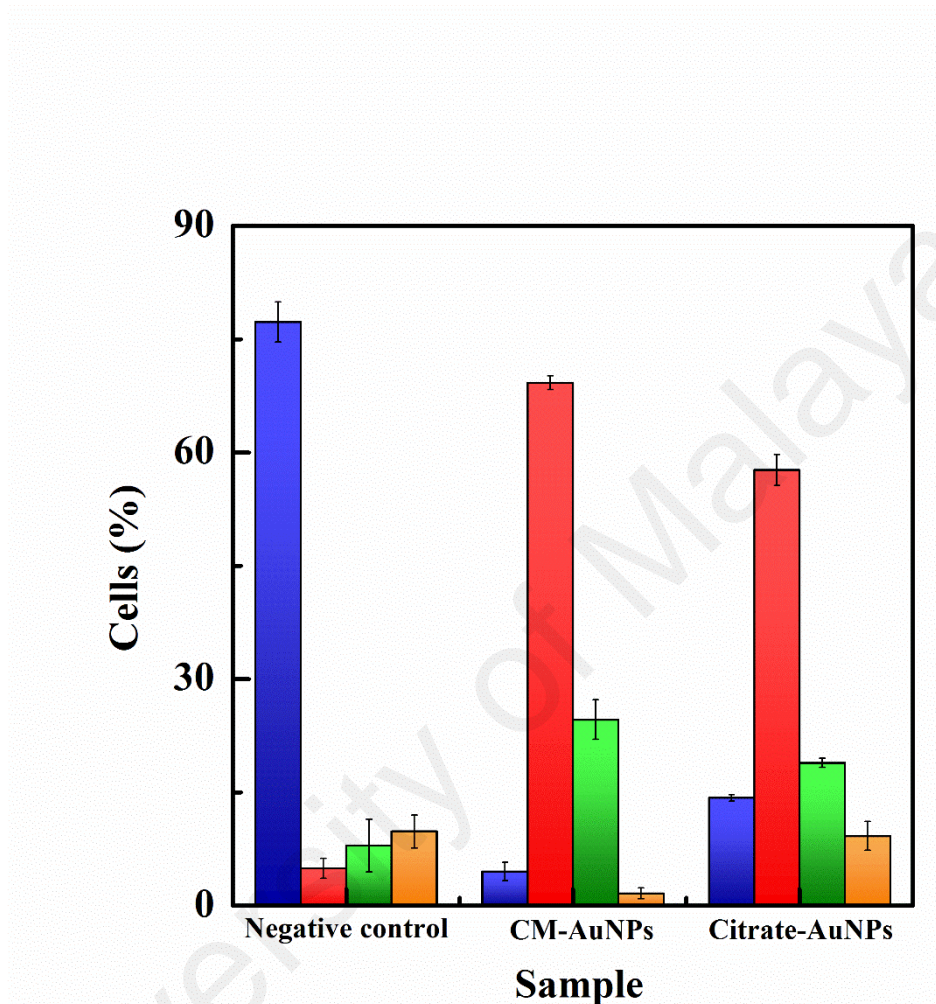


Figure 4.42: Bar diagram for analysis of the percentage of cell population in each quadrant of the dot plots, shown in Figure 4.41. Different cell populations are shown with different colours: viable (blue); early apoptotic (red); late apoptotic (green); and dead cells/ debris (orange).

can be attributed to the absence of phagocytes to remove the apoptotic cells (Melamed et al., 2015). PT-induced apoptosis upon treatment with gold nanoprisms has been reported earlier, where apoptosis was suggested to be primarily mediated by intrinsic mitochondrial pathway (Pérez-Hernández et al., 2015). In view of it, PTT with CM-AuNPs using laser (3 W/cm², 120 s) triggered cell death of MCF-7 cells through apoptosis, while PTT with citrate-AuNPs induced cell death involving both apoptotic and necrotic mechanisms. Therefore, PTT using CM-AuNPs has the advantage and can be preferred over the use of chemically synthesized AuNPs.

University of Malaya

CHAPTER 5: CONCLUSIONS AND FUTURE PERSPECTIVES

5.1 Conclusions

This study has shown a successful green synthesis of CM-AuNPs from precursor Au³⁺ ions, using CM extract as a reducing and stabilizing agent. CM-AuNPs were found to be homogeneous and spherical in shape with an average particle diameter of 15.6 nm. The reactive functional group of CM extract, responsible for reduction of Au³⁺ ions was identified as carbonyl group of terpenoids. CM-AuNPs were found to possess relatively greater stability than citrate-AuNPs in various buffers / media. Furthermore, they did not show significant cytotoxicity towards CCD-18Co and MRC-5 cells up to 25 µg/ml. They were also found to be blood compatible, showing <10% hemolysis and absence of RBCs aggregation up to 50 µg/ml. CM-AuNPs showed moderate binding affinity ($K_a = 0.97 \times 10^4 \text{ M}^{-1}$ at 25°C) towards HSA, involving hydrophobic interactions as the major force in the CM-AuNPs-HSA complexation. It binds specifically to Sudlow's site II, located in subdomain IIIA of HSA and this binding leads to microenvironmental changes around protein fluorophores as well as tertiary structural change. Photothermal heating efficiency of CM-AuNPs was evident from the heating curves and photothermal treatment with CM-AuNPs have been found to effectively reduce the percentage viability of MCF-7 cells through apoptosis. In view of the above results, CM-AuNPs have great potential to be used as photothermal agent for cancer treatment.

5.2 Future perspectives

Photothermal treatment of CM-AuNPs irradiated with visible light can be applied for treatment of shallow tumors, such as skin and breast cancers as well as cancer in transparent organ (e.g. eye). However, visible light has lower tissue penetration depth, which limited its application in cancer therapy. Photothermal treatment using NIR light for treatment of deep-seeded tumors are preferred due to deeper penetration of NIR light into fluids and tissues (Mendes et al., 2017). Since optical properties of AuNP are tunable

by changing its size, shape or structure, SPR band of CM-AuNPs can be tuned to NIR region for PTT using NIR light.

In addition, CM-AuNPs are capable to be further developed as multifunctional NPs for theranostic purpose. Owing to high X-ray absorption of AuNPs, CM-AuNPs can be a potential contrast agent for CT imaging. This could be useful for monitoring *in vivo* distribution of NPs and detecting local and metastasized cancer as well as imaging-guided PTT. The possibility of conjugation of targeting moieties to CM-AuNP can provide active targeting property to improve their selectivity and efficacy. Different targeting moieties, such as folic acid, aptamer and targeting peptide can be conjugated to specifically target different type of cancers (Zhou et al., 2016; Shi et al., 2014; Wang et al., 2015). For example, anti-human epidermal growth factor receptor 2 (HER2) antibody can be conjugated to AuNPs to specifically target HER2 overexpressing breast cancer cells (Mu et al., 2015). In addition, synthetic oligodeoxynucleotides containing unmethylated cytosine-phosphate-guanine conjugated to gold nanoparticles have been used for cancer immunotherapy to enhance macrophage stimulation and inhibit tumor growth (Lin et al., 2013). Gold based-nanovaccines have also been synthesized by conjugation of tumor-associated antigens (TAA) or TAA-derived peptides with gold nanoparticles, which can stimulate antitumor response by inducing activation and maturation of dendritic cells (Lin et al., 2013). Besides, photosensitizers or chemotherapeutic drugs can also be loaded to CM-AuNPs for combinational therapy of PTT with PDT or chemotherapy.

Despite the positive outcomes obtained from this study, *in vivo* study using animal models is necessary before these CM-AuNPs can be used for clinical applications. *In vivo* study is important to provide more information on the distribution of CM-AuNPs as well as toxicity profile and efficacy of these CM-AuNPs.

REFERENCES

- Abadeer, N. S., & Murphy, C. J. (2016). Recent progress in cancer thermal therapy using gold nanoparticles. *The Journal of Physical Chemistry C*, *120*(9), 4691-4716.
- Abdelhalim, M. A. K., Mady, M. M., & Ghannam, M. M. (2012). Physical properties of different gold nanoparticles: Ultraviolet-visible and fluorescence measurements. *Journal of Nanomedicine Nanotechnology*, *3*(3), 178-194.
- Abou-Zied, O. K., & Al-Shihi, O. I. K. (2008). Characterization of subdomain IIA binding site of human serum albumin in its native, unfolded, and refolded states using small molecular probes. *Journal of the American Chemical Society*, *130*(32), 10793-10801.
- Aghili, Z., Taheri, S., Zeinabad, H. A., Pishkar, L., Saboury, A. A., Rahimi, A., & Falahati, M. (2016). Investigating the interaction of Fe nanoparticles with lysozyme by biophysical and molecular docking studies. *PLoS ONE*, *11*(10), e0164878.
- Ahmad, T., Bustam, M. A., Irfan, M., Moniruzzaman, M., Asghar, H. M. A., & Bhattacharjee, S. (2018). Green synthesis of stabilized spherical shaped gold nanoparticles using novel aqueous *Elaeis guineensis* (oil palm) leaves extract. *Journal of Molecular Structure*, *1159*, 167-173.
- Ahmadi, T. S., Logunov, S. L., & El-Sayed, M. A. (1996). Picosecond dynamics of colloidal gold nanoparticles. *The Journal of Physical Chemistry*, *100*(20), 8053-8056.
- Ahmed, N., Fessi, H., & Elaissari, A. (2012). Theranostic applications of nanoparticles in cancer. *Drug Discovery Today*, *17*(17), 928-934.
- Alexandridis, P., & Tsianou, M. (2011). Block copolymer-directed metal nanoparticle morphogenesis and organization. *European Polymer Journal*, *47*(4), 569-583.
- Ali, M., Kumar, A., Kumar, M., & Pandey, B. N. (2016). The interaction of human serum albumin with selected lanthanide and actinide ions: Binding affinities, protein unfolding and conformational changes. *Biochimie*, *123*, 117-129.
- Ali, M. R. K., Rahman, M. A., Wu, Y., Han, T., Peng, X., Mackey, M. A., . . . El-Sayed, M. A. (2017). Efficacy, long-term toxicity, and mechanistic studies of gold nanorods photothermal therapy of cancer in xenograft mice. *Proceedings of the National Academy of Sciences*, *114*(15), E3110.
- Ali, M. S., Al-Lohedan, H. A., Atta, A. M., Ezzat, A. O., & Al-Hussain, S. A. A. (2015). Interaction of human serum albumin with silver nanoparticles functionalized with polyvinylthiol. *Journal of Molecular Liquids*, *204*, 248-254.
- Alinejad, Z., Khakzad, F., & Mahdavian, A. R. (2018). Efficient approach to *in-situ* preparation of anisotropic and assemblable gold nanoparticles mediated by stimuli-responsive PDMAEMA. *European Polymer Journal*, *104*, 106-114.

- Alkilany, A. M., & Murphy, C. J. (2010). Toxicity and cellular uptake of gold nanoparticles: What we have learned so far? *Journal of Nanoparticle Research*, *12*(7), 2313-2333.
- Alkilany, A. M., Nagaria, P. K., Hexel, C. R., Shaw, T. J., Murphy, C. J., & Wyatt, M. D. (2009). Cellular uptake and cytotoxicity of gold nanorods: Molecular origin of cytotoxicity and surface effects. *Small*, *5*(6), 701-708.
- Amin, M., Anwar, F., Janjua, M. R. S. A., Iqbal, M. A., & Rashid, U. (2012). Green synthesis of silver nanoparticles through reduction with *Solanum xanthocarpum* L. berry extract: Characterization, antimicrobial and urease inhibitory activities against *Helicobacter pylori*. *International Journal of Molecular Sciences*, *13*(8), 9923-9941.
- Amoresano, A., Andolfo, A., Siciliano, R. A., Cozzolino, R., Minchiotti, L., Galliano, M., & Pucci, P. (1998). Analysis of human serum albumin variants by mass spectrometric procedures. *Biochimica et Biophysica Acta-Protein Structure and Molecular Enzymology*, *1384*(1), 79-92.
- Amroabadi, M. K., Taheri-Kafrani, A., Saremi, L. H., & Rastegari, A. A. (2018). Spectroscopic studies of the interaction between alprazolam and apo-human serum transferrin as a drug carrier protein. *International Journal of Biological Macromolecules*, *108*, 263-271.
- Anselmo, A. C., & Mitragotri, S. (2015). A review of clinical translation of inorganic nanoparticles. *The AAPS Journal*, *17*(5), 1041-1054.
- Aromal, S. A., & Philip, D. (2012). Green synthesis of gold nanoparticles using *Trigonella foenum-graecum* and its size-dependent catalytic activity. *Spectrochimica Acta Part A: Molecular and Biomolecular Spectroscopy*, *97*, 1-5.
- Avramis, V. I., & Tiwari, P. N. (2006). Asparaginase (native ASNase or pegylated ASNase) in the treatment of acute lymphoblastic leukemia. *International Journal of Nanomedicine*, *1*(3), 241-254.
- Ayala-Orozco, C., Urban, C., Knight, M. W., Urban, A. S., Neumann, O., Bishnoi, S. W., . . . Joshi, A. (2014). Au nanomatryoshkas as efficient near-infrared photothermal transducers for cancer treatment: Benchmarking against nanoshells. *ACS Nano*, *8*(6), 6372-6381.
- Aziz, M. A., Kim, J. P., & Oyama, M. (2014). Preparation of monodispersed carboxylate-functionalized gold nanoparticles using pamoic acid as a reducing and capping reagent. *Gold Bulletin*, *47*(1-2), 127-132.
- Bagatolli, L. A., Kivatinitz, S. C., Aguilar, F., Soto, M. A., Sotomayor, P., & Fidelio, G. D. (1996). Two distinguishable fluorescent modes of 1-anilino-8-naphthalenesulfonate bound to human albumin. *Journal of Fluorescence*, *6*(1), 33-40.
- Baker, S., & Satish, S. (2015). Biosynthesis of gold nanoparticles by *Pseudomonas veronii* AS41G inhabiting *Annona squamosa* L. *Spectrochimica Acta Part A: Molecular and Biomolecular Spectroscopy*, *150*, 691-695.

- Bao, C., Nicolas, B., Pablo, d. P., Beatriz, P., Giovani, E., Tian, F., . . . Cui, D. (2013). Gold nanoprisms as optoacoustic signal nanoamplifiers for *in vivo* bioimaging of gastrointestinal cancers. *Small*, 9(1), 68-74.
- Basha, S. K., Govindaraju, K., Manikandan, R., Ahn, J. S., Bae, E. Y., & Singaravelu, G. (2010). Phytochemical mediated gold nanoparticles and their PTP 1B inhibitory activity. *Colloids and Surfaces B: Biointerfaces*, 75(2), 405-409.
- Bennet, C., Rajini, N., Jappes, J. T. W., Siva, I., Sreenivasan, V. S., & Amico, S. C. (2015). Effect of the stacking sequence on vibrational behavior of *Sansevieria cylindrica*/coconut sheath polyester hybrid composites. *Journal of Reinforced Plastics and Composites*, 34(4), 293-306.
- Bharathiraja, S., Bui, N. Q., Manivasagan, P., Moorthy, M. S., Mondal, S., Seo, H., . . . Oh, J. (2018). Multimodal tumor-homing chitosan oligosaccharide-coated biocompatible palladium nanoparticles for photo-based imaging and therapy. *Scientific Reports*, 8(1), 500.
- Bhat, R., Sharanabasava, V. G., Deshpande, R., Shetti, U., Sanjeev, G., & Venkataraman, A. (2013). Photo-bio-synthesis of irregular shaped functionalized gold nanoparticles using edible mushroom *Pleurotus florida* and its anticancer evaluation. *Journal of Photochemistry and Photobiology B: Biology*, 125, 63-69.
- Bhatia, S. (2016). Nanoparticles types, classification, characterization, fabrication methods and drug delivery applications. In *Natural polymer drug delivery systems* (pp. 33-93). Switzerland: Springer.
- Bhogale, A., Patel, N., Mariam, J., Dongre, P. M., Miotello, A., & Kothari, D. C. (2014). Comprehensive studies on the interaction of copper nanoparticles with bovine serum albumin using various spectroscopies. *Colloids and Surfaces B: Biointerfaces*, 113, 276-284.
- Bi, S., Ding, L., Tian, Y., Song, D., Zhou, X., Liu, X., & Zhang, H. (2004). Investigation of the interaction between flavonoids and human serum albumin. *Journal of Molecular Structure*, 703(1), 37-45.
- Blanco, E., Shen, H., & Ferrari, M. (2015). Principles of nanoparticle design for overcoming biological barriers to drug delivery. *Nature Biotechnology*, 33(9), 941-951.
- Bortolotti, A., Wong, Y. H., Korsholm, S. S., Bahring, N. H. B., Bobone, S., Tayyab, S., . . . Stella, L. (2016). On the purported "backbone fluorescence" in protein three-dimensional fluorescence spectra. *RSC Advances*, 6(114), 112870-112876.
- Boulos, S. P., Davis, T. A., Yang, J. A., Lohse, S. E., Alkilany, A. M., Holland, L. A., & Murphy, C. J. (2013). Nanoparticle-protein interactions: A thermodynamic and kinetic study of the adsorption of bovine serum albumin to gold nanoparticle surfaces. *Langmuir*, 29(48), 14984-14996.
- Bozich, J. S., Lohse, S. E., Torelli, M. D., Murphy, C. J., Hamers, R. J., & Klaper, R. D. (2014). Surface chemistry, charge and ligand type impact the toxicity of gold nanoparticles to *Daphnia magna*. *Environmental Science: Nano*, 1(3), 260-270.

- Brannon-Peppas, L., & Blanchette, J. O. (2004). Nanoparticle and targeted systems for cancer therapy. *Advanced Drug Delivery Reviews*, 56(11), 1649-1659.
- Brown, K. R., Fox, A. P., & Natan, M. J. (1996). Morphology-dependent electrochemistry of cytochrome c at Au colloid-modified SnO₂ electrodes. *Journal of the American Chemical Society*, 118(5), 1154-1157.
- Brunmark, P., Harriman, S., Skipper, P. L., Wishnok, J. S., Amin, S., & Tannenbaum, S. R. (1997). Identification of subdomain IB in human serum albumin as a major binding site for polycyclic aromatic hydrocarbon epoxides. *Chemical Research in Toxicology*, 10(8), 880-886.
- Cañaveras, F., Madueño, R., Sevilla, J. M., Blázquez, M., & Pineda, T. (2012). Role of the functionalization of the gold nanoparticle surface on the formation of bioconjugates with human serum albumin. *The Journal of Physical Chemistry C*, 116(18), 10430-10437.
- Caracciolo, G., Callipo, L., De Sanctis, S. C., Cavaliere, C., Pozzi, D., & Laganà, A. (2010). Surface adsorption of protein corona controls the cell internalization mechanism of DC-Chol-DOPE/DNA lipoplexes in serum. *Biochimica et Biophysica Acta (BBA) - Biomembranes*, 1798(3), 536-543.
- Carter, D. C., & Ho, J. X. (1994). Structure of serum albumin. In C. B. Anfinsen, J. T. Edsall, F. M. Richards & D. S. Eisenberg (Eds.), *Advances in protein chemistry* (pp. 153-203). New York: Academic Press.
- Castro-Longoria, E., Vilchis-Nestor, A. R., & Avalos-Borja, M. (2011). Biosynthesis of silver, gold and bimetallic nanoparticles using the filamentous fungus *Neurospora crassa*. *Colloids and Surfaces B: Biointerfaces*, 83(1), 42-48.
- Cattoni, D. I., Kaufman, S. B., & Flecha, F. L. G. (2009). Kinetics and thermodynamics of the interaction of 1-anilino-naphthalene-8-sulfonate with proteins. *Biochimica et Biophysica Acta-Proteins and Proteomics*, 1794(11), 1700-1708.
- Cheheltani, R., Ezzibdeh, R. M., Chhour, P., Pulaparthy, K., Kim, J., Jurcova, M., . . . Cormode, D. P. (2016). Tunable, biodegradable gold nanoparticles as contrast agents for computed tomography and photoacoustic imaging. *Biomaterials*, 102, 87-97.
- Chen, C. H., Wu, Y.-J., & Chen, J.-J. (2015). Gold nanotheranostics: Photothermal therapy and imaging of mucin 7 conjugated antibody nanoparticles for urothelial cancer. *BioMed Research International*, 2015, 8.
- Chen, H., Li, B., Ren, X., Li, S., Ma, Y., Cui, S., & Gu, Y. (2012). Multifunctional near-infrared-emitting nano-conjugates based on gold clusters for tumor imaging and therapy. *Biomaterials*, 33(33), 8461-8476.
- Chen, J., Saeki, F., Wiley, B. J., Cang, H., Cobb, M. J., Li, Z.-Y., . . . Xia, Y. (2005). Gold nanocages: Bioconjugation and their potential use as optical imaging contrast agents. *Nano Letters*, 5(3), 473-477.

- Chen, M., He, Y., Liu, X., Zhu, J., & Liu, R. (2017). Synthesis and optical properties of size-controlled gold nanoparticles. *Powder Technology*, *311*, 25-33.
- Chen, Q., Li, K., Wen, S., Liu, H., Peng, C., Cai, H., . . . Shi, X. (2013). Targeted CT/MR dual mode imaging of tumors using multifunctional dendrimer-entrapped gold nanoparticles. *Biomaterials*, *34*(21), 5200-5209.
- Chen, W., Ayala-Orozco, C., Biswal, N. C., Perez-Torres, C., Bartels, M., Bardhan, R., . . . Joshi, A. (2014). Targeting of pancreatic cancer with magneto-fluorescent theranostic gold nanoshells. *Nanomedicine*, *9*(8), 1209-1222.
- Chen, W. H., Yang, C. X., Qiu, W. X., Luo, G. F., Jia, H. Z., Lei, Q., . . . Zhang, X. Z. (2015). Multifunctional theranostic nanoplatform for cancer combined therapy based on gold nanorods. *Advanced Healthcare Materials*, *4*(15), 2247-2259.
- Chen, Y. H., Yang, J. T., & Martinez, H. M. (1972). Determination of the secondary structures of proteins by circular dichroism and optical rotatory dispersion. *Biochemistry*, *11*(22), 4120-4131.
- Cheng, B., He, H., Huang, T., Berr, S. S., He, J., Fan, D., . . . Xu, P. (2016). Gold nanosphere gated mesoporous silica nanoparticle responsive to near-infrared light and redox potential as a theranostic platform for cancer therapy. *Journal of Biomedical Nanotechnology*, *12*(3), 435-449.
- Cheng, K., Kothapalli, S. R., Liu, H., Koh, A. L., Jokerst, J. V., Jiang, H., . . . Cheng, Z. (2014). Construction and validation of nano gold tripods for molecular imaging of living subjects. *Journal of the American Chemical Society*, *136*(9), 3560-3571.
- Cheng, Y., Dai, Q., Morshed, R., Fan, X., Wegscheid, M. L., Wainwright, D. A., . . . Lesniak, M. S. (2014). Blood-brain barrier permeable gold nanoparticles: An efficient delivery platform for enhanced malignant glioma therapy and imaging. *Small*, *10*(24), 5137-5150.
- Choi, H. S., Liu, W., Misra, P., Tanaka, E., Zimmer, J. P., Iyengar, B., . . . Frangioni, J. V. (2007). Renal clearance of quantum dots. *Nature Biotechnology*, *25*(10), 1165-1170.
- Choi, J., Yang, J., Bang, D., Park, J., Suh, J. S., Huh, Y. M., & Haam, S. (2012). Targetable gold nanorods for epithelial cancer therapy guided by near-IR absorption imaging. *Small*, *8*(5), 746-753.
- Ciccolini, J., Serdjebi, C., Peters, G. J., & Giovannetti, E. (2016). Pharmacokinetics and pharmacogenetics of gemcitabine as a mainstay in adult and pediatric oncology: An EORTC-PAMM perspective. *Cancer Chemotherapy and Pharmacology*, *78*(1), 1-12.
- Corbierre, M. K., Cameron, N. S., & Lennox, R. B. (2004). Polymer-stabilized gold nanoparticles with high grafting densities. *Langmuir*, *20*(7), 2867-2873.
- Coughlin, A. J., Ananta, J. S., Deng, N., Larina, I. V., Decuzzi, P., & West, J. L. (2014). Gadolinium-conjugated gold nanoshells for multimodal diagnostic imaging and photothermal cancer therapy. *Small*, *10*(3), 556-565.

- Croissant, J. G., Zhang, D., Alsaïari, S., Lu, J., Deng, L., Tamanoi, F., . . . Khashab, N. M. (2016). Protein-gold clusters-capped mesoporous silica nanoparticles for high drug loading, autonomous gemcitabine/doxorubicin co-delivery, and *in-vivo* tumor imaging. *Journal of Controlled Release*, *229*, 183-191.
- Cukalevski, R., Lundqvist, M., Oslakovic, C., Dahlbäck, B., Linse, S., & Cedervall, T. (2011). Structural changes in apolipoproteins bound to nanoparticles. *Langmuir*, *27*(23), 14360-14369.
- Curry, S. (2009). Lessons from the crystallographic analysis of small molecule binding to human serum albumin. *Drug Metabolism and Pharmacokinetics*, *24*(4), 342-357.
- D'Hollander, A., Mathieu, E., Jans, H., Vande Velde, G., Stakenborg, T., Van Dorpe, P., . . . Lagae, L. (2016). Development of nanostars as a biocompatible tumor contrast agent: Toward *in vivo* SERS imaging. *International Journal of Nanomedicine*, *11*, 3703-3714.
- Daniel, M. C., & Astruc, D. (2004). Gold nanoparticles: Assembly, supramolecular chemistry, quantum-size-related properties, and applications toward biology, catalysis, and nanotechnology. *Chemical Reviews*, *104*(1), 293-346.
- Du, S., Kendall, K., Toloueinia, P., Mehrabadi, Y., Gupta, G., & Newton, J. (2012). Aggregation and adhesion of gold nanoparticles in phosphate buffered saline. *Journal of Nanoparticle Research*, *14*(3), 758.
- Dugaiczuk, A., Law, S. W., & Dennison, O. E. (1982). Nucleotide sequence and the encoded amino acids of human serum albumin mRNA. *Proceedings of the National Academy of Sciences*, *79*(1), 71-75.
- Ealia, S. A. M., & Saravanakumar, M. (2017). A review on the classification, characterisation, synthesis of nanoparticles and their application. *IOP Conference Series: Materials Science and Engineering*, *263*, 032019.
- Eghtedari, M., Liopo, A. V., Copland, J. A., Oraevsky, A. A., & Motamedi, M. (2009). Engineering of hetero-functional gold nanorods for the *in vivo* molecular targeting of breast cancer cells. *Nano Letters*, *9*(1), 287-291.
- El-Sayed, I. H., Huang, X., & El-Sayed, M. A. (2005). Surface plasmon resonance scattering and absorption of anti-EGFR antibody conjugated gold nanoparticles in cancer diagnostics: Applications in oral cancer. *Nano Letters*, *5*(5), 829-834.
- El-Sayed, I. H., Huang, X., & El-Sayed, M. A. (2006). Selective laser photo-thermal therapy of epithelial carcinoma using anti-EGFR antibody conjugated gold nanoparticles. *Cancer Letters*, *239*(1), 129-135.
- Elahi, N., Kamali, M., & Baghersad, M. H. (2018). Recent biomedical applications of gold nanoparticles: A review. *Talanta*, *184*, 537-556.
- Evani, S. J., & Ramasubramanian, A. K. (2011). Hemocompatibility of nanoparticles. In B. Sitharaman (Ed.), *Nanobiomaterials handbook* (pp. 31-1 - 31-13). Boca Raton: CRC Press.

- Evans, B. C., Nelson, C. E., Shann, S. Y., Beavers, K. R., Kim, A. J., Li, H., . . . Duvall, C. L. (2013). *Ex vivo* red blood cell hemolysis assay for the evaluation of pH-responsive endosomolytic agents for cytosolic delivery of biomacromolecular drugs. *Journal of Visualized Experiments*, 73, e50166.
- Evelo, C. T. A., Spooren, A. A. M. G., Bisschops, R. A. G., Baars, L. G. M., & Neis, J. M. (1998). Two mechanisms for toxic effects of hydroxylamines in human erythrocytes: Involvement of free radicals and risk of potentiation. *Blood Cells, Molecules, and Diseases*, 24(3), 280-295.
- Fang, J., Nakamura, H., & Maeda, H. (2011). The EPR effect: Unique features of tumor blood vessels for drug delivery, factors involved, and limitations and augmentation of the effect. *Advanced Drug Delivery Reviews*, 63(3), 136-151.
- Feng, S. S., & Chien, S. (2003). Chemotherapeutic engineering: Application and further development of chemical engineering principles for chemotherapy of cancer and other diseases. *Chemical Engineering Science*, 58(18), 4087-4114.
- Feng, W., Chen, L., Qin, M., Zhou, X., Zhang, Q., Miao, Y., . . . He, C. (2015). Flower-like PEGylated MoS₂ nanoflakes for near-infrared photothermal cancer therapy. *Scientific Reports*, 5, 17422.
- Ferrer, M. L., Duchowicz, R., Carrasco, B., de la Torre, J. G., & Acuña, A. U. (2001). The conformation of serum albumin in solution: A combined phosphorescence depolarization-hydrodynamic modeling study. *Biophysical Journal*, 80(5), 2422-2430.
- Figge, J., Rossing, T., & Fencl, V. (1991). The role of serum proteins in acid-base equilibria. *The Journal of Laboratory and Clinical Medicine*, 117(6), 453-467.
- Foo, Y. Y., Periasamy, V., Kiew, L. V., Kumar, G., & Malek, S. N. A. (2017). *Curcuma mangga*-mediated synthesis of gold nanoparticles: Characterization, stability, cytotoxicity, and blood compatibility. *Nanomaterials*, 7(6), 123-137.
- Forman, D., & Ferlay, J. (2014). The global and regional burden of cancer. In B. W. Stewart & C. P. Wild (Eds.), *World cancer report 2014*. Lyon, France: International Agency for Research on Cancer.
- Forssen, E. A., & Ross, M. E. (1994). Daunoxome treatment of solid tumors: Preclinical and clinical investigations. *Journal of Liposome Research*, 4(1), 481-512.
- Frens, G. (1973). Controlled nucleation for the regulation of the particle size in monodisperse gold suspensions. *Nature Physical Science*, 241, 20-22.
- Gao, S., Zhang, L., Wang, G., Yang, K., Chen, M., Tian, R., . . . Zhu, L. (2016). Hybrid graphene/Au activatable theranostic agent for multimodalities imaging guided enhanced photothermal therapy. *Biomaterials*, 79, 36-45.
- Gao, X., Yue, Q., Liu, Z., Ke, M., Zhou, X., Li, S., . . . Li, C. (2017). Guiding brain-tumor surgery via blood-brain-barrier-permeable gold nanoprobe with acid-triggered MRI/SERRS signals. *Advanced Materials*, 29(21), 1603917.

- Gao, Y., Li, Y., Chen, J., Zhu, S., Liu, X., Zhou, L., . . . Shi, J. (2015). Multifunctional gold nanostar-based nanocomposite: Synthesis and application for noninvasive MR-SERS imaging-guided photothermal ablation. *Biomaterials*, *60*, 31-41.
- Gatoo, M. A., Naseem, S., Arfat, M. Y., Mahmood Dar, A., Qasim, K., & Zubair, S. (2014). Physicochemical properties of nanomaterials: Implication in associated toxic manifestations. *BioMed Research International*, *2014*, 498420.
- Gharatape, A., & Salehi, R. (2017). Recent progress in theranostic applications of hybrid gold nanoparticles. *European Journal of Medicinal Chemistry*, *138*, 221-233.
- Ghisaidoobe, A. B. T., & Chung, S. J. (2014). Intrinsic tryptophan fluorescence in the detection and analysis of proteins: A focus on Förster resonance energy transfer techniques. *International Journal of Molecular Sciences*, *15*(12), 22518-22538.
- Gholami-Shabani, M., Shams-Ghahfarokhi, M., Gholami-Shabani, Z., Akbarzadeh, A., Riazi, G., Ajdari, S., . . . Razzaghi-Abyaneh, M. (2015). Enzymatic synthesis of gold nanoparticles using sulfite reductase purified from *Escherichia coli*: A green eco-friendly approach. *Process Biochemistry*, *50*(7), 1076-1085.
- Ghuman, J., Zunszain, P. A., Petitpas, I., Bhattacharya, A. A., Otagiri, M., & Curry, S. (2005). Structural basis of the drug-binding specificity of human serum albumin. *Journal of Molecular Biology*, *353*(1), 38-52.
- Glantz, M. J., Jaeckle, K. A., Chamberlain, M. C., Phuphanich, S., Recht, L., Swinnen, L. J., . . . Howell, S. B. (1999). A randomized controlled trial comparing intrathecal sustained-release cytarabine (DepoCyt) to intrathecal methotrexate in patients with neoplastic meningitis from solid tumors. *Clinical Cancer Research*, *5*(11), 3394-3402.
- Goncharov, N. V., Belinskaia, D. A., Shmurak, V. I., Terpilowski, M. A., Jenkins, R. O., & Avdonin, P. V. (2017). Serum albumin binding and esterase activity: Mechanistic interactions with organophosphates. *Molecules*, *22*(7), 1201.
- González-Ballesteros, N., Prado-López, S., Rodríguez-González, J. B., Lastra, M., & Rodríguez-Argüelles, M. C. (2017). Green synthesis of gold nanoparticles using brown algae *Cystoseira baccata*: Its activity in colon cancer cells. *Colloids and Surfaces B: Biointerfaces*, *153*, 190-198.
- Goy-López, S., Juárez, J., Alatorre-Meda, M., Casals, E., Puentes, V. F., Taboada, P., & Mosquera, V. (2012). Physicochemical characteristics of protein-NP bioconjugates: The role of particle curvature and solution conditions on human serum albumin conformation and fibrillogenesis inhibition. *Langmuir*, *28*(24), 9113-9126.
- Grossman, J. H., & McNeil, S. E. (2012). Nanotechnology in cancer medicine. *Physics Today*, *65*(8), 38-42.
- Guan, T., Shang, W., Li, H., Yang, X., Fang, C., Tian, J., & Wang, K. (2017). From detection to resection: Photoacoustic tomography and surgery guidance with indocyanine green loaded gold nanorod@liposome core-shell nanoparticles in liver cancer. *Bioconjugate Chemistry*, *28*(4), 1221-1228.

- Guo, J., Rahme, K., He, Y., Li, L.L., Holmes, J. D., & O'Driscoll, C. M. (2017). Gold nanoparticles enlighten the future of cancer theranostics. *International Journal of Nanomedicine*, *12*, 6131-6152.
- Haiss, W., Thanh, N. T., Aveyard, J., & Fernig, D. G. (2007). Determination of size and concentration of gold nanoparticles from UV-Vis spectra. *Analytical Chemistry*, *79*(11), 4215-4221.
- Hanahan, D., & Weinberg, R. A. (2011). Hallmarks of cancer: The next generation. *Cell*, *144*(5), 646-674.
- Hao, Y., Zhang, B., Zheng, C., Ji, R., Ren, X., Guo, F., . . . Zhang, Y. (2015). The tumor-targeting core-shell structured DTX-loaded PLGA@Au nanoparticles for chemophotothermal therapy and X-ray imaging. *Journal of Controlled Release*, *220*, 545-555.
- Hawe, A., Poole, R., & Jiskoot, W. (2010). Misconceptions over Förster resonance energy transfer between proteins and ANS/bis-ANS: Direct excitation dominates dye fluorescence. *Analytical Biochemistry*, *401*(1), 99-106.
- He, X., Liu, F., Liu, L., Duan, T., Zhang, H., & Wang, Z. (2014). Lectin-conjugated Fe₂O₃@Au core@shell nanoparticles as dual mode contrast agents for *in vivo* detection of tumor. *Molecular Pharmaceutics*, *11*(3), 738-745.
- He, X., Wolkers, W. F., Crowe, J. H., Swanlund, D. J., & Bischof, J. C. (2004). *In situ* thermal denaturation of proteins in dunning AT-1 prostate cancer cells: Implication for hyperthermic cell injury. *Annals of Biomedical Engineering*, *32*(10), 1384-1398.
- He, X. M., & Carter, D. C. (1992). Atomic structure and chemistry of human serum albumin. *Nature*, *358*(6383), 209-215.
- Her, S., Jaffray, D. A., & Allen, C. (2017). Gold nanoparticles for applications in cancer radiotherapy: Mechanisms and recent advancements. *Advanced Drug Delivery Reviews*, *109*, 84-101.
- Holm, J., Lawaetz, A. J., & Hansen, S. I. (2012). Ligand binding induces a sharp decrease in hydrophobicity of folate binding protein assessed by 1-anilinonaphthalene-8-sulphonate which suppresses self-association of the hydrophobic apo-protein. *Biochemical and Biophysical Research Communications*, *425*(1), 19-24.
- Hou, H., Chen, L., He, H., Chen, L., Zhao, Z., & Jin, Y. (2015). Fine-tuning the LSPR response of gold nanorod-polyaniline core-shell nanoparticles with high photothermal efficiency for cancer cell ablation. *Journal of Materials Chemistry B*, *3*(26), 5189-5196.
- Hou, W., Xia, F., Alfranca, G., Yan, H., Zhi, X., Liu, Y., . . . Cui, D. (2017). Nanoparticles for multi-modality cancer diagnosis: Simple protocol for self-assembly of gold nanoclusters mediated by gadolinium ions. *Biomaterials*, *120*, 103-114.

- Hu, C., Peng, Q., Chen, F., Zhong, Z., & Zhuo, R. (2010). Low molecular weight polyethylenimine conjugated gold nanoparticles as efficient gene vectors. *Bioconjugate Chemistry*, 21(5), 836-843.
- Hu, D. H., Sheng, Z. H., Zhang, P. F., Yang, D. Z., Liu, S. H., Gong, P., . . . Cai, L. T. (2013). Hybrid gold-gadolinium nanoclusters for tumor-targeted NIRF/CT/MRI triple-modal imaging *in vivo*. *Nanoscale*, 5(4), 1624-1628.
- Hu, H., Huang, P., Weiss, O. J., Yan, X., Yue, X., Zhang, M. G., . . . Chen, X. (2014). PET and NIR optical imaging using self-illuminating ⁶⁴Cu-doped chelator-free gold nanoclusters. *Biomaterials*, 35(37), 9868-9876.
- Huang, J., Guo, M., Ke, H., Zong, C., Ren, B., Liu, G., . . . Zhang, Z. (2015). Rational design and synthesis of $\gamma\text{Fe}_2\text{O}_3@Au$ magnetic gold nanoflowers for efficient cancer theranostics. *Advanced Materials*, 27(34), 5049-5056.
- Huang, X., & El-Sayed, M. A. (2010). Gold nanoparticles: Optical properties and implementations in cancer diagnosis and photothermal therapy. *Journal of Advanced Research*, 1(1), 13-28.
- Huang, X., & El-Sayed, M. A. (2011). Plasmonic photo-thermal therapy (PPTT). *Alexandria Journal of Medicine*, 47(1), 1-9.
- Huang, X., Kang, B., Qian, W., Mackey, M. A., Chen, P. C., Oyelere, A. K., . . . El-Sayed, M. A. (2010). Comparative study of photothermolysis of cancer cells with nuclear-targeted or cytoplasm-targeted gold nanospheres: Continuous wave or pulsed lasers. *Journal of Biomedical Optics*, 15(5), 058002.
- Hughes, W. L. (1954). Interstitial proteins: The proteins of blood plasma and lymph. In H. Neurath & K. Bailey (Eds.), *The proteins* (pp. 663-754). New York: Academic Press.
- Hunter, M. J. (1966). A method for the determination of protein partial specific volumes. *The Journal of Physical Chemistry*, 70(10), 3285-3292.
- Hunter, M. J., & McDuffie, F. C. (1959). Molecular weight studies on human serum albumin after reduction and alkylation of disulfide bonds. *Journal of the American Chemical Society*, 81(6), 1400-1406.
- Husseiny, M. I., El-Aziz, M. A., Badr, Y., & Mahmoud, M. A. (2007). Biosynthesis of gold nanoparticles using *Pseudomonas aeruginosa*. *Spectrochimica Acta Part A: Molecular and Biomolecular Spectroscopy*, 67(3), 1003-1006.
- Iancu, C., Mocan, L., Bele, C., Orza, A. I., Tabaran, F. A., Catoi, C., . . . Mocan, T. (2011). Enhanced laser thermal ablation for the *in vitro* treatment of liver cancer by specific delivery of multiwalled carbon nanotubes functionalized with human serum albumin. *International Journal of Nanomedicine*, 6, 129-141.
- Inoue, M., Hirata, E., Morino, Y., Nagase, S., Chowdhury, J. R., Chowdhury, N. R., & Arias, I. M. (1985). The role of albumin in the hepatic transport of bilirubin: Studies in mutant analbuminemic rats. *The Journal of Biochemistry*, 97(3), 737-743.

- Irfan, M., Moniruzzaman, M., Ahmad, T., Mandal, P. C., Abdullah, B., & Bhattacharjee, S. (2017). Growth kinetic study of ionic liquid mediated synthesis of gold nanoparticles using *Elaeis guineensis* (oil palm) kernels extract under microwave irradiation. *Arabian Journal of Chemistry*. Retrieved on November 14, 2018, from <https://doi.org/10.1016/j.arabjc.2017.07.005>
- Jain, P. K., Lee, K. S., El-Sayed, I. H., & El-Sayed, M. A. (2006). Calculated absorption and scattering properties of gold nanoparticles of different size, shape, and composition: Applications in biological imaging and biomedicine. *The Journal of Physical Chemistry B*, *110*(14), 7238-7248.
- Jain, T., Kumar, S., & Dutta, P. K. (2016). Dibutylchitin nanoparticles as novel drug carrier. *International Journal of Biological Macromolecules*, *82*, 1011-1017.
- Jana, N. R., Gearheart, L., & Murphy, C. J. (2001). Seeding growth for size control of 5–40 nm diameter gold nanoparticles. *Langmuir*, *17*(22), 6782-6786.
- Jang, B., Park, J.Y., Tung, C.H., Kim, I.H., & Choi, Y. (2011). Gold nanorod-photosensitizer complex for near-infrared fluorescence imaging and photodynamic/photothermal therapy *in vivo*. *ACS Nano*, *5*(2), 1086-1094.
- Jia, Y. P., Ma, B. Y., Wei, X. W., & Qian, Z. Y. (2017). The *in vitro* and *in vivo* toxicity of gold nanoparticles. *Chinese Chemical Letters*, *28*(4), 691-702.
- Jin, Y. Z., Hahn, Y. B., Nahm, K. S., & Lee, Y. S. (2005). Preparation of stable polyurethane-polystyrene copolymer emulsions via RAFT polymerization process. *Polymer*, *46*(25), 11294-11300.
- Jing, L., Liang, X., Deng, Z., Feng, S., Li, X., Huang, M., . . . Dai, Z. (2014). Prussian blue coated gold nanoparticles for simultaneous photoacoustic/CT bimodal imaging and photothermal ablation of cancer. *Biomaterials*, *35*(22), 5814-5821.
- Jitoe, A., Masuda, T., Tengah, I., Suprpta, D. N., Gara, I., & Nakatani, N. (1992). Antioxidant activity of tropical ginger extracts and analysis of the contained curcuminoids. *Journal of Agricultural and Food Chemistry*, *40*(8), 1337-1340.
- Johnson, J. D., El-Bayoumi, M. A., Weber, L. D., & Tulinsky, A. (1979). Interaction of α -chymotrypsin with the fluorescent probe 1-anilinonaphthalene-8-sulfonate in solution. *Biochemistry*, *18*(7), 1292-1296.
- Jokerst, J. V., Cole, A. J., Van de Sompel, D., & Gambhir, S. S. (2012). Gold nanorods for ovarian cancer detection with photoacoustic imaging and resection guidance via Raman imaging in living mice. *ACS Nano*, *6*(11), 10366-10377.
- Kabir, M. Z., Tee, W. V., Mohamad, S. B., Alias, Z., & Tayyab, S. (2016). Interaction of an anticancer drug, gefitinib with human serum albumin: Insights from fluorescence spectroscopy and computational modeling analysis. *RSC Advances*, *6*(94), 91756-91767.

- Kamazeri, T. S. A. T., Samah, O. A., Taher, M., Susanti, D., & Qaralleh, H. (2012). Antimicrobial activity and essential oils of *Curcuma aeruginosa*, *Curcuma mangga*, and *Zingiber cassumunar* from Malaysia. *Asian Pacific Journal of Tropical Medicine*, 5(3), 202-209.
- Kang, S., Bhang, S. H., Hwang, S., Yoon, J. K., Song, J., Jang, H. K., . . . Kim, B. S. (2015). Mesenchymal stem cells aggregate and deliver gold nanoparticles to tumors for photothermal therapy. *ACS Nano*, 9(10), 9678-9690.
- Karmani, L., Labar, D., Valembois, V., Bouchat, V., Nagaswaran, P. G., Bol, A., . . . Bonifazi, D. (2013). Antibody-functionalized nanoparticles for imaging cancer: Influence of conjugation to gold nanoparticles on the biodistribution of ⁸⁹Zr-labeled cetuximab in mice. *Contrast Media & Molecular Imaging*, 8(5), 402-408.
- Kelly, K. L., Coronado, E., Zhao, L. L., & Schatz, G. C. (2003). The optical properties of metal nanoparticles: The influence of size, shape, and dielectric environment. *The Journal of Physical Chemistry B*, 107(3), 668-677.
- Kelly, S. M., Jess, T. J., & Price, N. C. (2005). How to study proteins by circular dichroism. *Biochimica et Biophysica Acta - Proteins and Proteomics*, 1751(2), 119-139.
- Kerker, M. (1969). Electromagnetic waves. In E. M. Loebl (Ed.), *The scattering of light and other electromagnetic radiation* (pp. 8-26). New York: Academic Press.
- Khanna, N., Tokuda, M., & Waisman, D. (1986). Conformational changes induced by binding of divalent cations to calregulin. *Journal of Biological Chemistry*, 261(19), 8883-8887.
- Khullar, P., Singh, V., Mahal, A., Dave, P. N., Thakur, S., Kaur, G., . . . Singh Bakshi, M. (2012). Bovine serum albumin bioconjugated gold nanoparticles: Synthesis, hemolysis, and cytotoxicity toward cancer cell lines. *The Journal of Physical Chemistry C*, 116(15), 8834-8843.
- Kim, Y. H., Jeon, J., Hong, S. H., Rhim, W. K., Lee, Y. S., Youn, H., . . . Nam, J. M. (2011). Tumor targeting and imaging using cyclic RGD - PEGylated gold nanoparticle probes with directly conjugated iodine-125. *Small*, 7(14), 2052-2060.
- Kirana, C., Record, I. R., McIntosh, G. H., & Jones, G. P. (2003). Screening for antitumor activity of 11 species of Indonesian Zingiberaceae using human MCF-7 and HT-29 cancer cells. *Pharmaceutical Biology*, 41(4), 271-276.
- Kolovskaya, O. S., Zamay, T. N., Belyanina, I. V., Karlova, E., Garanzha, I., Aleksandrovsky, A. S., . . . Kichkailo, A. S. (2017). Aptamer-targeted plasmonic photothermal therapy of cancer. *Molecular Therapy - Nucleic Acids*, 9, 12-21.
- Korolenko, E. A., Korolik, E. V., Korolik, A. K., & Kirkovskii, V. V. (2007). Estimation of the binding ability of main transport proteins of blood plasma with liver cirrhosis by the fluorescent probe method. *Journal of Applied Spectroscopy*, 74(4), 561-566.

- Kragh-Hansen, U. (1985). Relations between high-affinity binding sites of markers for binding regions on human serum albumin. *Biochemical Journal*, 225(3), 629-638.
- Kragh-Hansen, U., Chuang, V. T. G., & Otagiri, M. (2002). Practical aspects of the ligand-binding and enzymatic properties of human serum albumin. *Biological and Pharmaceutical Bulletin*, 25(6), 695-704.
- Kumar, K. P., Paul, W., & Sharma, C. P. (2011). Green synthesis of gold nanoparticles with *Zingiber officinale* extract: Characterization and blood compatibility. *Process Biochemistry*, 46(10), 2007-2013.
- Kumari, M., Mishra, A., Pandey, S., Singh, S. P., Chaudhry, V., Mudiam, M. K. R., . . . Nautiyal, C. S. (2016). Physico-chemical condition optimization during biosynthesis lead to development of improved and catalytically efficient gold nano particles. *Scientific Reports*, 6, 27575.
- Kusolkamabot, K., Sae-ung, P., Niamnont, N., Wongravee, K., Sukwattanasinitt, M., & Hoven, V. P. (2013). Poly(N-isopropylacrylamide)-stabilized gold nanoparticles in combination with tricationic branched phenylene-ethynylene fluorophore for protein identification. *Langmuir*, 29(39), 12317-12327.
- Kuznetsova, I. M., Sulatskaya, A. I., Povarova, O. I., & Turoverov, K. K. (2012). Reevaluation of ANS binding to human and bovine serum albumins: Key role of equilibrium microdialysis in ligand-receptor binding characterization. *PLoS ONE*, 7(7), e40845.
- Lacerda, S. H. D. P., Park, J. J., Meuse, C., Pristiniski, D., Becker, M. L., Karim, A., & Douglas, J. F. (2010). Interaction of gold nanoparticles with common human blood proteins. *ACS Nano*, 4(1), 365-379.
- Lakowicz, J. (2006). *Principle of fluorescence spectroscopy* (Vol. 13). New York: Springer.
- Lakshmi, P. T., Mondal, M., Ramadas, K., & Natarajan, S. (2017). Molecular interaction of 2,4-diacetylphloroglucinol (DAPG) with human serum albumin (HSA): The spectroscopic, calorimetric and computational investigation. *Spectrochimica Acta Part A: Molecular and Biomolecular Spectroscopy*, 183, 90-102.
- Lancet, J. E., Cortes, J. E., Hogge, D. E., Tallman, M. S., Kovacsovics, T. J., Damon, L. E., . . . Feldman, E. J. (2014). Phase 2 trial of CPX-351, a fixed 5:1 molar ratio of cytarabine/daunorubicin, vs cytarabine/daunorubicin in older adults with untreated AML. *Blood*, 123(21), 3239-3246.
- Lao, J., Madani, J., Puértolas, T., Álvarez, M., Hernández, A., Pazo-Cid, R., . . . Antón Torres, A. (2013). Liposomal doxorubicin in the treatment of breast cancer patients: A review. *Journal of Drug Delivery*, 2013, 456409.
- Li, L., Fu, S., Chen, C., Wang, X., Fu, C., Wang, S., . . . Liu, H. (2016). Microenvironment-driven bioelimination of magnetoplasmonic nanoassemblies and their multimodal imaging-guided tumor photothermal therapy. *ACS Nano*, 10(7), 7094-7105.

- Li, S. Q., Zhu, R. R., Zhu, H., Xue, M., Sun, X. Y., Yao, S. D., & Wang, S. L. (2008). Nanotoxicity of TiO₂ nanoparticles to erythrocyte *in vitro*. *Food and Chemical Toxicology*, *46*(12), 3626-3631.
- Li, W., Zhang, X., Zhou, M., Tian, B., Yu, C., Jie, J., . . . Zhang, X. (2014). Functional core/shell drug nanoparticles for highly effective synergistic cancer therapy. *Advanced Healthcare Materials*, *3*(9), 1475-1485.
- Li, X., Takashima, M., Yuba, E., Harada, A., & Kono, K. (2014). PEGylated PAMAM dendrimer-doxorubicin conjugate-hybridized gold nanorod for combined photothermal-chemotherapy. *Biomaterials*, *35*(24), 6576-6584.
- Li, Y., Jia, B., Wang, H., Li, N., Chen, G., Lin, Y., & Gao, W. (2013). The interaction of 2-mercaptobenzimidazole with human serum albumin as determined by spectroscopy, atomic force microscopy and molecular modeling. *Colloids and Surfaces B: Biointerfaces*, *104*, 311-317.
- Libutti, S. K., Paciotti, G. F., Byrnes, A. A., Alexander, H. R., Gannon, W. E., Walker, M., . . . Tamarkin, L. (2010). Phase I and pharmacokinetic studies of CYT-6091, a novel PEGylated colloidal gold-rhTNF nanomedicine. *Clinical Cancer Research*, *16*(24), 6139-6149.
- Lim, S. H., Ahn, E.Y., & Park, Y. (2016). Green synthesis and catalytic activity of gold nanoparticles synthesized by *Artemisia capillaris* water extract. *Nanoscale Research Letters*, *11*, 474.
- Lin, A. Y., Almeida, J. P. M., Bear, A., Liu, N., Luo, L., Foster, A. E., & Drezek, R. A. (2013). Gold nanoparticle delivery of modified CpG stimulates macrophages and inhibits tumor growth for enhanced immunotherapy. *PLoS ONE*, *8*(5), e63550.
- Lin, A. Y., Lunsford, J., Bear, A. S., Young, J. K., Eckels, P., Luo, L., . . . Drezek, R. A. (2013). High-density sub-100-nm peptide-gold nanoparticle complexes improve vaccine presentation by dendritic cells *in vitro*. *Nanoscale Research Letters*, *8*(1), 72-72.
- Lin, Y. S., & Haynes, C. L. (2010). Impacts of mesoporous silica nanoparticle size, pore ordering, and pore integrity on hemolytic activity. *Journal of the American Chemical Society*, *132*(13), 4834-4842.
- Link, S., Burda, C., Mohamed, M. B., Nikoobakht, B., & El-Sayed, M. A. (1999). Laser photothermal melting and fragmentation of gold nanorods: Energy and laser pulse-width dependence. *The Journal of Physical Chemistry A*, *103*(9), 1165-1170.
- Link, S., Burda, C., Mohamed, M. B., Nikoobakht, B., & El-Sayed, M. A. (2000). Femtosecond transient-absorption dynamics of colloidal gold nanorods: Shape independence of the electron-phonon relaxation time. *Physical Review B*, *61*(9), 6086-6090.
- Liu, Y., Ashton, J. R., Moding, E. J., Yuan, H., Register, J. K., Fales, A. M., . . . Vo-Dinh, T. (2015). A plasmonic gold nanostar theranostic probe for *in vivo* tumor imaging and photothermal therapy. *Theranostics*, *5*(9), 946-960.

- Liu, Y., & Nair, M. G. (2011). Labdane diterpenes in *Curcuma mangga* rhizomes inhibit lipid peroxidation, cyclooxygenase enzymes and human tumour cell proliferation. *Food Chemistry*, *124*(2), 527-532.
- Liu, Y., Shipton, M. K., Ryan, J., Kaufman, E. D., Franzen, S., & Feldheim, D. L. (2007). Synthesis, stability, and cellular internalization of gold nanoparticles containing mixed peptide-poly(ethylene glycol) monolayers. *Analytical Chemistry*, *79*(6), 2221-2229.
- Liu, Y., Tu, W., & Cao, D. (2010). Synthesis of gold nanoparticles coated with polystyrene-block-poly(N-isopropylacrylamide) and their thermoresponsive ultraviolet-visible absorbance. *Industrial & Engineering Chemistry Research*, *49*(6), 2707-2715.
- Liu, Y., Yang, M., Zhang, J., Zhi, X., Li, C., Zhang, C., . . . Cui, D. (2016). Human induced pluripotent stem cells for tumor targeted delivery of gold nanorods and enhanced photothermal therapy. *ACS Nano*, *10*(2), 2375-2385.
- Lu, W., Melancon, M. P., Xiong, C., Huang, Q., Elliott, A., Song, S., . . . Li, C. (2011). Effects of photoacoustic imaging and photothermal ablation therapy mediated by targeted hollow gold nanospheres in an orthotopic mouse xenograft model of glioma. *Cancer Research*, *71*(19), 6116-6121.
- Luk, K. H., Hulse, R. M., & Phillips, T. L. (1980). Hyperthermia in cancer therapy. *Western Journal of Medicine*, *132*(3), 179-185.
- Luo, C.H., Shanmugam, V., & Yeh, C.S. (2015). Nanoparticle biosynthesis using unicellular and subcellular supports. *NPG Asia Materials*, *7*, e209.
- Luo, C. H., Huang, C. T., Su, C. H., & Yeh, C. S. (2016). Bacteria-mediated hypoxia-specific delivery of nanoparticles for tumors imaging and therapy. *Nano Letters*, *16*(6), 3493-3499.
- Maeda, H. (2001). The enhanced permeability and retention (EPR) effect in tumor vasculature: The key role of tumor-selective macromolecular drug targeting. *Advances in Enzyme Regulation*, *41*(1), 189-207.
- Maeda, H., Nakamura, H., & Fang, J. (2013). The EPR effect for macromolecular drug delivery to solid tumors: Improvement of tumor uptake, lowering of systemic toxicity, and distinct tumor imaging *in vivo*. *Advanced Drug Delivery Reviews*, *65*(1), 71-79.
- Magdi, H. M., & Bhushan, B. (2015). Extracellular biosynthesis and characterization of gold nanoparticles using the fungus *Penicillium chrysogenum*. *Microsystem Technologies*, *21*(10), 2279-2285.
- Maity, S., Sen, I. K., & Islam, S. S. (2012). Green synthesis of gold nanoparticles using gum polysaccharide of *Cochlospermum religiosum* (katira gum) and study of catalytic activity. *Physica E: Low-dimensional Systems and Nanostructures*, *45*, 130-134.
- Majno, G., & Joris, I. (1995). Apoptosis, oncosis, and necrosis: An overview of cell death. *The American Journal of Pathology*, *146*(1), 3.

- Malarkodi, C., Rajeshkumar, S., Vanaja, M., Paulkumar, K., Gnanajobitha, G., & Annadurai, G. (2013). Eco-friendly synthesis and characterization of gold nanoparticles using *Klebsiella pneumoniae*. *Journal of Nanostructure in Chemistry*, 3(1), 30.
- Malek, S. N. A., Lee, G. S., Hong, S. L., Yaacob, H., Wahab, N. A., Faizal Weber, J. F., & Shah, S. A. A. (2011). Phytochemical and cytotoxic investigations of *Curcuma mangga* rhizomes. *Molecules*, 16(6), 4539-4548.
- Maltzahn, G. v., Park, J. H., Agrawal, A., Bandaru, N. K., Das, S. K., Sailor, M. J., & Bhatia, S. N. (2009). Computationally guided photothermal tumor therapy using long-circulating gold nanorod antennas. *Cancer Research*, 69(9), 3892-3900.
- Mefford, O. T., Carroll, M. R. J., Vadala, M. L., Goff, J. D., Mejia-Ariza, R., Saunders, M., . . . Riffle, J. S. (2008). Size analysis of PDMS–magnetite nanoparticle complexes: Experiment and theory. *Chemistry of Materials*, 20(6), 2184-2191.
- Meir, R., Shamalov, K., Betzer, O., Motiei, M., Horovitz-Fried, M., Yehuda, R., . . . Cohen, C. J. (2015). Nanomedicine for cancer immunotherapy: Tracking cancer-specific T-Cells *in vivo* with gold nanoparticles and CT imaging. *ACS Nano*, 9(6), 6363-6372.
- Melamed, J. R., Edelstein, R. S., & Day, E. S. (2015). Elucidating the fundamental mechanisms of cell death triggered by photothermal therapy. *ACS Nano*, 9(1), 6-11.
- Mendes, R., Pedrosa, P., Lima, J. C., Fernandes, A. R., & Baptista, P. V. (2017). Photothermal enhancement of chemotherapy in breast cancer by visible irradiation of gold nanoparticles. *Scientific Reports*, 7(1), 10872.
- Menon, S., S, R., & S, V. K. (2017). A review on biogenic synthesis of gold nanoparticles, characterization, and its applications. *Resource-Efficient Technologies*, 3(4), 516-527.
- Miele, E., Spinelli, G. P., Miele, E., Tomao, F., & Tomao, S. (2009). Albumin-bound formulation of paclitaxel (Abraxane ABI-007) in the treatment of breast cancer. *International Journal of Nanomedicine*, 4, 99-105.
- Mieszawska, A. J., Mulder, W. J., Fayad, Z. A., & Cormode, D. P. (2013). Multifunctional gold nanoparticles for diagnosis and therapy of disease. *Molecular Pharmaceutics*, 10(3), 831.
- Minotti, G., Menna, P., Salvatorelli, E., Cairo, G., & Gianni, L. (2004). Anthracyclines: Molecular advances and pharmacologic developments in antitumor activity and cardiotoxicity. *Pharmacological Reviews*, 56(2), 185-229.
- Mocan, L., Tabaran, F. A., Mocan, T., Bele, C., Orza, A. I., Lucan, C., . . . Iancu, C. (2011). Selective *ex-vivo* photothermal ablation of human pancreatic cancer with albumin functionalized multiwalled carbon nanotubes. *International Journal of Nanomedicine*, 6, 915-928.

- Moore, T. L., Rodriguez-Lorenzo, L., Hirsch, V., Balog, S., Urban, D., Jud, C., . . . Petri-Fink, A. (2015). Nanoparticle colloidal stability in cell culture media and impact on cellular interactions. *Chemical Society Reviews*, 44(17), 6287-6305.
- Mosmann, T. (1983). Rapid colorimetric assay for cellular growth and survival: Application to proliferation and cytotoxicity assays. *Journal of Immunological Methods*, 65(1), 55-63.
- Mu, Q., Kievit, F. M., Kant, R. J., Lin, G., Jeon, M., & Zhang, M. (2015). Anti-HER2/neu peptide-conjugated iron oxide nanoparticles for targeted delivery of paclitaxel to breast cancer cells. *Nanoscale*, 7(43), 18010-18014.
- Narayanan, K. B., Park, H. H., & Han, S. S. (2015). Synthesis and characterization of biomatrixed-gold nanoparticles by the mushroom *Flammulina velutipes* and its heterogeneous catalytic potential. *Chemosphere*, 141, 169-175.
- Nath, D., & Banerjee, P. (2013). Green nanotechnology-A new hope for medical biology. *Environmental Toxicology and Pharmacology*, 36(3), 997-1014.
- Nguyen, V. H., & Lee, B. J. (2017). Protein corona: A new approach for nanomedicine design. *International Journal of Nanomedicine*, 12, 3137-3151.
- Oncley, J. L., Scatchard, G., & Brown, A. (1947). Physical-chemical characteristics of certain of the proteins of normal human plasma. *The Journal of Physical and Colloid Chemistry*, 51(1), 184-198.
- Padmanabhan, P., Kumar, A., Kumar, S., Chaudhary, R. K., & Gulyás, B. (2016). Nanoparticles in practice for molecular-imaging applications: An overview. *Acta Biomaterialia*, 41, 1-16.
- Painter, L., Harding, M. M., & Beeby, P. J. (1998). Synthesis and interaction with human serum albumin of the first 3,18-disubstituted derivative of bilirubin. *Journal of the Chemical Society, Perkin Transactions 1*(18), 3041-3044.
- Park, J., Park, J., Ju, E. J., Park, S. S., Choi, J., Lee, J. H., . . . Choi, E. K. (2015). Multifunctional hollow gold nanoparticles designed for triple combination therapy and CT imaging. *Journal of Controlled Release*, 207, 77-85.
- Park, K. (2013). Facing the truth about nanotechnology in drug delivery. *ACS Nano*, 7(9), 7442-7447.
- Park, S. Y., & Kim, I. S. (2017). Engulfment signals and the phagocytic machinery for apoptotic cell clearance. *Experimental & Molecular Medicine*, 49, e331.
- Pattani, V. P., Shah, J., Atalis, A., Sharma, A., & Tunnell, J. W. (2015). Role of apoptosis and necrosis in cell death induced by nanoparticle-mediated photothermal therapy. *Journal of Nanoparticle Research*, 17(1), 20.
- Peng, C., Zheng, L., Chen, Q., Shen, M., Guo, R., Wang, H., . . . Shi, X. (2012). PEGylated dendrimer-entrapped gold nanoparticles for *in vivo* blood pool and tumor imaging by computed tomography. *Biomaterials*, 33(4), 1107-1119.

- Peng, Q., Zhang, S., Yang, Q., Zhang, T., Wei, X. Q., Jiang, L., . . . Lin, Y. F. (2013). Preformed albumin corona, a protective coating for nanoparticles based drug delivery system. *Biomaterials*, 34(33), 8521-8530.
- Pérez-Hernández, M., del Pino, P., Mitchell, S. G., Moros, M., Stepien, G., Pelaz, B., . . . de la Fuente, J. M. (2015). Dissecting the molecular mechanism of apoptosis during photothermal therapy using gold nanoprisms. *ACS Nano*, 9(1), 52-61.
- Peters Jr, T. (1996). *All about albumin: Biochemistry, genetics, and medical applications*. San Diego: Academic Press.
- Petryayeva, E., & Krull, U. J. (2011). Localized surface plasmon resonance: Nanostructures, bioassays and biosensing-A review. *Analytica Chimica Acta*, 706(1), 8-24.
- Pfeiffer, C., Rehbock, C., Hühn, D., Carrillo-Carrion, C., de Aberasturi, D. J., Merk, V., . . . Parak, W. J. (2014). Interaction of colloidal nanoparticles with their local environment: The (ionic) nanoenvironment around nanoparticles is different from bulk and determines the physico-chemical properties of the nanoparticles. *Journal of The Royal Society Interface*, 11(96), 20130931.
- Philip, K., Malek, S. N., Sani, W., Shin, S. K., Kumar, S., Lai, H. S., . . . Rahman, S. N. (2009). Antimicrobial activity of some medicinal plants from Malaysia. *American Journal of Applied Sciences*, 6(8), 1613.
- Piao, J. G., Wang, L., Gao, F., You, Y. Z., Xiong, Y., & Yang, L. (2014). Erythrocyte membrane is an alternative coating to polyethylene glycol for prolonging the circulation lifetime of gold nanocages for photothermal therapy. *ACS Nano*, 8(10), 10414-10425.
- Pillai, G. (2014). Nanomedicines for cancer therapy: An update of FDA approved and those under various stages of development. *SOJ Pharmacy & Pharmacological Sciences*, 1(2), 13.
- Pillai, G., & Ceballos-Coronel, M. L. (2013). Science and technology of the emerging nanomedicines in cancer therapy: A primer for physicians and pharmacists. *SAGE Open Medicine*, 1, 2050312113513759.
- Polte, J., Erler, R., Thunemann, A. F., Sokolov, S., Ahner, T. T., Rademann, K., . . . Kraehnert, R. (2010). Nucleation and growth of gold nanoparticles studied via in situ small angle X-ray scattering at millisecond time resolution. *ACS Nano*, 4(2), 1076-1082.
- Prabhu, S., & Poulouse, E. K. (2012). Silver nanoparticles: Mechanism of antimicrobial action, synthesis, medical applications, and toxicity effects. *International Nano Letters*, 2(1), 32.
- Prodan, E., Radloff, C., Halas, N. J., & Nordlander, P. (2003). A hybridization model for the plasmon response of complex nanostructures. *Science*, 302(5644), 419-422.

PubChem Compound Database. Retrieved on June 21, 2018, from National Center for Biotechnology Information, National Institutes of Health <https://pubchem.ncbi.nlm.nih.gov/compound/22959485>

Qin, J., Li, Y., He, C., Yang, X., Xie, Y., Hu, X., . . . Liao, F. (2014). Selective and sensitive homogenous assay of serum albumin with 1-anilinonaphthalene-8-sulphonate as a biosensor. *Analytica Chimica Acta*, 829, 60-67.

Rajan, A., MeenaKumari, M., & Philip, D. (2014). Shape tailored green synthesis and catalytic properties of gold nanocrystals. *Spectrochimica Acta Part A: Molecular and Biomolecular Spectroscopy*, 118, 793-799.

Rajathi, F. A. A., Parthiban, C., Kumar, V. G., & Anantharaman, P. (2012). Biosynthesis of antibacterial gold nanoparticles using brown alga, *Stoechospermum marginatum* (kützing). *Spectrochimica Acta Part A: Molecular and Biomolecular Spectroscopy*, 99, 166-173.

Rajeshkumar, S., Malarkodi, C., Gnanajobitha, G., Paulkumar, K., Vanaja, M., Kannan, C., & Annadurai, G. (2013). Seaweed-mediated synthesis of gold nanoparticles using *Turbinaria conoides* and its characterization. *Journal of Nanostructure in Chemistry*, 3(1), 44.

Ranjitha, V. R., & Rai, V. R. (2017). Actinomycetes mediated synthesis of gold nanoparticles from the culture supernatant of *Streptomyces griseoruber* with special reference to catalytic activity. *3 Biotech*, 7(5), 299.

Regmi, R., Gumber, V., Rao, V. S., Kohli, I., Black, C., Sudakar, C., . . . Mukhopadhyay, A. (2011). Discrepancy between different estimates of the hydrodynamic diameter of polymer-coated iron oxide nanoparticles in solution. *Journal of Nanoparticle Research*, 13(12), 6869-6875.

Roche, M., Rondeau, P., Singh, N. R., Tarnus, E., & Bourdon, E. (2008). The antioxidant properties of serum albumin. *FEBS Letters*, 582(13), 1783-1787.

Ross, P. D., & Subramanian, S. (1981). Thermodynamics of protein association reactions: Forces contributing to stability. *Biochemistry*, 20(11), 3096-3102.

Rowinsky, E. K. (1997). The development and clinical utility of the taxane class of antimicrotubule chemotherapy agents. *Annual Review of Medicine*, 48(1), 353-374.

Sadhasivam, S., Shanmugam, P., Veerapandian, M., Subbiah, R., & Yun, K. (2012). Biogenic synthesis of multidimensional gold nanoparticles assisted by *Streptomyces hygroscopicus* and its electrochemical and antibacterial properties. *BioMetals*, 25(2), 351-360.

Sajanlal, P. R., Sreepasad, T. S., Samal, A. K., & Pradeep, T. (2011). Anisotropic nanomaterials: Structure, growth, assembly, and functions. *Nano Reviews*, 2(1), 5883.

- Sharma, A. S., & Ilanchelian, M. (2015). Comprehensive multispectroscopic analysis on the interaction and corona formation of human serum albumin with gold/silver alloy nanoparticles. *The Journal of Physical Chemistry B*, 119(30), 9461-9476.
- Shi, H., Ye, X., He, X., Wang, K., Cui, W., He, D., . . . Jia, X. (2014). Au@Ag/Au nanoparticles assembled with activatable aptamer probes as smart "nano-doctors" for image-guided cancer thermotherapy. *Nanoscale*, 6(15), 8754-8761.
- Shi, L., Buhler, E., Boué, F., & Carn, F. (2017). How does the size of gold nanoparticles depend on citrate to gold ratio in Turkevich synthesis? Final answer to a debated question. *Journal of Colloid and Interface Science*, 492, 191-198.
- Shi, X., Li, D., Xie, J., Wang, S., Wu, Z., & Chen, H. (2012). Spectroscopic investigation of the interactions between gold nanoparticles and bovine serum albumin. *Chinese Science Bulletin*, 57(10), 1109-1115.
- Silverman, J. A., & Deitcher, S. R. (2013). Marqibo (vincristine sulfate liposome injection) improves the pharmacokinetics and pharmacodynamics of vincristine. *Cancer Chemotherapy and Pharmacology*, 71(3), 555-564.
- Singaravelu, G., Arockiamary, J. S., Kumar, V. G., & Govindaraju, K. (2007). A novel extracellular synthesis of monodisperse gold nanoparticles using marine alga, *Sargassum wightii* Greville. *Colloids and Surfaces B: Biointerfaces*, 57(1), 97-101.
- Singh-Zocchi, M., Andreasen, A., & Zocchi, G. (1999). Osmotic pressure contribution of albumin to colloidal interactions. *Proceedings of the National Academy of Sciences of the United States of America*, 96(12), 6711-6715.
- Singh, M., Kalaivani, R., Manikandan, S., Sangeetha, N., & Kumaraguru, A. K. (2013). Facile green synthesis of variable metallic gold nanoparticle using *Padina gymnospora*, a brown marine macroalga. *Applied Nanoscience*, 3(2), 145-151.
- Singhal, J. P., & Ray, A. R. (2002). Synthesis of blood compatible polyamide block copolymers. *Biomaterials*, 23(4), 1139-1145.
- Smith, B. (1999). *Infrared spectral interpretation: A systematic approach*. Boca Raton, FL, USA: CRC Press.
- Sokolov, K., Follen, M., Aaron, J., Pavlova, I., Malpica, A., Lotan, R., & Richards-Kortum, R. (2003). Real-time vital optical imaging of precancer using anti-epidermal growth factor receptor antibodies conjugated to gold nanoparticles. *Cancer Research*, 63(9), 1999-2004.
- Song, A. S., Najjar, A. M., & Diller, K. R. (2014). Thermally induced apoptosis, necrosis, and heat shock protein expression in three-dimensional culture. *Journal of Biomechanical Engineering*, 136(7), 071006.
- Song, J., Yang, X., Orit, J., Huang, P., Sun, X., Lin, L., . . . Chen, X. (2015). Ultrasmall gold nanorod vesicles with enhanced tumor accumulation and fast excretion from the body for cancer therapy. *Advanced Materials*, 27(33), 4910-4917.

- Song, W., Gong, J., Wang, Y., Zhang, Y., Zhang, H., Zhang, W., . . . Yin, W. (2016). Gold nanoflowers with mesoporous silica as “nanocarriers” for drug release and photothermal therapy in the treatment of oral cancer using near-infrared (NIR) laser light. *Journal of Nanoparticle Research*, 18(4), 101.
- Sperling, R. A., & Parak, W. (2010). Surface modification, functionalization and bioconjugation of colloidal inorganic nanoparticles. *Philosophical Transactions of the Royal Society of London A: Mathematical, Physical and Engineering Sciences*, 368(1915), 1333-1383.
- Steichen, S. D., Caldorera-Moore, M., & Peppas, N. A. (2013). A review of current nanoparticle and targeting moieties for the delivery of cancer therapeutics. *European Journal of Pharmaceutical Sciences*, 48(3), 416-427.
- Sudlow, G., Birkett, D. J., & Wade, D. N. (1975). The characterization of two specific drug binding sites on human serum albumin. *Molecular Pharmacology*, 11(6), 824-832.
- Sugio, S., Kashima, A., Mochizuki, S., Noda, M., & Kobayashi, K. (1999). Crystal structure of human serum albumin at 2.5 Å resolution. *Protein Engineering*, 12(6), 439-446.
- Sujitha, M. V., & Kannan, S. (2013). Green synthesis of gold nanoparticles using Citrus fruits (*Citrus limon*, *Citrus reticulata* and *Citrus sinensis*) aqueous extract and its characterization. *Spectrochimica Acta Part A: Molecular and Biomolecular Spectroscopy*, 102, 15-23.
- Suman, T. Y., Radhika Rajasree, S. R., Ramkumar, R., Rajthilak, C., & Perumal, P. (2014). The green synthesis of gold nanoparticles using an aqueous root extract of *Morinda citrifolia* L. *Spectrochimica Acta Part A: Molecular and Biomolecular Spectroscopy*, 118, 11-16.
- Sun, C., Yang, J., Wu, X., Huang, X., Wang, F., & Liu, S. (2005). Unfolding and refolding of bovine serum albumin induced by cetylpyridinium bromide. *Biophysical Journal*, 88(5), 3518-3524.
- Sun, W., Du, Y., Chen, J., Kou, J., & Yu, B. (2009). Interaction between titanium dioxide nanoparticles and human serum albumin revealed by fluorescence spectroscopy in the absence of photoactivation. *Journal of Luminescence*, 129(8), 778-783.
- Sun, X., Huang, X., Yan, X., Wang, Y., Guo, J., Jacobson, O., . . . Chen, X. (2014). Chelator-free ⁶⁴Cu-integrated gold nanomaterials for positron emission tomography imaging guided photothermal cancer therapy. *ACS Nano*, 8(8), 8438-8446.
- Tanford, C. (1950). Preparation and properties of serum and plasma proteins. XXIII. Hydrogen ion equilibria in native and modified human serum albumins. *Journal of the American Chemical Society*, 72(1), 441-451.
- Tedja, R., Lim, M., Amal, R., & Marquis, C. (2012). Effects of serum adsorption on cellular uptake profile and consequent impact of titanium dioxide nanoparticles on human lung cell lines. *ACS Nano*, 6(5), 4083-4093.

- Tewtrakul, S., & Subhadhirasakul, S. (2007). Anti-allergic activity of some selected plants in the Zingiberaceae family. *Journal of Ethnopharmacology*, 109(3), 535-538.
- Thakker, J. N., Dalwadi, P., & Dhandhukia, P. C. (2013). Biosynthesis of gold nanoparticles using *Fusarium oxysporum* f. sp. *ubense* JT1, a plant pathogenic fungus. *ISRN Biotechnology*, 2013, 5.
- Thomas, D. A., Sarris, A. H., Cortes, J., Faderl, S., O'Brien, S., Giles, F. J., . . . Kantarjian, H. (2006). Phase II study of sphingosomal vincristine in patients with recurrent or refractory adult acute lymphocytic leukemia. *Cancer*, 106(1), 120-127.
- Tian, M., Lu, W., Zhang, R., Xiong, C., Ensor, J., Nazario, J., . . . Gupta, S. (2013). Tumor uptake of hollow gold nanospheres after intravenous and intra-arterial injection: PET/CT study in a rabbit VX2 liver cancer model. *Molecular Imaging and Biology*, 15(5), 614-624.
- Togashi, D. M., & Ryder, A. G. (2008). A Fluorescence Analysis of ANS Bound to Bovine Serum Albumin: Binding Properties Revisited by Using Energy Transfer. *Journal of Fluorescence*, 18(2), 519-526.
- Trump, B. E., Berezesky, I. K., Chang, S. H., & Phelps, P. C. (1997). The pathways of cell death: Oncosis, apoptosis, and necrosis. *Toxicologic Pathology*, 25(1), 82-88.
- Tunn, U. W. (2011). A 6-month depot formulation of leuprolide acetate is safe and effective in daily clinical practice: A non-interventional prospective study in 1273 patients. *BMC Urology*, 11(1), 15.
- Turkevich, J., Stevenson, P. C., & Hillier, J. (1951). A study of the nucleation and growth processes in the synthesis of colloidal gold. *Discussions of the Faraday Society*, 11(0), 55-75.
- Twine, S. M., Gore, M. G., Morton, P., Fish, B. C., Lee, A. G., & East, J. M. (2003). Mechanism of binding of warfarin enantiomers to recombinant domains of human albumin. *Archives of Biochemistry and Biophysics*, 414(1), 83-90.
- Uppal, M. A., Kafizas, A., Lim, T. H., & Parkin, I. P. (2010). The extended time evolution size decrease of gold nanoparticles formed by the Turkevich method. *New Journal of Chemistry*, 34(7), 1401-1407.
- Ventola, C. L. (2017). Progress in nanomedicine: Approved and investigational nanodrugs. *Pharmacy and Therapeutics*, 42(12), 742-755.
- Vermes, I., Haanen, C., Steffens-Nakken, H., & Reutelingsperger, C. (1995). A novel assay for apoptosis flow cytometric detection of phosphatidylserine expression on early apoptotic cells using fluorescein labelled annexin V. *Journal of Immunological Methods*, 184(1), 39-51.
- Vert, M., Doi, Y., Hellwich, K.-H., Hess, M., Hodge, P., Kubisa, P., . . . Schué, F. (2012). Terminology for biorelated polymers and applications (IUPAC Recommendations 2012). *Pure and Applied Chemistry*, 84(2), 377-410.

- Wan, J., Wang, J.H., Liu, T., Xie, Z., Yu, X.F., & Li, W. (2015). Surface chemistry but not aspect ratio mediates the biological toxicity of gold nanorods *in vitro* and *in vivo*. *Scientific Reports*, *5*, 11398.
- Wang, A., Ng, H. P., Xu, Y., Li, Y., Zheng, Y., Yu, J., . . . Fu, L. (2014). Gold nanoparticles: Synthesis, stability test, and application for the rice growth. *Journal of Nanomaterials*, *2014*, 3.
- Wang, F., Yu, L., Monopoli, M. P., Sandin, P., Mahon, E., Salvati, A., & Dawson, K. A. (2013). The biomolecular corona is retained during nanoparticle uptake and protects the cells from the damage induced by cationic nanoparticles until degraded in the lysosomes. *Nanomedicine: Nanotechnology, Biology and Medicine*, *9*(8), 1159-1168.
- Wang, L., Yuan, Y., Lin, S., Huang, J., Dai, J., Jiang, Q., . . . Shuai, X. (2016). Photothermo-chemotherapy of cancer employing drug leakage-free gold nanoshells. *Biomaterials*, *78*, 40-49.
- Wang, X., Wang, H., Wang, Y., Yu, X., Zhang, S., Zhang, Q., & Cheng, Y. (2016). A facile strategy to prepare dendrimer-stabilized gold nanorods with sub-10-nm size for efficient photothermal cancer therapy. *Scientific Reports*, *6*, 22764.
- Wang, Y., Liu, Y., Luehmann, H., Xia, X., Brown, P., Jarreau, C., . . . Xia, Y. (2012). Evaluating the pharmacokinetics and *in vivo* cancer targeting capability of Au nanocages by positron emission tomography imaging. *ACS Nano*, *6*(7), 5880-5888.
- Wang, Z., Chen, Z., Liu, Z., Shi, P., Dong, K., Ju, E., . . . Qu, X. (2014). A multi-stimuli responsive gold nanocage-hyaluronic platform for targeted photothermal and chemotherapy. *Biomaterials*, *35*(36), 9678-9688.
- Wang, Z., Sun, J., Qiu, Y., Li, W., Guo, X., Li, Q., . . . You, J. (2015). Specific photothermal therapy to the tumors with high EphB4 receptor expression. *Biomaterials*, *68*, 32-41.
- Weid, P.Y. v. d., & Zawieja, D. C. (2004). Lymphatic smooth muscle: The motor unit of lymph drainage. *The International Journal of Biochemistry & Cell Biology*, *36*(7), 1147-1153.
- Weiss, J. N. (1997). The Hill equation revisited: Uses and misuses. *The FASEB Journal*, *11*(11), 835-841.
- Wolfram, J., Yang, Y., Shen, J., Moten, A., Chen, C., Shen, H., . . . Zhao, Y. (2014). The nano-plasma interface: Implications of the protein corona. *Colloids and Surfaces B: Biointerfaces*, *124*, 17-24.
- Xie, H., Wang, Z. J., Bao, A., Goins, B., & Phillips, W. T. (2010). *In vivo* PET imaging and biodistribution of radiolabeled gold nanoshells in rats with tumor xenografts. *International Journal of Pharmaceutics*, *395*(1), 324-330.
- Xu, R. (2008). Progress in nanoparticles characterization: Sizing and zeta potential measurement. *Particuology*, *6*(2), 112-115.

- Xuan, M., Shao, J., Dai, L., Li, J., & He, Q. (2016). Macrophage cell membrane camouflaged Au nanoshells for *in vivo* prolonged circulation life and enhanced cancer photothermal therapy. *ACS Applied Materials & Interfaces*, 8(15), 9610-9618.
- Yallapu, M. M., Chauhan, N., Othman, S. F., Khalilzad-Sharghi, V., Ebeling, M. C., Khan, S., . . . Chauhan, S. C. (2015). Implications of protein corona on physico-chemical and biological properties of magnetic nanoparticles. *Biomaterials*, 46, 1-12.
- Yamasaki, K., Chuang, V. T. G., Maruyama, T., & Otagiri, M. (2013). Albumin-drug interaction and its clinical implication. *Biochimica et Biophysica Acta - General Subjects*, 1830(12), 5435-5443.
- Yamasaki, K., Maruyama, T., Kragh-Hansen, U., & Otagiri, M. (1996). Characterization of site I on human serum albumin: Concept about the structure of a drug binding site. *Biochimica et Biophysica Acta - Protein Structure and Molecular Enzymology*, 1295(2), 147-157.
- Yang, H. W., Liu, H. L., Li, M. L., Hsi, I. W., Fan, C. T., Huang, C. Y., . . . Wei, K. C. (2013). Magnetic gold-nanorod/ PNIPAAmMA nanoparticles for dual magnetic resonance and photoacoustic imaging and targeted photothermal therapy. *Biomaterials*, 34(22), 5651-5660.
- Yelin, D., Oron, D., Thiberge, S., Moses, E., & Silberberg, Y. (2003). Multiphoton plasmon-resonance microscopy. *Optics Express*, 11(12), 1385-1391.
- Yin, M., Dong, P., Chen, W., Xu, S., Yang, L., Jiang, F., & Liu, Y. (2017). Thermodynamics and mechanisms of the interactions between ultra-small fluorescent gold nanoclusters and human serum albumin, γ -globulins and transferrin: A spectroscopic approach. *Langmuir*, 33(21), 2108-2116.
- Youichiro, N., Jun, W., Ruth, D., Jiří, S., Karel, U., Takaaki, A., & Hiroshi, M. (1998). Early phase tumor accumulation of macromolecules: A Great difference in clearance rate between tumor and normal tissues. *Japanese Journal of Cancer Research*, 89(3), 307-314.
- Zamble, D. B., & Lippard, S. J. (1995). Cisplatin and DNA repair in cancer chemotherapy. *Trends in Biochemical Sciences*, 20(10), 435-439.
- Zanganeh, S., Spitler, R., Erfanzadeh, M., Alkilany, A. M., & Mahmoudi, M. (2016). Protein corona: Opportunities and challenges. *The International Journal of Biochemistry & Cell Biology*, 75, 143-147.
- Zhang, J., Li, C., Zhang, X., Huo, S., Jin, S., An, F.-F., . . . Liang, X. J. (2015). *In vivo* tumor-targeted dual-modal fluorescence/CT imaging using a nanoprobe co-loaded with an aggregation-induced emission dye and gold nanoparticles. *Biomaterials*, 42, 103-111.
- Zhang, P., Yang, X. X., Wang, Y., Zhao, N. W., Xiong, Z. H., & Huang, C. Z. (2014). Rapid synthesis of highly luminescent and stable Au₂₀ nanoclusters for active tumor-targeted imaging *in vitro* and *in vivo*. *Nanoscale*, 6(4), 2261-2269.

- Zhang, X. D., Wu, H. Y., Wu, D., Wang, Y. Y., Chang, J. H., Zhai, Z. B., . . . Fan, F. Y. (2010). Toxicologic effects of gold nanoparticles *in vivo* by different administration routes. *International Journal of Nanomedicine*, 5, 771-781.
- Zhang, Z., Wang, J., Nie, X., Wen, T., Ji, Y., Wu, X., . . . Chen, C. (2014). Near infrared laser-induced targeted cancer therapy using thermoresponsive polymer encapsulated gold nanorods. *Journal of the American Chemical Society*, 136(20), 7317-7326.
- Zhao, P., Li, N., & Astruc, D. (2013). State of the art in gold nanoparticle synthesis. *Coordination Chemistry Reviews*, 257(3), 638-665.
- Zhao, Y., Pang, B., Luehmann, H., Detering, L., Yang, X., Sultan, D., . . . Liu, Y. (2016). Gold nanoparticles doped with ¹⁹⁹Au atoms and their use for targeted cancer imaging by SPECT. *Advanced Healthcare Materials*, 5(8), 928-935.
- Zhao, Y., Sultan, D., Detering, L., Luehmann, H., & Liu, Y. (2014). Facile synthesis, pharmacokinetic and systemic clearance evaluation, and positron emission tomography cancer imaging of ⁶⁴Cu-Au alloy nanoclusters. *Nanoscale*, 6(22), 13501-13509.
- Zhou, B., Yang, J., Peng, C., Zhu, J., Tang, Y., Zhu, X., . . . Shi, X. (2016). PEGylated polyethylenimine-entrapped gold nanoparticles modified with folic acid for targeted tumor CT imaging. *Colloids and Surfaces B: Biointerfaces*, 140, 489-496.
- Zhou, J., Wang, Z., Li, Q., Liu, F., Du, Y., Yuan, H., . . . You, J. (2015). Hybridized doxorubicin-Au nanospheres exhibit enhanced near-infrared surface plasmon absorption for photothermal therapy applications. *Nanoscale*, 7(13), 5869-5883.
- Zou, L., Wang, H., He, B., Zeng, L., Tan, T., Cao, H., . . . Li, Y. (2016). Current approaches of photothermal therapy in treating cancer metastasis with nanotherapeutics. *Theranostics*, 6(6), 762.
- Zsila, F. (2013). Subdomain IB is the third major drug binding region of human serum Albumin: Toward the three-sites model. *Molecular Pharmaceutics*, 10(5), 1668-1682.
- Zunszain, P. A., Ghuman, J., Komatsu, T., Tsuchida, E., & Curry, S. (2003). Crystal structural analysis of human serum albumin complexed with hemin and fatty acid. *BMC Structural Biology*, 3, 6-6.

LIST OF PUBLICATIONS AND PAPER PRESENTED

Publications

1. **Foo, Y. Y.**, Kabir, M. Z., Periasamy, V., Malek, S. N. A., & Tayyab, S. (2018). Spectroscopic studies on the interaction of green synthesized-gold nanoparticles with human serum albumin. *Journal of Molecular Liquids*, 265, 105–113.
2. Shakir, S., **Foo, Y. Y.**, Rizan, N., Abd-ur-Rehman, H. M., Yunus, K., Moi, P. S., & Periasamy, V. (2018). Electro-catalytic and structural studies of DNA templated gold wires on platinum/ITO as modified counter electrode in dye sensitized solar cells. *Journal of Materials Science: Materials in Electronics*, 29(6), 4602-4611.
3. **Foo, Y. Y.**, Periasamy, V., Kiew, L. V., Kumar, G., & Malek, S. N. A. (2017). *Curcuma mangga*-mediated synthesis of gold nanoparticles: Characterization, stability, cytotoxicity, and blood compatibility. *Nanomaterials*, 7(6), 123–137.
4. **Foo, Y. Y.**, Periasamy, V., & Malek, S. N. A. (2015). Green synthesis of gold nanoparticles using aqueous ethanol extract of *Curcuma mangga* rhizomes as reducing agent. *AIP Conference Proceedings*, 1657(060008), 1–8.

Paper presented

- Oral presentations

1. **Foo, Y. Y.**, Periasamy, V., & Malek, S. N. A. (2017). Synthesis of biocompatible gold nanoparticle mediated by *Curcuma mangga* extract as a potential drug carrier. The Malaysian Local Chapter of the Controlled Release Society Inc. (MyCRS): Academia Networking Day. University of Malaya, Kuala Lumpur, Malaysia, 8th August 2017.
2. **Foo, Y. Y.**, Periasamy, V., & Malek, S. N. A. (2016). Photothermal effect of green-synthesized gold nanoparticles using aqueous ethanol extract of *Curcuma mangga* rhizomes on MCF-7 breast cancer cell. 21st Biological Sciences Graduate Congress 2016, University of Malaya, Kuala Lumpur, Malaysia, 15th–16th December 2016.
3. Manganelli, Serena, **Foo, Y.Y.**, Garcia, Alba, & Rubio, Laura. (2015). Genotoxicity of nanomaterials. Nanotoxicology – Potential Risks of Engineered Nanomaterials to Human Health and the Environment, Karolinska Institutet, Stockholm, Sweden, 20th–24th April 2015.
4. **Foo, Y. Y.**, Periasamy, V., & Malek, S. N. A. (2014). Green synthesis of gold nanoparticles using aqueous ethanol extract of *Curcuma mangga* rhizome. National Physics Conference (Perfik) 2014, Sunway Resort Hotel & Spa, Kuala Lumpur, Malaysia, 18th–19th November 2014.

- **Poster presentations**

1. **Foo, Y. Y.**, Periasamy, V., & Malek, S. N. A. (2017). Synthesis of biocompatible gold nanoparticle mediated by *Curcuma mangga* extract as a potential drug carrier. The Malaysian Local Chapter of the Controlled Release Society Inc. (MyCRS): Academia Networking Day. University of Malaya, Kuala Lumpur, Malaysia, 8th August 2017.
2. **Foo, Y. Y.**, Periasamy, V., & Malek, S. N. A. (2015). Green synthesis of biocompatible gold nanoparticles using methanol extract of *Curcuma mangga* rhizomes for biomedical applications. 20th Biological Sciences Graduate Congress 2015, Chulalongkorn University, Bangkok, Thailand, 9th–11th December 2015.

University of Malaya